TRANSPORTATION RESEARCH

RECORD

No. 1476

Bridges, Other Structures, and Hydraulics and Hydrology

Steel, Concrete, and Wood Bridges

A peer-reviewed publication of the Transportation Research Board

TRANSPORTATION RESEARCH BOARD
NATIONAL RESEARCH COUNCIL

NATIONAL ACADEMY PRESS
WASHINGTON, D.C. 1995

Transportation Research Record 1476
ISSN 0361-1981
ISBN 0-309-06114-8
Price: $37.00

Subscriber Category
IIC bridges, other structures, and hydraulics and hydrology

Printed in the United States of America

Sponsorship of Transportation Research Record 1476

GROUP 2—DESIGN AND CONSTRUCTION OF TRANSPORTATION FACILITIES
Chairman: Michael G. Katona, U.S. Air Force Armstrong Laboratory

Structures Section
Chairman: David B. Beal, New York State Department of Transportation

Committee on General Structures
Chairman: Donald J. Flemming, Minnesota Department of Transportation
John J. Ahlskog, Amar Bhajandas, Charles H. Bryant, Martin P. Burke, Jr., Frank J. Constantino, Paul F. Csagoly, Sheila Rimal Duwadi, Ian M. Friedland, C. Stewart Gloyd, Frederick Gottemoeller, Clellon Lewis Loveall, Ayaz H. Malik, Dennis R. Mertz, John Minor, Fred Moses, Andrzej S. Nowak, William J. Rogers, Ferdinand Tschemmernegg

Committee on Steel Bridges
Chairman: Charles W. Roeder, University of Washington
John J. Ahlskog, David R. Anderson, Charles J. Arnold, Mark D. Bowman, William G. Byers, Karen C. Chou, R. Scott Christie, Donald J. Flemming, Dan M. Frangopol, C. Stewart Gloyd, Michael A. Grubb, Tim J. Ingham, Ray W. James, Michael J. Koob, Abba G. Lichtenstein, Ayaz H. Malik, Richard A. Parmelee, Camille George Rubeiz, Robert A. P. Sweeney, John A. Van Lund, Ivan M. Viest, Gerald M. White, Stanley W. Woods, Ben T. Yen

Committee on Concrete Bridges
Chairman: Robert A. P. Sweeney, CN Rail-Operations
A. Emin Aktan, Robert N. Bruce, Jr., George A. Christian, John A. Corven, Anthony Ralph Cusens, Catherine French, C. Stewart Gloyd, H. Henrie Henson, James J. Hill, James R. Hoblitzell, Michael E. Kreger, Susan N. Lane, Rafael Manzanarez, Barney T. Martin, Bruno Massicotte, David I. McLean, Charles M. Minervino, Philip C. Perdikaris, Basile G. Rabbat, James E. Roberts, Henry G. Russell, David H. Sanders, Joseph Showers, Holger S. Svensson, Julius F. J. Volgyi, Jr., Stanley W. Woods

Committee on Dynamics and Field Testing of Bridges
Chairman: Andrzej S. Nowak, University of Michigan
Secretary: Harold R. Bosch, Federal Highway Administration
Baidar Bakht, Michael G. Barker, Ian G. Buckle, Juan Ramon Casas Ruis, James D. Cooper, Bruce M. Douglas, Dan M. Frangopol, Gongkang Fu, Yozo Fujino, Michel Ghosn, Hidayat N. Grouni, Robert J. Heywood, F. Wayne Klaiber, Sudhakar R. Kulkarni, Przemyslaw Maliszkiewicz, John C. Mathis, Wallace T. McKeel, Jr., Fred Moses, John A. Olandt, Suresh G. Pinjarkar, Mohsen A. Shahawy, Kwok-Nam Shiu, Robert A. P. Sweeney, Sami W. Tabsh, Ivan M. Viest, Ben T. Yen, Robert C. Y. Young

Transportation Research Board Staff
Robert E. Spicher, Director, Technical Activities
D. W. Dearasaugh, Jr., Engineer of Design
Nancy A. Ackerman, Director, Reports and Editorial Services
Naomi Kassabian, Editor

Sponsorship is indicated by a footnote at the end of each paper. The organizational units, officers, and members are as of December 31, 1994.

Transportation Research Record 1476

Contents

Foreword

This volume is composed of 21 papers that were presented in five different sessions sponsored by the TRB Structures Section at the 1995 TRB Annual Meeting.

The Committee on Steel Bridges and the Committee on Concrete Bridges sponsored sessions at which the first four papers were presented. Barker uses load factor ratings to show significant reserve capacity of slab-on-steel girder bridges. Tabsh and Marchese investigate the span capability of typical composite beams designed with AASHTO's conventional method and the alternative approach of the American Institute for Steel Construction. Expansion of inelastic design provisions to include noncompact steel bridge sections is discussed by Hartnagel et al., and results from the testing of two full-size long-span, high-strength prestressed concrete bridge girders are presented by Ahlborn et al.

The next 13 papers were presented in two sessions sponsored by the Committee on Dynamics and Field Testing of Bridges. Roschke describes the testing of a posttensioned flat slab bridge using a series of actuators to simulate dynamic wheel loads. Saunders et al. investigate several retrofitting measures for improving the seismic performance of existing bridge substructures. Uzgider et al. describe a damage detection procedure to identify rehabilitation required for bridges on the Turkish railway system, and Casas investigates the feasibility and accuracy of various models to predict dynamic behavior of various bridge types. The dynamic load factor under truck traffic of various load ranges and axle configurations is determined by Nassif and Nowak, who conclude that it needs to be considered on the basis of girders of maximum stress values. Cook et al. model the interface between friction piles and loessial soil for analysis when the structure being supported is subjected to seismic loading. Barker investigates the impact of AASHTO guide specifications for evaluation of bridge strength on 73 bridges in Missouri. Deatherage et al. examine data collected during testing of an existing bridge near Knoxville, Tennessee, using controlled loads. Pentas et al. describe a comprehensive experimental investigation conducted to obtain thermally induced movements of a bridge in Louisiana. Aktan et al. present nondestructive dynamic field testing and structural identification studies of three steel-stringer bridges. Fugler et al. perform a comprehensive statistical analysis of data from underwater inspection of bridges in Louisiana. Siros and Spyrakos utilize a three-dimensional model for nonlinear creep analysis of composite integral bridges. Hasan et al. conduct a field evaluation to assess the in-service performance in Indiana of bridge decks reinforced with epoxy-coated steel.

The Committee on General Structures sponsored a session in which the final four papers were presented. Thippeswamy and GangaRao analyze five in-service jointless bridges for primary live and dead loads and also for secondary loads caused by temperature, creep, shrinkage, settlement, and other forces. Fenske et al. present a computer-based bridge analysis procedure that incorporates nonprismatic member behavior. Wojakowski and Hossain conduct long-term monitoring of six bridge decks in Kansas that have interlayer membranes. Dober-Young and Tsiatas evaluate the results of monitoring a red oak stress-laminated timber bridge.

Load Rating and Ultimate Capacity Evaluation of Compact Steel Girder Bridges

MICHAEL G. BARKER

Slab-on-steel girder bridges are highly redundant structures and show significant redistribution capacity and a large reserve capacity in the inelastic range. To achieve consistent levels of safety over the bridge inventory, consideration should be given to the ultimate capacity of the system. First-hinge and inelastic limit rating methods for a single-span and a three-span composite bridge were examined. The rating methods were the AASHTO load factor rating maximum-strength operating level rating, the AASHTO Guide Specifications for the Strength Evaluation of Existing Steel and Concrete Bridges rating, and the single-girder and the system shakedown limit ratings. Examination of limits beyond the first hinge yielded insight into the available reserve capacity. A comparison of the methods showed that even simple-span bridges have significant reserve capacity beyond the first hinge. The additional capacity was attributed to transverse redistribution of forces. However, the total reserve capacity was not uniform for all bridges. The three-span bridge example shows that, in addition to this transverse component, longitudinal redistribution of forces adds even more to the reserve capacity. The first-hinge rating methods do not reflect the relative ultimate load-carrying capacities of one-span and multispan bridges.

Bridges in the United States must be inspected periodically for maintenance reasons and to ensure bridge safety to the public. Along with the visual inspection, the load-carrying capacity (bridge rating) must be evaluated to determine the maximum truck loads allowed on the structure. The specific outcome of a bridge rating is the rating factor (RF), which is the ratio of the calculated live load capacity of the bridge to the rating vehicle live load effects (*1*). Typically, standard AASHTO rating vehicles, or state specific vehicles, are used to approximate the live load effects. The RF multiplied by the rating truck weight is the rating load. If RF is greater than unity, the bridge is deemed adequate for the rating vehicle weight. If RF falls below one, the bridge is considered under capacity for that rating truck load, and the bridge needs to be posted for restrictive loading or speed, or both, or some other action must be implemented.

Currently there are three AASHTO methods for rating beam and girder bridges: the allowable stress rating (ASR) (*1*), the load factor rating (LFR), (*1*) and the Guide Specifications for the Strength Evaluation of Existing Steel and Concrete Bridges (*2*) (to be abbreviated herein as STRENGTH). For ASR, the nominal live loads on the structure and all other nominal loads shall not produce stresses in the member that exceed allowable stresses. For LFR, the criteria are that factored live loads and factored other loads must not exceed the nominal strength of the member. The STRENGTH method is a load and resistance factor method using variable site-specific factors. Factored live loads and factored other loads must not exceed the factored member capacity.

Department of Civil Engineering, E2509 EBE, University of Missouri-Columbia, Columbia, Mo. 65211.

All three of the above rating methods use the AASHTO Manual for Maintenance Inspection of Bridges (*2*) as a guide for bridge inspection. The ASR and LFR methods are also contained in the manual. Although not used in this paper there is also the newly approved AASHTO Manual for Condition Evaluation of Bridges (*3*). The STRENGTH method is similar to the LFR method. However, the load, resistance, and impact factors are variable and depend on site-specific characteristics. The nominal capacity is the same as the LFR maximum-strength capacity, and both methods use the same level of structural usefulness (i.e., single flexural hinge).

The STRENGTH method is a product of NCHRP reports by Imbsen et al. and Moses and Verma, (*4,5*). The researchers' goal was to produce "a flexible comprehensive approach to bridge evaluation which best utilizes the economic resources available and yet maintains consistent and definable criteria for bridge safety." To achieve this, a reliability framework was adopted that allowed a range of load and resistance factors (partial load factors), depending on site-specific bridge characteristics and the level of effort in the rating process. The result is a rating method that approaches a uniform level of safety for the first hinge limit state for steel bridges.

Slab-on-steel multigirder bridges are highly redundant structures and show significant redistribution capacity and a large reserve capacity in the inelastic range. To properly evaluate the ultimate safety of a bridge, this reserve capacity should be considered. Barker and Galambos (*6*) present a method to examine the ultimate load-carrying capacity of bridges on the basis of the inelastic system limit states. The ultimate limit is the maximum shakedown (incremental collapse) limit of the multigirder system. Galambos et al. (*7*) concluded in an NCHRP report that the shakedown limit of the system, coupled with the load and resistance factors developed for the STRENGTH method, is a rational and consistent method to rate existing bridges for the ultimate safety.

The shakedown limit state of a statically indeterminate structure subjected to variable repeated loads is that extreme load set that will just prevent incremental collapse (*8*). Consider a moving load, or a set of moving loads, that exceed the elastic limit load but are less than the plastic collapse load. As these loads cross an indeterminate structure, increments of inelastic rotation occur at sections along the structure. If the loads are less than or equal to the shakedown limit load (incremental collapse load), on further loadings the incremental increase in rotations and deflections decrease in magnitude and eventually vanish. After the permanent deformations stabilize, all future loadings not exceeding the shakedown limit load are resisted in an elastic manner without producing further damage

The shakedown limit state of the bridge system shows significant additional capacity over the single-girder first-hinge methods. This reserve capacity is from (*a*) more realistic elastic distribution of

forces, (*b*) bridge system redistribution of forces in the longitudinal and transverse directions, and (*c*) implementation of inelastic system limit states. However, as expected, this additional capacity is not uniform for all bridges. Therefore, even though the single-girder first-hinge methods may yield the same rating factor for two particular bridges, the ultimate system capacity of the bridges may be very different. Although both bridges may meet or exceed intended safety requirements, this leads to inconsistency in the ultimate safety of the structures.

OBJECTIVES

To achieve consistent levels of safety over the bridge inventory, consideration should be given to the ultimate capacity of the system or, stated relative to current rating methods, consideration must be given to the reserve capacity beyond the first hinge limit. This paper examines rating methods for two existing bridges comprising compact sections: a single-span composite bridge and a three-span composite bridge. The rating methods are the LFR maximum-strength operating level rating, the STRENGTH rating, and the single-girder and the system shakedown limit ratings using STRENGTH method load and resistance factors. The specific objectives are to

1. Compare LFR and STRENGTH single-girder first-hinge ratings to single-girder shakedown limit state ratings. These comparisons will illustrate the reserve capacity available in the longitudinal direction,
2. Compare LFR and STRENGTH single-girder first-hinge ratings to system shakedown limit state ratings. These comparisons will illustrate the system reserve capacity available in the longitudinal and transverse directions, and
3. Examine the relative reserve capacities between the single-span bridge and the three-span bridge. This will illustrate the inconsistency inherent in the current single-girder first-hinge rating methods when considering ultimate load capacities.

LFR AND STRENGTH RATING PROCEDURES

For the LFR maximum-strength operating level and the STRENGTH method, the general load capacity rating equation is

$$\Gamma_D D_n + (RF)\Gamma_L L_n(DF)(1 + I) = \Phi M_n \tag{1}$$

or, solving for the rating factor,

$$RF = \frac{\Phi M_n - \Gamma_D D_n}{\Gamma_L L_n(DF)(1 + I)} \tag{2}$$

where

RF = rating factor ($RF \geq 1$ is sufficient capacity),
Γ_D = dead load factor,
Γ_L = live load factor,
Φ = resistance factor,
M_n = nominal resistance,
D_n = nominal dead load,
L_n = nominal live load from the rating vehicle,
DF = lateral distribution factor, and
I = impact factor.

Table 1 shows the respective factors for the LFR and STRENGTH rating equations. For the STRENGTH ratings, the factors are selected from site-specific load and resistance characteristics (*2*). Because both the LFR and STRENGTH methods are first hinge limits, the RF is determined by the critical first hinge section.

SHAKEDOWN PROCEDURES

As a moving load that exceeds the elastic limit but is less than the plastic-collapse limit crosses a statically indeterminate structure, increments of inelastic rotation occur at various sections in the structure. If this load is less than the incremental collapse load, the incremental inelastic rotations during each load pass decrease in magnitude and eventually vanish. After the incremental inelastic rotations vanish, all future loadings are resisted in an elastic manner.

In a statically indeterminate structure, inelastic behavior is characterized by internal residual moments that remain after removal of the load (similar to a support settlement). Thus, after loading and unloading, the structure contains internal forces and moments that are self-equilibrating. For this structure to resist the subsequent load elastically, the applied elastic dead and live load moments plus the internal residual moment must remain in the elastic range at each section. Using the assumption of an ideal elastic-plastic moment-curvature relationship (to represent work-hardening of the compact section) and including the rating factor, this criterion can be written:

$$(RF)M_L^+ + M_D + m_r = M_P^+ \quad \text{for positive moment, and} \tag{3a}$$

$$(RF)M_L^- + M_D + m_r = M_P^- \quad \text{for negative moment} \tag{3b}$$

everywhere in the structure, where

RF = rating factor,
$M_L^{+,-}$ = positive and negative live load moments,
M_D = dead load moment,
m_r = residual moment, and
$M_P^{+,-}$ = positive and negative moment capacity.

TABLE 1 Load and Resistance Factors for Rating Methods

RATING METHOD	Resistance Factor Φ	Dead Load Factor Γ_D	Live Load Factor Γ_L	Impact Factor I
LFR Operating	1.00	1.30	1.30	50/(L+125)≤0.3 based on span length (ft)
STRENGTH and Shakedown Limit	0.90 slight deterioration with vigorous maintenance	1.20 with 20% additional depth on the overlay thickness	1.30 low truck volume and effective weight enforcement	0.10 smooth riding surface

At the maximum shakedown limit, the left and right sides of Equation 3 are equal for the critical moment direction at the critical sections. Shakedown is a limit state controlled by variable repeated loads or moving loads; thus, shakedown is a major concern for bridges.

Shakedown Limit for Single-Girder Analyses

For the single-girder shakedown limit analyses, the lateral distribution factor is used to estimate the loads applied to the girder and the shakedown analysis assumes only longitudinal redistribution of forces and no lateral or transverse system interaction.

The shakedown limit upper-bound mechanism (*6*) method can be employed to find the shakedown limit state rating factor. The equation is based on virtual work of moments working through a mechanism motion. Using Figure 1, the mechanism equation can be written:

$$(RF)[M_L^1\theta^1 + M_L^2\theta^2 + M_L^3\theta^3] + [M_D^1\theta^1 + M_D^2\theta^2 + M_D^3\theta^3] = [M_P^1\theta^1 + M_P^2\theta^2 + M_P^3\theta^3] \quad (4)$$

or, solving for the rating factor,

$$RF = \frac{[M_P^1\theta^1 + M_P^2\theta^2 + M_P^3\theta^3] - [M_D^1\theta^1 + M_D^2\theta^2 + M_D^3\theta^3]}{[M_L^1\theta^1 + M_L^2\theta^2 + M_L^3\theta^3]} \quad (5)$$

where the mechanism rotations θ are shown in Figure 1. The controlling shakedown rating factor is the minimum calculated from assumed kinematically admissible incremental mechanisms.

The STRENGTH method load, resistance, and impact factors are used in this paper for the shakedown limit analyses. Substituting in the STRENGTH method factors, the governing rating factor equation becomes

$$RF = \frac{\Phi[M_n^1\theta^1 + M_n^2\theta^2 + M_n^3\theta^3] - \Gamma_D[D_n^1\theta^1 + D_n^2\theta^2 + D_n^3\theta^3]}{\Gamma_L[L_n^1\theta^1 + L_n^2\theta^2 + L_n^3\theta^3](DF)(1 + I)} \quad (6)$$

Shakedown Limit for System Analyses

Determining the shakedown limit of a single isolated girder entails finding the moment envelopes and solving Equation 6. In a bridge system, however, the longitudinal girders are no longer isolated and the interaction of the girders, slab, and transverse diaphragms make up a complicated load-resisting system. The bridge system shakedown limit state model is derived from the shakedown requirements, the bridge system elastic behavior, and global equilibrium equations (*5*). To develop the method, the bridge is assumed to have a global incremental collapse mechanism similar to that shown in Figure 1. For two-lane bridges under typical truck loading, Grundy (*9*) shows that a global mechanism controls for the collapse limit state. Only in a wide multilane bridge would one expect a local collapse mechanism.

The system shakedown limit equation involves condensing the system's elastic response and resistance into a global kinematic incremental collapse mechanism. Across a critical global bridge section, each girder must reach the Equation 3 shakedown condition. Summing the individual requirements across the transverse section:

For positive moment:

$$(RF)\sum_i M_L^+ + \sum_i M_D^+ + \sum_i m_r = \sum_i M_P^+ \quad (7a)$$

For negative moment:

$$(RF)\sum_i M_L^- + \sum_i M_D^- + \sum_i m_r = \sum_i M_P^- \quad (7b)$$

where Σ is the summing of the various moment quantities across the transverse section of the bridge.

In Equation 7, the individual girder residual moment fields, m_r, adjust to attain individual girder shakedown, but they are not necessarily in equilibrium in the individual girder sense. Transverse residual forces change the single-girder equilibrium requirements to meet system equilibrium. However, the system residual moment field, Σm_r, must still be in equilibrium with no applied loads.

The shakedown limit upper-bound mechanism method can again be employed to find the shakedown limit state rating factor of the entire bridge system. Using Figure 1, the mechanism equation can be written as follows:

$$(RF)\sum_i [M_L^1\theta^1 + M_L^2\theta^2 + M_L^3\theta^3] + \sum_i [M_D^1\theta^1 + M_D^2\theta^2 + M_D^3\theta^3] = \sum_i [M_P^1\theta^1 + M_P^2\theta^2 + M_P^3\theta^3] \quad (8)$$

or, solving for the rating factor and substituting in the STRENGTH method factors as was done for Equation 6:

$$RF = \frac{\Phi\sum_i [M_n^1\theta^1 + M_n^2\theta^2 + M_n^3\theta^3] - \Gamma_D\sum_i [D_n^1\theta^1 + D_n^2\theta^2 + D_n^3\theta^3]}{\Gamma_L\sum_i [L_n^1\theta^1 + L_n^2\theta^2 + L_n^3\theta^3](1 + I)} \quad (9)$$

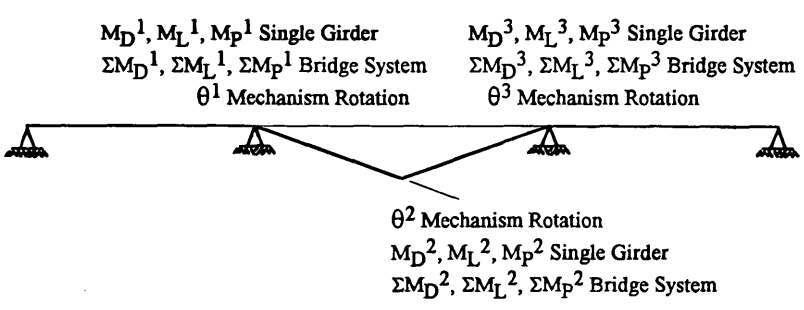

FIGURE 1 Single-girder and system shakedown mechanism.

where the global mechanism rotations, θ, are illustrated in Figure 1. Because the system analysis calculates the elastic live load moment in each girder, the equation no longer contains the lateral distribution factor. Equation 9 illustrates that the system shakedown limit state can be reduced to an equivalent single-girder analysis where the equivalent elastic moment envelope is the summation of all the individual girder elastic envelopes across the bridge section. Likewise, the equivalent dead load and resistance moments are the respective sums of the individual moments across the section. The controlling shakedown rating factor is the minimum calculated from assumed global kinematically admissible incremental mechanisms.

BRIDGE RATING EXAMPLES

Following are LFR maximum-strength operating, STRENGTH, single-girder shakedown limit, and system shakedown limit ratings for two example bridges (*10*). The first is a single-span composite bridge with a 13.4-m (44-ft) span, five girders spaced at 2.24 m (7.33 ft), and a 160-mm (6.25-in.) structural concrete deck with a 28-day compressive strength of 27.6 MPa (4,000 psi). The interior girders are W24 × 84 and the exterior girders are W24 × 76, both of 248-MPa (36-ksi) material. The second is a three-span continuous composite bridge with spans of 12.5, 16.2, and 12.5 m (41, 53, and 41 ft), five girders spaced at 2.24 m (7.33 ft), and a 171-mm (6.75-in.) structural concrete deck with a 28-day compressive strength of 27.6 MPa (4,000 psi). All the girders are W24 × 68 made of 248 MPa (36 ksi) material. The reinforcing steel over the interior pier supports is assumed to act compositely with the steel sections for both bridges. The bridges were selected to be similar in construction except for the longitudinal redundancy (three-span versus simple-span). Because the objective of this paper is to compare relative capacity ratings, for brevity, detailed specifics are not presented.

The AASHTO Type 3 rating vehicle is used because it yields the lowest rating factors for both bridges. For the STRENGTH method and the shakedown limit procedures, the factors are assumed as follows (Table 1): $\Phi = 0.90$, $\Gamma_D = 1.2$ with an increase of 20 percent on the overlay thickness, $\Gamma_L = 1.3$, and $I = 0.10$. The AASHTO S/D lateral distribution factors are used for all the single-girder analyses.

A grillage analysis routine developed specifically to analyze bridge systems for first hinge and shakedown limit states (*11*) is used for the single-girder and system dead load and live load force effect analyses. A post processor uses the results of the analysis to apply the rating equations (Equations 2, 6, and 9). The grillage program discretizes each span into tenth points and assumes admissible mechanism-positive rotations at each tenth point of each span.

Single-Span Bridge Example

The simple-span bridge has an LFR impact factor of 0.296, a lateral distribution factor of 1.257 (exterior girder controls for single-girder analyses), and a uniform dead load of 12.3 kN/m (0.84 kips/ft) of which 1.0 kN/m (0.07 kips/ft) is attributed to the wearing surface. Therefore, for the ratings using the STRENGTH factors, the nominal dead load moments are multiplied by a factor of $(11.3 + 1.2 * 1)/12.3 = 1.02$ to adjust for the 20 percent surface thickness increase.

Figure 2 illustrates the nominal dead and live load moments for the span. The single-girder LFR operating rating and STRENGTH rating from Equation 2 and Table 1 are:

$$RF = \frac{1605 - 1.3(275)}{1.30(268)1.257(1 + 0.296)}$$

$$= 2.20 \quad \text{(LFR operating rating), and}$$

$$RF = \frac{0.90(1605) - 1.2(1.02 * 275)}{1.30(268)1.257(1 + 0.10)}$$

$$= 2.30 \quad \text{(STRENGTH Rating)}$$

The STRENGTH rating is 4.6 percent higher than the LFR operating rating. This is expected because the STRENGTH factors represent a bridge that has good load and resistance characteristics. Barker et al. (*10*) compare the LFR and STRENGTH method on a data base of existing bridges elsewhere, and the results are not repeated here. Both methods are included here for reference purposes.

The single-girder shakedown limit is identical to a first hinge limit because there is no redundancy in the girder. This can be shown by Equation 5:

$$RF = \frac{0.90[0 + 1605(2\theta) + 0] - 1.2(1.02)[0 + 275(2\theta) + 0]}{1.3[0 + 268(2\theta) + 0](1.257)(1 + 0.10)}$$

$$= 2.30 \quad \text{(single-girder shakedown rating)}$$

As can be seen, a free hinge has no moment resistance or applied moment and, therefore, does not resist load or cause work in the equation. Because a simple-span isolated girder is not redundant, the first hinge is a failure and, thus, the rating is identical to the STRENGTH rating.

A simple-span bridge system, however, is redundant. A single hinge in one girder does not cause failure because the system has the capacity to redistribute forces in the transverse direction. Using the equivalent girder global moment summations in Figure 2 and Equation 9, the shakedown limit capacity of the system is

$$RF = \frac{0.90[0 + 8522(2\theta) + 0] - 1.2(1.02)[0 + 1326(2\theta) + 0]}{1.3[0 + 1491(2\theta) + 0](1 + 0.10)}$$

$$= 2.84 \quad \text{(system shakedown rating)}$$

The one-span bridge system contains redundancy in the transverse direction. As shown by the system shakedown rating factor, the system has additional capacity beyond the first hinge.

Three-Span Bridge Example

The three-span bridge has LFR impact factors of 0.30 in the outer two spans, 0.29 over the interior pier supports, and 0.28 in the center span. The lateral distribution factor is 1.333 (interior girder controls for single-girder analyses) and a uniform dead load of 14 kN/m (0.96 kips/ft) of which 1.2 kN/m (0.08 kips/ft) is attributed to the wearing surface. Therefore, for the ratings using the STRENGTH factors, the nominal dead load moments are multiplied by a factor of $(12.8 + 1.2 * 1.2)/14 = 1.02$ to adjust for the 20 percent wearing surface thickness increase.

Figure 3 illustrates the nominal dead and live load moments for the span. The controlling first hinge location for the LFR operating rating and the STRENGTH rating is at the centerline of the center span. From Equation 2 and Table 1, the ratings are as follows:

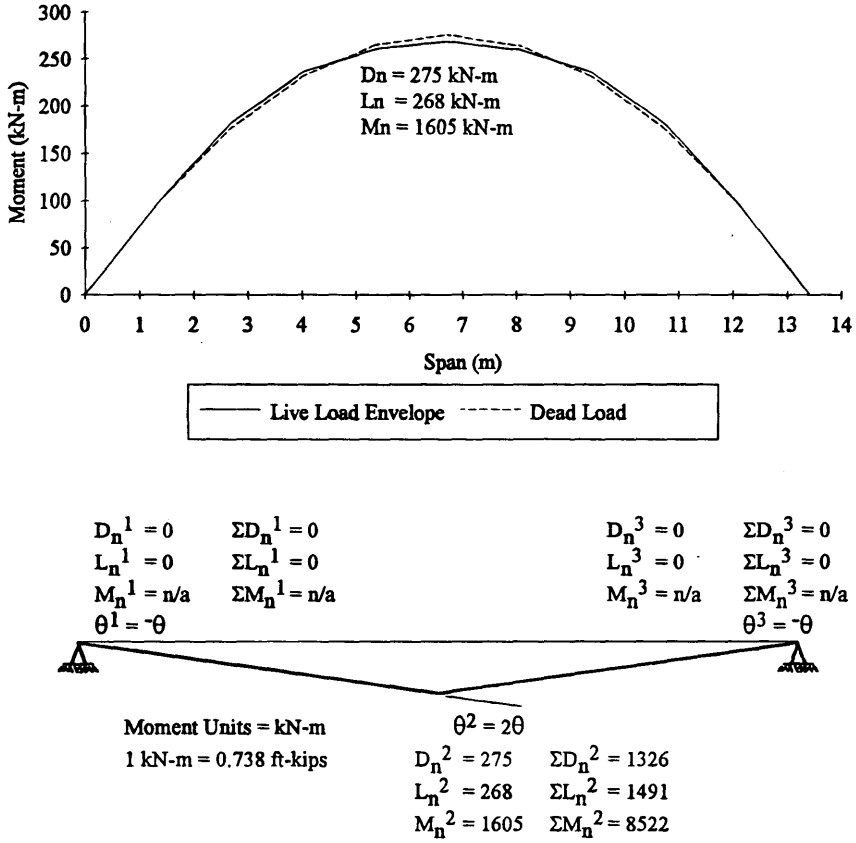

FIGURE 2 Simple-span nominal moments and incremental collapse mechanism.

$$RF = \frac{1483 - 1.3(187)}{1.30(221)1.333(1 + 0.28)}$$

$= 2.53$ (LFR operating rating), and

$$RF = \frac{0.90(1483) - 1.2(1.02 * 187)}{1.30(221)1.333(1 + 0.10)}$$

$= 2.63$ (STRENGTH Rating)

Again the STRENGTH rating is slightly higher (4 percent) than the LFR operating rating.

Unlike a simple-span bridge, a three-span single-girder bridge has redundancy in the longitudinal direction and, therefore, has reserve capacity beyond the first hinge. For this example, the critical incremental collapse mechanism is in the center span as shown in Figure 3. According to Equation 5, the single-girder shakedown limit rating is

$$RF = \{0.90[1466\theta + 1483(2\theta) + 1466\theta] - 1.2(1.02)[270\theta + 187(2\theta) + 270\theta]\}/\{1.3[129\theta + 221(2\theta) + 129\theta](1.333) \times (1 + 0.10)\} = 3.14 \text{ (single-girder shakedown rating)}$$

For the redundant center span, all three hinges in the mechanism do work. The single-girder shakedown limit is considerably higher (19.4 percent) than the STRENGTH method first hinge rating. However, the structure still has the capacity to redistribute forces in the transverse direction. According to Equation 9 and the same critical global incremental collapse mechanism shown in Figure 3, the system shakedown limit is

$$RF = \{0.90[7446\theta + 7416(2\theta) + 7446\theta] - 1.2(1.02)[1253\theta + 929(2\theta) + 1353\theta]\}/\{1.3[754\theta + 1273(2\theta) + 754\theta] \times (1 + 0.10)\} = 3.65 \text{ (system shakedown rating)}$$

The three-span bridge system is a highly redundant system and, as shown by the system shakedown rating factor, it has a large reserve capacity over the first hinge.

COMPARISON OF RATING METHODS

Table 2 shows the ratings for the different methods. For both bridges, the STRENGTH ratings exceed the LFR operating ratings by a few percent. For the STRENGTH factors chosen, this is typical. If the bridges showed significant deterioration or higher truck volume, the results would be reversed (*10*).

Because the shakedown rating analyses use the STRENGTH method load and resistance factors, only comparisons between these methods are presented. The one-span single-girder shakedown rating is the same as the STRENGTH first-hinge rating. The simple-span bridge has no redundancy to redistribute forces longitudinally after this hinging. However, the three-span single-girder bridge has longitudinal redundancy at the negative pier regions. This redistribution capacity results in a load capacity increase of 19.4 percent

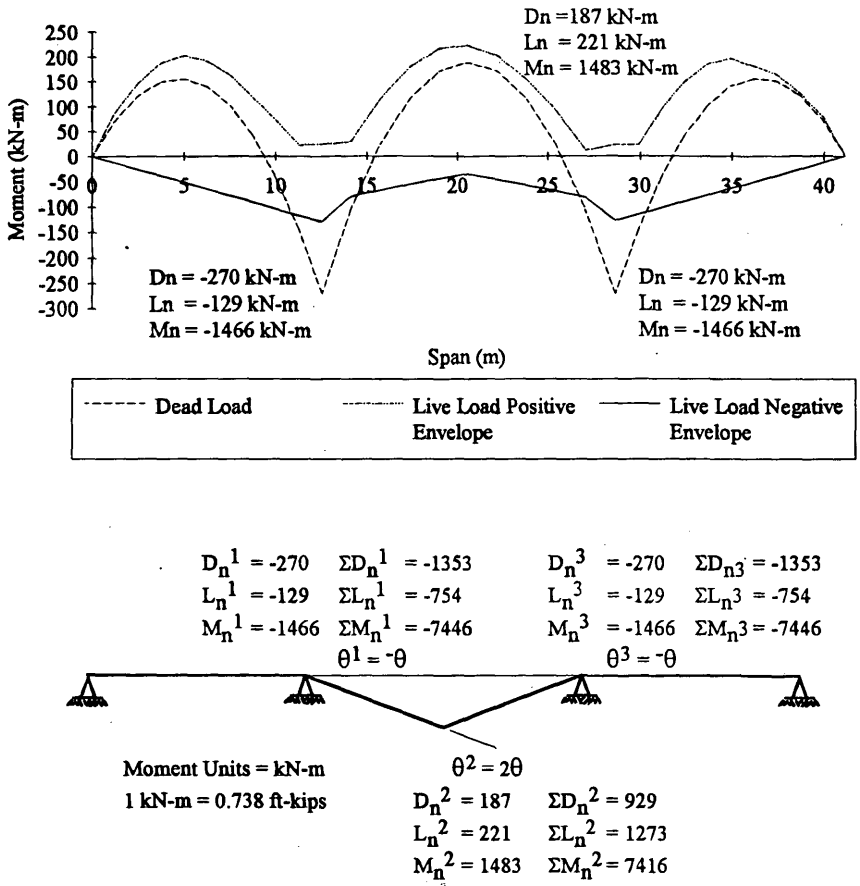

FIGURE 3 Three-span nominal moments and incremental collapse mechanism.

over the STRENGTH rating. Therefore, for single-girder analyses, although there is no additional capacity over the first hinge for simple-span bridges, there is significant reserve capacity for multi-span bridges.

The system shakedown limit considers both longitudinal and transverse redundancy in the structure. The results are as follows: the single-span system shakedown rating is 23.5 percent larger than the first-hinge STRENGTH rating and the three-span system shakedown rating is 38.8 percent larger than the first-hinge STRENGTH rating. The STRENGTH method infers consistent safety for both bridges for a first hinge limit. However, Table 2 shows that the safety is no longer consistent when examining the ultimate shakedown limit rating.

Both bridges show a significant load capacity increase caused by transverse redundancy: 23.5 percent for the simple-span bridge and 16.2 percent for the three-span bridge as illustrated by the percent increase of the system shakedown rating over the single-girder shakedown rating. This value represents the reserve capacity inher-

TABLE 2 Summary of Ratings

Rating Method	One-Span Bridge Example	Three-Span Bridge Example
LFR Operating Rating	2.20	2.53
STRENGTH Rating	2.30	2.63
Single-Girder Shakedown Rating	2.30	3.14
System Shakedown Rating	2.84	3.65
Single Girder Shakedown % Increase Over STRENGTH	0%	19.4%
System Shakedown % Increase Over STRENGTH	23.5%	38.8%
System Shakedown % Increase Over Single-Girder Shakedown	23.5%	16.2%

ent in any multigirder structure. Therefore, if this reserve capacity is similar for all multigirder bridges, it does not reflect inconsistency in the ultimate safety between the bridges.

The ultimate safety difference stems from the longitudinal redistribution characteristics. This is directly illustrated by the single-girder shakedown rating increase over the STRENGTH ratings. The three-span girder shows 19.4 percent additional strength and the one-span girder has no additional strength.

SUMMARY AND CONCLUSIONS

Multigirder steel bridges are highly redundant structures and show a large reserve capacity in the inelastic range over the capacity calculated from first hinge limit methods. To achieve consistent levels of safety over the bridge inventory, consideration should be given to the ultimate capacity of the system. This paper examines rating methods for a single-span and a three-span bridge. The rating methods are the LFR maximum strength operating level rating, the STRENGTH rating, and the single-girder and the system shakedown limit ratings. The following are conclusions from this work.

1. The three-span single-girder shakedown rating is 19.4 percent higher than the first-hinge STRENGTH method rating. This is because of longitudinal redundancy. There is no increase for the one-span single-girder ratings because the girder is not redundant. The current LFR and STRENGTH methods do account for some longitudinal redistribution by allowing a 10 percent redistribution of negative pier moments for bridges comprising compact sections. However, this adjustment is arbitrary and does not apply to this three-span bridge because the positive moment region is critical for the first hinge rating.
2. The system shakedown ratings were significantly higher than the STRENGTH first hinge ratings. The additional capacity can be divided between longitudinal and lateral redundancy. The lateral redundancy shows a somewhat uniform increase for the two bridges and is not responsible for the higher overall increase for the three-span bridge. This larger increase is a result of longitudinal redistribution as discussed earlier. However, it is important to note that even the simple-span bridge shows a 23.5 percent reserve capacity over that of the first-hinge rating.
3. The important rating comparison for examining the consistency of rating methods is the additional load capacity caused by the longitudinal redistribution. This is because the transverse redistribution is nearly uniform for the two bridges, thus making this contribution irrelevant for comparing reserve capacities at ultimate limits. However, the increase as a result of longitudinal redundancy is pronounced with the three-span bridge and nonexistent for the one-span bridge. This illustrates inconsistency in ultimate capacity when using single-hinge limit rating methods.

FUTURE WORK

To consider the ultimate load capacity of bridges in a rating procedure, either inelastic limit state procedures must be standardized or a longitudinal redundancy adjustment must be incorporated. In addition, this paper presents results for bridges comprising compact sections. To encompass all types of bridges, the redistribution characteristics for bridges comprising noncompact sections need to be investigated. To study these topics, a current research project (*12*) is testing three large-scale composite bridge girders: 1 three-span girder with compact sections and 2 two-span girders with noncompact sections. One major objective of this work is to develop comprehensive inelastic design and rating procedures for steel-girder bridges. In addition, this work assumes a global incremental collapse mechanism. Transverse contributions in a local mechanism may occur in wider bridges.

REFERENCES

1. *Manual for Maintenance Inspection of Bridges*. AASHTO, Washington, D.C., 1983.
2. *Guide Specifications for Strength Evaluation of Existing Steel and Concrete Bridges*. AASHTO, Washington, D.C., 1989.
3. Manual for Condition Evaluation of Bridges, AASHTO, Washington, D.C., 1994.
4. Imbsen, R., W. Liu, R. Schamber, and R. Nutt. *NCHRP Report 292: Strength Evaluation of Existing Reinforced Concrete Bridges*. TRB, National Research Council, Washington, D.C., 1987.
5. Moses, F., and D. Verma. *NCHRP Report 301: Load Capacity Evaluation of Existing Bridges*, TRB, National Research Council, Washington, D.C., 1987.
6. Barker, M. G., and T. V. Galambos. Shakedown Limit State of Compact Steel Girder Bridges. *Journal of Structural Engineering*, ASCE, Vol. 118, No. 4, April 1992, pp. 986–998.
7. Galambos, T. V., R. T, Leon, C. E. French, M. G. Barker, and B. E. Dishongh. *NCHRP Report 352: Inelastic Rating Procedures for Steel Beam and Girder Bridges*. TRB, National Research Council, Washington, D.C., 1993.
8. Neal, B. G. *The Plastic Methods of Structural Analysis*, John Wiley & Sons, New York, 1956.
9. Grundy, P. Shakedown Design of Bridges. Presented at 1st National Structural Engineering Conference, Institute of Engineering, Australia, Aug. 1987.
10. Barker, M. G., D. M. Koenig, and L. M. Magruder. *Load Rating Steel and Concrete Girder Bridges in Missouri*. Missouri Cooperative Highway Research Program Report 91-1. Missouri Highway and Transportation Department, Jefferson City, 1994.
11. Barker, M. G. *The Shakedown Limit State of Slab-On-Girder Bridges*. Thesis, University of Minnesota, Minneapolis, June 1990.
12. Barker, M. G. *Development and Experimental Verification of Inelastic Design Procedures for Steel Bridges Comprising Noncompact Sections*. National Science Foundation, Washington, D.C., 1993–1996.

Publication of this paper sponsored by Committee on Steel Bridges.

Span Capability of Noncompact Composite Steel Bridge Beams

SAMI W. TABSH AND DAVID MARCHESE

Typical composite beams made from rolled sections that do not satisfy the ductility requirement of AASHTO, as presented by Equation 10-128a of the specifications, are investigated for span capability. The analysis considers various sized rolled sections and three beam spacings. The sections are designed in accordance with AASHTO's conventional method and American Institute for Steel Construction, (AISC's) alternative approach. The conventional method is based on limiting the flexural capacity of such sections to the moment at the onset of yielding. AISC's alternative approach, on the other hand, is based on partial plastic stress distribution across the section and has been adopted by AASHTO in its 1994 interim. A parametric study was carried out to investigate the effects of live load intensity, material strengths, and cross-section dimensions on the span capability. The study indicates that AISC's alternative approach can extend the span length of rolled steel beams by about 15 percent over beam designs that are based on AASHTO's conventional method.

In general, steel bridges designed according to AASHTO's load factor design method (*1*) are proportioned for several conditions. They are required to satisfy the maximum design load, overloading condition, and service load. Designing for the maximum load ensures that a bridge is capable of supporting extremely heavy traffic in a rare emergency situation while undergoing some permanent deformations. The maximum design load is based on multiples of the service loads with an additional coefficient for the live load component, including impact. The ultimate capacity of a girder in flexure, ϕM_n, should be at least equal to the factored load effect, M_u:

$$\phi M_n \geq M_u \tag{1}$$

where $\phi = 1.0$ and M_u is defined by AASHTO Group I loading as

$$M_u = 1.3\,[M_{DL1} + M_{DL2} + (5/3)\,M_{L+I}] \tag{2}$$

where

M_{DL1} = dead load moment on noncomposite steel section,
M_{DL2} = superimposed dead load moment on composite section, and
M_{L+I} = live load and impact moment.

The overload case is needed for control of permanent deformations in a bridge member caused by occasional passing of overly heavy vehicles weighing 167 percent more than the design live load and impact. Maximum stress associated with dead load and live load flexural effects in the steel section for this case is limited to 95 percent of the yield stress, F_y, that is,

$$f_{DL1} + f_{DL2} + (5/3) f_{L+I} \leq 0.95\,F_y \tag{3}$$

where

f_{DL1} = stress caused by dead load on noncomposite steel section,
f_{DL2} = stress caused by superimposed dead load on composite section,
f_{L+I} = stress caused by live load plus impact on composite section.

Other design requirements include checking live load deflection and fatigue life of structural members at service load conditions. Shear load rarely governs for composite sections made up of rolled steel beams and concrete decks because the selection of the steel section is often dictated by flexure. Such a selection usually results in a large area of web.

Recently, Tabsh (*2*) showed that composite steel bridge girders that do not pass the ductility requirement of AASHTO, as presented by Equation 10-128a of the specifications, possess more ductility than many reinforced concrete sections with reinforcement that satisfies the code. In this study, typical composite steel girders in flexure are analyzed for span capability. The sections are designed following both current AASHTO's conventional method and American Institute for Steel Construction's (AISC's) alternative approach. The alternative approach was published in a 1992 newsletter by AISC (*3*). The newsletter proposes a method for computing the ultimate strength of composite sections in positive bending that does not satisfy the ductility requirement of AASHTO. The approach is based on limiting the concrete compressive strain at the top of the deck to 0.002 instead of 0.003. The lower limit on the top strain ensures that the steel section starts yielding before concrete crushes. The 0.002 strain level at the top of the concrete slab satisfies the current requirement, which is based indirectly on a factor of safety on the order of 1.625. AISC's approach has been adopted recently by AASHTO in its 1994 interim (*1*).

AASHTO'S DESIGN PROCEDURE

The ultimate strength of compact composite steel beams designed by AASHTO is based on the fully plastic stress distribution shown in Figure 1. Composite beams in positive bending qualify as compact when their steel section meets two requirements. First, the distance from the compression flange to the neutral axis in plastic bending, D_{cp}, should satisfy the following inequality:

$$\frac{D_{cp}}{t_w} \leq \frac{9615}{\sqrt{F_y}} \tag{4}$$

S. W. Tabsh, Department of Civil and Environmental Engineering, University of Houston, Houston, Tex. 77204-4791. D. Marchese, Modjeski and Masters, Inc., P.O. Box 2345, Harrisburg, Pa. 17105.

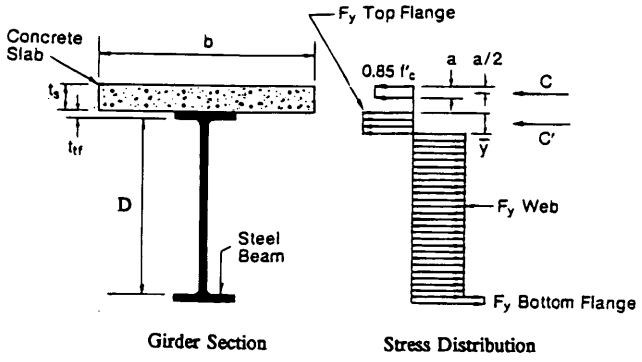

FIGURE 1 Stress distribution for compact composite beams.

where t_w is the web thickness and F_y is in megapascals The second requirement limits the compression depth from the top of the concrete slab in plastic bending, D_p, to the following value:

$$D_p \leq \frac{d + t_s + t_h}{7.5} \tag{5}$$

where

d = depth of steel section (cm),
t_s = thickness of concrete slab (cm), and
t_h = thickness of the concrete haunch (cm).

For constructibility purposes, AASHTO limits the ratio of the projecting top compression flange width, b', to its thickness, t, not to exceed the value determined by the following formula:

$$\frac{b'}{t} = \frac{2200}{\sqrt{1.3\,(f_{DL1})_{tf}}} \tag{6}$$

where $(f_{DL1})_{tf}$ is the top flange compressive stress (in megapascals caused by noncomposite dead load. The limitation imposed on the flange in Equation 6 should be satisfied by both compact and noncompact composite beams.

When the steel section does not satisfy the compactness requirements of Equations 4 and 5, AASHTO requires that the maximum strength of the section to be taken be equal to the moment capacity at first yield, M_y. For this case it is more convenient to work with stresses instead of moments; thus, the total stress should satisfy the following:

$$1.3\,[f_{DL1} + f_{DL2} + (5/3)\,f_{L+I}] \leq F_y \tag{7}$$

where f_{DL1}, f_{DL2}, and f_{L+I} were defined earlier.

AISC'S ALTERNATIVE APPROACH

The basis behind AASHTO's Equation 10-128a, as presented in Equation 5, is to ensure a ductile mode of failure. Therefore, to prevent a potential crushing of the concrete deck before significant strains are developed in the steel section, the maximum allowable strain at the top of the deck, ϵ_c, is set equal to $0.003/F$, where F is a factor of safety greater than 1.0. With ϵ_c equal to this value, the strain at the bottom of the steel section, ϵ_s, is set equal to 0.012, which is about ten times the yield strain for AASHTO M270 Grade 36 steel, as shown in Figure 2. From similar triangles, the following expression for the compression depth, D_p, can be obtained:

$$D_p = \frac{d + t_s + t_h}{0.012 + (0.003/F)}\,(0.003/F) \tag{8}$$

which becomes the same as Equation 5 if $F = 1.625$.

As mentioned earlier, an alternative approach to replace AASHTO's ductility requirement has been recently proposed by AISC (*3*) and is now adopted by AASHTO in its 1994 interim. This approach is based on compatibility of strains and equilibrium of forces. The maximum strength of the composite section is evaluated using a cross section with an assumed strain distribution consistent with the current requirement. AISC suggests that ϵ_c be equal to 0.003 divided by the factor F (equal to 1.625), thus resulting in ϵ_c approximately equal to 0.002. The maximum capacity of the composite girder is then computed by taking the first moment of all tensile and compressive forces on the cross section about the neutral axis. The location of the neutral axis involves an iterative procedure. Whitney's concrete block model cannot be used here because ϵ_c is not equal to 0.003. Therefore, Hognestad's parabola (*4*) can be used to model the stress-strain curve for $\epsilon_c \leq \epsilon_o$ as given by

$$f_c = f'_c\left[2\left(\frac{\epsilon_c}{\epsilon_o}\right) - \left(\frac{\epsilon_c}{\epsilon_o}\right)^2\right] \tag{9}$$

where ϵ_o is the value of the concrete strain at the maximum compressive stress, usually taken equal to 0.002.

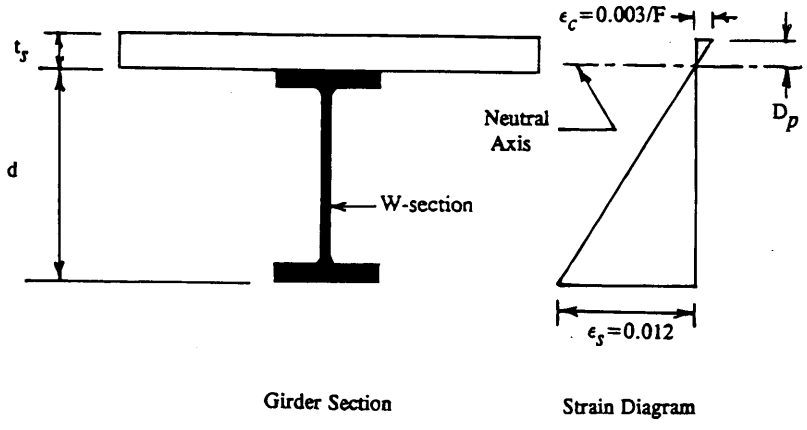

FIGURE 2 Derivation of AASHTO's ductility requirement.

The average height of the concrete stress block (normalized with respect to f'_c), k_1, can be computed from the following:

$$k_1 = \frac{\text{(Average Stress)}}{f'_c} = \frac{1}{f'_c}\left[\frac{1}{\epsilon_c}\int_0^{\epsilon_c} f_c\, d\epsilon_c\right] \tag{10}$$

which, when combined with Equation 9, reduces to

$$k_1 = \alpha - \frac{1}{3}\alpha^2 \tag{11}$$

where α is equal to the ratio ϵ_c/ϵ_o. Further, the location of the centroid of the concrete stress block from the top (normalized with respect to the compression depth), k_2, can be obtained from

$$k_2 = 1 - \frac{\int_0^{\epsilon_c} f_c\,\epsilon_c\, d\epsilon_c}{\epsilon_c \int_0^{\epsilon_c} f_c\, d\epsilon_c} \tag{12}$$

which, after integration, takes the following form:

$$k_2 = \frac{4-\alpha}{12-4\alpha} \tag{13}$$

in which α is equal to 1.0 because $\epsilon_c = \epsilon_o = 0.002$. Substitution of $\alpha = 1.0$ in Equations 11 and 13 results in k_1 and k_2 equal to 2/3 and 3/8, respectively. Graphical definition of k_1 and k_2 is shown in Figure 3.

DUCTILITY CONSIDERATIONS

Structural design specifications usually impose some limitations on the design variables to ensure a ductile mode of failure in flexure. For example, AASHTO requires the compression depth of the neutral axis in plastic bending of compact sections, D_p, not to exceed the value presented in Equation 5. Otherwise, the section is labeled noncompact, and the capacity is reduced accordingly.

Moment-curvature (M-ϕ) relationships can be used to investigate the ductility of sections in flexure. The shape of the (M-ϕ) curve depends on the section dimensions, material strength and distribution, and the presence of axial loads. In general, ductility measures are usually derived on the basis of the ratio of the maximum deformation to the deformation at the onset of yielding. Ductility can be assessed in terms of the curvature, ϕ, as follows:

$$\eta_{cur} = \frac{\phi_{max}}{\phi_y} \tag{14}$$

where

η_{cur} = curvature ductility ratio,
ϕ_{max} = curvature at ultimate, and
ϕ_y = curvature at yield.

The curvature at ultimate is normally obtained at a point that corresponds to a maximum concrete strain in compression equal to 0.003. The use of η_{cur} to measure the ductility has an advantage because it is a function of the cross-sectional geometric and strength properties only.

Several composite steel girders are considered in the ductility analysis. The composite sections are composed of a concrete slab either 1.83 m (72 in.) wide by 20.3 cm (8 in.) thick or 2.74 m (108 in.) wide by 22.9 cm (9 in.) thick; a 2.54-cm (1-in.) concrete haunch; and a rolled steel beam. Nominal concrete compressive strength of 27.5 MPa (4,000 psi) and AASHTO M270 Grade 36 steel are specified for the deck and rolled beams, respectively. For simplicity, the reinforcement in the concrete deck is neglected in the analysis. Investigation of all composite steel beams in plastic bending indicated that 13 out of the 16 beams do not satisfy the ductility requirement and are thus considered noncompact according to AASHTO.

Curvature ductility ratios are evaluated for all the composite steel sections. Typical results of the generated (M-ϕ) curves for three composite beams are shown in Figure 4. A summary of the curvature ductility ratios for all beams is presented in Table 1.

SPAN CAPABILITY OF ROLLED BEAMS

Simply supported composite steel girders are designed following both conventional AASHTO and AISC's alternative approach. Five

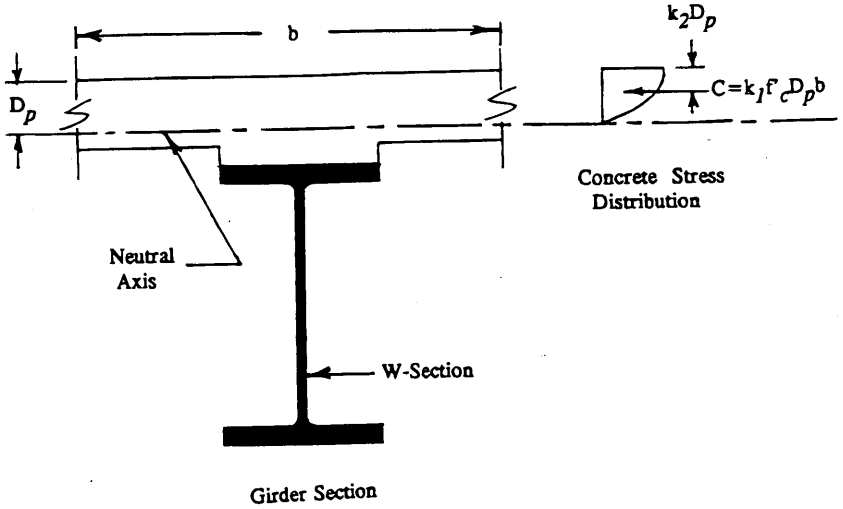

FIGURE 3 Definition of k_1 and k_2 for Hognestad's concrete stress model.

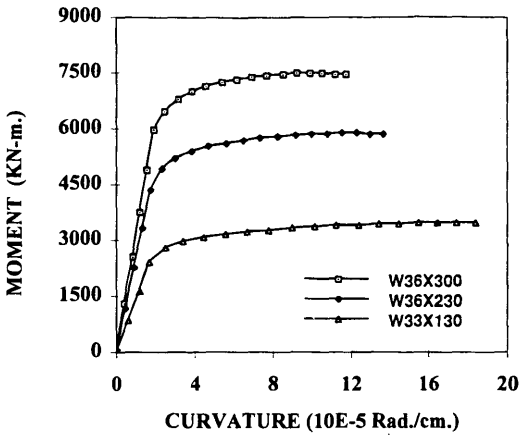

FIGURE 4 Moment-curvature curves for composite beams (1 kip-in. = 0.113 kN-m, 1 in. = 2.54 cm).

steel sections of varying sizes are considered: W36 × 300, W36 × 260, W36 × 230, W36 × 182, and W36 × 150. The span capability of the composite sections is determined on the basis of an HS-20 loading and taking into account different beam spacings. For uniformity of the analysis, all bridges are assumed to be 12.8 m (42 ft) wide. Table 2 shows the number of girders, girder spacing, and slab thickness for each bridge layout. Each bridge is considered to have two normal-size parapets weighing 7.36 kN/m (505 lb/ft) each; an integral wearing surface 1.27 cm (0.5 in.) thick; stay-in-place forms 0.718 kPa (15 psf); and a future wearing surface of 1.44 kPa (30 psf). The composite girders are assumed to have an average concrete haunch 2.54 cm (1 in.), nominal concrete strength of 27.6 MPa (4,000 psi) and AASHTO M270 Grade 36 structural steel. The weight of miscellaneous details, such as diaphragms and cross bracing on an interior girder is approximated at 146 N/m (10 lb/ft).

The study showed that 12 of the 15 beams considered are classified noncompact according to AASHTO, as shown in Table 3. The noncompact beams satisfied all requirements but the one related to ductility (Equation 5). The span capability of the 12 noncompact beams was governed by the maximum bottom flange stress requirement (Equation 7). On the other hand, the remaining three compact beams and the beams designed using AISC's alternative approach were all governed by AASHTO's overloading criteria (Equation 3). The study showed that designs based on AISC's approach can extend the span capabilities by approximately 15 percent, depending on the size and spacing of the girders.

PARAMETRIC STUDY

In this section, the parametric study considers unshored interior simply supported composite bridge beams. The reference design is composed of a concrete slab 1.83 m (72 in.) wide by 20.3 cm (8 in.) thick; a concrete haunch 2.54 cm (1 in.) thick; and a W36 × 230 steel beam. Nominal concrete strength of 27.6 MPa (4,000 psi) and AASHTO M270 Grade 36 steel are used in the slab and rolled beam, respectively. The stay-in-place forms weight is assumed to be 0.718 kPa (15 psf). Superimposed dead load includes the weight of parapets and 30 psf (1.44 kPa) future wearing surface. The weight of the diaphragms and bracing is estimated at 146 N/m (10 lb/ft). The analysis showed that the span capability of this rolled section for HS20 loading using AASHTO's conventional approach and AISC's alternative method is 24.1 and 27.5m (79.0 and 90.0 ft), respectively.

The reference girder is investigated for various live loads. Figure 5 shows that the span capability of the section increases by 7 percent if H20 loading is used. The corresponding decrease in the span for HS25 loading is about 8 percent.

TABLE 1 Curvature Ductility Ratio for Composite Steel Beams

Beam Section	b (m.)	t_s (cm.)	$(d+t_s+t_h)/7.5$ (cm.)	D_p (cm.)	ϕ_y (10^{-5} Rad/cm.)	ϕ_{max} (10^{-5} Rad/cm.)	η_{cur}
W36x300	1.83	20.3	15.8	25.4	1.71	11.5	6.74
	2.74	22.9	16.2	25.7	1.52	13.5	8.94
W36x280	1.83	20.3	15.7	24.9	1.69	12.0	7.13
	2.74	22.9	16.1	23.9	1.50	14.1	9.37
W36x260	1.83	20.3	15.7	24.5	1.67	12.6	7.52
	2.74	22.9	16.0	22.2	1.49	14.6	9.79
W36x230	1.83	20.3	15.5	23.8	1.65	13.5	8.16
	2.74	22.9	15.9	19.6	1.48	15.7	10.6
W36x210	1.83	20.3	15.8	23.6	1.59	13.8	8.64
	2.74	22.9	16.2	18.0	1.43	16.8	11.7
W36x182	1.83	20.3	15.7	23.3	1.55	14.9	9.62
	2.74	22.9	16.0	15.6	1.41	19.4	13.8[a]
W36x150	1.83	20.3	15.5	19.2	1.52	16.6	10.9
	2.74	22.9	15.9	12.8	1.38	23.5	17.1[a]
W36x130	1.83	20.3	14.6	16.6	1.60	18.1	11.4
	2.74	22.9	14.9	11.1	1.46	27.2	18.6[a]

[a]These sections are compact

1 cm. = 0.394 in., 1 m. = 3.28 ft.

TABLE 2 Bridge Design Cases Considered in the Analysis

Case	Bridge Width (m.)	Number of Girders	Girder Spacing (m.)	Thickness of Slab[a] (cm.)
1	12.8	7	1.83	20.3
2	12.8	5	2.75	22.9
3	12.8	4	3.66	25.4

[a]Slab thickness includes 1.27 cm. (0.5 in.) integral wearing surface
1 m. = 3.28 ft., 1 cm. = 0.394 in.

The effect of increasing the material strengths on the girder capacity is studied. An increase of 23 percent in the span capability can be obtained if the yield stress of the rolled beam, F_y, is increased to 345 MPa (50 ksi) and all other design variables are kept the same, as indicated in Figure 6. However, the analysis showed that increasing the nominal concrete strength from 27.6 to 41.4 MPa (4,000 to 6,000 psi) resulted in a negligible gain in the span length. This gain is because the decrease in the compression depth of the neutral axis in plastic bending as a result of the increase in f'_c was not enough to qualify the section as compact. When a high-yield strength is used, together with the AISC's alternative approach, the span capability of the rolled beam may become so large that it may be difficult to satisfy the allowable live load deflection, particularly if the bridge is designed for HS25 live loading.

The sensitivity of the span length to changes in the geometry of the composite section is presented in Figures 7 and 8. Figure 7 shows the effect of increasing the web depth of the *W*-section, whereas Figure 8 investigates the addition of a cover plate along the bottom flange of the rolled beam. The analysis indicated that a 32 percent increase in the span can be achieved with a "fictitious" section having the same flanges of a W36 × 230 but with a web depth of 1.27 m (50 in.). The amount of increase in the span length caused by the addition of a cover plate 1.91 cm (0.75 in.) thick to the bottom flange is 22 percent. The analysis also showed that an increase in the thickness of the concrete slab does not add much to the capacity of the composite beam because the neutral axis is in the slab.

For all the cases considered in the parametric study, the span capability of the design ratio of AISC to AASHTO remained within a narrow range (between 1.13 and 1.15).

SUMMARY AND CONCLUSIONS

AASHTO's conventional design method and AISC's alternative approach for composite beams in positive bending are outlined. The ductility of composite beams is evaluated for several sections using the curvature ductility ratio. The span capability of typical rolled steel sections is obtained for designs based on AASHTO's load factor design method and AISC's alternative approach. The sensitivity of the span capability of the beam to changes in the design variables is also included. The results of the study suggests the following conclusions, which are relevant for simply supported composite beams:

TABLE 3 Span Capabilities Based on Conventional AASHTO and AISC's Alternative Approach

Steel Beam	Girder Spacing (m.)	AASHTO (m.)	AISC (m.)	AISC / AASHTO
W36x300	1.83	28.1	32.0	1.14
	2.75	22.3	25.6	1.15
	3.66	18.9	21.7	1.15
W36x260	1.83	25.9	29.6	1.14
	2.75	20.7	23.5	1.13
	3.66	17.4	19.8	1.14
W36x230	1.83	24.1	27.5	1.14
	2.75	19.2	21.7	1.13
	3.66	16.2	18.3	1.13
W36x182	1.83	20.7	23.8	1.15
	2.75	16.5	18.9	1.15
	3.66	15.9	15.9	1.00[a]
W36x150	1.83	18.3	21.0	1.15
	2.75	16.5	16.5	1.00[a]
	3.66	14.0	14.0	1.00[a]

[a]Section is compact and governed by AASHTO's overloading criteria
1 m. = 3.28 ft.

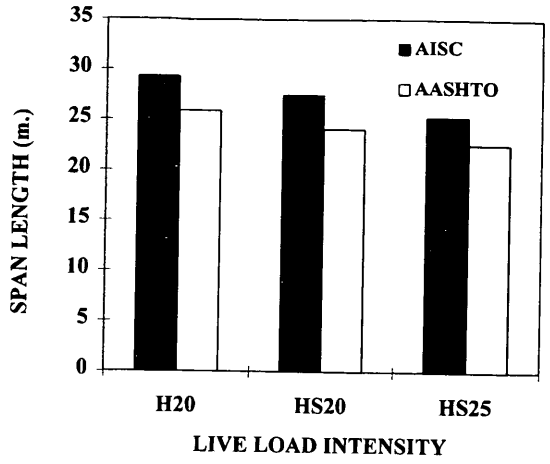

FIGURE 5 Sensitivity analysis for live load intensity (1 ft = 0.305 m).

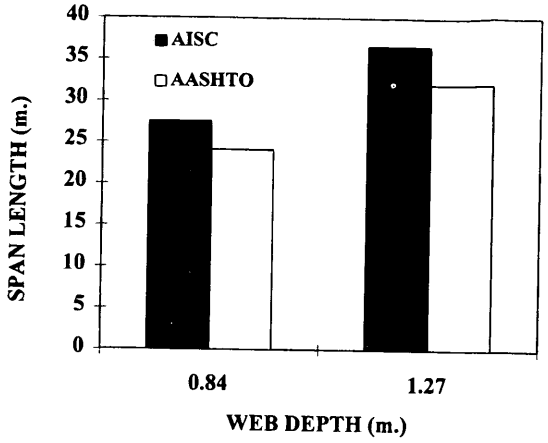

FIGURE 7 Sensitivity analysis for web depth (1 in. = 2.54 cm).

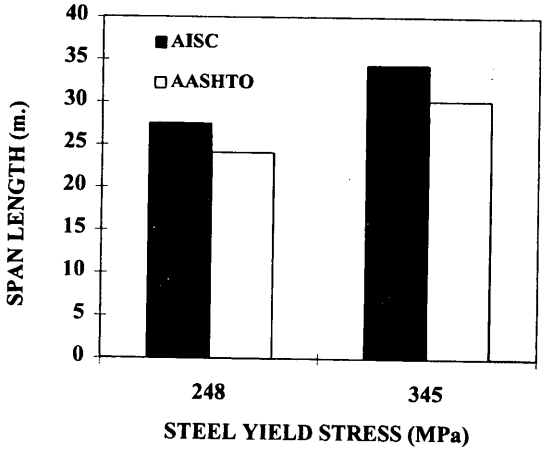

FIGURE 6 Sensitivity analysis for steel grade (1 ksi = 6.89 MPa).

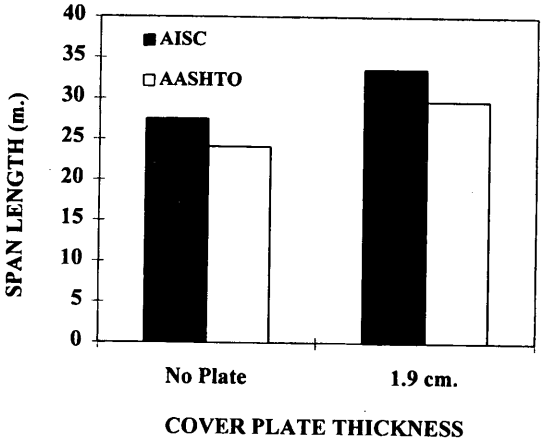

FIGURE 8 Sensitivity analysis for bottom flange cover plate (1 in. = 2.54 cm).

1. The curvature ductility ratio of typical noncompact beams that do not satisfy the ductility requirement of Equation 128-a in the AASHTO specifications varies between 6 and 12.
2. Most composite beams with W36 rolled sections do not satisfy AASHTO's ductility requirement and hence are considered noncompact.
3. Designs based on the alternative approach can extend the span capability of rolled beams over AASHTO's conventional method by about 15 percent, depending on the size and spacing of the beams.
4. Span capability of rolled beams significantly increases with an increase in yield stress and web depth and with the presence of a cover plate on the bottom flange. Slab thickness and concrete strength have a negligible effect on the beam capacity.

The maximum allowable live load deflection requirement may become difficult to satisfy when the alternative approach is used together with a high-yield strength, particularly for designs based on the HS25 loading.

REFERENCES

1. *Standard Specifications for Highway Bridges*, 15th ed. and 1994 Interim. AASHTO, Washington, D.C., 1992.
2. Tabsh, S. W. Ductility of Non-Compact Composite Steel Bridge Beams. *Engineering Journal*, AISC, Vol. 31, No. 1, 1994, pp. 21–30.
3. *Highway Structures Design Handbook, Alternative Approach to Satisfy the AASHTO Ductility Requirement for Compact Composite Sections in Positive bending*, 3rd issue. AISC Marketing, Inc., May 1992.
4. Kent, D. C., and R. Park. Flexural Members with Confined Concrete. *Journal of the Structural Division*, ASCE, Vol. 97, No. ST7, July 1971, pp. 1969–1990.

Publication of this paper sponsored by Committee on Steel Bridges.

Experimental Verification of Load and Resistance Factor Inelastic Design Limits

BRYAN A. HARTNAGEL, MICHAEL G. BARKER, AND DAVID C. WEBER

More economical steel bridge designs can be realized using inelastic design provisions. However, current provisions apply only to compact steel bridges. Expanding inelastic design provisions to include noncompact sections is desirable because of the wide use of plate girders with thin webs. Previous research has shown that noncompact girders have predictable moment-rotation behavior that can be incorporated into inelastic design provisions. However, even though the analytical tools exist, large-scale testing is necessary to validate theoretical engineering practice. A report is given of the first of three composite continuous girder tests from a project with the objectives of validating current inelastic design procedures and developing new provisions for bridges comprising noncompact girders. The first girder test was a half-scale, three-span composite beam with compact sections extracted from a prototype bridge designed using inelastic procedures. The two future tests will be two-span composite beams with noncompact sections. The results of the first girder test show that current analytical techniques effectively predict the elastic and inelastic behavior of compact girders. The first test also validated the inelastic design provisions at all design limit states.

Alternate load factor design (ALFD) procedures (*1*) were adopted by AASHTO in 1986. The procedures account for the reserve strength inherent in multiple-span steel girder bridges by allowing redistribution of negative elastic moments at piers to adjacent positive moment regions. The redistribution causes slight inelastic rotation at the interior pier sections and some residual permanent deflection. After the redistribution, the structure achieves shakedown (*2*): deformations stabilize and future loads are resisted elastically.

ALFD procedures allow the designer more flexibility and the possibility of more economical designs by eliminating the need for providing cover plates and numerous flange transitions at negative moment regions (*3*). However, ALFD provisions apply only to steel beam bridges comprising compact sections. Expanding inelastic design provisions to include noncompact sections is desirable because of the wide use of plate girders with thin webs. The ALFD provisions are incorporated into the new AASHTO load and resistance factor design (LRFD) bridge design specifications (*4*).

A joint National Science Foundation, American Institute for Steel Construction, American Iron and Steel Institute, and Missouri Highway and Transportation Department project (*5*), Development and Experimental Verification of Inelastic Design Procedures for Steel Bridges Comprising Noncompact Sections, will consist of three composite, single-girder tests. Simulated moving loads in the elastic and inelastic range will be cyclically applied to the test girders. Afterward, the girders will be tested to failure. The first test consists of a three-span, compact, rolled section, whereas the other two tests will be two-span girders with typical noncompact plate girder sections. The project will verify design limit behavior of current inelastic design provisions for compact bridges and extend the inelastic procedures to include noncompact plate girder designs. This paper presents the design, modeling, and experimental results from the first three-span rolled-beam test (*6*).

Department of Civil Engineering, E2509 EBE, University of Missouri-Columbia, Columbia, Mo. 65211.

INELASTIC DESIGN OF STEEL GIRDER BRIDGES

The ALFD inelastic design procedures (*1*) specify requirements at service load levels (nominal dead load plus normal traffic), overload levels (nominal dead load plus an occasional heavy vehicle), and maximum load levels (factored dead load plus a one-time maximum vehicle). Inelastic LRFD provisions (*4*) specify these load combinations as Service I, Service II, and Strength I, respectively. The LRFD procedures also have a separate fatigue load combination. Following are the LRFD load combinations at the respective load levels:

$$\text{Fatigue—}D + 0.75L(1 + I), \quad (1a)$$
$$\text{Service I—}D + 1.00L(1 + I), \quad (1b)$$
$$\text{Service II—}D + 1.30L(1 + I), \text{ and} \quad (1c)$$
$$\text{Strength I—}1.25DC + 1.50DW + 1.75L(1 + I), \quad (1d)$$

where

D = dead load,
L = live load with lateral distribution factor,
I = impact factor (33 percent),
DC = component dead load (slab, beam, and barrier curbs), and
DW = wearing surface.

Fatigue and Service I load levels are for fatigue and live-load deflection checks. At the Service II level, after interior pier elastic moments are redistributed to adjacent positive moment regions, the design requirement or limit-state criterion is a limiting stress at positive moment regions. Finally, at the Strength I level, a mechanism must not form with the application of the factored loads.

PROTOTYPE BRIDGE DESIGN

The three-span (18.3, 23.2, and 18.3 m) (60, 76, and 60 ft), two-lane prototype bridge was designed according to the LRFD bridge design specifications using the inelastic design provisions (*4*). Four W30 × 108 rolled beam girders with a girder spacing of 3.05 m (10 ft) were used to support the 11.0-m (36-ft) wide roadway. Yield strength of the steel was 345 MPa (50 ksi). The deck was 203 mm (8 in.) thick with 27.6 MPa (4,000 psi) compressive strength concrete and Grade 60 reinforcing steel. A future wearing surface of 0.57 kPa (12 psf) [about 25 mm (1 in.) of asphalt] and barrier curbs

weighing 4.45 kN/m (305 plf) [a standard 406-mm (16-in.) concrete barrier curb] were considered as composite dead loads. The bridge was designed assuming unshored construction. Also, the LRFD HS20 design vehicle in combination with a 9.34 kN/m (640 plf) lane load was used for determining live load effects. The 1/2-scale experimental test girder models an interior girder from the bridge system. Following is a description of the design procedures used to check an interior girder from the prototype bridge (*6*).

Elastic Analysis Techniques

A prismatic elastic analysis was used to compute the noncomposite dead load moments, and elastic nonprismatic analyses were used to determine the composite dead load moments and the live load plus impact moment envelopes. LRFD lateral distribution factors were used to approximate the amount of live load applied to a single girder. According to the LRFD specifications (*4*), the lateral distribution factor is 0.77 lanes per girder for moment and 0.95 lanes per girder for shear and reactions. Figure 1 shows the total live and dead load moment envelopes for the prototype girder including impact and distribution factors.

Design Limit States

Fatigue Limit State

The LRFD provisions provide spacing requirements for shear studs on the basis of fatigue and strength limits. Stud fatigue controlled the overall fatigue requirements for this design. A total of 204 pairs of shear studs 25 mm (1 in.) in diameter by 127 mm (5 in.) in length were spaced at 305 mm (12 in.) on center along the girder, except for a spacing of 152 mm (6 in.) on center at the end supports.

Service I Deflection Limit State

LRFD live-load deflection criteria for slab-on-girder bridges are subject to designer discretion (*4*). However, LRFD provisions do allow the use of past practice for deflection control. The current deflection limit (*7*) suggested by AASHTO is equal to the span length L, in feet, divided by 800 for bridges with no pedestrian traffic. The controlling design deflection resulted from two loaded lanes of the design truck plus impact. Assuming equal distribution of load to all the girders, a distribution factor of two lanes/four girders = 0.5, along with an elastic nonprismatic analysis, was used to calculate the maximum live load plus impact deflection of 30 mm (1.18 in.). The suggested AASHTO deflection limit is calculated as 76 ft × 12 in./800 = 1.14 in. or 29 mm for the prototype.

Service II Limit State

The Service II check ensures that the nominal dead load plus occasional overload vehicles equal to $1.30L(1 + I)$ will not cause excessive deformations. Elastic overload moments are redistributed because of inelastic pier rotations, θ, caused by localized yielding at the pier. The pier sections resist bending according to the following relationship (*4*):

$$M = M_P[0.7 - 60.0(\theta)] \leq 1.0 \qquad (2)$$

where $-0.008 \leq \theta \leq 0$ radians, and

M = LRFD moment rotation curve for pier sections,
θ = inelastic rotation at pier in radians (negative), and
M_P = section plastic moment capacity.

Residual moments that remain in the beam after the load is removed can be related to the pier rotation through an inelastic conjugate beam analysis developed by Dishongh (*8*). The moments at the piers, M_a and M_b, and the residual moment are

$$M_a = \frac{\frac{EI\theta_i}{L}}{\left[-\frac{A}{3} - \frac{1}{2} + \frac{\frac{B}{6} + \frac{1}{4}}{B+1}\right]} \qquad M_b = \frac{-M_a}{2B+2}$$

$$M_R = M_a + M_b \qquad (3a, 3b, 3c)$$

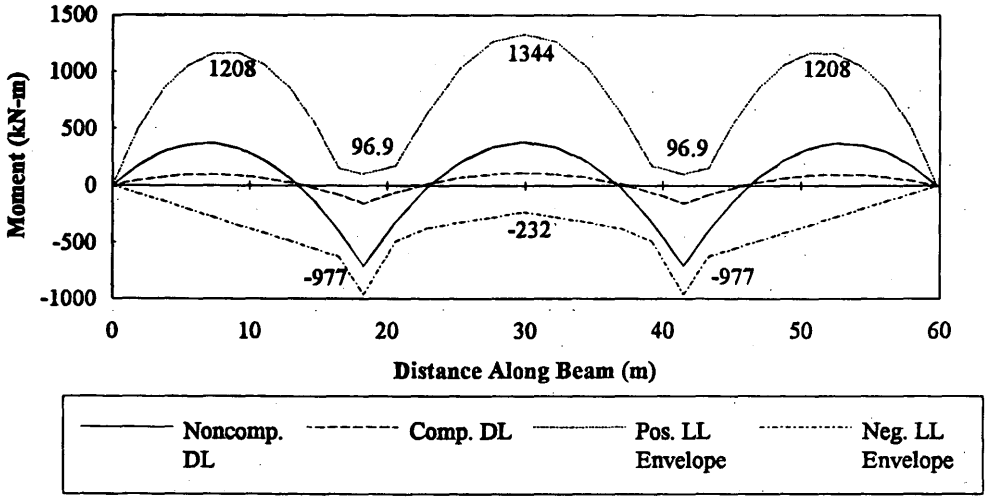

FIGURE 1 Moment envelopes for the prototype girder.

where A and B are ratios of the two outer-span lengths to the center-span length equal to 18.3/23.2 = 0.79. At the pier section, the applied Service II moment [$D + 1.30L(1 + I)$] (Equation 1c), plus the residual moment (Equation 3c) is equal to the actual moment defined by the moment rotation relationship (Equation 2) for the pier sections:

$$[D + 1.30L(1 + I)] + M_R = M_P[0.7 - 60(\theta)] \quad (4)$$

Solving Equation 4 for the plastic rotation at the pier section yields $\theta = -0.00083$ radians. The residual moment was computed to be M_R = 46 kN-m (34 kip-ft) at the two pier sections and throughout the middle span and linearly decreased to 0 at the end supports. The residual moment field is symmetric because of the symmetry of the bridge design.

At the Service II load level, centerline stresses in the center span were found to be maximum. LRFD states that the applied stresses must be less than or equal to 0.95 of the flange yield stress, F_y, for a composite section in positive bending. The maximum Service II stress is determined by superposition of stresses where the live load moment stress component is equal to the elastic moment plus the redistributed residual moment. The total stress was calculated as 330 MPa (47.9 ksi), which is approximately equal to the requirement of 0.95 F_y = 327 MPa (47.5 ksi).

Strength I Limit State

To satisfy the ultimate strength requirement, a plastic collapse mechanism must not form with the application of Strength I factored loads. LRFD inelastic provisions use an effective plastic moment, M_{PE}, at the negative moment pier hinge sections. The effective plastic moment ensures adequate inelastic rotation capacity at rotating hinges. The mechanism check was carried out by applying the factored dead loads [$1.25DC + 1.50DW$], moving the factored design truck [$1.75L(1 + I)$] over the entire beam in tenth-point increments, and calculating the plastic collapse load factors for all truck positions (*9*). The critical mechanism, using M_{PE} at the pier sections, was the maximum positive center-span loading configuration. The plastic collapse load factor was found to be 1.38. The structure can withstand 38 percent more factored live loads than is caused by the Strength I factored design live loads. Thus, Strength I requirements did not control the design.

Summary of Design Limits

The Service I level maximum live-load deflection was 30 mm (1.18 in.). The Service II limit state was the controlling design limit with a maximum centerline stress of 330 MPa (47.9 ksi) versus an allowable stress of 327 MPa (47.5 ksi). Strength I loads did not control the design of the prototype; the theoretical collapse capacity is 38 percent higher than the Strength I factored loads.

TEST GIRDER MODEL DESIGN

The test girder was a scaled interior girder extracted from the prototype bridge. Structural modeling techniques were employed to determine the theoretical scale factors, S, for the fundamental measures of interest in the 1/2 scale model. Steel and concrete properties for the prototype and the model were identical; therefore, the independent variables were chosen as elastic modulus E (S_E = 1) and length L (S_L = 2). A half-scale model of the deck effective width, deck thickness, deck reinforcement, shear studs, and bearing stiffeners was easily produced. However, an exact half-scale model of the W30 × 108 rolled shape did not exist so a W14 × 26 was chosen as the best alternative. Because of this choice, the actual scale factors for several fundamental measures did not match the theoretical scale factors. A summary of important cross-sectional properties is presented in Table 1, along with the theoretical and actual scale factors of these properties. In Table 1

- I^+ = positive bending section moment of inertia in positive moment regions,
- I^- = negative bending section moment of inertia in negative moment regions,

TABLE 1 Prototype and Model Girder Properties

Item	Prototype	Model	P/M = S_{actual}	P/M = S_{theory}
$I^+_{LL,COMP}$ (10^6mm^4)	5,620	313	17.96	16
$I^+_{DL,COMP}$ (10^6mm^4)	4,330	241	17.97	16
$I^-_{DL\&LL,COMP}$ (10^6mm^4)	2,900	158	18.35	16
I_{STEEL} (10^6mm^4)	1,860	102	18.24	16
$S_x{}^+_{LL,COMP}$ (10^3mm^3)	7,560	891	8.48	8
$S_x{}^+_{DL,COMP}$ (10^3mm^3)	6,920	815	8.49	8
$S_x{}^-_{DL\&LL,COMP}$ (10^3mm^3)	5,940	698	8.51	8
S_{xSTEEL} (10^3mm^3)	4,910	578	8.49	8
$b_f / 2t_f$	6.9	6.0	1.15	1
d / t_w	54.7	54.5	1.00	1
$M_P{}^+_{COMP}$ (kN-m)	3,680	428	8.60	8
$M_P{}^-_{COMP}$ (kN-m)	2,810	316	8.89	8
$M_{PE}{}^-_{COMP}$ (kN-m)	2,250	252	8.93	8

10^6mm^4 = 2.4025 in^4; 10^3mm^3 = 61.024 10^{-3}in^3; 1 kN-m = 0.7368 kip-ft

$COMP$ = composite section (steel + rebar for I^-)
S_x = section modulus,
S_{actual} = P/M = actual scale factor (prototype/model scale factor),
S_{theory} = P/M = theoretical scale factor (prototype/model scale factor),
b_f = width of flange,
t_f = thickness of flange,
d = section depth, and
t_w = thickness of web.

Loading applied to the model was scaled to simulate equal stresses in the model and the prototype. Because scale factors for all the section moduli were approximately 8.5, as shown by the shaded portion of Table 1, to model equal stresses, all prototype bending moments were factored by 1/8.5. Also shown in Table 1 are scale factors computed for the plastic moment capacities at the critical sections.

Compensatory dead load was added to accurately simulate dead load stresses because a half-scale model weighs only one-quarter of the prototype. Ten concrete blocks weighing 8.9 kN (2,000 lb) were hung from the bottom of the W-shape before the concrete deck was placed to compensate for the self-weight lost because of scaling. Additional concrete blocks were placed on top of the deck after it hardened to represent the composite dead loads (wearing surface, guard rails, etc.).

Moving live loads were simulated with four discrete loading points on the test beam, as indicated in Figure 2 (P1 and P2 shown on figure; P3 and P4 symmetric). Influence lines for each of the four loading points were used to determine the sequence of loads needed to simulate a moving truck. The total moment envelope produced by the four discrete loading points is shown in Figure 3 along with the scaled theoretical design truck [$L(1+I)$] moment envelopes. The truck load sequence could be linearly adjusted to represent any percentage of the modeled truck design weight (LL).

Several different measurements were recorded for the test, including deck slip, rotation, deflection, reaction, and strain gauge readings. Dial gauges were used to measure deflections. An 890-kN (200-kip) compression load cell was placed under each support to measure the reactions of the beam. The locations of these measurements are shown in Figure 2.

TEST SEQUENCE

The modeled live loads were applied to the test beam cyclically at various load levels. The following design load levels and collapse loads were examined rigorously because of their importance:

1. Service I,
2. Service II,
3. Strength I, and
4. Plastic collapse load (Strength I loads proportionally increased until failure).

The entire loading history of the test is as follows. Elastic low-level tests were carried out at 10, 20, 40, 60, 70, 80, and 90 percent LL. These provided an opportunity to confirm elastic behavior and

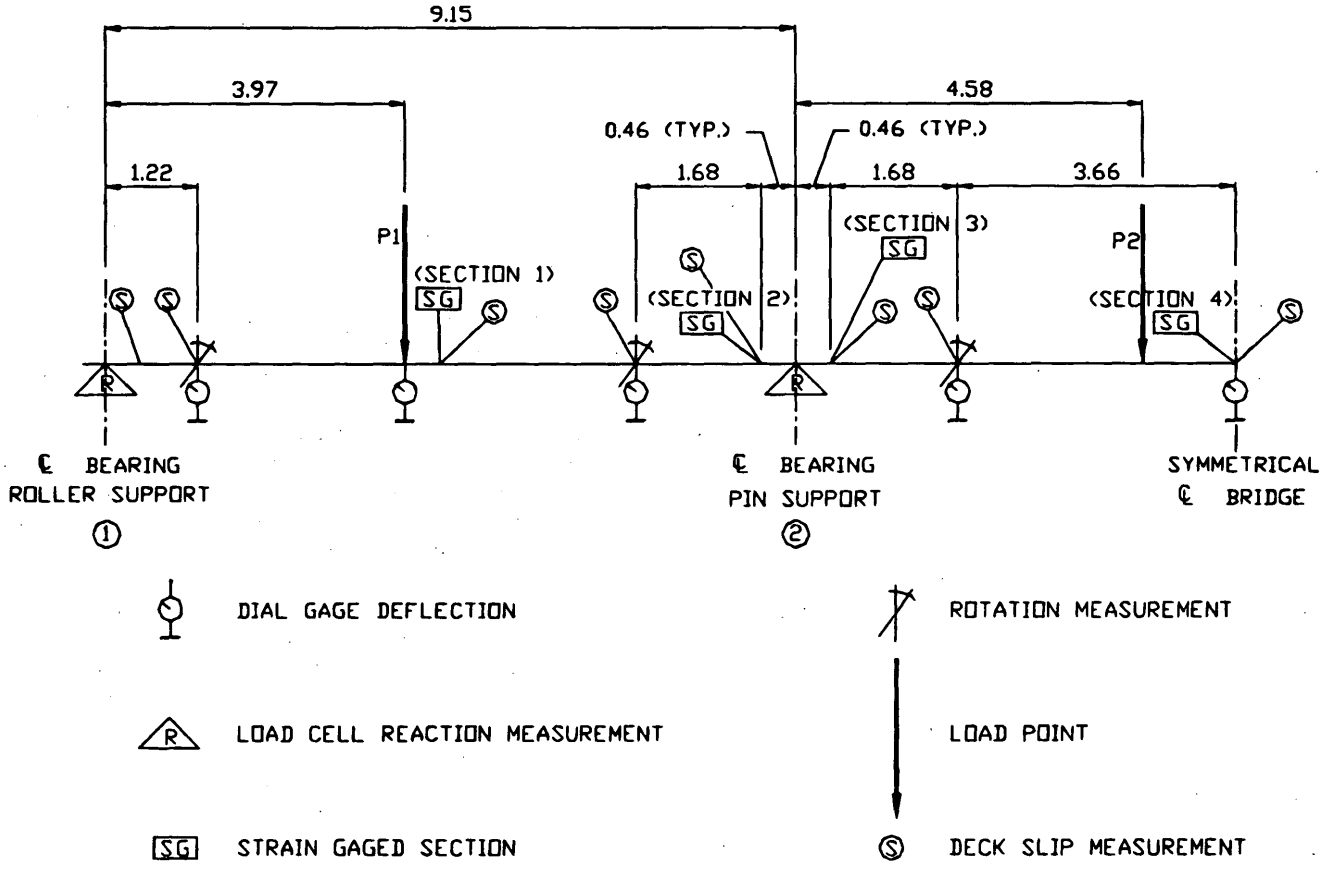

FIGURE 2 Measurement and load locations.

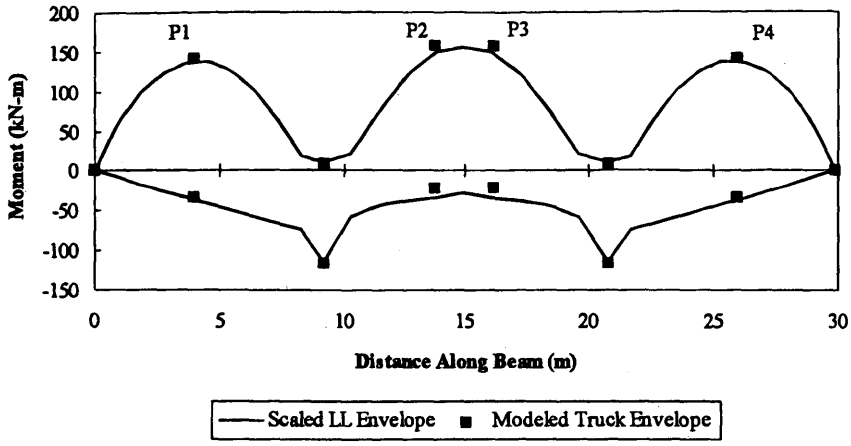

FIGURE 3 Modeled truck moment envelope.

instrumentation performance. Service I level live loads (100 percent LL) were applied to examine fatigue (ratioed to 75 percent LL) and deflection requirements of the LRFD provisions. Increasing the loads toward the Service II level, live loads of 110 and 120 percent LL were applied to examine the behavior in this range of loads.

At the Service II live-load level (130 percent LL), the girder experienced controlled inelastic behavior. After seven cycles, deflections stabilized and the girder behaved elastically for additional cycles. The inelastic behavior is characterized by residual deflection or permanent set. Design provisions predict this residual deflection and limit stresses in positive moment portions of the structure to control the amount of permanent set. Live loads were applied at 140, 155, and 166 percent LL to examine the inelastic behavior above the Service II level. The last simulated moving load test was at 175 percent LL plus factored dead loads. This loading represents the worst possible maximum design load level applied to a bridge.

After the cyclic tests, the girder was tested to failure by monotonically increasing loads proportioned to represent the theoretical design collapse configuration. This configuration simulated a stationary truck where the center axle of the truck was located at the centerline of the middle span. The additional factored dead load was applied by adding extra simulated loads to the P1 through P4 discrete load locations.

DESIGN LIMIT TEST RESULTS

Service I Level Behavior

The main design concerns at the Service I load level are fatigue and live-load deflection control. Fatigue stress criteria limited the allowable fatigue stress range to 40 MPa (5.8 ksi); the corresponding strain is 200 με. Strains (ratioed to 75 percent LL) at the top flange of Sections 1 and 2 (Figure 2) were 71 and 158 με, respectively. Thus, the model met the Category C fatigue stress requirement.

There was 1.9 mm (0.08 in.) of permanent set measured at the bridge centerline before applying the 100 percent LL sequence. After four 100 percent LL cycles, residual deflection at the center of the bridge was 3.1 mm (0.12 in.). The largest live load deflection at 100 percent LL occurred in the middle span (with P2 and P3 loaded) and was measured as 31.0 mm (1.22 in.). Theoretical deflection of the model was computed as 29.5 mm (1.16 in.) using a nonprismatic analysis and the actual loads at P2 and P3. This indicates that the model represented effectively the prototype bridge live-load deflection behavior.

Service II Level Behavior

As the load level was increased to 130 percent LL, strain measurements at negative bending sections were substantially higher than the theoretical elastic strains, indicating that some yielding had occurred. LRFD provisions require that the stresses in positive bending regions be less than 0.95 F_y after redistribution of moments. A maximum strain of 1449 με occurred at Section 4. The maximum strain allowed by LRFD for 345 MPa (50 ksi) steel is 0.95 × 1724 με = 1,638 με. Therefore, the structure met the Service II limit-state criterion.

A permanent set of 9.6 mm (0.38 in.) occurred at Section 4 after seven 130 percent LL cycles. Theoretical residual deflections at the Service II level can be calculated from the prototype design residual moments and rotations, 46 kN-m (34 kip-ft) and 0.00083 radians, respectively, previously determined using the LRFD pier moment-inelastic rotation curve. Two theoretical prototype residual deflections were calculated using the conjugate beam analogy (*6*). The first used a prismatic beam with a weighted average for the moment of inertia and found the scaled residual deflection to be 3.3 mm (0.13 in.). Another method used a nonprismatic beam with a reduced moment of inertia for 20 percent of the span on each side of the interior piers. The second method yielded a scaled residual deflection of 6.6 mm (0.26 in.). The 9.6-mm (0.38-in.) actual residual deflection was nearly three times the scaled theoretical value of (6.55/2) = 3.3 mm (0.13 in.). Calculated residual deflections did not reflect the measured values because the LRFD pier moment-inelastic rotation curve apparently does not describe the observed softer behavior of the model pier section (*6*). Residual deflections were also computed using a softer pier moment-inelastic rotation curve presented in the unified autostress method (UAM) developed by Schilling (*10*). The softer UAM pier moment-inelastic rotation curve produced a higher residual moment and inelastic rotation [132 kN-m (97 kip-ft) and 0.0024 radians]. Again, two residual deflections were computed using the conjugate beam analogy. These residual deflections were 9.1 mm (0.36 in.) and 18.3 mm

(0.72 in.) for the prismatic averaged inertia and the nonprismatic analysis, respectively. Therefore, the 9.6-mm (0.38-in.) measured residual deflection corresponds well with the scaled value calculated using the softer pier moment-rotation relationship of (18.31/2) = 9.2 mm (0.36 in.).

Strength I Level Behavior

The Strength I mechanism test was conducted by first applying the simulated factored portion of the dead load to P1, P2, P3, and P4. Live loads were then applied to P1, P2, and P3 to recreate the prototype mechanism moment diagram. The P1 and P4 loads were set to load control for the duration of the collapse test while the P2 and P3 loads were slowly increased under stroke control until the girder failed by concrete crushing. Figure 4 is the total load at P2 and P3 (P2 + P3) plotted against the deflection at the girder centerline. The figure shows the Strength I factored load level in relation to the load-deflection response. The figure clearly shows that the girder had excess capacity (36 percent) beyond the Strength I loading in accordance with the design calculations.

SHAKEDOWN BEHAVIOR

Each modeled truck weight level percentage loading was repeated until the residual deflections stabilized and the bridge experienced shakedown. Figure 5 shows the residual deflection at the centerline of the bridge in terms of the percent live load level. This shakedown plot shows how the structure experienced increasing permanent set as the live load level increased. The onset of permanent set occurred at 70 percent LL. After the last cycle of loads, the girder had a residual deflection at the centerline of 65 mm (2.56 in.).

Stabilization of residual deflections was achieved at all live load levels except for the 175 percent LL level. The 175 percent LL level was somewhat different from that of other load sequences because it included extra loads to simulate the factored portion of the dead load. The 175 percent LL level was actually the Strength I load level as defined by the LRFD provisions.

Three cycles were carried out at the Strength I load level; each cycle resulted in large increases in residual deflection. The cyclic live loading portion of the test concluded at this level because some slight web buckling at the pier sections was detected. At the Strength I load level, the structure may or may not have shaken down, so this level was not necessarily the incremental collapse load. However, it can be concluded that the incremental collapse load occurred above the 166 percent LL level.

Figure 6 shows the percent of modeled truck weight versus deflection relationship for the outer span of the model structure. The theoretical elastic deflections were calculated with an elastic nonprismatic analysis of the structure under the modeled loads applied at location P1. This figure indicates that after the 120 percent LL cycle, this portion of the structure begins to behave nonlinearly. The percent of modeled truck weight versus deflection relationship for the middle span of the test bridge (for P2 and P3 loaded) is shown in Figure 7. The middle span portion of the specimen began to behave nonlinearly at the 70 percent LL cycle.

PLASTIC COLLAPSE BEHAVIOR

The theoretical plastic collapse load was calculated using the effective plastic moment at the pier sections and the plastic moment capacity of the section at location P2. As indicated in Figure 4, the experimental plastic collapse capacity exceeded the Strength I load level by 36 percent, which was consistent with the design. The actual collapse load was within 1 percent of the theoretical collapse load.

After sustaining about 356 mm (14 in.) of deflection at the bridge centerline [in addition to the 65 mm (2.56 in.) from the shakedown tests], the concrete crushed at the bridge centerline. This deflection (length/deflection = 33) illustrates that this compact girder had tremendous ductility. Once the concrete crushed, the load was removed from the specimen. Over 51 mm (2 in.) of elastic deflection was recovered during unloading.

SUMMARY AND CONCLUSIONS

More economical steel bridge designs (for compact girders) can be realized using inelastic design provisions. Inelastic design provisions can reduce material and fabrication costs by eliminating the

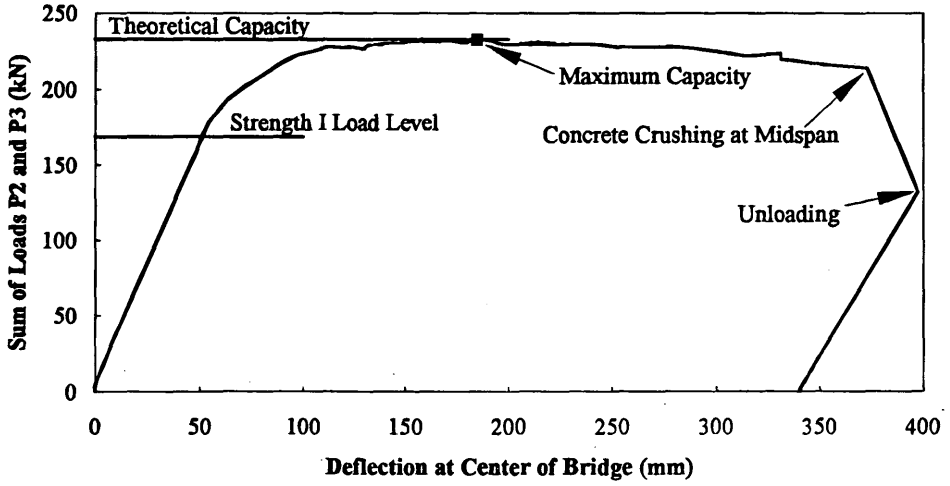

FIGURE 4 Collapse test middle span load: deflection response.

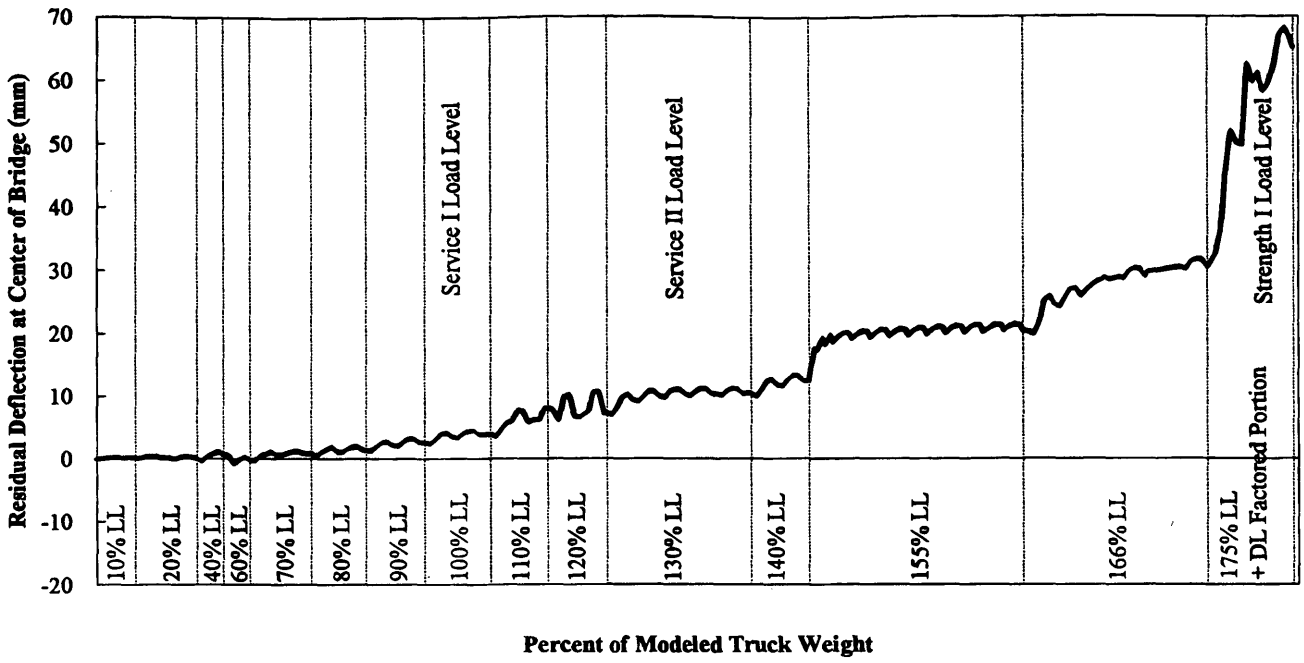

FIGURE 5 Residual deflection versus percent of modeled truck weight.

need for numerous flange transitions and cover plates at interior piers (*3*). Bridge safety is not compromised because, after the structure has experienced several passes of the design limit loads, future loads are resisted elastically. Results from this test validate the LRFD inelastic provisions at all design limit states. Extending provisions to allow inelastic design for bridges comprising noncompact sections would also be beneficial. However, even though the analytical tools exist (*8*) for developing inelastic design procedures for these girders, large-scale testing is necessary to validate theoretical engineering practice.

The test results reported herein give an overview of the general elastic, inelastic, and plastic behavior of a 1/2-scale three-span composite compact test beam. The experimental results compared well with theoretical expectations. However, the LRFD inelastic design provisions significantly underestimated the measured Service II load level (130 percent LL) residual deflections. For inelastic design, this permanent set could be included in the camber with the dead load deflections. Using other behavior models, the residual deflection was more accurately estimated. Future analysis of this test and others will yield insight into the best approach for estimating these deflections.

The plastic collapse test illustrated the available ductility in compact composite beams. The measured collapse load was within 1 percent of the predicted ultimate capacity. The primary reason that the beam behaved so well is that it is compact with the flanges being well below the compactness requirements (ultracompact) (*10*). In the next two girder tests planned for this project, the flanges will still be ultracompact, but the webs will have typical ratios of plate girder

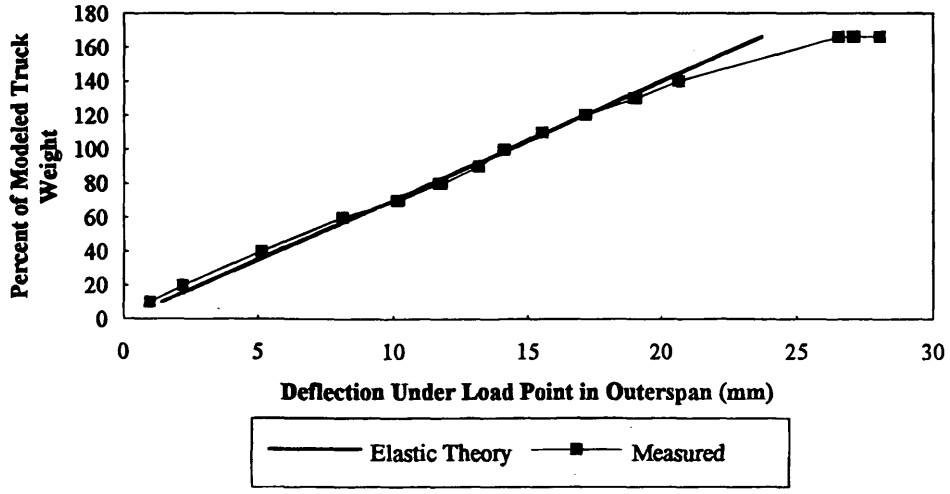

FIGURE 6 Outer span percent of modeled truck weight: deflection response.

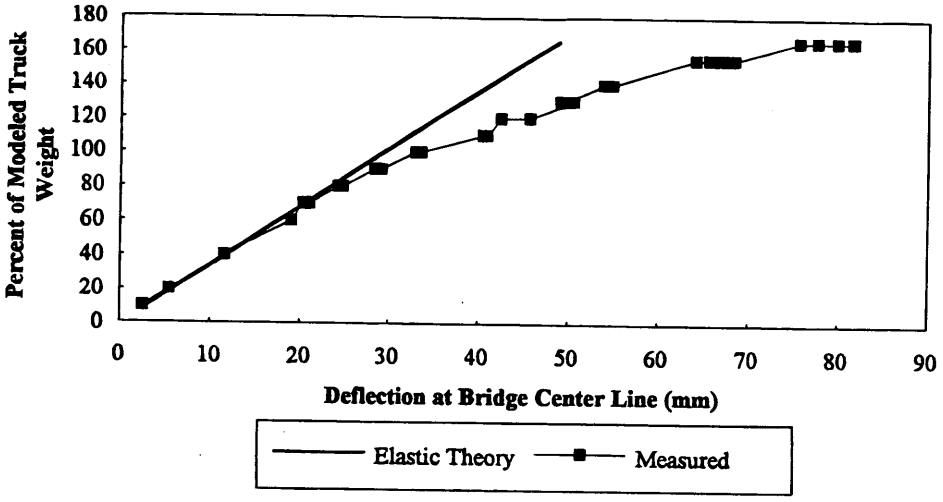

FIGURE 7 Middle span percent of modeled truck weight: deflection response.

width to thickness. However, previous work has shown that, although these girders are not as ductile, the noncompact sections have predictable moment-rotation behavior (*8*) that can be incorporated into inelastic design provisions. The second two noncompact girder tests from this project will provide vital information for the development of inelastic design provisions for noncompact girders.

ACKNOWLEDGMENTS

The authors gratefully acknowledge the sponsors of this work: the National Science Foundation, the American Iron and Steel Institute, the American Institute for Steel Construction, the Missouri Highway and Transportation Department, Louisiana Transportation Research Center, Bethlehem Steel, Nucor-Yamato Steel, U.S. Steel, St. Louis Screw & Bolt Co., and Stupp Bros. Inc.

REFERENCES

1. *Guide Specification for Alternate Load-Factor Design Procedures for Steel Beam Bridges Using Braced Compact Sections.* AASHTO, Washington, D.C., 1986.
2. Neal, B. G. *The Plastic Methods of Structural Analysis.* John Wiley & Sons, 1956.
3. Barker, M. G. Inelastic Design and Rating of Steel Girder Bridges Proc., *1993 National Symposium on Steel Bridge Construction,* Atlanta, Nov. 1993, pp 2.1–2.17.
4. *AASHTO LRFD Bridge Design Specifications.* AASHTO, Washington, D.C., 1994.
5. Barker, M. G. *Development and Experimental Verification of Inelastic Design Procedures for Steel Bridges Comprising Noncompact Sections.* National Science Foundation, Washington, D.C., 1993–1996.
6. Weber, D. C., *Experimental Verification of Inelastic Load and Resistance Factor Design Limits.* Thesis. University of Missouri—Columbia, Aug. 1994.
7. *Standard Specification for Highway Bridges.* AASHTO, Washington, D.C., 1992.
8. Dishongh, B. E. *Residual Damage Analysis: A Method for the Inelastic Rating of Steel Girder Bridges.* Thesis. University of Minnesota, Minneapolis, June 1990.
9. Barker, M. G., and T. V. Galambos. Shakedown Limit State of Compact Steel Girder Bridges. *Journal of Structural Engineering,* ASCE, Vol. 118, No. 4, April 1992, pp. 986–998.
10. Schilling, C. G. A Unified Autostress Method. *Development of Design Specifications for Continuous Plate-Girder Bridges.* Project 51. American Iron and Steel Institute, 1989.

Publication of this paper sponsored by Committee on Steel Bridges.

Applications of High-Strength Concrete to Long-Span Prestressed Bridge Girders

THERESA M. AHLBORN, CATHERINE E. FRENCH, AND ROBERTO T. LEON

High-strength concrete can be used to achieve longer-span or more widely spaced prestressed bridge girders. Two full-size long-span, high-strength prestressed bridge girders were constructed to investigate the effects of high-strength concrete on transfer length, camber, prestress losses, fatigue, flexure, and shear strength. The results of studies on constructibility, transfer length, prestress losses, and camber are presented.

The design strength of concrete has steadily increased in prestressed bridge girder construction over the years. For example, standard concrete mix designs for prestressed bridge girders built for the Minnesota Department of Transportation (MnDOT) have gone from 31 to 48 MPa in the past decade. These higher concrete strengths are being produced with little difficulty from readily available materials. To achieve further economy, it is likely that these design strengths will continue to increase.

High-strength concrete (HSC) offers many advantages to prestressed bridge girders, including increased span lengths or wider girder spacings, or both. HSC alone can be used to increase span lengths for a fixed bridge cross section. Shallower HSC sections can be used in place of normal-strength concrete members of the same length, enabling greater bridge underclearances or lower bridge embankments. Alternatively placing HSC girders at a wider spacing enables fewer girder lines per constant length bridge. Fewer girders required leads to lower fabrication, transportation, and erection costs.

In the first part of the study reported herein, a parametric study was conducted to determine the viability of using high-strength concrete in prestressed bridge girders. For a given bridge cross section and loading parameters, the maximum span length and required number of strands were determined as a function of concrete strength and transverse girder spacing. The allowable stresses that control the design of the girders were considered at release and final conditions. For the case of wider-spaced girders, the allowable stresses at release tended to control because a large amount of prestress must be "stored" in the girders for use at service conditions. For the case of longer spans, the allowable stresses at final conditions tended to control because the self-weight of the girders is a much larger portion of the total loads. Allowable stress limits at release were taken as compression of $0.6 f'_c$ and tension of 1.38 MPa, unless supplemented by mild steel reinforcement, in which case the tension limit was 4.9 MPa. Allowable limits at final were compression of $0.4 f'_c$ and tension of $0.5 f'_c$, (f'_c in megapascals).

T. A. Ahlborn and C. E. French, Department of Civil Engineering, 122 Civil and Mineral Engineering Building, 500 Pillsbury Drive, S.E., University of Minnesota, Minneapolis, Minn. 55455-0220. R. T. Leon, School of Civil and Environmental Engineering, Georgia Institute of Technology, 790 Atlantic Avenue, Atlanta, Ga. 30332.

An example of the results is shown in Figure 1 for a MnDOT 45M girder 1140 mm deep. This girder is similar to an AASHTO Type IV girder except that it has a wider top flange and a shorter overall height (Figure 2). As can be seen from Figure 1, for a given span length, an increase in concrete strength enables a minor reduction in strands because of the increased allowable stresses corresponding with the increased concrete strength. Increased span lengths may be achieved with high-strength concrete by increasing the number of strands (amount of prestress) in the cross section. As more and more strands are added to the cross section, their effectiveness is reduced as they are placed further up in the cross section (at a lower eccentricity). Consequently, the viability of HSC prestressed bridge girders depends not only on reliably achieving higher strengths, but also on the amount and strength of prestressing strand that can be placed in the cross section. There is not a significant advantage in increasing the concrete compressive strengths much above 83 MPa for the example shown. Figure 1 also indicates the effect of high-strength concrete on transverse girder spacing. It may be possible to increase the girder spacing of a girder 35 m long, for example, from 1.22 to 2.13 m by increasing the concrete strength from 48 to 83 MPa.

Current design provisions of the American Concrete Institute (ACI) (*1*) and Transportation AASHTO (*2*) are based on empirical relationships developed from isolated tests of specimens with concrete compressive strengths in the range of 41.4 to 55.2 MPa. The scarcity of empirical data on higher-strength concrete has led to limits on the maximum compressive stress of 69 MPa to be used for shear and rebar development length provisions in design codes such as those of ACI. Consequently, it is of interest to investigate the implications of using higher-strength concretes.

DESCRIPTION OF EXPERIMENTAL PROGRAM

Two full-size high-strength concrete composite prestressed bridge girders have been instrumented and constructed and are being tested at the University of Minnesota to investigate issues such as transfer length, long-term prestress losses, fatigue, ultimate flexure, and shear strengths. The girders are MnDOT 45M sections 1140 mm deep and reinforced with 46 prestressing strands 15.3 mm in diameter and 1860 MPa spaced 50.8 mm on center. The cross section of the girders is shown in Figure 2. High-strength concrete was utilized to maximize the girder lengths. Such a case required closely spaced girders (1.22 m on center) in which case allowable service load stresses were the controlling factors rather than allowable release stresses. The span length of 40.5 m represented a 48 percent increase over the maximum span length currently produced using conventional 48 MPa concrete fabricated with 1860-MPa strands 12.7 mm in diameter.

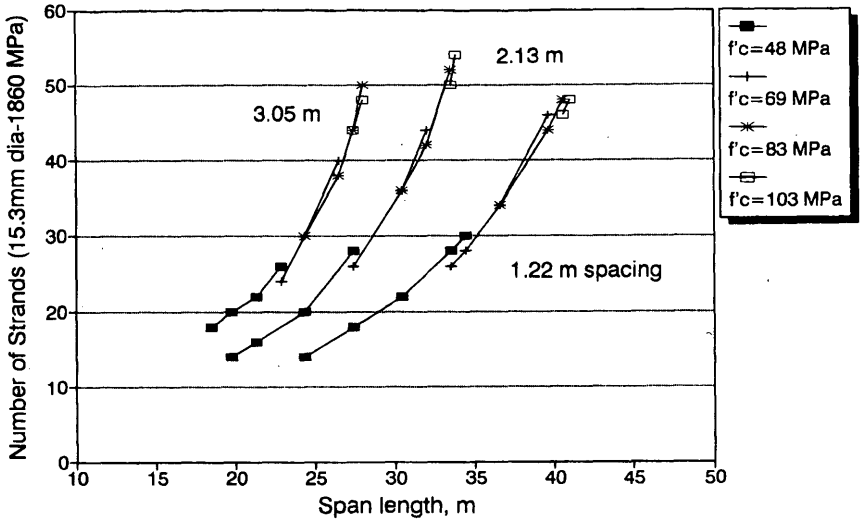

FIGURE 1 Effect of HSC on girder span length: strands required versus span length, MnDOT, 45m section.

The girders were designed to incorporate the following variables: concrete mix design, draping/debonding combinations, and stirrup configuration. Laboratory tests in a companion study (*3*) showed that local aggregates could be used to achieve high-strength concretes. Limestone aggregates provided mixes with the highest strengths, but mixes with glacial gravel aggregates reached similar strengths with the addition of microsilica. One girder (Girder I) was therefore cast with a limestone mix, and the second girder (Girder II) was cast with a glacial gravel mix incorporating 7.5 percent (replacement by weight of cement) microsilica. To investigate the effect of strand draping versus debonding on girder behavior, one end of one girder was fully draped (12 draped strands) to control end stresses, whereas the remaining three ends utilized a draping/debonding combination (optimized at four draped and eight debonded strands). Two epoxy-coated shear stirrup details were considered: a typical U stirrup and a modified-U stirrup using leg extensions along the length of the member. The modified-U stirrup was used to investigate the effect of better anchorage conditions. Figure 3 depicts the two test girders and their respective variables.

The girders were cast in August 1993 and have been monitored to determine the prestress losses and changes in camber over time. Each girder will be subjected to fatigue loading intended to simulate the maximum moment caused by a standard HS25 truck load. After approximately 1 million cycles, a static load test will be performed to determine the damage status before increasing the load level to the cracking load. Occasional overloads in both static and fatigue testing as previously recorded by MnDOT will be included.

The fatigue strength of prestressed concrete is controlled by the strand stress range. Presently, AASHTO specifications employ an indirect design criterion for flexural fatigue strength of prestressed concrete girders through limitation of the nominal concrete tensile stress in the precompressed tensile zone. Full-size girder tests can verify fatigue strength by investigating the strand stress ranges

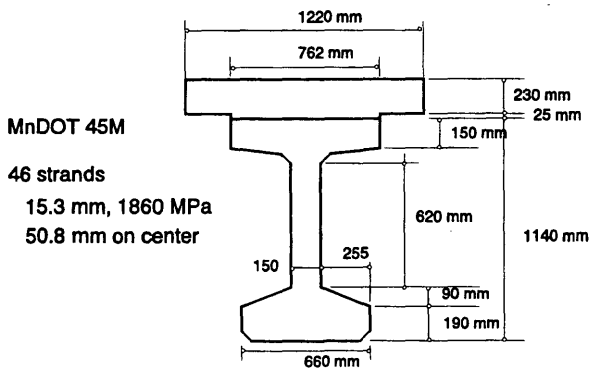

FIGURE 2 Cross section of test girders.

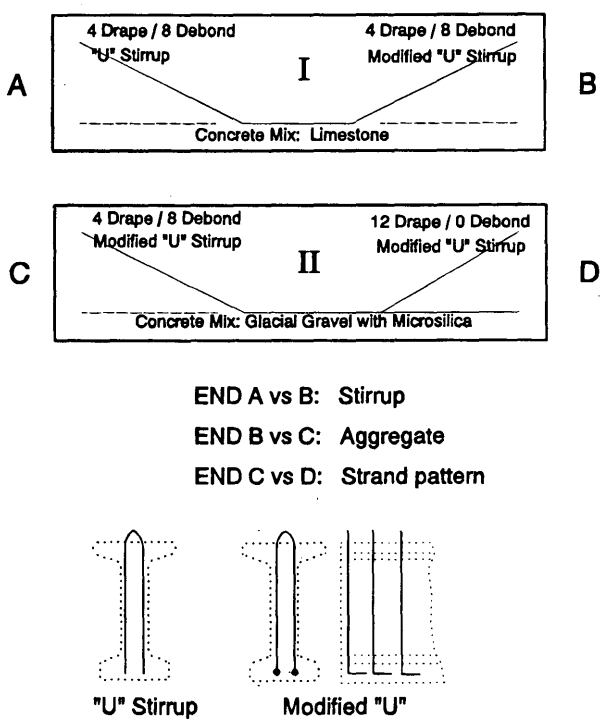

FIGURE 3 Test girder variables.

under load combinations. Strand stress ranges induced by the loading will be measured, along with the compressive stress distribution through the section depth. Comparisons will be made of the actual versus the predicted cracking load-deformation behavior. Additionally, any permanent deformation because of fatigue damage will be noted.

After the fatigue studies, each girder will be tested to ultimate in flexure. As with the fatigue tests, induced strand stresses will be measured, along with deflection and concrete stress distribution. Compression stress block distribution will be measured for verification of the neutral axis and composite action. Shear tests will then be performed by loading the ends at a low shear span-to-depth (a/d) ratio.

MATERIAL STRENGTHS

Prestressing Strands

The Grade 270 (1860-MPa) low-relaxation strands 15.3 mm in diameter used for the two girders were tested for ultimate strength and modulus of elasticity. The ultimate strength was found to be 1850 MPa, whereas the modulus was determined to be 200 700 MPa. The actual area was found to be 147 mm^2, compared with the nominal area of 139 mm^2. The rolls of prestressing strand were covered and stored outdoors at the prestressing yard for approximately 1 week before use. Strand surface condition appeared to be free of surface rust and oil.

Girder Concrete

The concrete mix used in Girder I consisted of Type III portland cement, sand, crushed limestone aggregate, and a superplasticizer. The mix had an average water/cement ratio of 0.32. The mix used for Girder II also used Type III portland cement, sand, and superplasticizer. However, rounded glacial gravel aggregate was used. In addition, microsilica was used at a rate of 7.5 percent replacement by weight of cementitious material. The mix for Girder II had an average water/cement ratio of 0.36.

A release strength of 61.5 MPa and a 28-day strength of 72.4 MPa were required of the girders. To ensure that these strengths would be achieved, the target nominal mix design strength was 83 MPa at 28 days. Actual concrete strengths achieved in the field were above specifications and are shown in Table 1. The glacial gravel mix incorporating microsilica achieved a strength of 71.9 MPa in 18 hr and continued to increase to 78 MPa by 28 days. The limestone mix surpassed the required release strength at 21 hr with a strength of 64 MPa. The strength then continued to increase well above the design requirement to a strength of 83.4 MPa at 28 days. Both mixes showed good workability and consolidation during placement, and no modifications were made to the standard construction techniques followed by the precast manufacturer. The high strengths obtained in these girders represented a 30 percent increase over those typically achieved with the manufacturer's current practice.

Deck Concrete

A standard MnDOT bridge deck mix was specified for the deck with a 27.6-MPa required strength. The required 28-day concrete strength of 27.6 MPa was surpassed at 7 days. Test results indicated the strength to be 35.3 MPa at 7 days and 40.4 MPa at 28-days. These results are tabulated in Table 1.

FABRICATION AND TRANSPORTABILITY

As noted previously, the girders were constructed in August 1993. Strands were specified to be tensioned to a level 0.75 f_{pu} after seating losses. Hydraulic jacks pulled each strand individually to 198 kN. On the basis of the nominal strand area of 139 mm^2, strands were tensioned to 76.7 percent before seating (72.4 percent before seating using actual measured area of 147 mm^2). A total of 92 strain gauges were installed on the strands and monitored throughout the tensioning process. A total of 83 percent of the gauges indicated that

TABLE 1 Material Properties

	Required	Actual
Girder Concrete Compressive Strength	18 hrs = 61.5 MPa 28 day = 72.4 MPa	I 21 hrs = 64.0 MPa 28 day = 83.4 MPa II 18 hrs = 71.9 MPa 28 day = 78.0 MPa
Deck Concrete Strength	28 day = 27.6 MPa	7 day = 35.3 MPa 28 day = 40.4 MPa
	Nominal	Measured
Prestressing Strand	Area = 139 mm^2 E_{ps} = 200,000 MPa f_{pu} = 1860 MPa	Area = 147 mm^2 E_{ps} = 200,700 MPa f_{pu} = 1853 MPa

the strands were tensioned to 1280 MPa or 72.9 percent of f_{pu} after seating based on the nominal area (69.1 percent after seating based on the measured strand area). A standard deviation of 40 MPa was recorded, and the remaining 17 percent of gauges were damaged during the tensioning process.

Concrete was mixed at the plant batch station. No additional heat or steam curing was incorporated. Formwork was stripped shortly after each girder reached the required release strength (18 to 21 hr). Because both girders were cast on the same bed, the girder with the glacial gravel mix was stripped and sat for nearly 4 hr before strands were released while waiting for the limestone mix to reach the required strength. Consequently shrinkage and temperature cracks occurred near the center and quarter points of the girder cast with the glacial gravel/microsilica combination. Cracks penetrated the cross section from the top flange to the bottom flange. These cracks fully closed once the strands were released. Cracks were not seen in the limestone girder because the strands were released within 1 hr after the formwork was removed.

At each end of the girders, strands were simultaneously flame cut. One to three cracks developed in each of the debonded end regions (*A* through *C*) during detensioning. Web cracking was observed in the draped end (*D*) of Girder II. The girders were then relocated in the prestressing yard until they were moved to the test site. Lift hooks were placed in the girder to ensure stability during handling. Placement was dictated by not exceeding allowable stress limits while assuming a small rotation about the roll axis in accordance with PCI stability criteria (*4*). A factor of safety of 2.0 governed the hook locations. No stability problems were encountered during handling.

In addition to the shrinkage cracks, the following cracks were observed. One to three cracks appeared in the bottom flange at each beam end, starting at the web-to-bottom flange interface and proceeding at a 45-degree angle longitudinally down the extreme edge of the bottom flange (approximately 8 in. from the end), then extending vertically downward to the lower edge of the bottom flange. Cracks did not occur on the bottom of the girder, and no splitting cracks were observed along or between the strands.

Both girders were transported to an off-campus testing facility in October 1993. No stability problem or additional cracking was observed during transportation. Deck formwork placement began shortly after the girders were located in the testing facility. A composite deck was cast on each girder individually in February 1994 using unshored construction.

INSTRUMENTATION

Instrumentation included strain gauges applied to the strands and transverse reinforcement, embedded concrete strain gauges and vibrating wire strain gauges, DEMEC (Detachable mechanical) gauges, and displacement transducers. The instrumentation was located in both the girder and the deck to optimize the information on prestress losses, creep and shrinkage, long-term deflections, transfer length of strands, composite interaction, flexure, shear, and cracking.

Of the 46 strands a total of 9 were instrumented with strain gauges to investigate tensioning and transfer length. The pairs of debonded strands were instrumented at 380, 560, and 760 mm from the end of their respective sheath points. At 0.45L (45 percent of the member length) and midspan of the girders, strands were instrumented to obtain data about the strain along the length of the strands at the time of prestress, stress ranges in the strands during fatigue tests, and strains in the strands at ultimate in flexure. In addition, 60 DEMEC gauges were applied to the surface of the concrete at the end regions of the beam spaced 150 mm on center to measure the external concrete strains. Vibrating wire gauges were used to investigate the change in concrete stress over time because of creep, shrinkage, and other environmental effects, and to provide additional information on prestress losses. Embedded concrete gauges were also placed at 0.2L, 0.3L, and midspan in the girders to investigate the width and depth distribution of concrete compression stress block during the ultimate flexure tests.

Deck instrumentation consisted of strain gauges on the longitudinal reinforcement and embedded concrete gauges to investigate width and depth distribution along the length of the member. Vibrating wire gauges were placed to maximize information on deck shrinkage and also to investigate compression stress block distribution during the flexure tests.

External instrumentation included tiltmeters, linear variable differential transformers (LVDTs), and acoustic emissions equipment for monitoring rotation, deflection, and first crack detection, respectively. Ambient temperature and relative humidity were continuously monitored. Data collection began with strand prestressing and continued through fabrication and deck casting. Data are being collected periodically until the tests are completed.

RESULTS

Transfer Length

Instrumentation used to investigate transfer length included surface-embedded DEMEC gauges, strain gauges mounted on individual strands, and vibrating wire gauges (Figure 4). Figure 5 shows the strain that was measured on Girder I (End A) using the DEMEC surface gauges at release. The figure also includes data obtained from a vibrating wire gauge located at a slightly greater eccentricity (Figure 4). Superimposed on Figure 5 is the calculated strain distribution obtained from the following equation:

$$\epsilon = \frac{\sigma}{E_c} = \frac{1}{E_c} * \left[-\frac{P}{A} \pm \frac{Pe * c}{I} \mp \frac{M_g * c}{I} \right] \quad (1)$$

where

ϵ = strain at distance c from center of gravity (cg) of cross section,
σ = stress at distance c from cg of cross section,
P = effective prestress,
e = strand eccentricity measured from cg of cross section,
A = cross-sectional area of concrete,
I = gross moment of inertia of concrete,
c = distance from cg of cross section to location at which strain/stress is to be determined,
M_g = external moment caused by self-weight, and
E_c = modulus of elasticity of concrete.

The calculated strain was determined using actual data obtained during tensioning and release to solve for the effective prestress level. The calculated strains were also based on the AASHTO assumed transfer length of 50 d_b (strand diameters). The shallow dips in the calculated strains reflect the effect of gravity load, causing a decrease in the concrete compression strain at the level of the

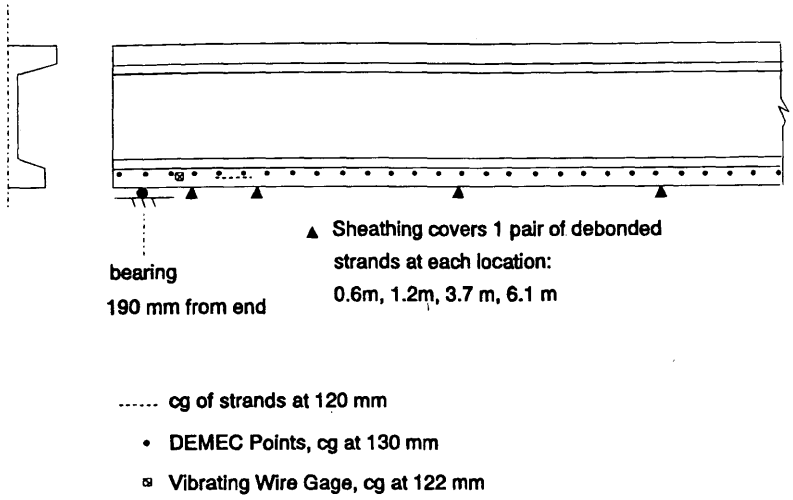

FIGURE 4 Instrumentation for transfer length measurements.

strands. The slight increases following the dips represent the initiation of bonding the pairs of debonded strands along the length of the girder. This increase effect appears minor because of the percentage of debonded strands becoming bonded versus the total bonded strands already in the cross section. The calculated strain is generally lower than the actual data indicate, although within reason. DEMEC gauges were placed near the center of gravity of strands to measured surface strains, and data include the localized effect of force concentration in the bottom flange of the girder.

The calculated transfer length values using the assumptions above give reasonable results. In addition, transfer lengths were determined graphically from the experimental data using methods proposed by Russell and Burns (*5*) and Cousins et al. (*6*). In the 95 percent average maximum strain method proposed by Russell and Burns, strain readings were first smoothed by averaging the data over three gauge lengths to reduce anomalies in the data. The average maximum strain was determined by computing the numerical average of the smoothed strains contained within the strain plateau. The intersection of a line corresponding with 95 percent of the average smoothed strain data and the smoothed strain profile represents the transfer length (Figure 6*a*). Using this procedure, transfer lengths in the range of 570 to 725 mm were obtained for the four girder ends.

The final average method employed by Cousins et al. (*6*) eliminates data points that lie outside the range of one standard deviation from the averaged strain plateau. The average strain of the remaining data points is then determined, and the transfer length is defined as the intersection of the final average strain and the data (Figure 6*b*). The results obtained with this method were similar to those obtained using the 95 percent average maximum strain method and ranged from 630 to 696 mm.

Reported transfer lengths are for straight strands that were fully bonded in the section and exclude the debonded strands. As shown by the calculated strain in Figure 5, the additional force introduced by the pairs of debonded strands is on the order of 4 percent of the total stress introduced at the ends of the girders. Reported transfer

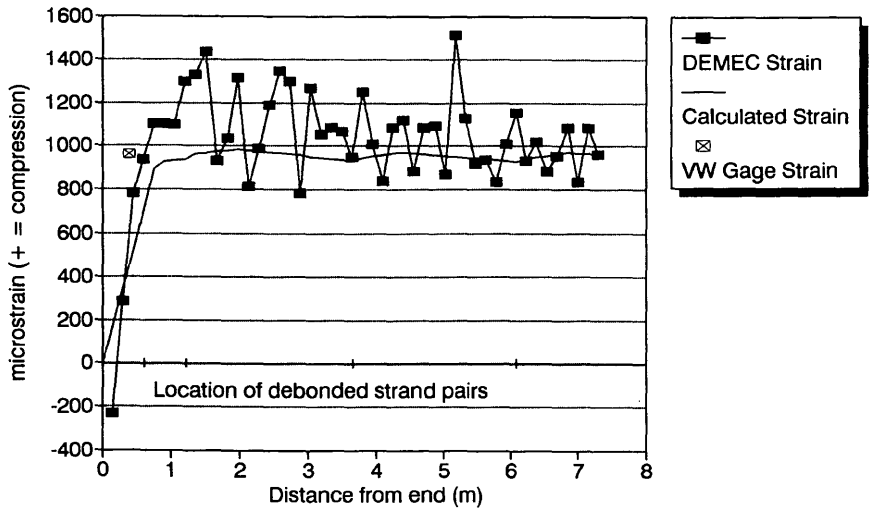

FIGURE 5 Measured and calculated strains for transfer length: UMN Test Girder I, End A, bottom flange.

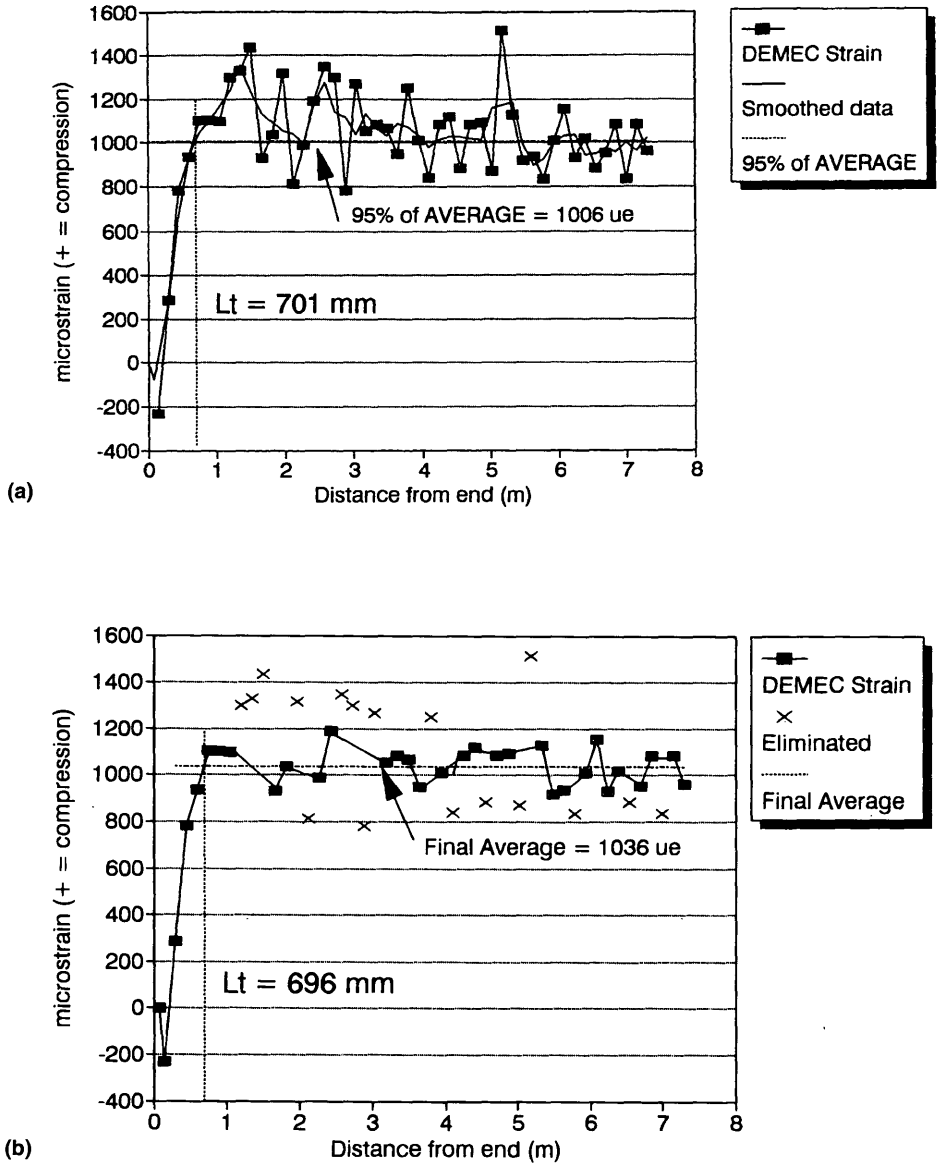

FIGURE 6 Transfer length, UMN Test Girder I, End A: (*a*) 95 percent average maximum strain method; (*b*), final average method.

lengths are therefore only for the initial force transfer of the bonded strands in the end of the girder.

A wide variation in data exists for determination of transfer length, and there is a lack of data available for strands embedded in high-strength concrete. One study about the effect of high-strength concrete on transfer length of strands 15.7 mm in diameter was reported by Mitchell et al. (*7*). Concrete strengths ranged from 31 to 89 MPa. It was shown that an increase in concrete compressive strength at the time of strand release resulted in a reduction of transfer length. Transfer lengths for single-strand rectangular specimens (200 by 250 mm) ranged from 435 to 872 mm for concrete strengths up to 65 MPa. Design expressions were proposed that take into account the concrete compressive strength at the time of force transfer and service. The Mitchell study varied from the current investigation in two ways. The Mitchell study used a third method—the slope-intercept method—for determining transfer length, and a gradual release method was employed for detensioning the strands. Both of these variations can result in shorter transfer lengths.

Russell et al. (*5*) investigated the effect of lateral spacing on the transfer length of strands 15.3 mm in diameter. Concrete strengths varied in the study from 34 to 53 MPa for these tests. Results indicated that higher concrete strengths at release result in shorter transfer lengths. Transfer lengths were 1057 mm for single-strand and 1070 mm for three- and five-strand rectangular specimens and AASHTO-type (560-mm-deep) girders with 50.8-mm strand spacing.

Table 2 summarizes transfer length estimations for the four girder ends using the two graphical approaches described earlier. Transfer lengths can be predicted using relationships from AASHTO (*2*) and ACI (*1*) (Table 2). Table 2 also summarizes the observed test data from Mitchell et al. (*7*) and Russell et al. (*5*).

TABLE 2 Transfer Length Summary

Measured Transfer Length - UMN Test Girders (mm)				
Graphical Methods Using Measured Surface Strain Data	Girder End			
	I-A	I-B	II-C	II-D
95% Average Maximum Strain Method (Russell, 5)	701	725	570†	565
Final Average Method (Cousins, 6)	696	569	630	676
AVERAGE of Methods (mm)	699	647	600	621
Predicted Transfer Lengths (mm)				
AASHTO (2)	780			
ACI (1)	782			
Observed Transfer Lengths of 15.7 mm Strand from Other Studies (mm)				
Mitchell (7)	435 - 872 (single strand rectangular specimens, slow release)			
Observed Transfer Lengths of 15.3 mm Strand from Other Studies (mm)				
Russell (5)	1057 (single strand rectangular specimen) 1070 (3 and 5 strand rectangular specimens, AASHTO type 560 mm deep girders, all with 50.8 mm strand spacing)			

† A spuriously high data point was omitted which indicated a transfer length of 376 mm.

Prestress Losses

Prestress losses occur instantaneously because of elastic shortening at release and over time because of steel relaxation and creep and shrinkage of concrete. Nearly all prestress losses occur in the girder within the first 6 to 12 months of being cast. Creep and shrinkage will considerably slow down after this time, and deflections will have stabilized. Vibrating wire gauges were installed at the center of gravity of the strands in each girder to measure prestress losses with time. One gauge was installed at each of the following locations: 0.45L, 0.50L, and 0.55L. The gauges were monitored continuously for 2 weeks after casting and periodically to date. Figure 7 illustrates the strain change over time for a gauge located at the center of gravity of the strands near midspan of Girder I.

Table 3 summarizes initial and time-dependent losses. Concrete strains measured immediately after release were used to provide an indication of prestress losses because of elastic shortening. Losses were also determined 28 and 200 days after girder casting. Day 200 corresponds to the week before deck casting. The level of stress loss in megapascals is tabulated for each time step (noncumulative), whereas the percent loss listed represents the cumulative loss through that time step. The percent loss was based on the measured strand tensioning level of 1280 MPa immediately before release.

AASHTO (2) specifications contain provisions for calculating initial and long-term prestress losses caused by elastic shortening, steel relaxation, concrete creep, and concrete shrinkage. PCI (8) and Naaman (9) use a time-step approach to determine losses for any given time. Using known material properties and transformed geometric section properties for each girder, losses were calculated for each method and are summarized in Table 3. Known properties include concrete compressive strengths and moduli of elasticity at different ages, measured creep coefficient of 1.0, prestressing steel yield and ultimate strengths, and strand tensioning level.

Measured losses were lower in Girder II than Girder I, although within a reasonable range. The difference in losses between the two girders reflects the difference in initial concrete compressive strength and elastic moduli. The greatest portion of losses occurred at transfer because of elastic shortening and varied in each beam from 173 MPa in Girder I (limestone) to 156 MPa in Girder II (glacial gravel/microsilica), as indicated in Table 3. An additional 76.5 and 46.6 MPa occurred in each girder, respectively, within the first 28 days after casting, and much smaller losses have occurred since (24.8 and 13.2 MPa). The calculated losses give reasonable estimates of the observed prestress losses when using properties appropriate for high-strength concrete.

Camber

Estimating camber and deflection of precast prestressed members is complex because of the interaction of prestress losses, loadings, and concrete strength gain with time. Camber calculations take into consideration prestressing effects, dead load, live load, erection loads, creep and shrinkage of concrete, and steel relaxation.

A rational method of estimation using multipliers to predict camber and deflection at erection and final service conditions has been adopted by the PCI (4). The PCI Design Handbook tabulates multipliers for prestressed concrete beams with and without a composite topping. These multipliers were based on general experience from use of normal-strength concrete and need to be reevaluated for use with high-strength concrete.

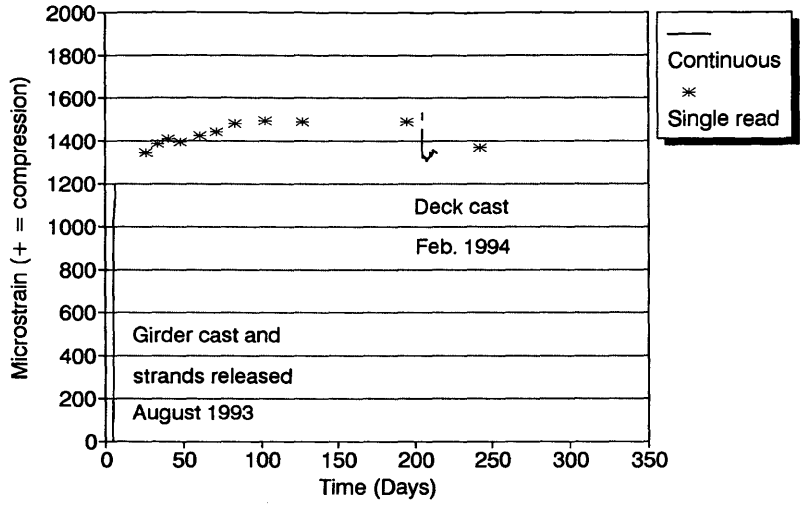

FIGURE 7 Strain change over time for prestress loss calculations: UMN Test Girder I, midspan.

Camber and deflection have been monitored for both girders since the time of strand release. Figure 8 illustrates centerline camber of both girders over time. Girder I (limestone) had an initial camber of 121 mm and increased to a maximum of 230 mm within 2 months. Girder II (glacial gravel/microsilica) had an initial camber of 97 mm and increased to a maximum of 146 mm within 2 months. Both girders then showed slight reductions in camber until the time of deck casting. Neither girder reached the camber levels of 210 and 193 mm, respectively, as predicted by the PCI method. Each girder deflected relatively as predicted because of deck casting; however, neither again achieved the overall PCI predicted levels of 152 and 133 mm. The cambers of each girder are slowly leveling out with time.

SUMMARY

Two MnDOT 45M girders (1140 mm deep) with spans of 40.5 m designed to be placed 1.22 m on center have been constructed. One girder was cast with limestone mix, and the second girder was cast with round glacial gravel mix incorporating microsilica. The girders were fabricated with 1860-MPa strands that were 15.3 mm in diameter, debonded at three ends (Ends A through C), and draped at one end (End D). The girders will be loaded cyclically to investigate fatigue and subsequently will be tested to determine their flexural and shear strengths. Data about constructibility, transfer lengths, prestress losses, and camber have been obtained.

TABLE 3 Prestress Losses

	† Measured		‡ PCI Committee (8)		‡ Naaman (9)		‡ AASHTO (2)	
	MPa	Losses	MPa	Losses	MPa	Losses	MPa	Losses
Girder I - Limestone Aggregate								
Release	173	13.5%	184	14.4%	184	14.4%	150	11.8%
28 days	76.5	19.3%	80.7	20.7%	50.3	18.3%		
200 days	24.8	21.5%	71.4	26.3%	37.6	21.3%		
Long-term losses*							258	31.9%
Girder II - Glacial Gravel with Microsilica								
Release	156	12.2%	170	13.3%	170	13.3%	139	10.8%
28 days	46.6	15.8%	81.7	19.7%	50.8	17.3%		
200 days	13.2	16.8%	72.6	25.4%	38.3	20.3%		
Long-term losses*							258	31.0%

† Measured losses were obtained by averaging 3 gages located at the center of gravity of the strands at 0.45L, 0.50L, and 0.55L along the girder length. This change in concrete strain was assumed to be equal to the change in steel strain.

‡ Losses were calculated at the center of gravity of the strands at 0.50L along the girder length. Losses at locations 0.45L and 0.55L were within ½% of that tabulated.

* Long-term losses include effect of long-term loads due to deck.

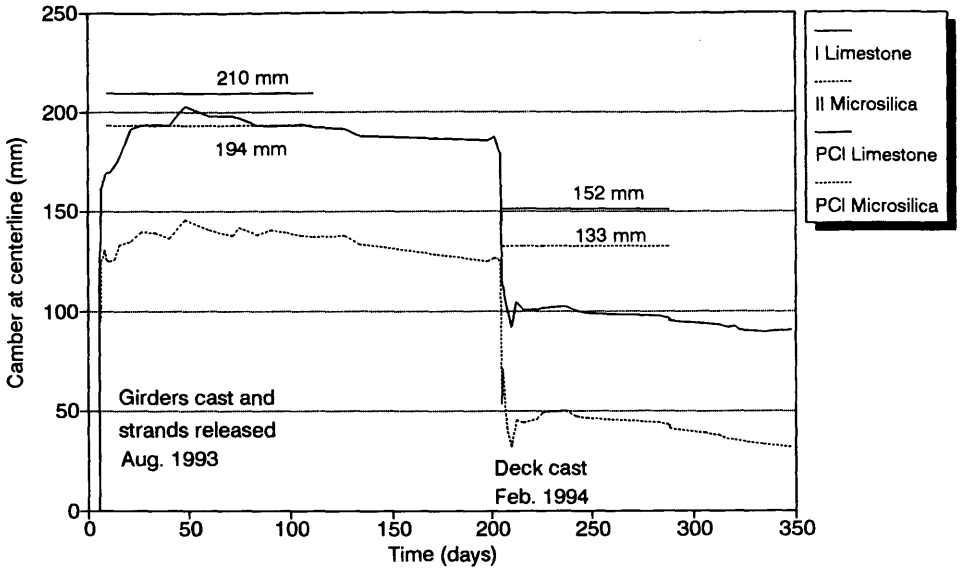

FIGURE 8 Camber change over time: UMN-HSC bridge girder tests.

The girders were fabricated with readily available materials and achieved their release strengths within 18 to 21 hr from the time of casting. There were no problems encountered in the fabrication or transportation of the long-span girders. Results indicated that transfer lengths were approximately 80 percent of those predicted by AASHTO (*2*) and ACI (*1*). Prestress losses measured to 200 days were consistent with those predicted by PCI (*8*), Naaman (*9*), and AASHTO (*2*). Girder cambers were lower than those predicted by PCI (*4*), particularly for the girder containing the glacial gravel/microsilica mix with the draped and draped/debonded strand configurations in the end regions.

ACKNOWLEDGMENTS

This research investigation has been conducted under the joint sponsorship of the Minnesota Prestress Association, MnDOT University of Minnesota Center for Transportation Studies, Precast/Prestressed Concrete Institute, and a National Science Foundation grant. The authors acknowledge the generous donations of materials and equipment by Elk River Concrete Products, Union Wire & Rope, W.R. Grace & Co., Simcote, Inc., Lefebvre & Sons Trucking, Truck/Crane Services, and Golden Valley Rigging.

REFERENCES

1. *Building Code Requirements for Concrete, 318-89.* (Revised 1992). Committee 318. American Concrete Institute, Detroit, 1992.
2. AASHTO. *Standard Specifications for Highway Bridges*, 15th ed. AASHTO, Washington, D.C., 1993.
3. French, C. W., and A. Mokhtarzadeh. High Strength Concrete: Effects of Materials, Curing and Test Procedures on Short Term Compressive Strength. *PCI Journal*, Vol. 38, No. 3, May–June 1993, pp. 76–87.
4. *PCI Design Handbook*, 4th ed. Prestressed Concrete Institute, Chicago.
5. Russell, B. W., and N. H. Burns. *Design Guidelines for Transfer, Development, and Debonding of Seven Wire Strand in Pretensioned Concrete Girders*. Research Report 1210-5F. Center for Transportation Research, University of Texas at Austin, Jan 1993.
6. Cousins, T. E., J. M. Stallings, and M. B. Simmons. *Effect of Strand Spacing on Development Length of Prestressing Strand*. Final Report. Alaska Department of Transportation and Public Facilities, Juneau, Aug. 1993.
7. Mitchell, D., W. D. Cook, A. A. Khan, and T. Tham. Influence of High Strength Concrete on Transfer and Development Length of Pretensioned Strand. *PCI Journal*, Vol. 38, No. 3, May–June 1993, pp. 55–66.
8. PCI Committee on Prestress Losses, Recommendations for Estimating Prestress Losses. *PCI Journal*, Vol. 20, No. 4, July–Aug. 1975, pp. 44–75.
9. Naaman, A. E. *Prestressed Concrete Analysis and Design*, McGraw-Hill, New York, 1982.

The views expressed herein are those of the authors and do not necessarily reflect the views of the sponsors.

Publication of this paper sponsored by Committee on Concrete Bridges.

Dynamic Vehicle Loading on a Slab Bridge Using Multiple Actuators

PAUL N. ROSCHKE

An analytical method is presented that approximates passage along a bridge deck of discrete wheel loads by a group of actuators. Actuators are fixed in position but controlled in a sequential manner according to a mathematical algorithm developed from a flexibility matrix approach. As an example, a large-scale laboratory model of a posttensioned flat slab bridge is loaded by an array of four actuators that simulates dynamic movement of a heavy truck. A total of 200,000 cycles of service load is applied to the slab in a region where transverse posttensioning forces impose high gradients of stress. Experimental readings from the laboratory are compared with predictions from numerical simulation. The algorithm can be applied to other types of bridge structures that undergo dynamic traffic loads.

Transportation-related structures are, by nature, subjected to live loads that move in a continuous fashion from one end of the structure to the other. Stress waves from these loads in the structural members are dynamic rather than static. Expensive maintenance of bridge decks and fatigue of related members attest to the importance of loads of this type.

In most studies of bridges that involve moving traffic, a cyclic concentrated load at a fixed location is used to approximate stresses from the vehicle. By contrast, Perdikaris et al. (*1*) used a moving wheel load and found that the fixed location method results in higher fatigue strengths at a higher number of stress cycles for concrete bridge decks. A variation on the fixed location method utilizes a moving single concentrated load that moves in a stepwise manner. In this case failure strength is lower than that for the fixed location method and occurs at fewer cycles (*2*).

For the current study, multiple fixed-load locations are used to represent effects of passage of wheel loads from a vehicle (see Figure 1). Two lines of loads, one for each wheelpath, are applied by means of a spreader bar at each actuator. The number of load locations is limited only by the number of available actuators. A time-varying load is applied by a controller at each actuator. By correct sequencing of loads applied by the actuators, dynamic effects caused by high-speed passage of a vehicle can be closely approximated. Also, front and rear wheel interaction is included in the stress wave patterns.

ALGORITHM FOR LOADING

Consider a structure such as a flat plate that is loaded by a vehicle moving along a given path. To obtain the pseudostatic load-deflection relations, a flexibility approach can be used. The basic equation of flexibility is

$$P \times f = u \tag{1}$$

Department of Civil Engineering, Texas Transportation Institute, Texas A&M University, College Station, Tex. 77843-3136.

where

P = applied load at a specified location j on a structure,
f = deflection or flexibility coefficient at any location i caused by a unit load applied at j, and
u = deflection at i caused by the load P.

Using superposition this relation may be expanded to include n load locations as follows:

$$\sum_{j=1}^{n} P_j f_{ij} = u_i \tag{2}$$

As an example, four actuators that have a fixed location are used in this study to apply simulated wheel loads at the eight locations indicated in Figure 1. In this case four flexibility equations may be written that relate the combination of the actuator forces to the deflection at four points in the slab. Here, the deflections of interest are taken to be at the actuator locations themselves. The equations are written for application of forces that cause the same deflection at these locations as a vehicle that is at an arbitrary location along its path of travel. Dividing the load applied by an actuator into two equal loads (two wheels per axle) results in the following equation for the average deflection under actuator 1:

$$\sum_{j=1}^{4} A_j (f_{1jPa} + f_{1jb}) = (u_{1a} + u_{1b}) \tag{3}$$

where

A_j = load applied by actuator j, assuming $A_j/2 = A_{ja} = A_{jb}$ with A_{ja} and A_{jb} being the loads that are transferred to the slab at actuator j;
f_{1ja} = flexibility coefficient for left actuator load (left and right defined by looking in the direction of traffic);
f_{1jb} = flexibility coefficient for right actuator load;
u_{1a} = deflection of slab at actuator 1 for left load; and
u_{1b} = deflection of slab at actuator 1 for right load. A similar equation may be written for the other actuators. For the case of four actuators, the equations are given in Equation 4.

$$\begin{bmatrix} (f_{11a}+f_{11b}) & (f_{12a}+f_{12b}) & (f_{13a}+f_{13b}) & (f_{14a}+f_{14b}) \\ (f_{21a}+f_{21b}) & (f_{22a}+f_{22b}) & (f_{23a}+f_{23b}) & (f_{24a}+f_{24b}) \\ (f_{31a}+f_{31b}) & (f_{32a}+f_{32b}) & (f_{33a}+f_{33b}) & (f_{34a}+f_{34b}) \\ (f_{41a}+f_{41b}) & (f_{42a}+f_{42b}) & (f_{43a}+f_{43b}) & (f_{44a}+f_{44b}) \end{bmatrix} \begin{Bmatrix} A_1 \\ A_2 \\ A_3 \\ A_4 \end{Bmatrix} = \begin{Bmatrix} u_{1a}+u_{1b} \\ u_{2a}+u_{2b} \\ u_{3a}+u_{3b} \\ u_{4a}+u_{4b} \end{Bmatrix} \tag{4}$$

In an analogous manner, a set of equations may also be written that relate wheel loads from a vehicle to the deflection at each actuator location. For a vehicle that has two wheels attached to each of three axles the equations are as follows:

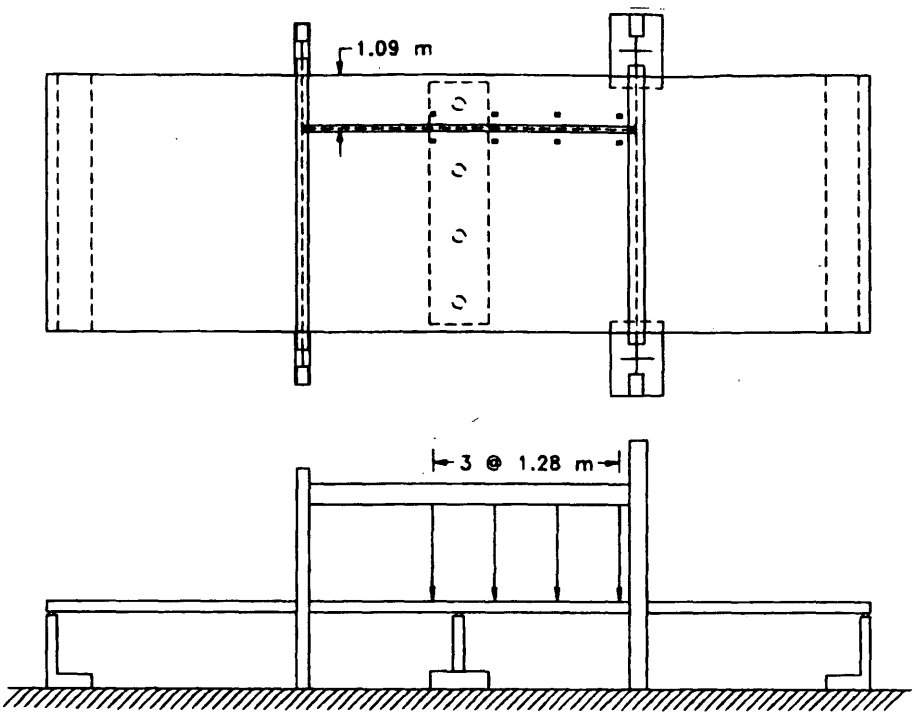

FIGURE 1 Fixed actuator locations for simulation of moving load.

$$\begin{bmatrix} (f^*_{11a}+f^*_{11b}) & (f^*_{12a}+f^*_{12b}) & (f^*_{13a}+f^*_{13b}) \\ (f^*_{21a}+f^*_{21b}) & (f^*_{22a}+f^*_{22b}) & (f^*_{23a}+f^*_{23b}) \\ (f^*_{31a}+f^*_{31b}) & (f^*_{32a}+f^*_{32b}) & (f^*_{33a}+f^*_{33b}) \\ (f^*_{41a}+f^*_{41b}) & (f^*_{42a}+f^*_{42b}) & (f^*_{43a}+f^*_{43b}) \end{bmatrix} \begin{Bmatrix} P_1 \\ P_2 \\ P_3 \end{Bmatrix} = \begin{Bmatrix} u_{1a}+u_{1b} \\ u_{2a}+u_{2b} \\ u_{3a}+u_{3b} \\ u_{4a}+u_{4b} \end{Bmatrix} \quad (5)$$

where

P_j = axle load;
f^*_{ija} = flexibility coefficient at the actuator for the left wheel load; and
f^*_{ijb} = flexibility coefficient at the actuator for the right wheel load.

As mentioned earlier, this set of pseudo-static equations holds for a given position of the moving vehicle.

Applying the condition at time t that deflections caused by the actuators (right side of Equation 4) be equivalent to those caused by the truck loads (right side of Equation 5), leads to the following relationship:

$$[f]\{A\} = [f^*]\{P\} \quad (6)$$

where matrixes f, f^*, A, and P are defined in Equations 4 and 5. Equation 6 can be solved for the required actuator forces for each position of the moving vehicle as it traverses the bridge.

EXAMPLE OF A SLAB BRIDGE

Recently, a 3/10-scale model of a two-span bidirectionally post-tensioned flat slab bridge (see Figure 2) was constructed and tested in a controlled laboratory environment (*3*). Dimensions of the slab are 16.9 × 5.33 × 0.229 m (55.5 ft × 17.5 ft × 9 in.). In addition to uniformly distributed longitudinal posttensioning, a band of tendons is placed in a narrow region above the four supporting columns. The slab rests directly on neoprene bearing pads that surmount the abutments and columns. No reinforcing steel connects the columns and abutments with the slab. Arrays of 185 strain gauges (see Figure 3), 18 linear variable differential transformers (LVDTs), 10 load cells, and 27 survey points serve to gather data for dead, live, and time-dependent loads.

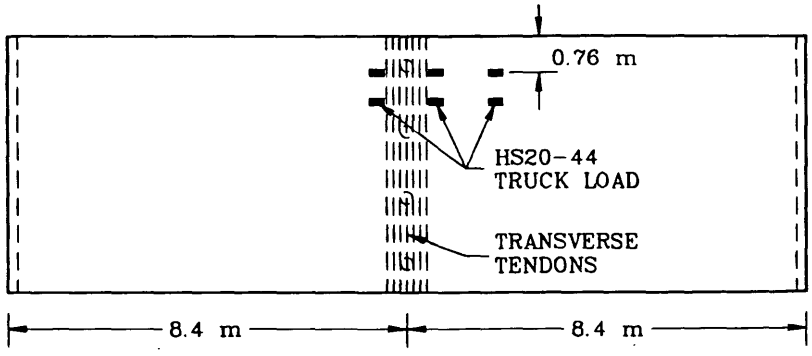

FIGURE 2 Slab geometry and example truck wheel load.

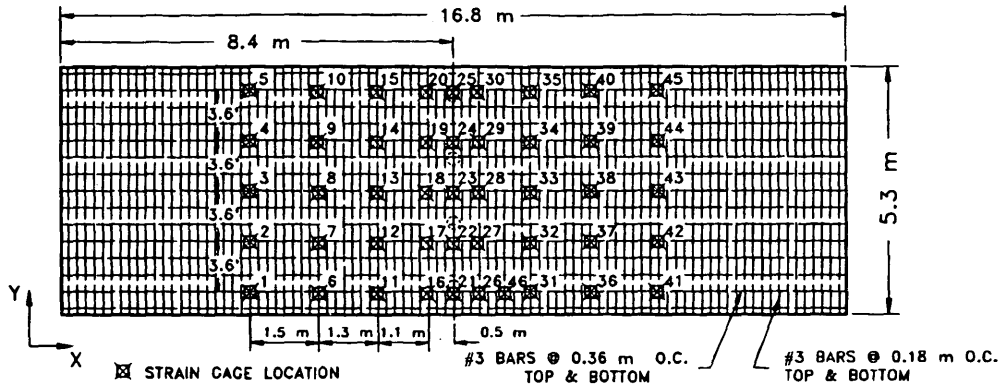

FIGURE 3 Location of strain gauges.

Factored and Scaled Truck Loads

Spacing and magnitude of the wheel loads on the laboratory model are determined by applying geometric and loading scale factors, along with impact and overload factors, to dimensions and load magnitudes of an AASHTO HS20-44 truck (see Figure 4). An impact factor of 0.30 is determined according to the following equation from AASHTO 3.8.2.1 (*4*):

$$I = \frac{50}{L_n + 125} \leq 0.3 \tag{7}$$

where

I = impact fraction (maximum 30 percent); and
L_n = length in feet of the portion of the span that is loaded to produce the maximum stress [for L_n = 8.38 m (27.5 ft) and I = 0.32, use 0.30].

Because design of the slab has been shown to be conservative (*3*), an overload factor of 1.67 (*4*) is also applied to increase the probability of inducing damage in the structure. The resulting wheel loads are multiplied by a similitude scale factor of 0.09 (*3*) to produce the wheel loads that are applied to the scale model bridge slab.

A region of the slab near the columns that has a high spatial gradient of stress was investigated for effects of repeated passage of heavy truck traffic. Traffic is assumed to flow across the bridge from right to left in Figures 1 through 3. Figure 2 shows a typical location of the truck tires along its path of travel. A beam attached to each actuator with a pin connection is used to transfer the load to pressure pads that are spaced equidistant from the center of the line of travel of the truck. These pads, which have the scaled dimensions of the area of contact of a truck tire, apply load to the bridge deck. The distance between actuators is equal to that of the scaled length of the wheelbase of the truck loading. This means that the actuator loads correspond to the given scaled truck loads at those instances in the loading cycle when the location of the simulated truck coincides with the pressure pads.

A preliminary static finite element analysis of the prestressed slab was carried out using TEXSLAB (*5*). The surface plot of Figure 5 shows the predicted normal stress in the transverse direction in the bottom layer of the slab as a result of prestressing and dead load. Figure 6 displays change in transverse stresses in the same bottom layer caused by the factored and scaled HS20-44 live load. Although stress ranges caused by live load are small, that is, approximately 345 kPa (50 psi), and a fatigue failure was not expected, it is still uncertain what damage might occur from the complex nature of the stress distribution in this region. Banding of transverse prestressing coupled with localized effects of column reactions may lead to a significant amount of microcracking when repeated loads are applied. To investigate this problem, 200,000 cycles of load are applied to the model.

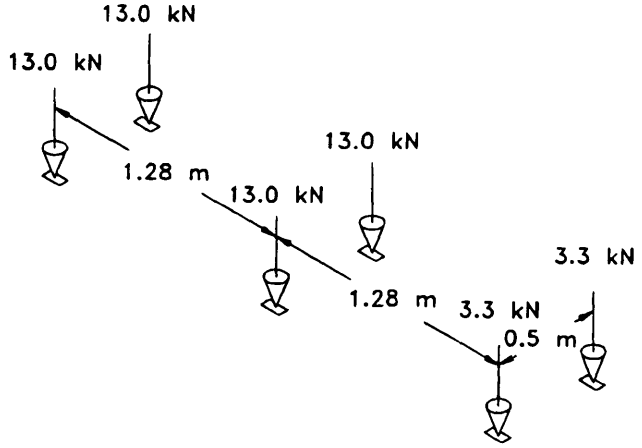

FIGURE 4 Wheel loads applied to scale model bridge slab.

Time History of Actuator Loading

Flexibility coefficients for Equation 6 are determined using the special-purpose finite element code mentioned earlier. A series of numerical simulations are carried out where the location of a unit load is varied by 0.61-m (2-ft) increments, beginning at the right end of the bridge deck. The load is placed in line with one of the paths of travel of a wheel (i.e., in line with the actuator pads), and deflection at each actuator pad is calculated. This gives one-half of the flexibility coefficients of Equation 6 for a given position of the load. A similar procedure is carried out for the other wheelpath. Then, knowing the flexibility coefficients and the magnitude of the truck wheel loads P_i (see Figure 4), leads to a simple solution for the actuator forces A_i that produce the same deflections at the actuators as the scaled vehicle.

Response time and mechanical constraints of the load actuators determine the maximum speed of load application for a single pas-

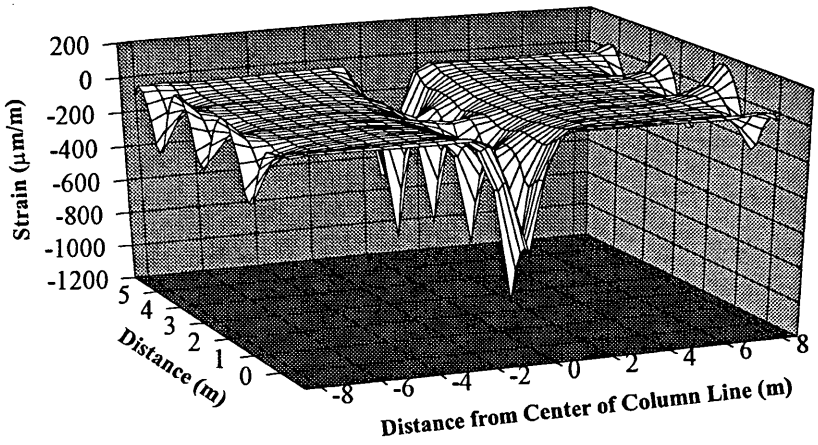

FIGURE 5 Transverse normal stress caused by dead load and prestressing.

sage of a vehicle. Because of hardware limitations of available actuators and their controllers, one full load cycle of travel may be applied in 1.66 sec. By applying a scale factor for velocity, it is determined that this corresponds to a truck traveling on the prototype bridge at 48 km/hr (30 mph). Correlation of time with truck position on the experimental slab gives a time history load curve for each actuator as shown in Figure 7*a*.

Two modifications of this procedure are made. Note that some negative (upward) values of load result as the actuators attempt to create the complex curvature of the structure. Because the lack of connectors on the surface of the experimental slab preclude tensile loads being applied by the actuators, a further approximation must be incurred. Equation 6 is solved by a trial-and-error procedure for each truck location with only one, two, or three actuators applying load. The combinations that result in no tensile load are used to create the necessary deflections.

Second, from Figure 7*a* the load from Actuator 4 becomes very high after the vehicle moves beyond the line of columns. This increase is because the fourth actuator is applying nearly all of the load to achieve the required deflection after the truck has passed this point. To reduce the influence of this actuator on the solution, the truck load is reduced to 0 after it moves past the center bent. The load curve that results from these special conditions is shown in Figure 7b.

Experimental Results

Consider a point on the slab that is 6.4 m (21 ft) from the beginning of the bridge and lies along a line that bisects the two lines of wheel loads. At this location, vertical displacement predicted by numerical simulation of the pseudostatic progression of the load is shown in Figure 8. Also shown in this plot is the actual displacement recorded by an LVDT from one cycle of the actuator loading. Differences between the curves are attributed to interaction of the dynamic response of the slab with the loads applied by the actuators. At the expense of rapid completion of the load cycles, the curve could be smoothed out with a slower application of the load. However, from the standpoint of fatigue, the additional spikes represent a more severe case of stress in the continuum than does a smooth curve.

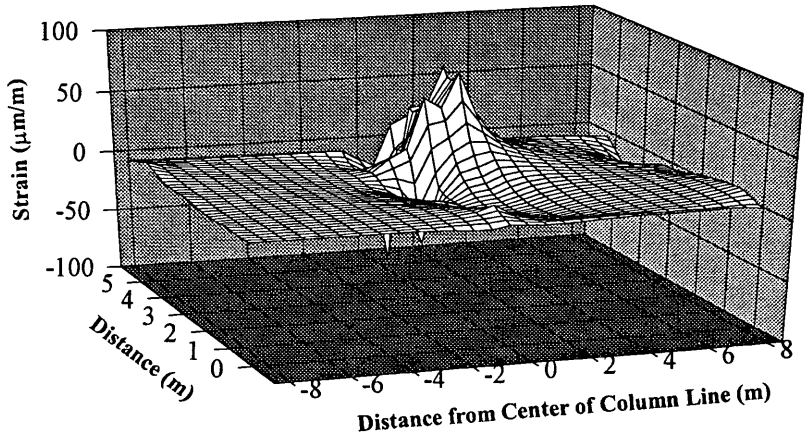

FIGURE 6 Change in transverse normal stress caused by live load.

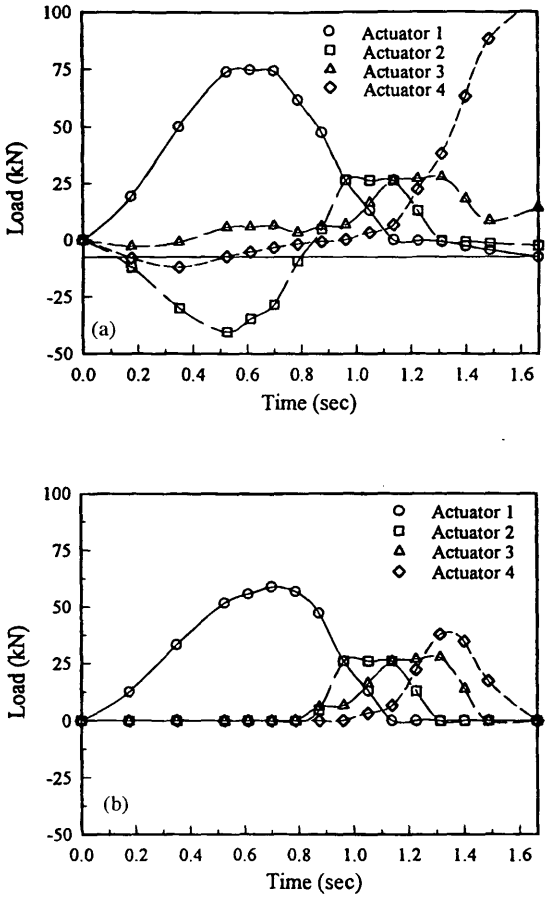

FIGURE 7 Load curves for application of cyclical load: (*a*) tensive forces allowed; (*b*) no tensile forces.

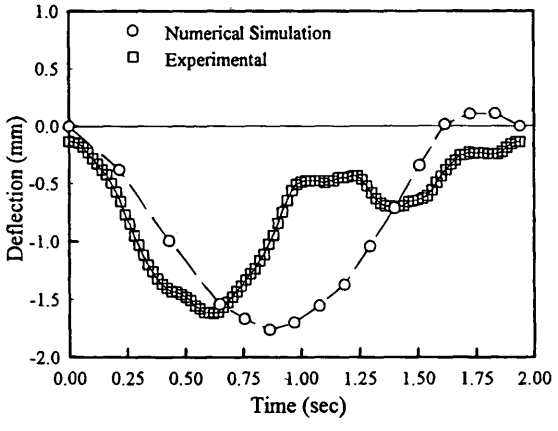

FIGURE 8 Comparison of experimental and theoretical deflection for one truck passage.

As described earlier, a total of 200,000 cycles of the HS20-44 truck was applied to the slab. Figure 9 shows a comparison of the initial deflection curve and one recorded during the last cycle at the same location as that described earlier. There are only small changes in the general shape and maximum deflection of the curves.

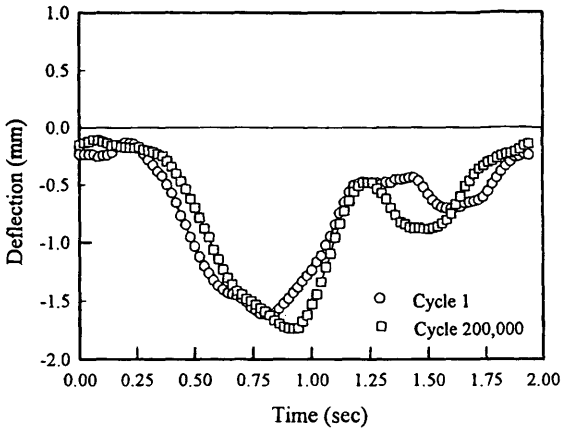

FIGURE 9 Comparison of deflection at first and last cycles.

Approximately once every 10,000 cycles, the dynamic loading was temporarily halted. A static load that is equivalent to the scaled and factored wheel loads was placed on the slab at the location shown in Figure 4. An LVDT located beneath the slab measured the deflection. For these static loads the measured deflection versus the number of load cycles is shown in Figure 10. During the first 20,000 cycles there is a decrease in vertical deflection resulting from the static load; this phenomenon is attributed to shifting of the structure and residual compression of the elastomeric bearing pads between the column and the slab. For the remaining 180,000 cycles the static deflection is relatively constant.

In addition to checking for change in vertical displacement at regular intervals of loading, attempts were also made to detect degradation of the concrete and to measure the change in transverse strain in the critical region near the columns. Cracking of concrete was monitored directly by visual inspection during application of the static load and, indirectly, by strain gauge readings. No visible cracks were observed on the top or bottom surface of the slab through the full number of cyclical loads. This lack of damage was confirmed by readings from the gauges attached to the rebars and embedded in the concrete (see Figure 3). Gauges located in the vicinity of the supporting columns recorded a change in strain of less than 5 microstrain for the static application of load. These negligible readings did not increase throughout the 200,000 cycles.

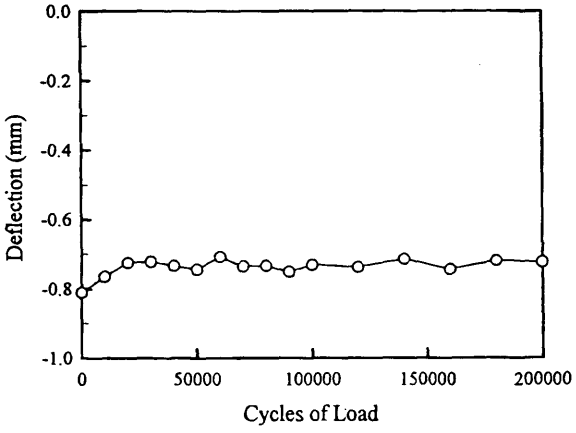

FIGURE 10 Static deflection versus cycles of load.

CONCLUSION

A method is presented that allows use of a series of actuators that are fixed in position to impose sequential loads that simulate passage of a vehicle along a bridge. The approach is demonstrated using a large-scale laboratory model of a slab bridge. Force time–history of each actuator is calculated from a system of simultaneous equations that govern each increment of time. Flexibility coefficients are determined from a static finite element analysis of the slab. Repetitive truck loading consisting of 200,000 cycles was applied to the slab at 2-sec intervals. Visual inspection and data from transducers show that no apparent damage to the concrete was sustained. Bidirectional posttensioning contributes to a conservative design of the slab that is not susceptible to fatigue damage at these load levels.

ACKNOWLEDGMENT

The author thanks the Texas Department of Transportation and FHWA for financial support for the study. VSL supplied post-tensioning equipment free of charge.

REFERENCES

1. Perdikaris, P. C., S. R. Beim, and S. N. Bousias. Slab Continuity Effect on Ultimate and Fatigue Strength of Reinforced Concrete Bridge Deck Models. *ACI Structural Journal,* Vol. 86, No. 4, 1989, pp. 483–491.
2. Okada, K., H. Okamura, and K. Sonoda. Fatigue Failure Mechanism of Reinforced Concrete Bridge Deck Slabs. In *Transportation Research Record 664*, TRB, National Research Council, Washington, D.C., 1978, pp. 136–144.
3. Roschke, P. N., K. R. Pruski, and C. D. Smith. *Experimental and Analytical Study of a Two-Span Post-Tensioned Bridge Slab.* Report FHWA/TX-90/1182-2. Texas Transportation Institute, Texas A&M University, College Station, 1992.
4. *Standard Specifications for Highway Bridges*, 14th ed. AASHTO, Washington, D.C., 1989.
5. Roschke, P. N., and K. R. Pruski. *Graphically-Oriented Analysis of Post-Tensioned Slab Bridges on Microcomputers.* Report FHWA/TX-90/1182-4F. Texas Transportation Institute, Texas A&M University, College Station, 1994.

Publication of this paper sponsored by Committee on Dynamics and Field Testing of Bridges.

Seismic Retrofitting of Bridge Substructures

THAD D. SAUNDERS, JAMES A. CAHILL, DAVID I. MCLEAN, M. LEE MARSH, AND CARLTON HO

Retrofitting measures for improving the seismic performance of the substructures of existing bridges were investigated. Experimental tests were conducted on 1/3-scale specimens consisting of a square column supported on a pile footing. Details of the column and footing were selected to represent deficiencies present in older bridges. Retrofit measures were applied to both the columns and footings. The specimens were subjected to increasing levels of cycled inelastic lateral displacements under constant axial load. Specimen performance was evaluated on the basis of load capacity, displacement ductility, strength degradation, and hysteretic behavior. Tests on the as-built specimen resulted in a brittle failure due to insufficient joint shear strength in the column and footing connection. An added reinforced concrete overlay provided an effective retrofit for the as-built footings. The overlay resulted in increased shear resistance, allowed for the addition of a top mat of reinforcement to provide negative moment strength, and increased the positive moment capacity by increasing the effective depth of the pile cap. All retrofitted specimens developed plastic hinging in the columns with a resulting ductile response under the simulated seismic loading. Special detailing was required in the column lap splice regions in order to maintain the integrity of the splices. In a specimen that was overturning critical, successful retrofitting was achieved by enlarging the footing plan size and providing additional piles.

Bridge structures have historically been vulnerable to seismic loading, with numerous examples of damage occurring to both superstructure and substructure elements and, in some cases, complete and catastrophic collapse. The watershed event in changing seismic design philosophies was the 1971 San Fernando earthquake. Bridges built under design criteria developed after 1971 have generally performed well in recent earthquakes. However, the vulnerability of older, pre-1971 bridges was clearly evident in the 1987 Whittier Narrows and 1989 Loma Prieta earthquakes. In the Loma Prieta earthquake alone, damage to bridges resulted in more than 40 deaths, $1.8 billion in damage to transportation structures, and severe economic disruptions due to the loss of major transportation routes (*1*).

As a result of the damage that occurred to older bridges, a major research effort was directed at developing strengthening or retrofit strategies to upgrade the performance of older bridges. Significant retrofit efforts began in California in the 1970s, with the initial focus of the retrofit schemes being to improve the performance of the superstructures in earthquakes. Following the 1987 Whittier Narrows earthquake in which extensive damage occurred to many columns, it became apparent that retrofit efforts must address the entire bridge structure. Column retrofit strategies were subsequently developed. Only recently have strengthening methods been developed for improving the performance of existing footings, and very limited testing has been performed to verify the methods.

The objective of this study was to experimentally evaluate retrofit methods for improving the seismic performance of existing footings. The focus was on pile-supported substructures. A detailed account of the research program can be found elsewhere (*2*). This paper presents an overview of the study and discussion of the test results and conclusions.

BRIDGE SUBSTRUCTURE RETROFITTING

Column Retrofitting

A common detail found in older bridge columns is an insufficient amount of transverse reinforcement. Typically, No. 3 or No. 4 hoops at 0.3 m (12 in.) on center were used in columns regardless of the column cross-sectional dimensions, and the hoops had short extensions and anchorage only by lapping the ends in the cover concrete. Further, intermediate ties were rarely used. This detail results in the susceptibility of many older columns to shear failures, and it provides little confinement for developing the full flexural capacity or preventing buckling of the longitudinal reinforcement.

Another detail commonly used in older bridges was splicing of the longitudinal bars at the bottom of the columns. Typically, starter bars were extended only 20 longitudinal bar diameters (d_b) from the foundations, which does not provide sufficient length to develop the yield strength of the reinforcement. Bond failure is also likely once the cover concrete spalls. These deficiencies result in a high potential for flexural strength degradation in the event of an earthquake.

Previous research (*3*) has shown that the most effective column retrofit method for both circular and rectangular columns is steel jacketing. The steel jacket is made slightly larger than the columns, and the space between the jacket and column is filled with grout. Research has shown that in order to achieve the needed lateral confinement with the retrofit, circular or elliptical jacketing is necessary. Test results showed that jacketing of the columns can improve the splice region performance (partial-height jacketing) and column shear performance (full-height jacketing).

On the basis of recent research studies (*4,3*), the California Department of Transportation (Caltrans) (*5*) implemented standardized column retrofit procedures: the Class P retrofit and the Class F retrofit. Steel jackets with a minimum thickness of 10 mm (3/8 in.) are used. Circular or elliptical jackets are used depending on whether the column is circular or rectangular. The Class P retrofit provides partial confinement in the plastic hinging region, with the intent of providing a pseudo pin at the bottom of the column. The Class F retrofit results in the preservation of the full flexural capacity of the column and typically requires retrofitting of the footing in order to carry the forces transferred from the column.

T. D. Saunders and M. L. Marsh, ABAM Consulting Engineers, 33301 Ninth Avenue South, Federal Way, Wash. 98003-6395. J. A. Cahill, U.S. Air Force, Ellsworth Air Force Base, Rapid City, S. Dak. 57706-5000. D. I. McLean and C. Ho, Department of Civil and Environmental Engineering, Washington State University, Pullman, Wash. 99164-2910.

Footing Retrofitting

Footings in older bridges were designed primarily for gravity loads. As a result, the footings often contain little or no top reinforcement and may be susceptible to brittle flexural failures in an earthquake. Older footings may also be susceptible to shear failures, both through the footings and at the column and footing joints. Many existing footings are vulnerable to overturning, pile failures, or both. All of these problems may be exacerbated by retrofit measures applied to other sections of a bridge, such as column jacketing.

Caltrans (*5*) developed procedures for designing footing retrofits. Based on the plastic moment capacity of the columns, the footing is checked for flexural and shear strengths and overturning. To increase overturning resistance, the footing may be enlarged, additional piles provided, or soil anchors added. To provide negative moment strength and to increase shear strength, a concrete overlay is added to the top of the existing footing. Horizontal reinforcement is incorporated into the overlay, and reinforcing dowels connect the overlay to the existing footing.

Xiao et al. (*6*) tested specimens with as-built and retrofitted footings. Tests on the as-built specimen resulted in a column and footing joint shear failure. Retrofitted specimens incorporating an overlay designed using current Caltrans standards performed better, but the researchers concluded that the standards do not adequately address the joint shear problem. An improved retrofit design using longer dowels to develop more effective joint shear resistance mechanisms was proposed and verified.

EXPERIMENTAL TESTING PROGRAM

Test Specimens and Parameters

For this study a section of a typical bridge substructure consisting of a single column and supporting pile footing was used as the basis for evaluating as-built and retrofitted substructure performance. The prototype column and pile footing were formulated by compiling design plans from the 1950s and 1960s for bridges in Washington State. Emphasis was placed on single-column bent bridges because these bridges are likely to be more critical than multicolumn bent bridges and thus would be the first type of bridges targeted for retrofit. The prototype substructure section chosen for study consisted of a 3.7- by 3.7-m (12- by 12-ft) square pile cap with a thickness of 0.9 m (3 ft) and a 0.9-m (3-ft) square column. The reinforcing ratios selected for the pile cap were 0.42 and 0.28 percent for the longitudinal and transverse steel, respectively, and the column reinforcing ratio selected was 2.5 percent. Details included column lap splice lengths of $20d_b$ and $35d_b$. Timber piles were selected for study in this investigation because they are common in many older foundations in Washington State. On the basis of the reviewed plans, the timber piles were typically spaced at 0.9-m (3-ft) intervals and were approximately 0.3 m (12 in.) in diameter.

The experimental tests were conducted on 1/3-scale specimens that modeled the prototype dimensions, reinforcing ratios and arrangement, deficient detailing, and material properties. Test parameters included the performance of as-built specimens and methods for improving the pile-cap shear strength and for increasing footing overturning resistance. The specimen columns incorporated both $20d_b$ and $35d_b$ splices. The columns of all specimens were retrofitted using circular steel jacketing in order to focus any distress into the footings. A summary of the test specimens is given in Table 1; five specimens were tested. Details of Specimen No. 1, representing as-built footing details, are shown in Figure 1. The various retrofit measures applied to the remaining specimens are discussed later along with the test results.

Test Setup and Procedures

The test specimens were supported on short wood piles in a sandy soil contained within a stiff box constructed of large glue-laminated wood beams. Soil was compacted between the piles before con-

TABLE 1 Summary of Test Specimens

Specimen No.	Pile-Cap Deficiency	Pile-Cap Retrofit Applied	Column Type	Column Deficiency	Axial Load $\frac{P}{f'_c A_g}$
1	Shear	None	Square	20 d_b hinge splice	0.104
2	Shear	Top Deck and Pedestal	Square	20 d_b hinge splice	0.104
3	Shear	Top Deck	Square	35 d_b hinge splice	0.104
4	Shear and Overturning	Top Deck and Low Tension Capacity Piles	Square	35 d_b hinge splice	0.069
5	Shear and Overturning	Top Deck, Low Tension Capacity Piles, and Added Piles	Square	35 d_b hinge splice	0.069

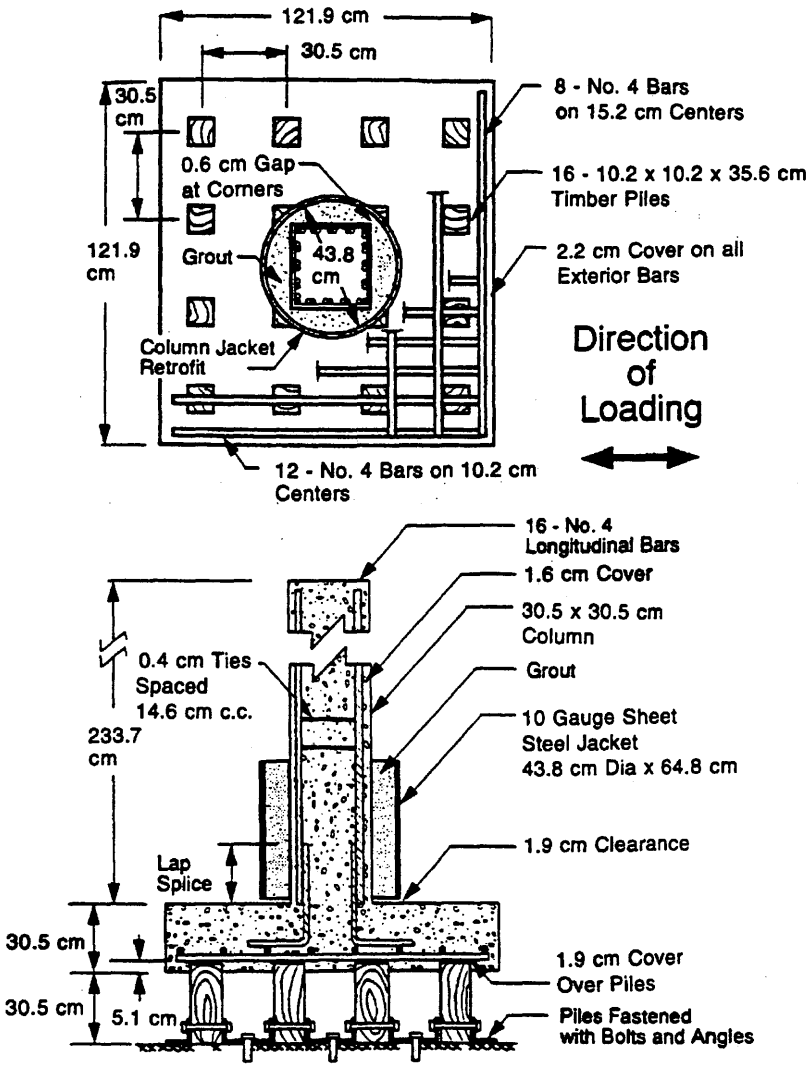

FIGURE 1 Details of specimen representing as-built conditions, Specimen No. 1 (1 in. = 2.5 cm).

struction of the pile cap and then around the pile cap after it was poured, as shown in Figure 2. The objectives of this test setup were to allow the pile cap to rotate and to approximately simulate the actual footing support conditions. This setup overconfines the soil when compared with field conditions, and there is significant labor involved in setting up and removing a specimen. However, the setup is more realistic than the support conditions often used in laboratory tests in which the footing is bolted to a strong floor, thus not allowing any footing rotations.

The overall test setup is shown in Figure 3. The specimens were subjected to reversed cyclic lateral loading under a constant axial load. Axial loads of 270 kN (60 kips) and 180 kN (40 kips) were used to facilitate the study of various failure mechanisms. A ram mounted on a low-friction trolley was used to apply the axial load. Lateral loads were applied using a horizontal actuator.

The determination of the column tip horizontal displacement at first yield (Δ_y) and the loading sequence were similar to the procedures used by Priestley and Park (*7*). The specimens were subjected to a simulated seismic loading pattern consisting of increasing multiples of Δ_y in order to demonstrate the ductility and hysteretic behavior of the test specimens. The loading pattern for the specimens consisted of two cycles at displacement levels of ± 1, ± 2, ± 3, ± 4, ± 6, ± 8, ± 10, and ± 12 times Δ_y unless failure occurred first.

Strain gauges were used to monitor the strains in the flexural and transverse reinforcement. Linear variable displacement transformers (LVDTs) and load cells measured column displacements and applied loads. LVDTs were also placed on the top of the pile cap to determine footing displacements and rotations. Several of the wood piles were instrumented with strain gauges and were calibrated under compressive loading in an attempt to monitor loads in the piles. All data were recorded intermittently during testing.

TEST RESULTS AND DISCUSSION

In this section results of the experimental tests are summarized. Results from Specimen No. 1 are presented first. These results were used to formulate the retrofits for the four subsequent specimens. A

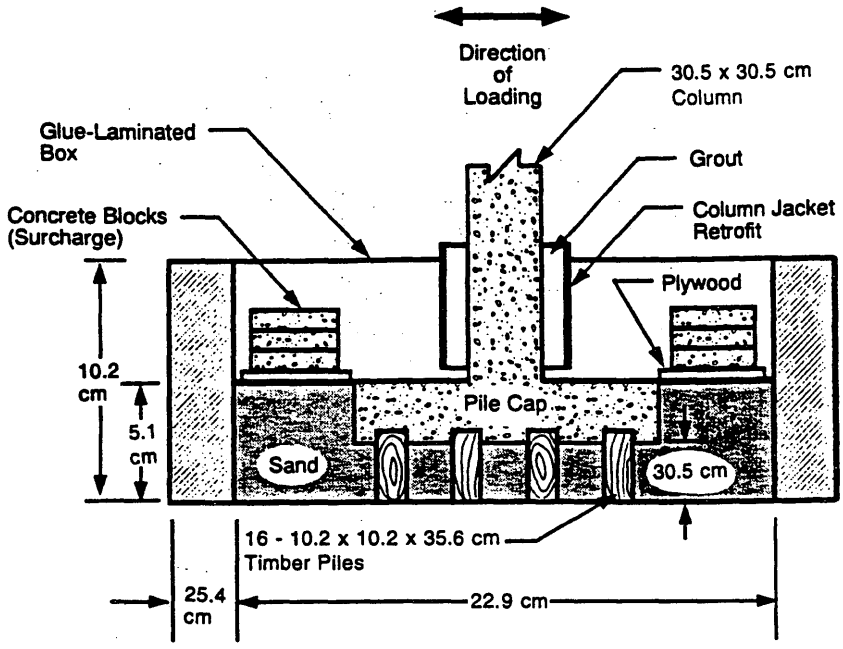

FIGURE 2 Testing support conditions (1 in. = 2.5 cm).

description of the retrofit methods applied and specimen performance is then presented for Specimen Nos. 2 through 5. Specimen performance was evaluated on the basis of moment capacity, displacement ductility, strength degradation, and hysteretic behavior.

Specimen No. 1

Specimen No. 1 was designed to be representative of as-built conditions in which the pile cap is shear critical. The performance of this specimen was intended as the basis for designing and evaluating retrofit methods for the subsequent specimens. The column of Specimen No. 1 contained a $20d_b$ lap splice and was retrofitted at the base with a steel jacket.

General Behavior

Failure in Specimen No. 1 occurred during loading to a displacement level of $2\Delta_y$. The resulting hysteresis curves for Specimen No. 1 are shown in Figure 4 and indicate little energy dissipation. The peak applied lateral load was 49.8 kN (11.2 kips) and occurred at a column tip displacement of 36.6 mm (1.44 in.). The column reached 65 percent of its moment capacity before the specimen failed and showed only minimal signs of cracking.

During testing, the top of the pile cap developed cracking radiating outward from the column. After the specimen was removed from the testing setup, cracks were also observed on all four sides of the pile cap. Only minor cracking was observed on the bottom of the pile cap. The major cracks occurring in Specimen No. 1 are shown in Figure 5.

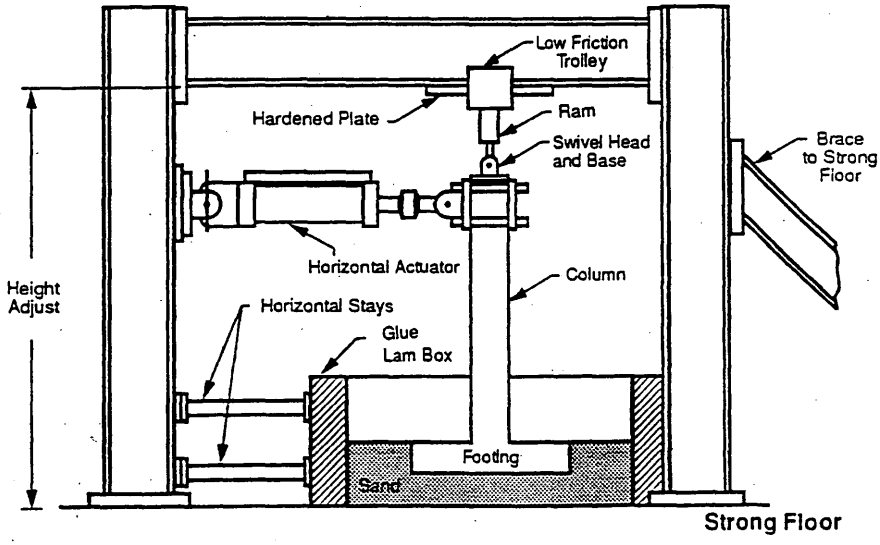

FIGURE 3 Testing setup (1 kip = 4.448 kN; 1 in. = 25.4 mm; 1 ft = 0.304 m).

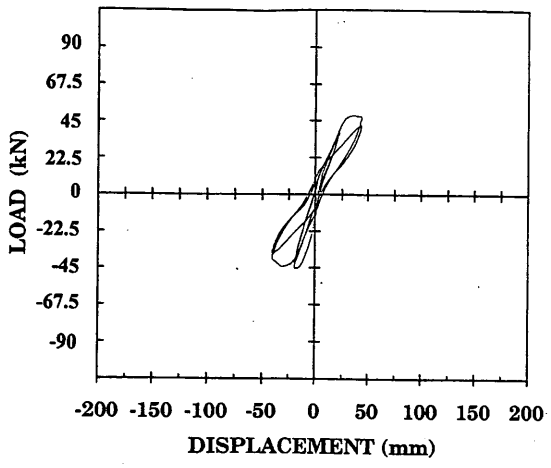

FIGURE 4 Load-deflection curves for Specimen No. 1 (1 kN = 0.2248 kip; 1 mm = 0.039 in.).

Failure Mechanism

The cracks observed in the pile cap of Specimen No. 1 are indicative of a shear failure. However, because of the cyclic loading, the exact sequence and the origin of the cracks were difficult to determine, resulting in some uncertainty as to the exact cause of the failure. It was postulated that failure in the pile cap was a result of one or more of the following failure modes: one-way beam shear, concrete failure associated with pullout of the dowel hooks forming the column splice, or a joint shear failure at the column and footing connection similar to that reported by Xiao et al. (*6*). To gain an understanding of the cause of the failure, a qualitative study (*8*) was conducted using small-scale specimens that replicated the details of Specimen No. 1. The small-scale specimens (approximately 1/18 scale) allowed for cross sectioning of the specimens after testing.

Tests on the small specimens resulted in the same apparent failure mode observed in the test on the larger-scale Specimen No. 1. A cross section showing the internal cracking patterns within the column and footing joint region is shown in Figure 6(*a*). A major diagonal crack developed within the column and footing connection. In Figure 6, loading was applied to the column from right to left. Thus, the inclination of the crack precludes a beam shear failure. Instead, the observed cracking is typical of that associated with a joint shear failure in a beam or column connection [see Figure 6(*b*)].

Priestley (*9*) has suggested a simple method of checking principal tensile stress in the column and footing joint region to assess joint shear failure. The principal tensile stress in the joint region is calculated using Mohr's circle for stress and accounting for the axial and shear stresses within the joint. Details of the procedure are given by Xiao et al.(*6*). A tensile stress value of 0.42 $\sqrt{f'_c}$ MPa

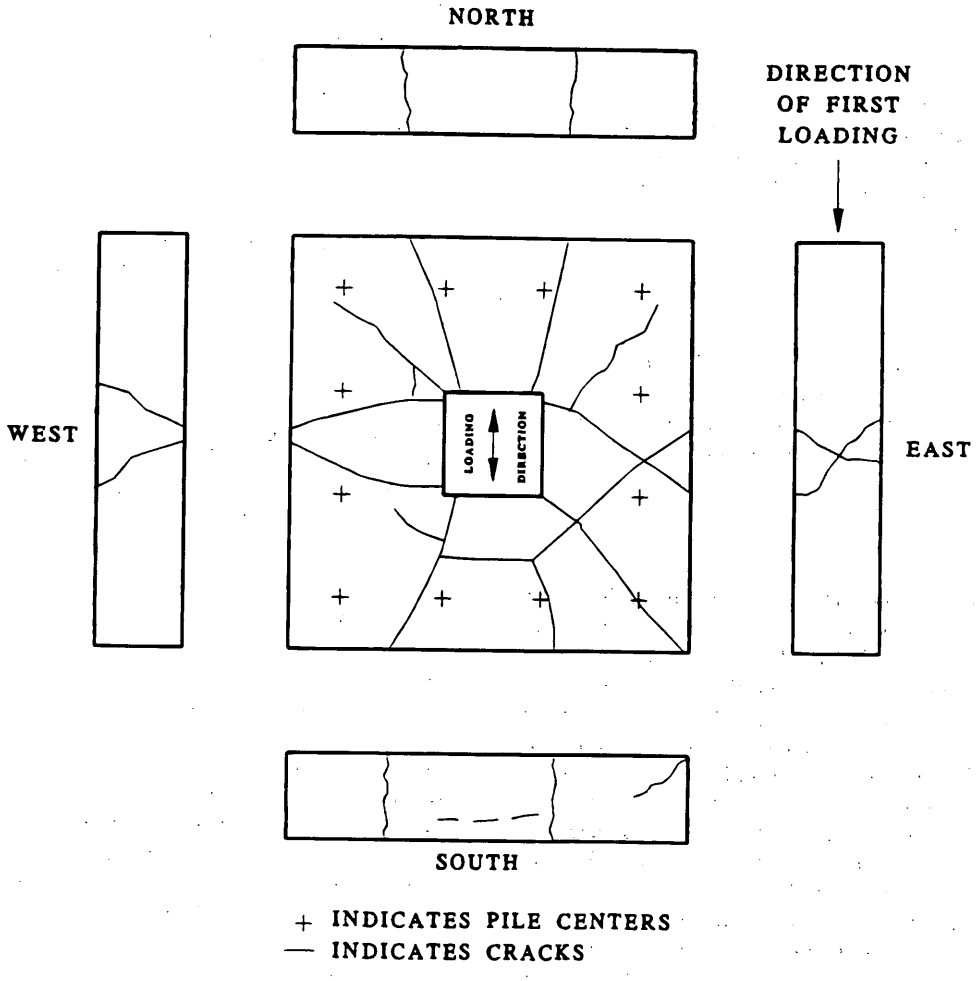

FIGURE 5 Cracking patterns in pile cap of Specimen No. 1.

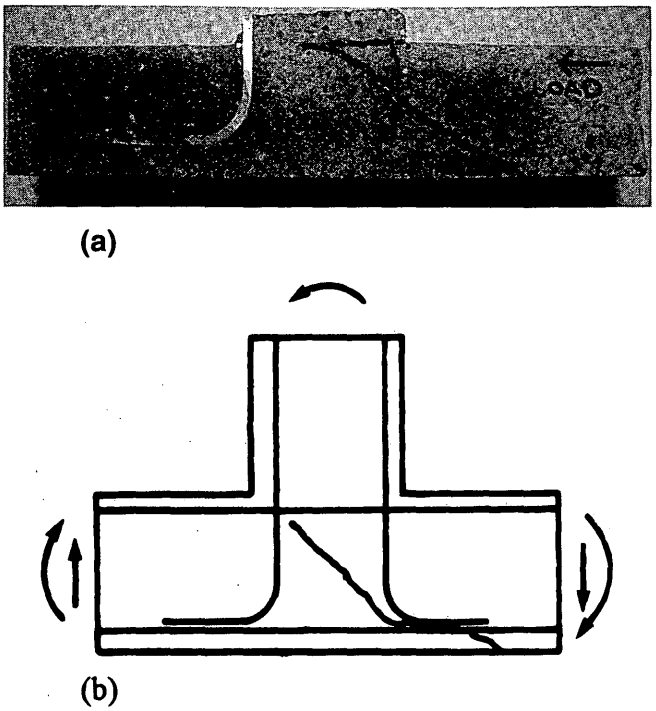

FIGURE 6 Cracking patterns in (*a*) small-scale column and footing joint and (*b*) column and beam joint.

($5.0\sqrt{f'_c}$ psi) was suggested as the limit at which joint failure will occur. Using this approach, a maximum tensile stress value of approximately $0.46\sqrt{f'_c}$ MPa ($5.5\sqrt{f'_c}$ psi) was calculated for Specimen No. 1, reinforcing the conclusion that a joint shear failure in the column and footing connection was the failure mechanism.

Specimen No. 2

Specimen No. 2 was constructed and detailed as in Specimen No. 1 except that the pile cap was retrofitted to increase its thickness by adding a concrete overlay. This overlay intersected the splice region of the column and thus required special detailing.

Retrofit Description

The overall thickness of the pile cap was increased by adding a reinforced concrete overlay on top of the existing pile cap. The overlay was designed to act compositely with the existing pile cap by providing dowels. The dowels were designed using shear friction theory and drilled and epoxied into the top of the existing pile cap. The ends of the dowel were anchored into the retrofit overlay with 180-degree hooks. The overlay also allowed for the addition of a mat of horizontal reinforcement, thus providing negative moment strength to the footing. The thickness of the overlay was selected to produce joint shear stresses below the limit proposed by Priestley (*9*) and to allow for development of the shear friction dowels. An overlay thickness of 13 cm (5 in.) was used in the specimen.

The $20d_b$ splice present in the column of Specimen No. 2 required special detailing since the overlay intersected the splice (in this case, at midheight of the splice). If the splice was intersected by the overlay, the working interface for the column hinging would be at the top of the overlay, and the embedment of the splice would no longer be $20d_b$. As a consequence, the column reinforcement may not fully develop and the splice may degrade, no matter what the amount of confinement provided. Thus, a pedestal extending to the top of the splice was incorporated into the retrofit scheme to maintain the integrity of the splice. Crack control steel consisting of a hoop and hairpins was provided in the pedestal. Figure 7 illustrates the details of the retrofit used for Specimen No. 2.

The column cover over the full height of the splice was removed before constructing the retrofit overlay to enable composite action and load transfer between the column and the added overlay. The column retrofit jacket was still required to provide confinement in the new plastic hinge region, now located at the top of the pedestal, because of the inadequate transverse reinforcement present in the as-built column.

Test Results

The specimen performed very well, with failure occurring at a displacement level of $10\Delta_y$, as illustrated by the hysteresis curves shown in Figure 8. The peak applied lateral load was 87.2 kN (19.6 kips) and occurred at a displacement of 118 mm (4.65 in.). During the second cycle of loading to a displacement level of $10\Delta_y$, a column longitudinal bar fractured. Before this low-cycle fatigue fracture of the reinforcement, the development of a plastic hinge at the base of the column resulted in a very ductile response. The hysteresis curves are large, show little pinching, and exhibit good energy dissipation.

Cracking in the pile cap, added overlay, and pedestal was minimal. Some cracking did occur in the pedestal around the column as a result of plastic hinge penetration. Pile cap movements and rotations were very small. On the basis of the instrumented piles, significant pile tension forces were observed despite the lack of any structural connection between the top of the wood piles and the pile cap.

Specimen No. 3

The as-built portion of Specimen No. 3 was detailed and constructed as in Specimen No. 1. However, the column of Specimen No. 3 incorporated a $35d_b$ lap splice rather than the $20d_b$ splice used in Specimen Nos. 1 and 2.

Retrofit Description

A concrete overlay retrofit was again used to improve the performance of the footing. With a lap splice length of $35d_b$, the use of a pedestal to fully contain the splice would result in an unreasonably large pedestal. As in Specimen No. 2, an overlay thickness of 13 cm (5 in.) was chosen on the basis of joint shear considerations. Thus, the overlay would intersect the splice at 13 cm (5 in.) or $10d_b$ from the bottom of the splice, leaving a $25d_b$ lap splice above the overlay. Previous research (*4*) has shown that a lap splice length of $20d_b$ can fully develop the reinforcement if proper confinement is present. Therefore, no pedestal was used in the retrofit. However, in order to maintain the original column strength and stiffness, the column longitudinal bars

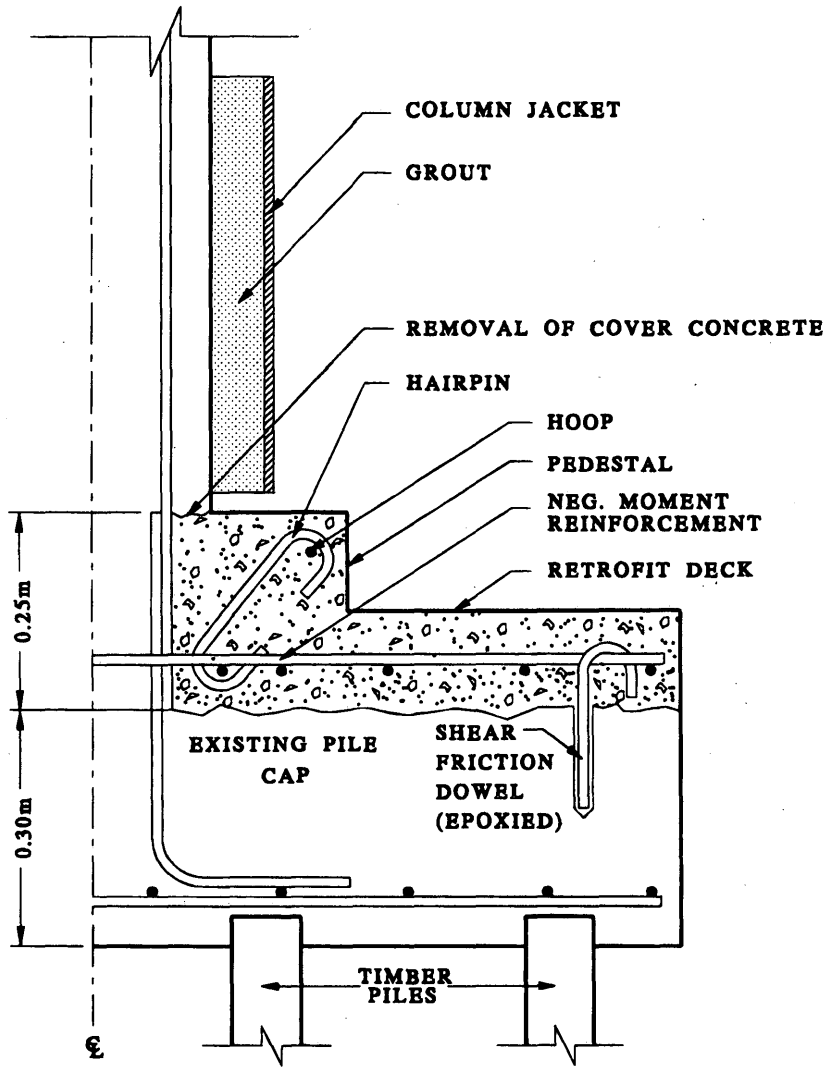

FIGURE 7 Retrofit scheme for Specimen No. 2 (1 m = 3.3 ft).

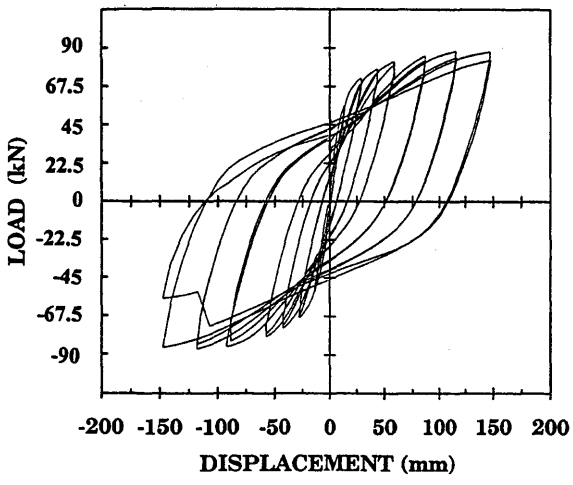

FIGURE 8 Load-deflection curves for Specimen No. 2 (1 kN = 0.2248 kip; 1 mm = 0.039 in.).

were cut at the top of the overlay before the retrofit was poured. All other details of the retrofit were the same as in Specimen No. 2. Figure 9 shows the retrofit measures applied to Specimen No. 3.

Test Results

The hysteresis curves for Specimen No. 3 are shown in Figure 10 and indicate good energy dissipation. The peak applied lateral load was 83.6 kN (18.8 kips) and occurred at a displacement of 90.1 mm (3.55 in.). During the first cycle to a displacement level of $12\Delta_y$, several dowel bars fractured and the test was stopped. Cracking resulting from plastic hinge penetration occurred in the top of the pile cap and was more extensive than the cracking observed in Specimen No. 2. After the specimen was removed from the test setup, some diagonal cracking was also evident in the as-built portion of the pile cap. However, the pile cap maintained its integrity and the overall performance of the specimen was satisfactory.

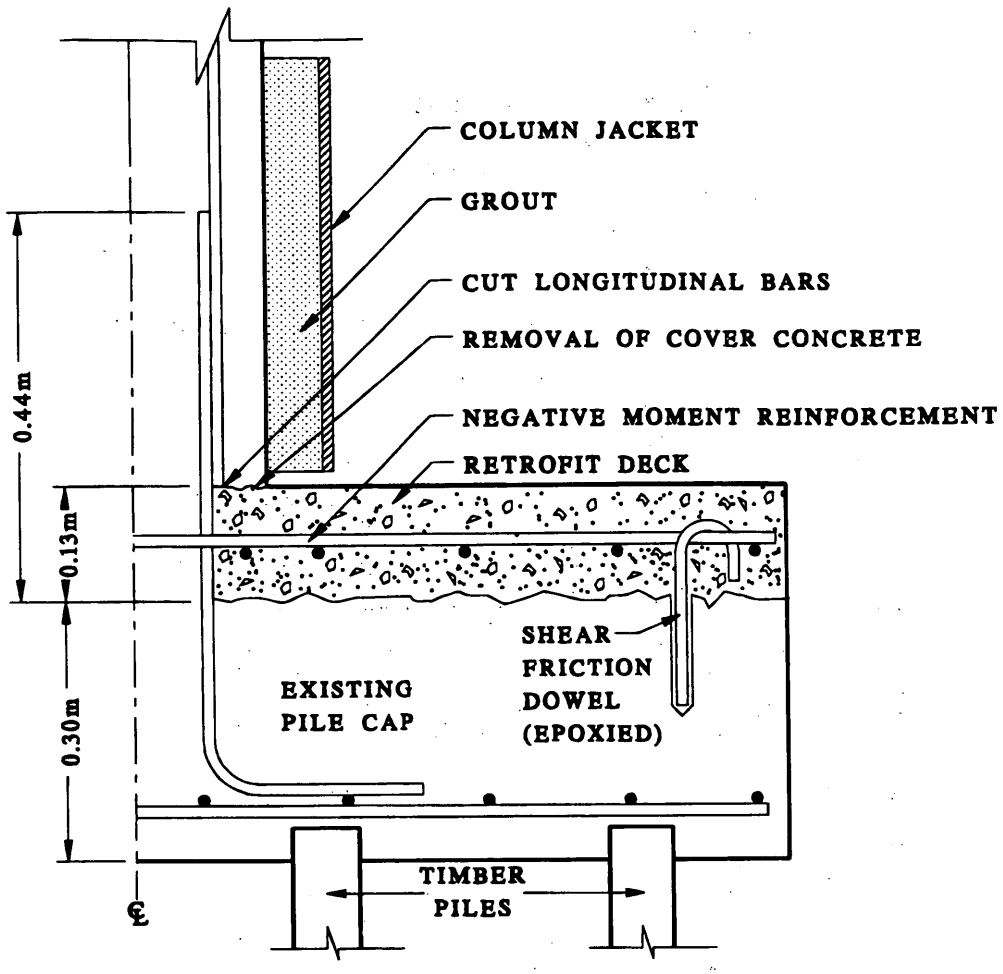

FIGURE 9 Retrofit scheme for Specimen No. 3 (1 m = 3.3 ft).

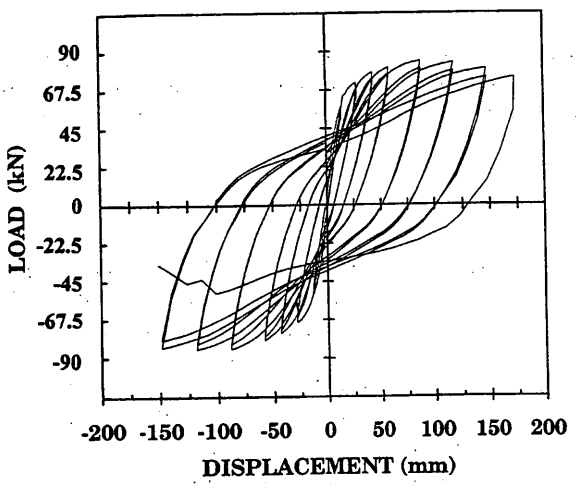

FIGURE 10 Load-deflection curves for Specimen No. 3 (1 kN = 0.2248 kip; 1 mm = 0.039 in.).

Specimen No. 4

Specimen No. 4 was designed to examine the "rocking" behavior of a footing system when the tension capacity of the piles is lost or nonexistent. In the previous tests, the timber piles were found to have a tensile capacity. If this tensile capacity was not present, the overturning resistance of the footing would be less than the column flexural capacity and overturning or rocking would occur. This rocking behavior would be relevant to foundations that, perhaps by choice, were not retrofitted.

Retrofit Description

Specimen No. 3 incorporated a $35d_b$ lap splice, and the details of the retrofit were identical to those used for Specimen No. 3. However, the tops of the piles were greased, and a layer of crushable foam was placed around the sides of the piles embedded in the pile cap. These

measures effectively destroyed the tensile capacity of the piles while at the same time preserving the compressive capacity. A reduced axial load was used on Specimen No. 4 to ensure that the specimen would be overturning critical.

Test Results

Figure 11 shows the hysteresis curves for Specimen No. 4. The S shape of the curves is the result of the uplift and rotation of the pile cap. The peak applied lateral load is approximately 67 kN (15 kips) and is only 80 percent of the column capacity. The hysteresis curves enclose small areas, indicating low energy dissipation. However, the response was very stable, indicating the potential for beneficial load redistribution and cost savings if some footings were left unretrofitted and allowed to rock.

Specimen No. 5

The tensile capacity of the piles in Specimen No. 5 was suppressed as in Specimen No. 4. However, Specimen No. 5 was retrofitted by enlarging the footing and adding additional piles to increase the overturning resistance.

Retrofit Description

The footing size for Specimen No. 5 was enlarged by adding 0.3 m (12 in.) to each end in the direction of loading. Eight additional piles were added, four at each end, to increase the overturning resistance. A $35d_b$ lap splice was present in the column, and an overlay was added to increase the shear resistance of the footing. The overlay was detailed in a manner similar to that for Specimen Nos. 3 and 4.

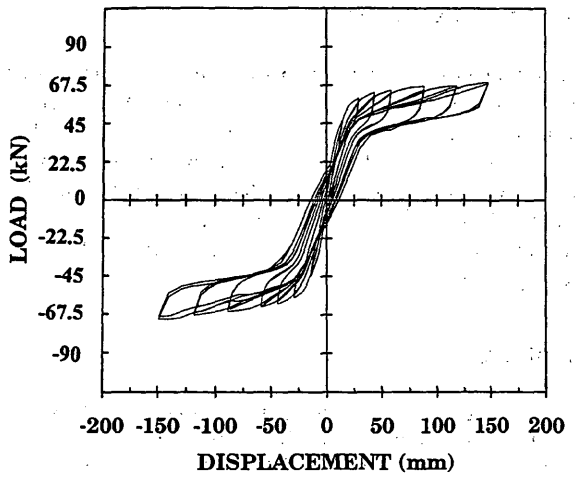

FIGURE 11 Load-deflection curves for Specimen No. 4 (1 kN = 0.2248 kip; 1 mm = 0.039 in.).

The additional piles were selected to represent steel-encased cast-in-place concrete piles. This type of pile was chosen for its tension capability, ease of construction, and the likelihood of its being used in actual retrofits. In the scaled specimen tests, the added piles consisted of concrete cast into steel tubing bolted to the floor. A reinforcing bar was cast into the center of the pile to provide tension capacity between the added piles and the cap.

Composite action between the existing and the enlarged sections of the pile cap was achieved by chipping out the concrete around the bottom mat of reinforcement in the existing footing and welding the existing and new positive reinforcement together. The top mat of reinforcement provided in the overlay also enhanced composite action between the sections. Shear reinforcement was provided in the enlarged portion of the pile caps. The retrofit design for Specimen No. 5 is shown in Figure 12.

Test Results

The hysteresis curves for Specimen No. 5 are shown in Figure 13. The pile cap experienced essentially no uplift. The peak applied lateral load was 81.4 kN (18.3 kips) and occurred at a displacement of 90.1 mm (3.55 in.). During cycling to a displacement level of $12\Delta_y$, five of the outermost dowel bars fractured because of low-cycle fatigue and testing was stopped. The hysteresis curves are large and exhibit good energy dissipation.

Similar to the cracking observed in Specimen No. 3, cracks developed in the top of the pile cap and extended toward the sides. Cracks also developed in the top of the pile cap around the column because of plastic hinge penetration. However, the cracking was controlled by the top mat of reinforcement in the retrofit overlay and specimen performance was very satisfactory.

CONCLUSIONS

The experimental test results from this study indicate that existing bridge footings may perform poorly under seismic loading. The as-built specimen exhibited significant cracking in the pile cap and failed as a result of inadequate joint shear strength in the column and footing connection. The failure was relatively brittle and showed little energy dissipation.

It was found that an added reinforced concrete overlay provided an effective retrofit for the as-built footings. The overlay resulted in increased shear resistance, allowed for the addition of a top mat of reinforcement to provide negative moment strength, and increased the positive moment capacity by increasing the effective depth of the pile cap. All retrofitted specimens developed plastic hinging in the columns with a resulting ductile response under the simulated seismic loading.

Special detailing was required in the column lap splice regions in order to maintain the integrity of the splices. With a $20d_b$ splice, a pedestal enclosing the full height of the splice was incorporated into the retrofit. With a $35d_b$ splice, no pedestal was used; however, the column bars were cut at the top of the overlay and a remaining confined splice length of at least $20d_b$ was maintained.

In a specimen that was overturning critical, successful retrofitting was achieved by enlarging the footing plan size and providing additional piles.

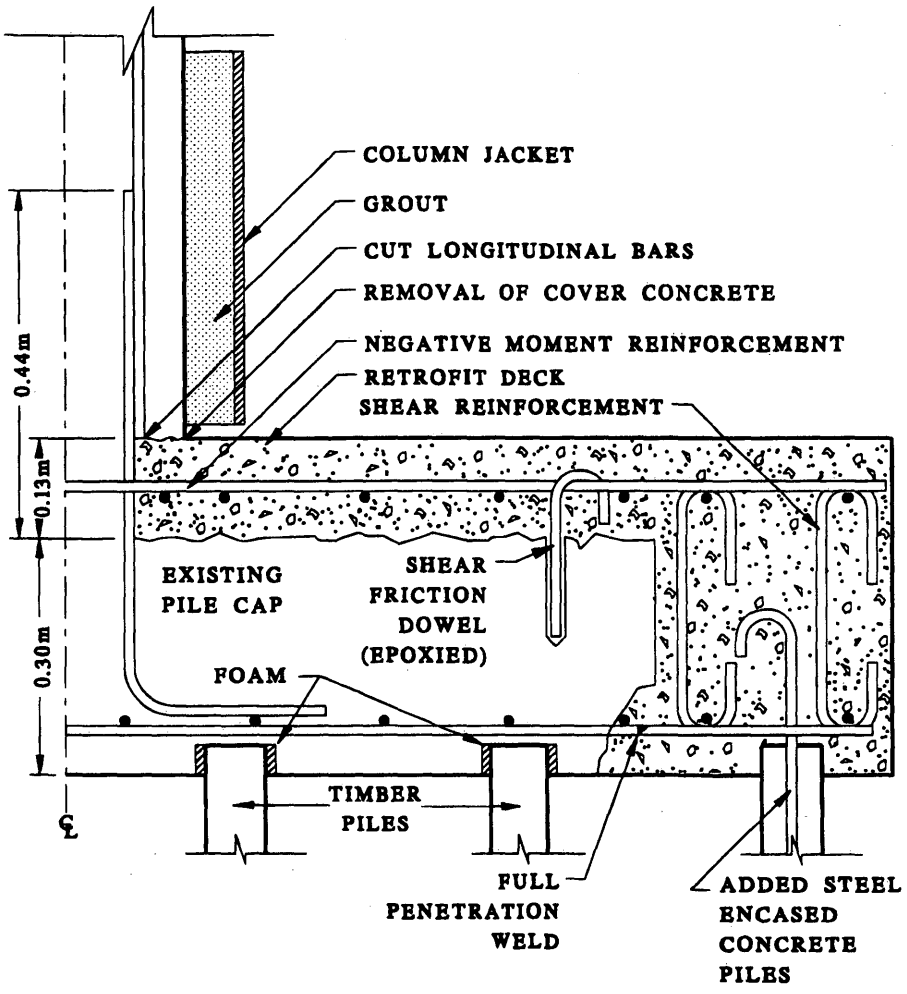

FIGURE 12 Retrofit scheme for Specimen No. 5 (1 m = 3.3 ft).

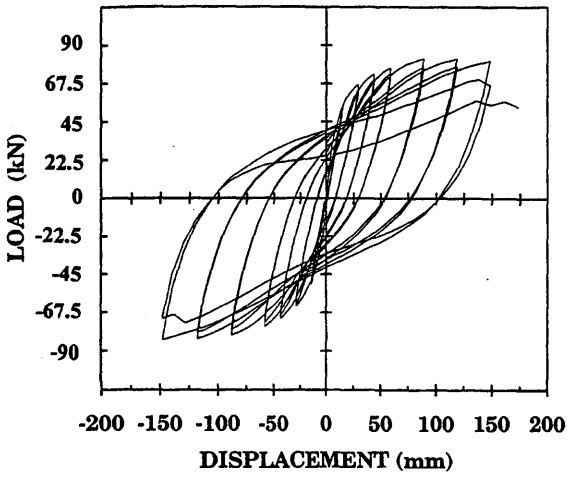

FIGURE 13 Load-deflection curves for Specimen No. 5 (1 kN = 0.2248 kip; 1 mm = 0.039 in.).

ACKNOWLEDGMENTS

The research presented in this paper was funded by the Washington State Department of Transportation through the Washington State Transportation Center (TRAC). The authors acknowledge the valuable contributions of Ed Henley and Harvey Coffman of the Washington State Department of Transportation. The many contributions by Harold Hahnenkratt, former graduate student at Washington State University, to the testing of the specimens of this study are gratefully acknowledged.

REFERENCES

1. Cooper, J. D., I. M., Friedland, I. G., Buckle, R. B. Nimis, and N. M. Bobb. The Northridge Earthquake: Progress Made, Lessons Learned in Seismic Resistant Bridge Design. *Public Roads*, Vol. 58, No. 1, Summer 1994.
2. Saunders, *Seismic Retrofit of Bridge Pile Caps*. M.S. thesis. Washington State University, Pullman, 1994, 164 pp.

3. Priestley, M. J. N., and F. Seible. Design of Seismic Retrofit Measures for Concrete Bridges. In *Seismic Assessment and Retrofit of Bridges*, Report SSRP 91/03, University of California, San Diego, 1991, pp. 197–234.
4. Chai, Y. H., M. J. N. Priestley, and F. Seible. Retrofit of Bridge Columns for Enhanced Seismic Performance. In *Seismic Assessment and Retrofit of Bridges*, Report SSRP 91/03, University of California, San Diego, 1991, pp. 177–196.
5. *Memo to Designers, 20-4*. California Department of Transportation, April 1992.
6. Xiao, Y., M. J. N. Priestley, F. Seible, and N. Hamada. *Seismic Assessment and Retrofit of Bridge Footings*. Report SSRP-94-11, University of California, San Diego, 1994, 167 pp.
7. Priestley, M. J. N., and R. Park. Strength and Ductility of Concrete Bridge Columns Under Seismic Loading. *ACI Structural Journal*, Vol. 84, No. 1, Jan.–Feb. 1987, pp. 61–76.
8. Cahill, J. A. *A Qualitative Study of Failure Mechanisms in 1/18 Scale Column-Footing Structures*. M.S. Special Project Report. Washington State University, Pullman, 1993, 82 pp.
9. Priestley, M. J. N. Seismic Assessment of Existing Bridges. In *Seismic Assessment and Retrofit of Bridges*, Report SSRP 91/03, University of California, San Diego, 1991, pp. 84–149.

Publication of this paper sponsored by Committee on Dynamics and Field Testing of Bridges.

Identification of Railway Bridges Using Traffic-Induced Vibrations

E. UZGIDER, A. K. ŞANLI, F. PIROĞLU, AND B.Ö. ÇAĞLAYAN

A program of full-scale bridge tests was undertaken as a principal part of the research project entitled Rehabilitation of Old Railway Bridges and primarily considered railway bridges located on the Turkish Railway Network. This program was financially supported by the North Atlantic Treaty Organization Science for Stability Program. Bridges were tested during the summers of 1991, 1992, 1993, and 1994. The test program followed a standard pattern for each bridge. An efficient damage detection procedure developed in the course of TU-BRIDGE research studies with application to the Çerkezköy Railway Bridge is described.

A research project entitled Rehabilitation of Old Railway Bridges and started on February 1990, was financially sponsored by the North Atlantic Treaty Organization (NATO) Science for Stability Program with the code name TU-850-BRIDGES. The main objective of this research program was to evaluate current structural conditions and reliability of these bridges, which are the most important part of the Turkish railway system. Repairing and strengthening procedures will be developed as needed.

In the framework of the TU-BRIDGES Project a rational procedure has been developed to detect any existing damage and deterioration globally on old railway bridges using collected acceleration data during their dynamic field test. Because labor needed to install acceleration transducers is considerably easier than that needed to install strain transducers, in less than one day the needed data can be collected, avoiding the costly rail traffic shutdowns. Thus, the procedure could be a tool for enhancing bridge inspection and identifying globally existing damages with their location. If global damage is detected for any bridge region, then the process must be completed by strain measurements focused on that region to achieve an element-level damage detection.

To avoid the rail traffic shutdowns of forced vibration test techniques, an ambient vibration technique in which a bridge structure is excited by the current rail traffic is used. The added mass effect of the bridge traffic is avoided by considering the acceleration data recorded after the train has left the bridge. Several previous studies (*1–5*) showed that current traffic is considered as an excitation mechanism.

Not all degrees of freedom can be measured during a test because an unreasonable amount of transducers are needed and, thus, not all modes are observed in the response records. On the other hand, adequate control of excitation, which is only the case for forced vibration tests under laboratory conditions, is essential for precise mode shape measurements, but it is not the case for the traffic-induced vibration tests performed on the real bridge structures. Thus, instead of considering element-level identification, stiffness parameters representing the stiffness changes in the selected structural segments containing some amount of structural members, can be defined more reliably, depending on the identified modal parameters.

The proposed method has been successfully employed for the data recorded from the 11 railway bridges tested within the framework of the TU-BRIDGES Project. The total process that is offered to follow to achieve element-level damage detection is described in Figure 1.

Department of Civil Engineering, Istanbul Technical University, 80626 Maslak, Istanbul, Turkey.

GLOBAL DAMAGE DETECTION METHOD

The proposed method consists of two main consecutive phases: (a) modal identification and (b) segmentary stiffness identification.

Modal Identification

After preprocessing the recorded acceleration data to eliminate possible noise contamination and removing existing trends and outliers as given in detail elsewhere (*6,7*), using the well-known spectral analysis method similar to that used by Felber (*5*), modal parameters are defined on the basis of the acceleration data recorded after the train has left the bridge.

Segmentary Stiffness Identification

Distress in civil engineering structures often may have a significant effect on stiffness, but not on mass. In steel structures, fatigue cracks reduce stiffness without loss of mass, and even a corrosion loss will affect stiffness to a much greater extent than it will affect mass. Thus, it is safely assumed that because of these structural damages, mass values are not changed. Then, stiffness identification can be used as an efficient tool to detect the structural changes with respect to the computer model. A dominant part of these changes may be assumed to be caused by the existing damages in the structure, if an accurate computer modeling technique has been employed during the identification process. On the other hand, a considerable simplification is possible in stiffness identification when the function of a member in a structure relies primarily on one stiffness. For example, floor beams in the bridge provide primarily flexural stiffness, whereas truss members provide primarily axial stiffness. In such cases, damage in a member will influence modal parameters through the primary stiffness only, and the change in a member stiffness may be represented by the change in its elasticity modulus. However, stiffness changes are not sensitive enough to small structural damages such as those caused by fatigue cracks or corrosion loss existing on a bridge member.

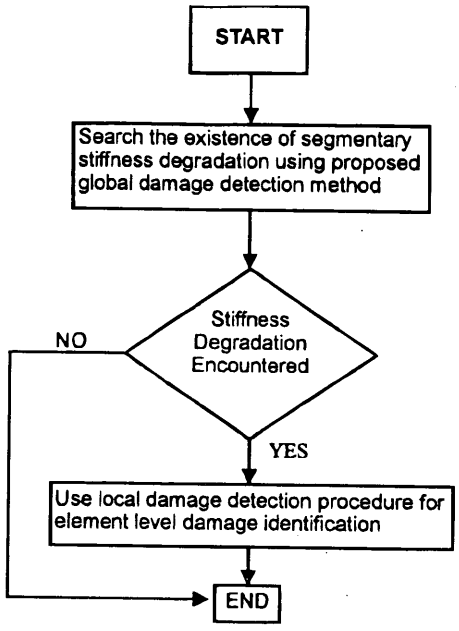

FIGURE 1 Element-level identification procedure.

Thus, instead of considering bridge members one by one, upper and lower lateral bracing system, two plane trusses, and vertical and longitudinal support springs of the bridge were divided into a set of segments in this identification process. The segmentation pattern employed in this study is shown in Figure 2. Then, the modulus of elasticity of each characteristic region is considered as the segmentary stiffness parameters to be identified. Then, a negative percent change of identified elasticity modulus of any segment with respect to the original value will be interpreted as the signature of the total stiffness degradation or damage occurring in the members covered by this segment. On the other hand, positive percent changes are considered as the result of the other sources of stiffness that cannot be incorporated into the computer model.

To estimate the segmentary stiffness parameters the weighted squares of the difference between the experimentally identified and computed modal parameters, subject to limits on the extreme values of the segmentary stiffness parameters will be minimized. The following is the associated constrained nonlinear optimization problem for the proposed least-squares estimator:

$$\underset{\boldsymbol{E}}{\text{minimize}}\ J(\boldsymbol{E}) = \sum_{i=1}^{n} gi\,[MMP_i - CMP_i(\boldsymbol{E})]^2 \tag{1}$$

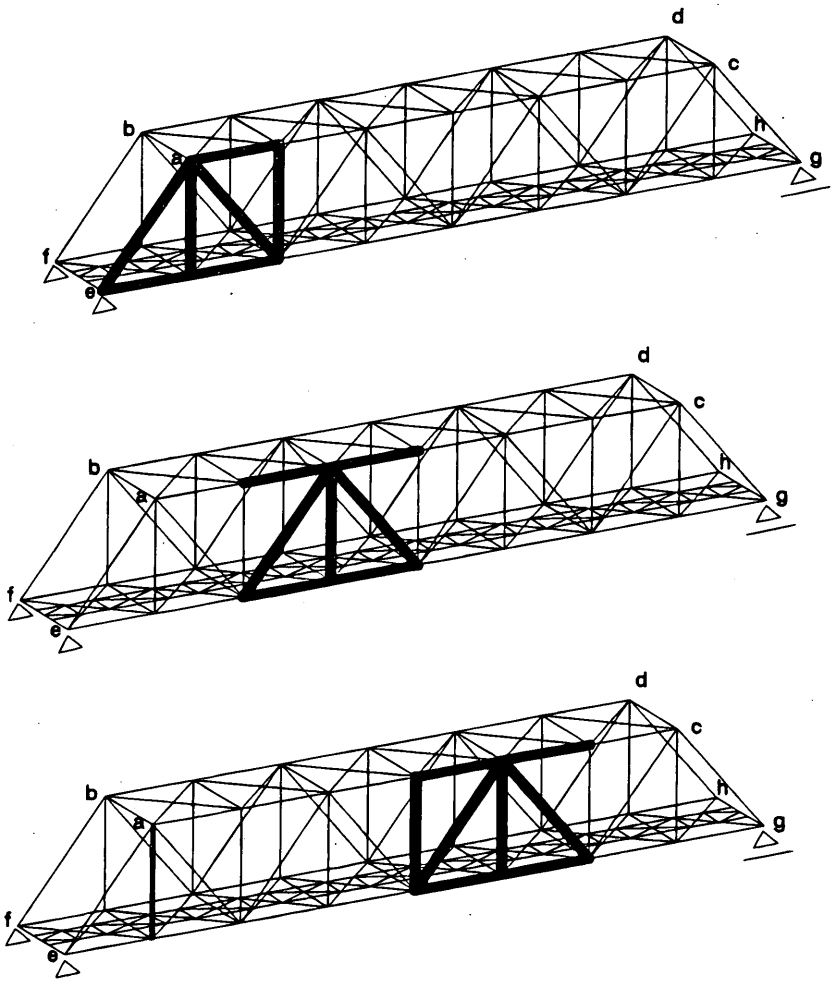

FIGURE 2 Structural segmentation.

subject to $\boldsymbol{E}^l \leq \boldsymbol{E} \leq \boldsymbol{E}^u$ where $\boldsymbol{E}$ is the segmentary stiffness parameter vector,

$$\boldsymbol{E} = \{E_1, E_2, \ldots, E_m\}^T \quad (1a)$$

MMP_i is the experimentally identified or measured modal parameters and n is the number of experimentally identified or measured modes. The vectors $\boldsymbol{E}^l$ and $\boldsymbol{E}^u$ are the lower and upper limit vectors, respectively, for the unknown segmentary stiffness parameters, and the inequalities are enforced component by component. These limits are available to enforce known characteristics of the stiffness parameters. For example, one might know in advance that a negative value in the modulus of elasticity is impossible on physical grounds, and the stiffness parameters are limited from above. These limits define the feasible region and are important because they eliminate the possibility of converging to physically unreasonable solutions. For this problem, the upper limit might be set as some multiple of nominal design values or expected parameter values to control the algorithm.

The weight g_i reflects the relative confidence in the test data. In this study, cross-correlation coefficients calculated between the data collected from the different measuring points of the bridges are employed as the weight. CMP_i $(\boldsymbol{E})$ stands for a set of scalar cubic functions simulating the variation of modal parameters with respect to the segmentary stiffness parameters. These scalar functions can be obtained in a way similar to that employed by Douglas and Reid (*8*).

A three dimensional finite element computer model covering all the geometric irregularities and stiffness changes existing on the considered bridge structure is employed for the free vibration analyses, in which consistent mass is employed for the bridge members. Point mass approximation is used for the mass contribution from nonstructural components such as sleepers, rails, or walkways, and so forth. Four vertical and two horizontal spring elements are also used to simulate the effective vertical stiffness of the combined bearing and abutment structure and the longitudinal restraints at the sliding bearings.

The following is a simple representation of the modal parameters as the cubic functions of the segmentary stiffness parameters used in this study:

$$CMP_i = A_i + \sum_{j=1}^{m} [B_{ij} \cdot E_j + C_{ij} \cdot E_j^2 + D_{ij} \cdot E_j^3] \qquad i = 1, \ldots, n \quad (2)$$

where

n and m = total number of parameters and total number of structural segments to be considered, respectively,
E_j = the jth segmentary stiffness parameter, and
A, B, C, and D = unknown constants to be determined.

Thus, to determine these constants, three different-level perturbations are given to the segmentary stiffness parameters in addition to their initial values:

$$E_{oj} = E \quad (2a)$$

$$E_{kj} = E + (\delta E)_k \qquad j = 1, \ldots, m \qquad k = 1, \ldots, 3 \quad (2b)$$

Then, by employing the aforementioned sophisticated computer model of the considered bridge, a set of free vibration analyses is performed for the initial segmentary stiffness values (Equation 2*a*) and for the three levels of segmentary stiffness perturbations given in Equation 2*b* considered sequentially for each segment. In this way, totally $\{n \times (m + 1)\}$ modal parameters are produced. To determine unknown constants of Equation 2, by employing these modal parameters the following equations can be written:

$$CMP_i^{(0)} = A_i + \sum_{j=1}^{m} [B_{ij} \cdot E_{oj} + C_{ij} \cdot E_{oj}^2 + D_{ij} \cdot E_{oj}^3] \quad (3)$$

$$CMP_{i,1}^{(k)} = A_i + B_{i1} \cdot E_{k1} + C_{i1} \cdot E_{k1}^2 + D_{i1} \cdot E_{k1}^3 + \sum_{j=2}^{m} [B_{ij} \cdot E_{oj} + C_{ij} \cdot E_{oj}^2 + D_{ij} \cdot E_{oj}^3] \quad (3a)$$

$$\vdots$$

$$CMP_{i,m}^{(k)} = A_i + \sum_{j=1}^{m-1} [B_{ij} \cdot E_{oj} + C_{ij} \cdot E_{oj}^2 + D_{ij} \cdot E_{oj}^3] + B_{im} \cdot E_{km} + C_{im} \cdot E_{km}^2 + D_{im} \cdot E_{km}^3 \qquad i = 1, \ldots, n \qquad k = 1,2,3 \quad (3b)$$

where $CMP_i^{(0)}$ is the ith modal parameter obtained by free vibration analysis for the initial segmentary stiffness values and $CMP_{i,m}^{(k)}$ is the ith modal parameter obtained by the same analysis for kth-level perturbed segmentary stiffness values of bridge segment m only. In this way, $\{n \times m \times (k = 3) + n\}$ linear equations can be produced for the same amount of unknowns. After having defined unknown coefficients of the cubic functions given in Equation 2, the constrained nonlinear optimization problem defined in Equation 1 can be solved to obtain unknown segmentary stiffness parameter values using any of a number of available optimization methods. In this study a sequential quadratic programming (SQP) method is used. An overview of SQP has been given by Fletcher (*9*), Gill et al. (*10*), and Hock and Schittowski (*11*).

As was previously discussed (*12*), nonlinear optimization algorithms usually give results that are strongly affected by the topography of the scalar error function J given in Equation 1. If this function has more than one local minimum, then the initial estimate made at the start for segmentary stiffness parameters controls the convergence of the algorithm to one of these local minima. In this study, to prevent the convergence of the algorithm to the local minima other than the true one, the bounding constraints are imposed on the segmentary stiffness parameters as explained earlier (Equation 1). On the other hand, a different rate of sensitivity of the modal parameters to the segmentary stiffness parameters makes the basin of attraction around the true local minimum a narrow valley with steep slopes for some of the segmentary stiffness parameters and shallow slopes for the rest. Consequently, the algorithm will not be able to easily reach the bottom of this valley or the local minimum. To cure the numerical difficulties caused by this problem, all the segmentary stiffness parameters were scaled depending on the rate of sensitivity of the modal parameters to them. Obviously, this transforms the shallow slopes that are associated with some of the segmentary stiffness parameters to steep enough slopes to eliminate the numerical problem. To perform such a scaling, the following coordinate transformation is used in this study:

$$\theta_j \cdot E_j = \overline{E}_j \quad (4)$$

in which θ_j is RMS of the jth column of the following sensitivity matrix:

$$S = \begin{bmatrix} \theta_{11}^{(k1)} & \theta_{12}^{(k1)} & \dots & \theta_{1m}^{(k1)} \\ \theta_{21}^{(k2)} & \theta_{22}^{(k2)} & \dots & \theta_{2m}^{(k2)} \\ \cdot & \cdot & \dots & \cdot \\ \cdot & \cdot & \dots & \cdot \\ \cdot & \cdot & \dots & \cdot \\ \theta_{n1}^{(kn)} & \theta_{n2}^{(kn)} & \dots & \theta_{nm}^{(kn)} \end{bmatrix} \begin{matrix} \downarrow \\ i = 1, \dots, n \end{matrix} \qquad (4a)$$

$$j = 1, \dots, m \rightarrow$$

$$\theta_j = \left(\frac{1}{n} \times \sum_{i=1}^{n} \theta_{ij}^{(ki)^2} \right)^{\frac{1}{2}} \qquad (4b)$$

Where

n and m = total number of modal parameters considered and total number of structural segments, respectively;

ki = segment number whose stiffness changes most affect the ith modal parameter's value; and

$\theta_{ij}^{(ki)}$ = dimensionless constant that can be expressed, depending on Equation 2, as follows:

$$\theta_{ij}^{(ki)} = \frac{\left(\frac{\partial CMP_i}{\partial E_j} \right)}{\left(\frac{\partial CMP_i}{\partial E_{ki}} \right)} \qquad (4c)$$

where $0 < \theta_{ij}^{(ki)} \leq 1$, $i = 1, \dots, n$; and $j = 1, \dots, ki, \dots, m$.

Experimental Verification of Method

To check the validity and efficiency of the proposed method, laboratory tests were performed for the simply supported steel beam model, part of which was braced by a steel plate in Segment 2. In the laboratory test, the test data acquisition system is Keithley 500 with 16 A/D channels, having a total sampling rate of 50,000 sps and coupled to a Toshiba T3200 laptop computer having a 16-MHz 80386 processor, 9 MByte RAM, and 40-MByte hard disk capacities. Accelerations were recorded at seven equally spaced locations on the beam by single-axial accelerometers made by Terra Technology Corporation. The beam model was excited by a pull-down and quick-release procedure. A schematic of the equipment setup is shown in Figure 3. After the collected acceleration data were preprocessed, the first flexural mode parameters were identified, (Table 1), along with the others computed using COSMOS/M Finite Element Software (*13*) by employing the computer model of the tested beam described in Figure 4.

The flexural stiffness change in Segment 2 can be reflected in the modulus of elasticity as follows:

$$E_2 = (I_2/I_1) * E$$

where $I_2 = 14.31$ cm^4 and $I_1 = 8.63$ cm^4 are the moments of inertia of the braced and regular cross sections, respectively. Thus,

$$E_2 = 1.6582\, E = 34\,820 \text{ kN/cm}^2$$
$$E_1 = E_3 = E_4 = E_5 = 21\,000 \text{ kN/cm}^2$$

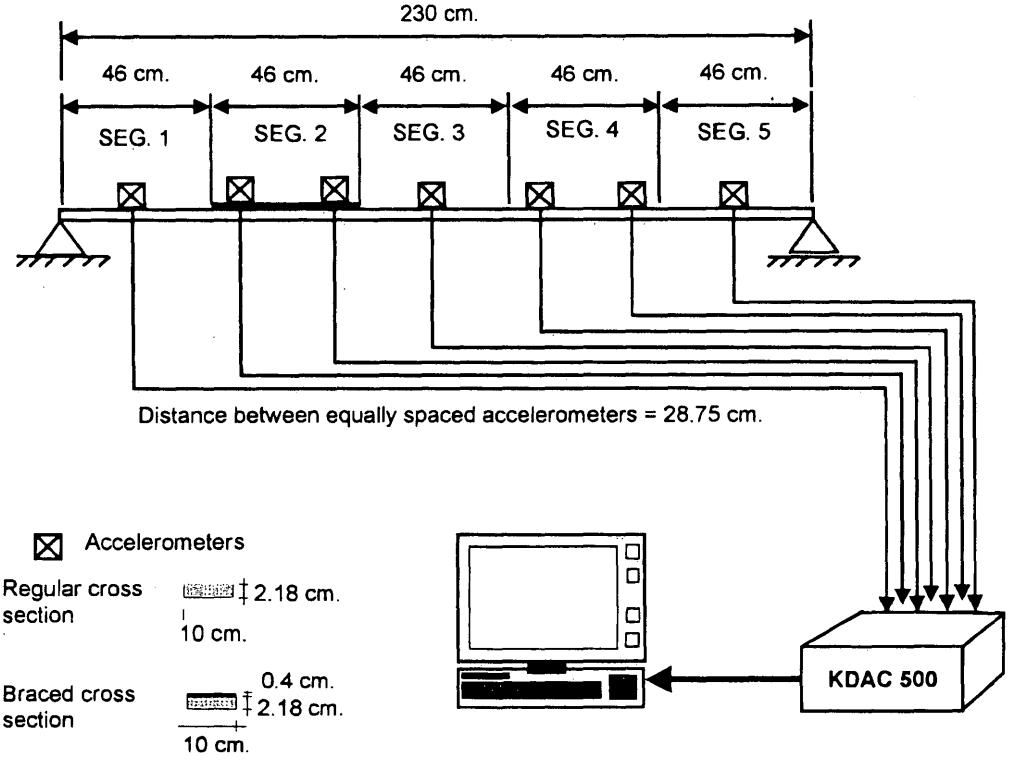

FIGURE 3 Laboratory test setup.

TABLE 1 First Flexural Mode

		Computer Analysis	Experimentally Identified
Frequency (Hz)		7.7925	7.9102
Mode Shape ratios	1	0.5173	0.4984
	2	0.8707	0.8838
	3	1.1321	1.1131
	4	1.2674	1.2753
	5	1.2195	1.2118
	6	1.0000	1.0000
	7	0.6380	0.6190

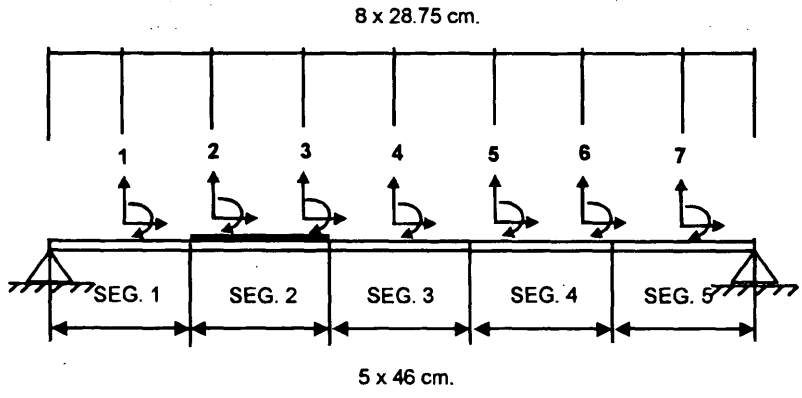

FIGURE 4 Computer model of the tested beam.

Then, by employing the proposed method for the modal parameters calculated for the numerical model and given in the first column of Table 1, the segmentary stiffness parameters of the numerical model were estimated and given in Table 2. In this table the actual segmentary stiffness parameters are given in the first column, and the results obtained without using any weighting or coordinate transformation are presented in the second column. In the fourth column, the results were produced by using the sensitivity-based coordinate transformation defined in Equation 4. In the third and fifth columns, percent differences of the obtained values are given.

Similarly, the segmentary stiffness parameters of the tested laboratory model were estimated by employing the proposed method for the modal parameters defined in the second column of Table 1. The results are presented in Table 3 using the same pattern as that used for Table 2. However, to produce the results presented in the fourth column in addition to the sensitivity-based coordinate transformation given in Equation 4, the weighting that reflects the relative confidence was used. The following upper and lower bounds (Equation 1) were set for the segmentary stiffness parameters:

$$0 < E_i \leq 1.5xE \qquad i = 1, \ldots, 5$$

The following initial values were estimated for unknown stiffness parameters:

$$E_{oi} = E \qquad i = 1, \ldots, 5$$

TABLE 2 Segmentary Stiffness Values × 10 kN/cm²: Numerical Model

Segment No.	Model (1)	Identified (2)	100x[(2)-(1)]/(1) (3)	Identified (4)	100x[(4)-(1)]/(1) (5)
1	2100	2398.9	14.23	2179.8	3.80
2	3482	2897.5	-16.79	3273.5	5.99
3	2100	2143.0	2.05	2110.2	0.49
4	2100	2004.1	4.57	2015.8	-4.00
5	2100	2102.3	0.11	2100.8	0.04

TABLE 3 Segmentary Stiffness Values × 10 kN/cm²: Laboratory Model

Segment No.	Model (1)	Identified (2)	100x[(2)-(1)]/(1) (3)	Identified (4)	100x[(4)-(1)]/(1) (5)
1	2100	2868.0	36.57	2199.8	4.75
2	3482	3578.2	2.76	3382.0	2.96
3	2100	2215.6	5.50	2273.6	8.27
4	2100	1995.0	-5.00	2033.2	3.18
5	2100	2464.2	17.34	2173.0	3.48

The results presented in Tables 2 and 3 showed the following:

1. That the proposed method works efficiently for the identification of the stiffness changes and successfully finds their locations and
2. That the sensitivity-based coordinate transformation presented in Equation and 4*a* and *b* effectively cures the accuracy and stability of the solutions.

LOCALIZED DAMAGE DETECTION METHOD

In the second phase, only the bridge members located in a segment for which global stiffness degradation is identified are instrumented properly for the strain measurements. However, for this case, in addition to the strain measurement axle loads and spacings, the location of the first axis of locomotive along the bridge and the train speed must be measured in the course of train passage.

After the static component of the recorded strain data is obtained, it is converted to stress to compare with the others coming from the computer analyses. To be able to compare properly both stress traces obtained from the measured strain data and the computer analysis, recorded data for the train movement must be reflected in the computer analysis to maintain a consistent rate of the movement of the train load on the bridge computer model. After the stress traces coming from the computer analysis and the recorded strain data are compared the damaged members are easily identified.

APPLICATION TO EXISTING RAILWAY BRIDGE

The field application of the procedure involved Çerkezköy Railway Bridge, a single span, single curved-track railroad bridge, 50 m long owned and operated by the Turkish State Railways Administration. The bridge structure consists of a single-deck steel-riveted truss. The bridge is part of the Istanbul-Edirne main railway line connecting Turkey with other European countries and was originally designed and constructed by Fried-Krupp A.G. in 1937 on the Sivas-Erzurum railway line in midwestern to eastern Anatolia and later relocated on the Istanbul-Edirne railway line.

All the stress and free vibration analyses needed for this application were performed by employing COSMOS/M Finite Element Software (*13*). SA-102 model uniaxial and SSA-302 model triaxial Terra Technology-made servo-accelerometers were used to measure accelerations of the bridge caused by passenger or freight train passages that occurred during the test. The acceleration transducer placement plan that was used in the course of the test is given in Figure 5.

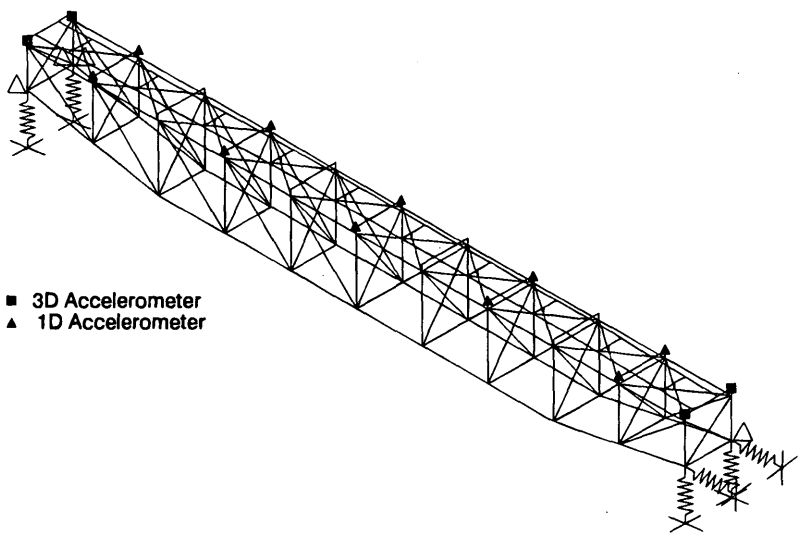

FIGURE 5 Acceleration transducer placement plan.

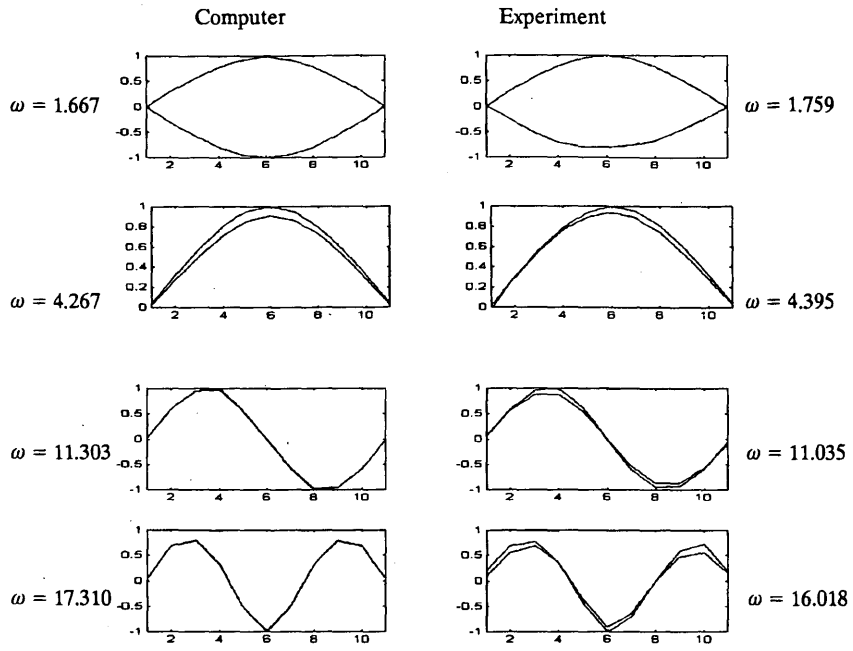

FIGURE 6 Comparison of the identified modes (all frequency values in hertz).

Because the bridge and train system constitute a coupled dynamic system having a time-dependent mass, the acceleration recordings following the time at which the train totally left the bridge were considered for this application.

Elevation views of the corresponding mode shapes are presented in Figure 6 along with the others obtained from computer analyses performed for the sophisticated bridge model.

Segmentary Stiffness Identification

Depending on the modal frequencies identified in the previous section and employing the method proposed for the global damage detection, segmentary stiffness parameters were identified and presented in Table 4 along with their percent variations with respect to the original values that were considered in the computer modeling.

TABLE 4 Identified Segmentary Stiffness Parameters

Number of Segment	$E_I \times 10^4$ [kN/cm^2]	$\frac{E_I - E_m}{E_m{}^a} \cdot 100$
1	1.9575	-6.79
2	2.0821	-0.85
3	1.6549	-21.20
4	2.1095	0.45
5	2.0152	-4.04
6	1.9775	-5.83
7	2.1161	0.77
8	1.7846	-15.02
9	2.1391	1.86
10	2.0130	-4.14

[a] $E_m = 2.1 \times 10^4$ kN/cm^2

It is clearly seen from Table 4 and Figure 7 that there is considerable stiffness degradation in Segments 3 and 8, which may be interpreted as a sign of existing damage. Similarly, for Segments 1, 5, 6, and 10 segments there are relatively small modulus of elasticity degradations.

Localized Damage Detection

After the noticeable global stiffness degradations for structural segments 1, 3, 5, 6, 8, and 10 were defined, selected bridge members located in these segments were instrumented for strain measurements. Strain readings were made through Hottinger Baldwin-made DS-5 model demountable strain transducers during passage of a DE24000 diesel locomotive during the test.

All the strain data recorded at various locations in the selected bridge members indicated in Figure 8 were filtered and converted to strain values for those members that seemed more informative. Obtained strain values are plotted in Figures 8 and 9 against time, corresponding to longitudinal locomotive positions, along with the others obtained from the computer analyses performed as mentioned in the preceding sections for the moving load model defined for the same locomotive passage.

It is clearly seen from the comparison of stress traces obtained from the data collected from the strain transducer locations on Members 30 and 32 (Figure 8) and 71 and 73 (Figure 9) that diagonal members having numbers 32 and 73, which are located in structural segments 3 and 8, respectively, work only for tension forces. They do not take compression force. As is seen from Figures 8 and 9, the stress trace peak for Members 30 and 71 in the region of compression has approximately the same value as the stress trace peak for Members 32 and 73 located in the region of tension, when the test locomotive is approaching from the Istanbul side. The same situation is valid for the test locomotive passage from the Edirne side to Istanbul. This abnormal working mechanism is caused by the existing loosening of the weak riveted joints connecting the upper chord members to Members 32 and 73.

From the observation of Figure 9 that demonstrates the stress traces obtained from the test data captured from the strain transducer locations on Members 39 and 80, which are located in Structural Segments 5 and 10, respectively, and obtained from the computed stress values, it is clearly seen that there is an obvious discrepancy between the stress traces obtained from the test and computer analyses. This abnormal behavior is caused by an improper working mechanism, which is exhibited by these members and is also the sign of existing joint loosening. Findings for Structural Segments 1 and 6 were similar to those obtained for Segments 5 and 10.

CONCLUSIONS

The following conclusions can be drawn from this study:

1. The global damage detection procedure developed in this study can be an effective tool for enhancing periodic bridge inspection and global damage identification.
2. If it is followed by the local damage detection procedure discussed in this study, localization of the globally identified damage is possible without using a large number of strain transducers.
3. The key to the efficiency of the method can be expressed as follows:
   a. The needed data can be recorded without closing the bridge to daily traffic and
   b. Current train traffic can be used as the excitation and loading mechanism; that is, no special loading vehicle is needed.

ACKNOWLEDGMENT

This paper is based on the research activities supported by NATO's Science for Stability Program under the contract name TU-BRIDGES. The authors wish to acknowledge numerous contributions from the Turkish Railways Administration.

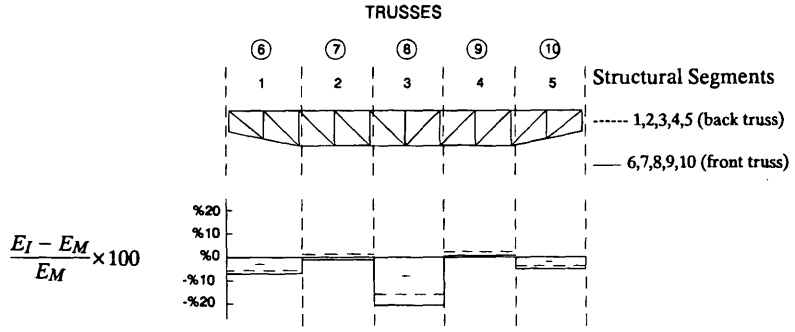

FIGURE 7 Characteristic regions and identified changes in modulus of elasticity.

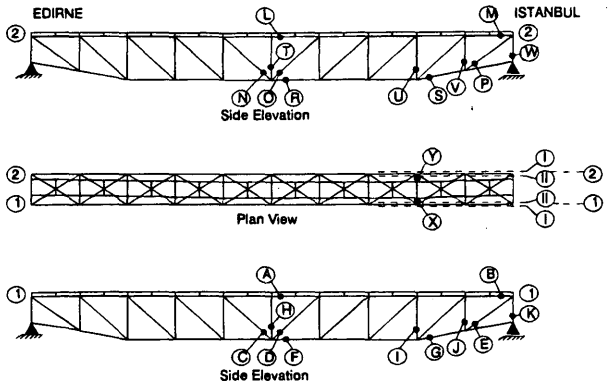

C

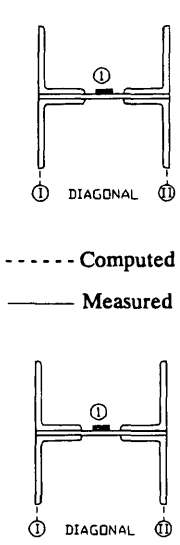

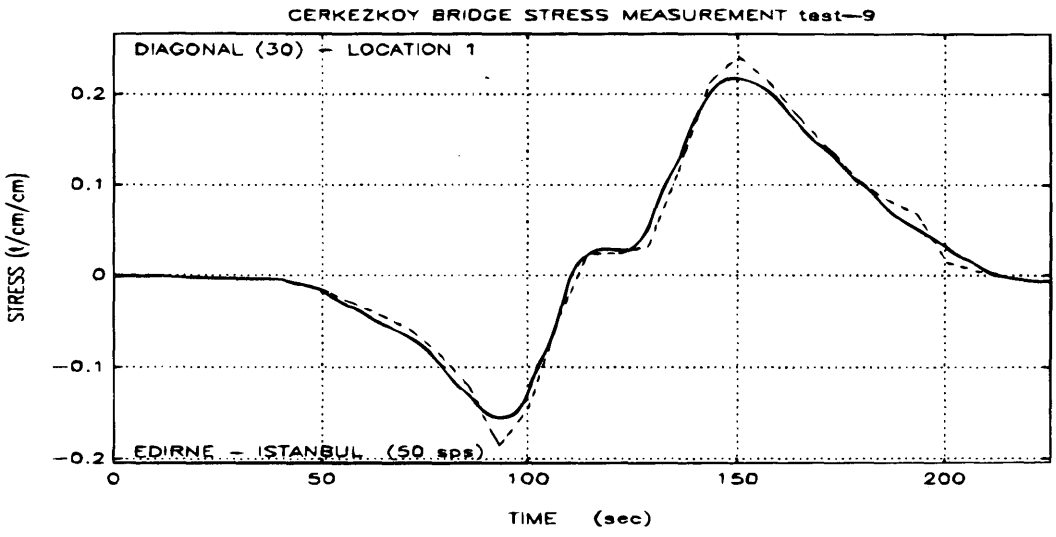

D

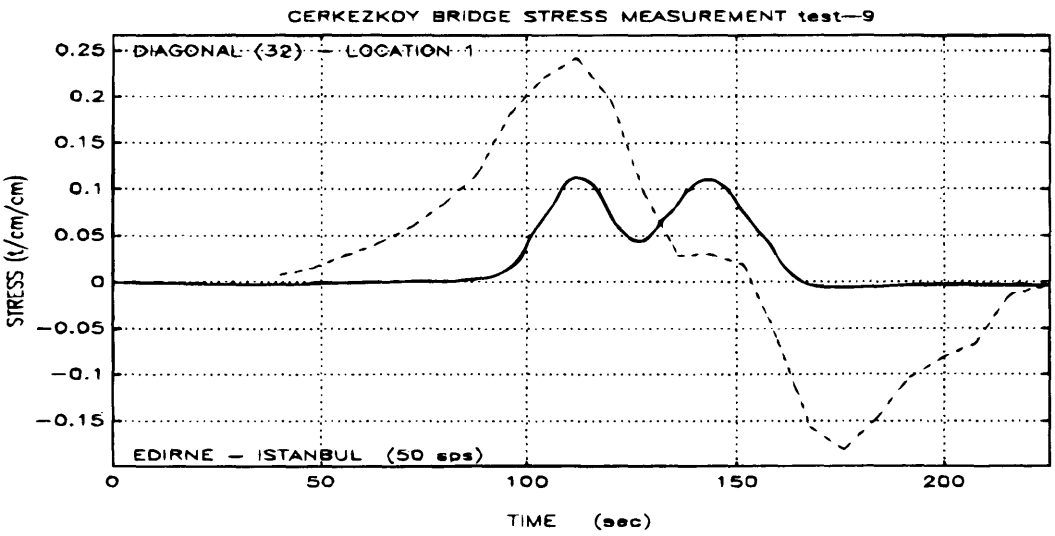

FIGURE 8 Computed and measured stress traces × 10 kN/cm².

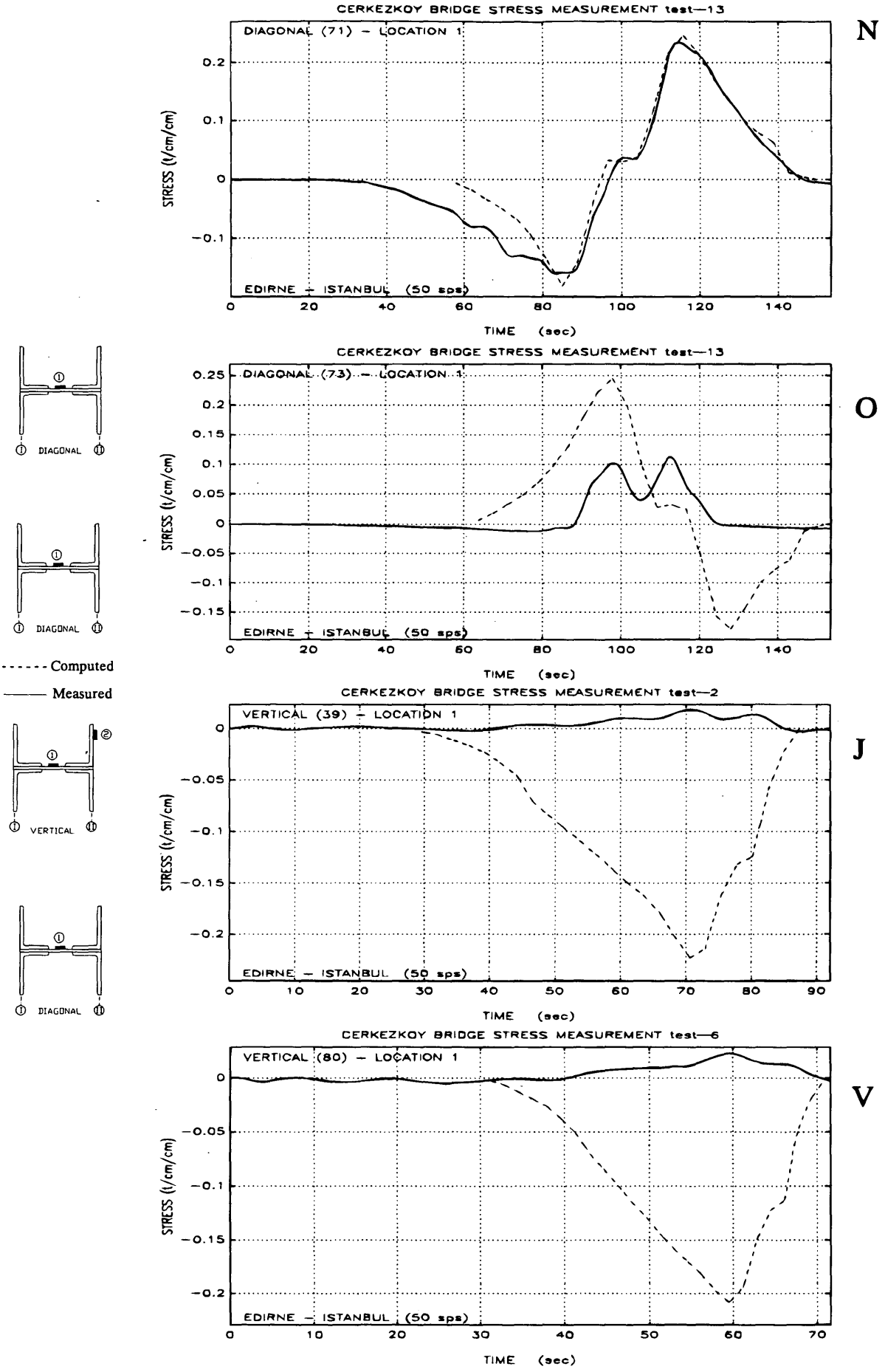

FIGURE 9 Computed and measured stress traces × 10 kN/cm².

REFERENCES

1. Bakht, B., and P. F. Csagoly. Testing of Perley Bridge. In *Ontario Ministry of Transportation and Communications*. RR207. Ontario, Canada, 1977.
2. Bakht, B., and P. F. Csagoly. Bridge Testing. In *Ontario Ministry of Transportation and Communications*. SRR-79-10. Ontario, Canada, 1979.
3. Billing, J. R. Dynamic Test of Bridges in Ontario, 1980: Data Capture, Test Procedures and Data Processing. In *Ontario Ministry of Transportation and Communications*. SRR-82-02. Ontario, Canada, 1982.
4. Mazurek, F., and J. T. DeWolf. Experimental Study of Bridge Monitoring Technique. *Journal of Structural Engineering* ASCE, Vol. 116, No. 9, Sept. 1990.
5. Felber, A. J. *Development of a Hybrid Bridge Evaluation System*. Ph.D. Dissertation. Department of Civil Engineering, University of British Columbia, Dec. 1993.
6. Safak, E. *Analysis of Recordings in Structural Engineering, Adaptive Filtering, Prediction and Control*. USGS Open-File Report 88-647. U.S. Geological Survey, 1988.
7. Bendat J. S., and A. G. Piersol. *Random Data: Analysis and Measurement Procedures*. Wiley Interscience, 1971.
8. Douglas, B. M., and W. H. Reid. Dynamic Tests and System Identification of the Bridges. *Journal of Structural Division*, ASCE, Vol. 108, 1982.
9. Fletcher, R. *Practical Methods of Optimization*, 2 vols. John Wiley & Sons, 1980.
10. Gill, P. E., W. Murry, and M. H. Wright. *Practical Optimization*. Academic Press, London, 1981.
11. Hock, H., and K. Schittowski. A Comparative Performance Evaluation of 27 Nonlinear Programming Codes. *Computing*, Vol. 30, 1983,
12. Bannan, M. R., and K. D. Hjelmstad. Parameter Estimation of Structures from Static Response, I. Computational Aspects. *Journal of Structural Engineering, ASCE*, Vol. 120, No.11, Nov. 1994.
13. COSMOS/M (386) Version 1.65 Finite Element System Software. *Structural Research and Analysis Corporation, Santa Monica, Calif. 1991.*

Publication of this paper sponsored by Committee on Dynamics and Field Testing of Bridges.

Dynamic Modeling of Bridges: Observations from Field Testing

JUAN R. CASAS

Different bridge types and design configurations used in bridge engineering result in largely different dynamic mechanisms of response. Therefore, one of the most important problems to resolve about their theoretical dynamic modeling is to choose the most adequate and simple model for a particular bridge. The work carried out during the dynamic testing of several bridges is reviewed. The objective was to check the feasibility and accuracy of various numerical and analytical models assumed for the dynamic behavior of various bridge types (box-girder, slab bridges, and cable-stayed). Experimental field test data were used to derive the dynamic properties of the bridges. The most appropriate analytical models and dynamic properties of the elements used in the discretization mesh were derived for each bridge type on the basis of the correlation between the theoretical and experimental results. Taking these results into account, a set of practical recommendations for the dynamic modeling of different bridge types is proposed.

In recent years there has been increased interest in studying the dynamic performance of bridges, even for those not subjected to important or high dynamic loads such as wind or earthquakes. At the same time, more reliable electronic equipment and measuring devices for recording dynamic field data have been more widely available. Therefore, the number of dynamic tests performed in bridges is constantly increasing. In Europe, dynamic tests are often performed in addition to the mandatory static tests to verify the acceptability of a bridge before opening it to traffic. Moreover, a dynamic loading test can also be used during the service life of the bridge to monitor its performance. The design of the field test and the analysis of the dynamic test results require a reliable dynamic theoretical model. The reliability and robustness of such a model in describing the dynamic behavior of the bridge are important for the following reasons:

1. During the preparation phase of the dynamic test, the results of the analytical model will help choose the best instrumentation for and the location of the bridge;
2. During the dynamic test, the model will be a tool to check the reliability and adequacy of the recorded data; and
3. During the analysis of the experimental data, a comparison between experimental and theoretical results can provide a warning about inadequate performance of the bridge.

Therefore, careful attention should be paid to the development of theoretical models for the dynamic analysis of bridges. Two factors must be kept in mind:

1. Dealing with a particular structure with an important flexural work and a specific geometry (such as a plane structure with loads orthogonal to this plane) it will be possible to achieve good results with specific and simplified models.
2. On the other hand, the highly different bridge typologies, both longitudinal and transversal, with different dynamic mechanisms of response will not allow the development of general models or modeling criteria valid for all bridge types.

Moreover, the bridge designer always has to perform a static analysis, therefore a static model is always available. For this reason it is of interest to derive dynamic models that require little additional effort than that required for the static analysis. Bearing all these factors in mind, this paper compares the results of theoretical dynamic analyses and dynamic testing of various bridge types. The comparison of the results leads to a set of conclusions and practical recommendations for the dynamic modeling of bridges using simple finite element models (as the grillage formed by beam elements) or theoretical expressions (Rayleigh's method).

FEASIBILITY AND ACCURACY OF SIMPLE DYNAMIC MODELS FOR BRIDGE ANALYSIS

The accuracy of the dynamic modeling of different bridges is checked via a comparison between the results of analytical models and field tests. The comparison is performed as a function of bridge type comparing only the vibration frequencies. This is because in most of the cases presented the complete mode shapes were not obtained by testing and only the relative amplitudes of displacements or accelerations in the points instrumented were used to identify the experimental frequency with the corresponding vibration mode. In all cases, the finite element method (FEM) dynamic model is based on beam elements forming a frame or grillage with flexural and torsional dynamic behavior represented in respective mass and stiffness matrixes (*1*). The calculation of theoretical natural frequencies and mode shapes from the mass and stiffness matrixes of the global structure is based on the subspace iteration method (*2*).

Box-Girder Prestressed Concrete Bridges

To avoid distortion of the cross section, box-girder prestressed concrete bridges are not constructed with transverse bracings or diaphragms besides those located at the supports. This results in more freedom in selecting the location of the nodes of the mesh.

Alfonso X Bridge

This was a seven-span continuous prestressed box-girder bridge. The deck was supported on each pier and abutment by two pot bear-

Department of Civil Engineering, Technical University of Catalunya, c/ Gran Capità SIN, Mòdul C-1, Barcelona 08034, Spain.

ings [i.e., an elastomeric pad confined in a metallic cylindrical body (*3*)]. The bridge was demolished in May 1985 for urban development. Before demolition, several static and dynamic tests were performed, including a test to failure (*4*). The dynamic test consisted in the placement of eight displacement transducers and two accelerometers in different spans of the bridge (midpoint and quarter-point). The bridge was dynamically excited by passages of a single, two-axle truck with a gross weight of 136 kN at various speeds from 2.8 to 14 m/sec, and quick releasing of a concrete cube (gross weight of 120 kN) previously loaded in the middle of the sixth span, obtaining a free-damped vibration of the bridge. The direction of the motion was vertical.

The analysis was carried out using a one-dimensional dynamic beam model (continuous beam) with 44 nodes and 10 elements per span. This finite element dynamic discretization using one-dimensional elements was chosen to be equal to the static model. The natural frequencies obtained by using the above model are compared with experimental ones in Table 1. In addition, the frequency of the first mode obtained using Rayleigh's method (*1*) was calculated, the magnitude of the self-weight being used as the applied load in the appropriate direction to obtain a deflection profile similar to the first vibration mode, and the previous discretization of the static model was also used. This assumption required almost no additional work because the static model was already defined. The result was $f_1 = 1.77$ Hz. This result is good (4 percent error), considering the simplicity of the applied method. As indicated in Table 1, the agreement with the FEM models is good for the lowest frequencies. The maximum error is 11 percent in Vibration Mode 5.

Diagonal Viaduct

The diagonal viaduct is a three-span (39-, 49.10-, and 39-m) continuous prestressed box-girder bridge. The cross section is 1.964 m deep, and the deck width is 10.95 m. The bridge is simply supported in bending and fixed in torsion on each support (Figure 1). In this case the instrumentation consisted of four displacement transducers and four accelerometers located in the bridge, as indicated in Figure 1. The vibration of the bridge was forced by

1. Passages of 1 two-axle truck (gross weight, 140 kN) at speeds from 2.7 to 22.2 m/sec over the undisturbed pavement;
2. Passages of the same truck over an artificial obstacle (the standardized RILEM plank) placed in the central section of the center span; and
3. Passages of 2 two-axle trucks with various relative positions and velocities to simulate controlled real traffic conditions.

TABLE 1. Natural Frequencies in Hertz in the Alfonso X Bridge

Mode	Theoretical	Experimental
f_1(Bending)	1.71	1.70
f_2(Bending)	3.05	2.97
f_3(Bending)	3.99	3.80
f_4(Bending)	4.99	4.50
f_5(Bending)	5.83	5.20

In all cases the direction of the recorded motion was in the vertical plane. For the dynamic analysis, a grillage model was used. The bridge was modeled as one longitudinal beam (spine model) that accounted for the overall mass, central moment of inertia, and flexural and torsion modulus of the overall cross section. The modification of the original statical model consisted of adding only the inertial characteristics (mass and rotational mass). Ten elements per span were used for the longitudinal beam. In addition, transverse elements are used to link the bearings and the longitudinal spine. The mechanical properties of the transverse beams were based on the properties of the diaphragms over the piers and the abutments. The theoretical results and those derived from the dynamic test performed are shown in Table 2. The first natural frequencies in bending and torsion are predicted almost exactly. Even for higher modes the error is less than 6 percent.

Box-Girder Composite Bridges

The bridges are located on Barcelona's littoral ring road over Highway A-19. These are 4 two-span bridges. The four bridges have the same longitudinal configuration with span lengths of 20.55 and 44.55 m. A typical cross section is shown in Figure 2. The steel box girder has a different thickness that ranged from 10 to 15 mm in the bottom flange and from 10 to 25 mm in the webs. To reduce the box distortion, a diaphragm is placed every 4.05 m. In addition, transverse stiffeners are placed at 1.35 m spacings. A total length of 16.20 m of the bottom flange centered on the pier is filled with concrete to better resist the negative bending. Two elastomeric bearing pads are used on the pier and abutments. For the dynamic test of this bridge displacement and acceleration transducers were also used. Two displacement transducers were placed close to the abutment section to check the possibility of uplifting associated with the important difference between span lengths. The instrumentation was disposed to measure the motion in the vertical direction. The excitation was achieved via the existing real traffic on the bridge.

Analogously to the diagonal viaduct, the dynamic model consisted of a simple FEM forming a grillage (therefore the finite elements are two-node beam elements) with a unique longitudinal element representing the overall cross section. A total of 38 beam elements and 39 nodes are used. The use of a one-dimensional model is possible thank to the presence of the bracings, which help avoid distortion of box shape. A node of the grillage was placed at the location of every transverse diaphragm to account for concentrated mass increments. The transverse elements over the piers and abutments linking the support nodes with the longitudinal spine were assumed as a rigid link in bending. This would accurately simulate the clamping action for torsion at the supports. Because of the unbalanced span lengths, the bridge is anchored in one abutment by means of high-strength bolts. Therefore, vertical springs were placed in the model at the nodes in this abutment. The properties of the springs are deduced from the total cross-sectional area of the bolts and corresponding modulus of elasticity.

Theoretical and experimental results are presented in Table 3. The experimental frequencies in torsion of the long span were not deduced because no instrumentation was placed to this end in the dynamic field test. Despite its simplicity, the models give results accurate enough for the lower modes in both bending and torsion.

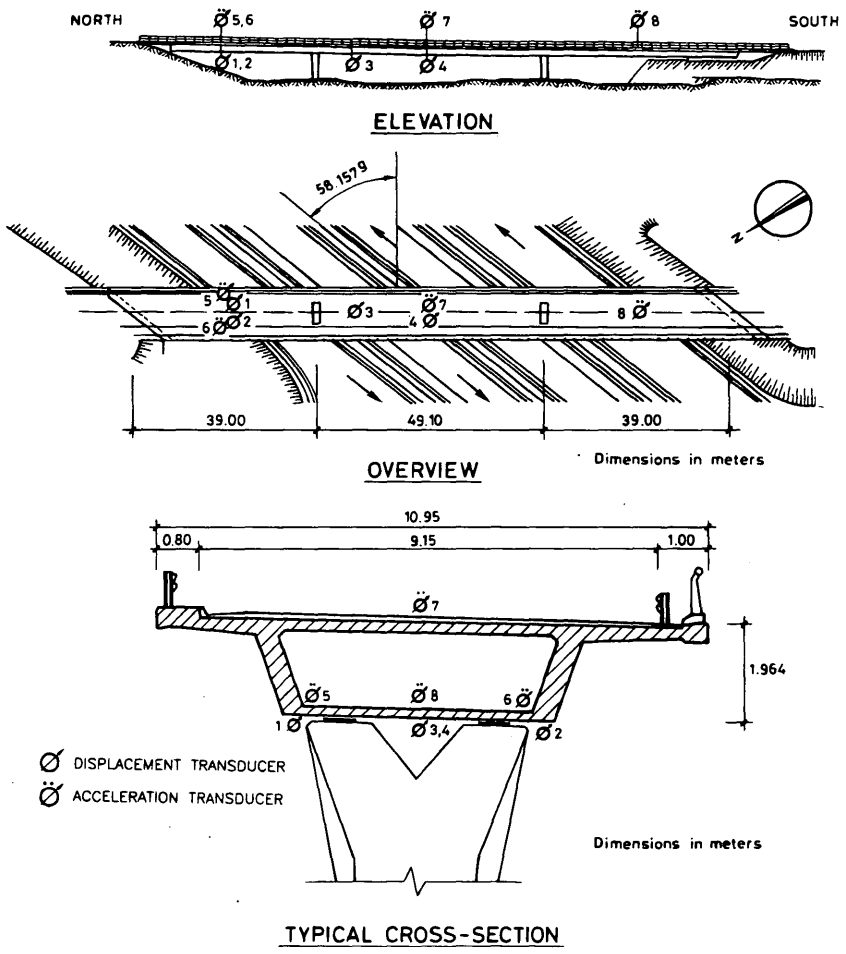

FIGURE 1. Description of diagonal viaduct.

Concrete Slab Bridges

Three prestressed concrete slab bridges with the following different geometric properties are presented:

1. Ratio of width to span,
2. Skewness, and
3. Horizontal curvature.

The comparisons between the results of these three bridges would provide a review of the model requirements to accurately evaluate the natural frequencies in torsion when the structural response is clearly two-dimensional (2-D) (slab) rather than one-dimensional (1-D) (beam).

Bridge OF-56.1 on Highway A-7

Bridge OF-56.1 is a prestressed concrete slab with four spans (11.5, 17.05, 17.05, and 11.05 m.). The deck is 6.5 m wide with circular voids of 45 cm in diameter (Figure 3). The bridge is straight, and two elastomeric bearings are placed at the piers and abutments.

The dynamic tests consisted in the placement of two accelerometers in the center of one of the longest spans and close to the sidewalks. The third accelerometer was placed in the center of the section located in the quarter-span of the contiguous shorter span. The vibration of the bridge was obtained using a two-axle truck with a total weight of 100 kN crossing the bridge at different speeds along one of the lanes, resulting in an eccentric (torsionally) excitation. Only the motion in the vertical direction was recorded and analyzed.

Because of the small width of the deck compared with its span length, a one-dimensional model (beam behavior) was used that would lead to good results. These were then compared with the results of a 2-D grillage model. The comparison is used to make recommendations for modeling wider, skewed, or curved slabs using 2-D grillage models (more than one longitudinal element in the cross section). Two dimensional grillage models are widely used by bridge designers in the static analysis of slab bridges. The calculation of properties (torsion modulus, bending stiffness) of the longitudinal and transverse elements of the grillage is very well documented for the analysis of static behavior of slab bridges (*5–8*). However, the main difficulty when a dynamic analysis is required that uses a grillage model is in deducing the inertial prop-

TABLE 2. Natural frequencies in Hertz in the Diagonal Viaduct

Mode	Theoretical	Experimental
f_1(Bending)	2.25	2.25
f_2(Bending)	3.53	3.48
f_3(Bending)	4.46	4.21
f_4(Torsion)	8.41	8.38

erties (mass and rotational mass) of longitudinal and transverse elements. To answer this question, the following dynamic models are defined:

1. A grillage model of the complete bridge with only one longitudinal member (1-D) and transverse members only in the sections over piers and abutments to adequately model the conditions at the supports.
2. A 2-D grillage of the main span only, with 5 longitudinal and 18 transversal fibers or ribs, resulting in 90 nodes and 157 elements. The following possibilities were also investigated: (2A) perfect clamping in bending at the supports and (2B) perfect hinge in bending at the supports. For each of the 2A and 2B assumptions, three cases were analyzed:
   a. Rotational mass (I_p) of longitudinal elements evaluated relative to the centroid of the global cross section,
   b. I_p of interior longitudinal elements evaluated with respect to own centroid and I_p of exterior elements relative to the edge grillage beam, and
   c. The same as Item 2 for interior elements and exterior elements with respect to the centroid of global cross section (Figure 4).

The mass and rotational mass of transverse elements in the grillage were always assumed to be 0.

3. Rayleigh's method is used to evaluate the torsional frequency using a 2-D static grillage. The load pattern consists of a set of concentrated loads in each of the edge nodes with the same magnitude and opposite direction, depending on the edge, to achieve a deformation similar to the torsional mode shape.

For the sake of comparison, the torsional frequency (f_T) was evaluated by means of the theoretical equation deduced for a beam model with both ends fixed in torsion and with uniform inertial and structural properties along the longitudinal axis (9) (Model 4):

$$f_T = \frac{1}{2L}\sqrt{\frac{GJ}{I_p}} \tag{1}$$

where G = transversal elasticity modulus,
J = torsional stiffness, and
L = span length under consideration.

The results are shown in Table 4. In this test, only the four lowest natural frequencies could be obtained (three in bending and one in torsion). The following observations can be made:

1. Model 1 gives very good results for bending modes,
2. In the case of this narrow slab, Model 1 gives also good results for torsion modes, but not as good as those of the bending modes,
3. For Model 2, the frequencies in bending are between those of Case 2A (ends fixed) and 2B (ends hinged).
4. The best results for the frequency in torsion are obtained when rotational inertia of the longitudinal members is calculated using Criterion c.
5. Rayleigh's method, which gives good results in bending, gives very bad results in torsion for a 2-D grillage model.
6. Despite the variations in mass and stiffness along the length of the bridge (because of absence of voids over piers and abutments) the theoretical expression (1) (Model 4) gives results similar to those of Model 1.

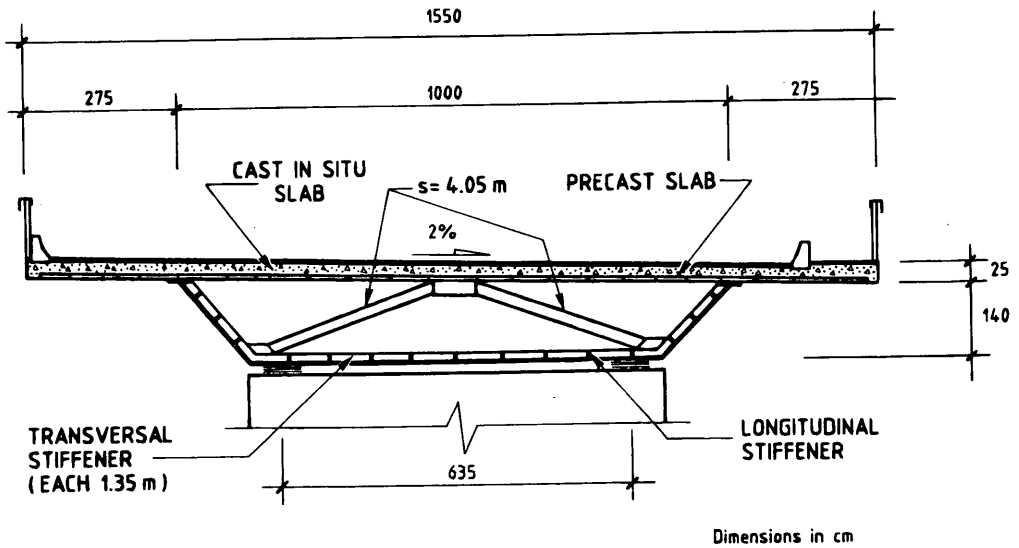

FIGURE 2. Cross section of bridges over Highway A-19.

TABLE 3. Natural Frequencies in Hertz in the littoral Ring-Road Bridges

Mode	Theoretical	Experimental
f_1(Bending)	1.73	1.70
f_2(Tor.long span)	2.24	-
f_3(Bending)	3.60	3.20
f_4(Tor.long span)	4.48	-
f_5(Tor.short span)	4.51	4.48
f_6(Bending)	6.75	6.90
f_7(Tor.long span)	6.85	-
f_8(Tor.long span)	9.05	-
f_9(Tor.short span)	9.10	10.30

(-) Not recorded

Bridge OF. 49-1 on Highway A-7

Bridge OF. 49-1 is a prestressed concrete slab with four spans (12.053, 17.649, 17.649, and 12.627 m). The deck width is 10.5 m with circular voids of 50 cm in diameter (Figure 5). The bridge is curved with a radius of 200 m. It is highly skewed at piers and abutments ($\alpha = 67.33^g$). As in the case of Bridge OF 56-1, three accelerometers were used, two of them placed at the halfway point of one of the longest spans and the other halfway across the shortest span to measure the motion in the vertical direction. The excitation of the bridge was achieved in the same way as that of Bridge OF 56-1. In this case, two models were used:

1. Grillage with only one longitudinal fiber where the mass and stiffness properties of the cross section are concentrated, resulting in 59 nodes and 58 elements. (The longitudinal fiber is divided into 12 beam elements per span to take into account the zone without circular voids over supports.)

2. Grillage model of the longest span with 9 longitudinal beams and 23 transverse beams, resulting in 207 nodes and 382 elements. Assigning structural and mass properties to the various elements was done while bearing in mind the conclusions derived from the slab bridge. Also the possibilities of perfect clamping and perfect hinging at both ends were investigated.

Table 5 shows the theoretical and experimental results obtained. As can be seen, even in this case of a wide, curved, and skewed slab bridge, the one-dimensional model gives good results for both bending and torsion frequencies. The frequency in torsion of Model 2 is also reasonably good.

Bridge OF.50-2 on Highway A-7

Bridge OF.50-2 is a prestressed concrete slab with four spans (17.014, 21.328, 26.555, and 21.328 m) and a deck width of 10 m. The cross section has four circular voids 0.85 cm in diameter. Two elastomeric bearing pads are placed in the abutments and only a single bearing is used at the circular piers. In this way, the slab is not restrained against torsion over the piers. This bridge presented an important sulfate-attack reaction in the concrete, and therefore extensive static and dynamic tests to check its structural performance were carried out. A total of 7 displacement transducers and 4 one-axial accelerometers and one triaxial accelerometer were used. In this case the directions of motion of interest were vertical and longitudinal and transverse in the horizontal plane. A total of 42 truck passages were performed with the following different configurations:

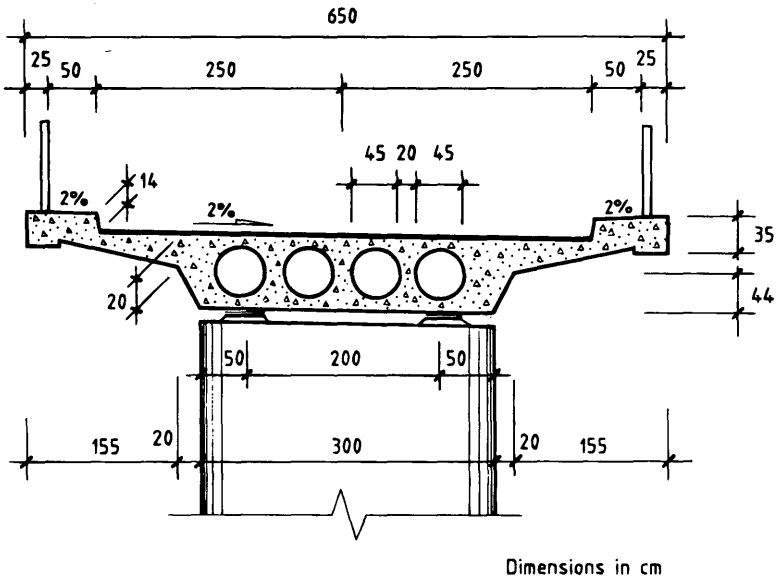

FIGURE 3. Cross section of Bridge OF-56.1.

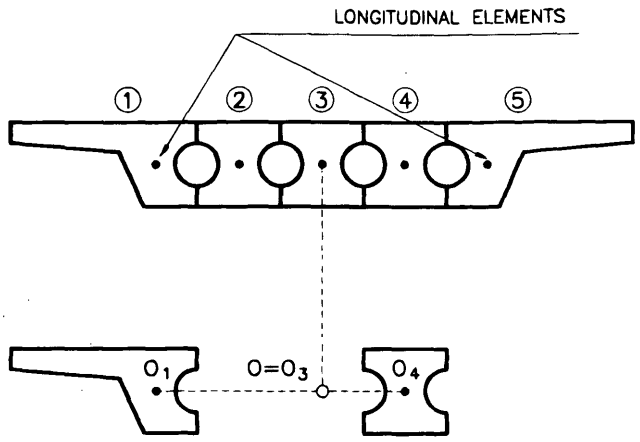

O = Centroid of overall cross section

O_i = Position of longitudinal beam element

$$I_p = I_0^1 + \sum_{i=2}^{n-1} I_{0_i}^i + I_0^n$$

FIGURE 4. Calculation of rotational mass of longitudinal members in a 2-D grillage.

1. In Phase 1, a single truck with a gross weight of 260 kN crossed the bridge at different velocities and centered with respect to the longitudinal axis of the deck.
2. Phase 2 was similar to Phase 1, but in this case the truck ran eccentrically, resulting in vibrations mainly controlled by the torsion characteristics of the deck.
3. Phase 3 consisted in the simulation of real traffic by crossing two trucks at the same time with different distances and relative velocities between them.
4. The last part of the test was a braking test in which a truck was suddenly stopped over the deck after reaching its maximum speed. In this case the triaxial accelerometer recorded the accelerations excited in the horizontal plane.

As in Model 1 of the previously discussed slab bridges, the model used for the dynamic analysis is the grillage with one longitudinal member (spine model) and transverse elements at the abutments, resulting in 45 nodes and 44 elements (Figure 6). Table 6 shows the correlation between the theoretical and experimental natural frequencies. The agreement in bending modes is good, even for the higher modes. The first torsional frequency presents an error of 1.5 percent, and the second presents an error of 9.6 percent.

TABLE 4. Theoretical Frequencies in Hertz Derived from Different Dynamic Models and Comparison with Experimental Model in Bridge OF-56.1

	Theor.									
		(2A)			(2B)					
Mode	(1)	a	b	c	a	b	c	(3)	(4)	Exp.
f_1(Bending)	6.04	11.29	11.29	11.29	4.98	4.98	4.98			6.09
f_2(Bending)	8.66	31.04	31.04	31.04	19.9	19.9	19.9			8.22
f_3(Bending)	13.5									13.4
f_4(Tor. long)	13.9	14.03	22.25	14.18	11.8	20.1	11.9	27.7	13.84	12.6
f_5(Bending)	14.4									-
f_6(Tor. short)	20.5								20.55	-
f_7(Tor.long)	28.2	29.30	48.10	29.55	25.1	44.3	25.3			-
f_8(Trans.Bend.)		39.31			39.2					-

(-) Not recorded

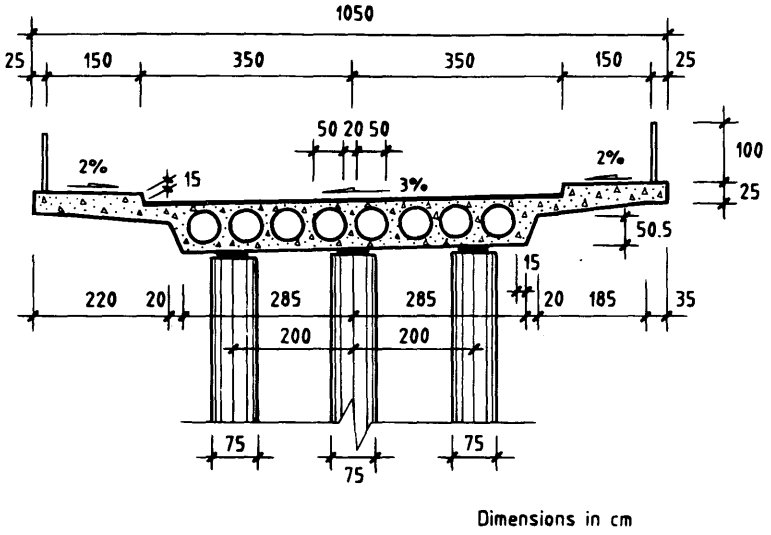

FIGURE 5. Cross section of Bridge OF-49.1.

Cable-Stayed Bridges

The Alamillo Bridge, located in Seville (Spain) over the Guadalquivir River, is a 200-m-span cable-stayed bridge with an inclined tower 130 m high and 13 pairs of cable stays. The deck width (3 × 2 lane of traffic + pedestrian lane) is 32 m, and the main dimensions of the cross section are shown in Figure 7. To compare the dynamic parameters of the constructed bridge with those of the model tested in a wind tunnel, a set of dynamic tests was decided with the following characteristics:

1. Location of a triaxial accelerometer at the top of the pylon to record motions in the three possible directions, and three uniaxial accelerometers to measure vertical accelerations on the deck. One displacement transducer was also installed close to the center span.
2. Excitation was achieved by means of passages of 2 two-axle trucks of 200 kN through the bridge deck at different speeds. Passages were made with and without a standardized obstacle in the pavement. Also the trucks ran symmetrically (one in each traffic direction) in some passages and eccentrically (the two trucks side by side in the same traffic direction) in the rest.

TABLE 5. Theoretical Frequencies in Hertz Derived from Different Dynamic Models and Comparison with Experimental Model in Bridge OF-49.1

	Theor.			
Mode	(1)	(2A)	(2B)	Exp.
f_1(Bending)	5.91	10.31	4.97	5.86
f_2(Bending)	6.39			6.10
f_3(Torsion)	7.47	9.57	8.21	7.60
f_4(Bending)	8.66			8.39
f_5(Torsion)	9.60			9.25
f_6(Trans. B.)		14.13	14.04	-
f_7(Bending)	17.0		16.68	-
f_8(Trans. B.)	17.3	17.50		-

(-) Not recorded

The dynamic model of the bridge was constructed with the following assumptions:

1. One-dimensional beam elements are used for the tower and deck, accounting for geometrical nonlinearity.
2. The bridge geometry is discretized as a plane (2-D model) with only one plane of cables and 3-D motions permitted.
3. The nodes were placed at the points where concentrated mass or inertia mass are present and where cables join the tower or deck.
4. A large number of elements is used to correctly account for the geometric variability. The model has a total of 81 nodes and 63 elements in the deck, 17 in tower and 13 in cables (total of 93 elements).
5. The elastic modulus of the cables was evaluated using the Ernst theory (*9*).

The bridge discretization is presented in Figure 7. Table 7 presents the experimental and theoretical natural frequencies, assuming (nonlinear) or not (linear) the geometric nonlinearity. As shown, neglecting the geometric nonlinearity did not significantly change the results. The experimental frequencies in the transverse direction of the deck were not measured. The observed good agreement validates the simplified theoretical model used. Rayleigh's method was used to evaluate the frequency of the first flexural mode by assuming a concentrated load in the deck to achieve a deflected shape similar to that of the vibration mode. The result was $f_B = 0.33$ Hz, similar to the measured value. Using Equation 1 for evaluation of torsion in the deck, the result was $f_T = 1.03$ Hz, which is in good agreement with the experimental value in spite of impor-

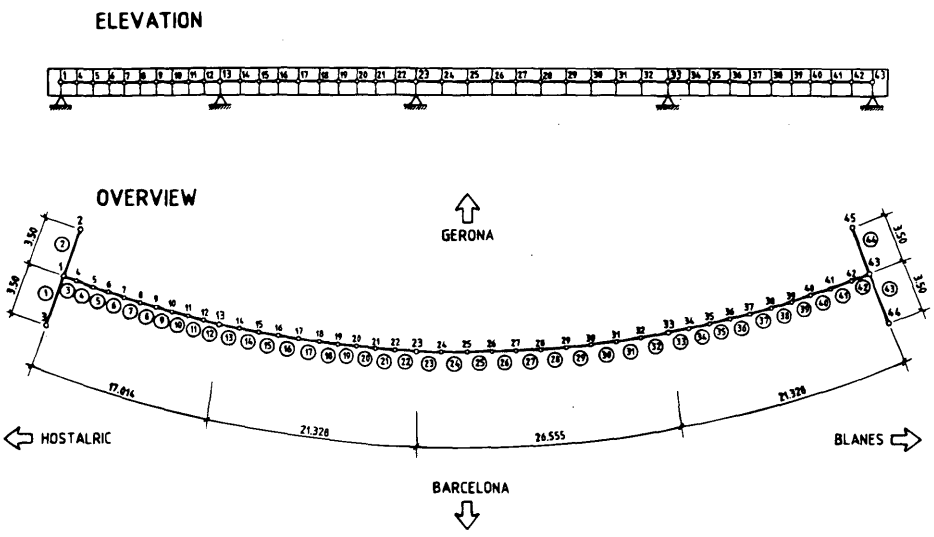

FIGURE 6. Discretization of Bridge OF-50.2.

TABLE 6. Natural Frequencies in Hertz in Bridge OF-50.2

Mode	Theoretical	Experimental
f_1(Torsion)	2.57	2.61
f_2(Bending)	3.98	3.98
f_3(Torsion)	5.00	4.52
f_4(Bending)	5.96	6.09
f_5(Bending)	7.11	7.00
f_6(Torsion)	7.49	–
f_7(Bending)	9.75	9.56

(–) Not recorded

tant variations in the geometry and the structural properties along the length of the deck. This is believed to be because of the lack of interaction between the torsion in the deck and the tower through the cables.

CONCLUSIONS AND RECOMMENDATIONS

The application of very simple dynamic models to the evaluation of the dynamic parameters of bridges is discussed. The observations made indicate that the grillage model, which is widely used for static analysis, can also be applied for the dynamic analysis with few additional calculations. The following recommendations are made concerning the dynamic models presented:

1. When the bridge has a clear 1-D behavior (beam) as in the case of box-girder bridges with one cell and slab bridges with width/span ratio less than 0.6, a model with only one longitudinal fiber reflecting the properties of the overall cross section produces accurate results if the following requirements are adhered to:

   a. A node is placed where important concentrated masses or inertia masses are present.
   b. A sufficiently large number of beam elements is used to divide the longitudinal fiber (see Figure 6) and to properly account for the geometric, inertial, or structural variations along the bridge. If the bridge does not present important variations it is proposed that a minimum of 10 elements per span be used.
   c. In addition to the data necessary for the static analysis, the mass and rotational mass per unit-length are required.

2. When the bridge has a 2-D response (such as slab bridges with a width/span ratio greater than 0.6 or precast girder bridges with upper slab) a grillage with several longitudinal beams is necessary. In this case, also the same static element properties of the static analysis are used. The mass should be located on the longitudinal elements. In addition, the rotational mass should be calculated for interior longitudinal elements with respect to their own centroid and for the exterior elements with respect to the centroid of the global cross section.

3. Rayleigh's method gives accurate results for frequency in bending but inaccurate results in the calculation of the frequency of torsion when using a grillage model with more than one longitudinal fiber with a load pattern to obtain a deflected shape that is similar to the first torsional mode (see Model 3 of Bridge OF-56.1). This is because in the model all the longitudinal members dissipate energy as a result of the torsional rotation and that rotation does not correspond to the real bridge deformation.

4. The analytical equation (Equation 1) gives accurate torsion frequencies when the bridge has more than one bearing device over piers or abutments (ends fixed to torsion), even if small variations of mass or stiffness are present along the longitudinal axis of the bridge.

5. In cable-stayed bridges the geometric nonlinearity can be neglected in the dynamic model of the complete bridge (see Table 7). Also the 1-D model gives good results even for wide bridges.

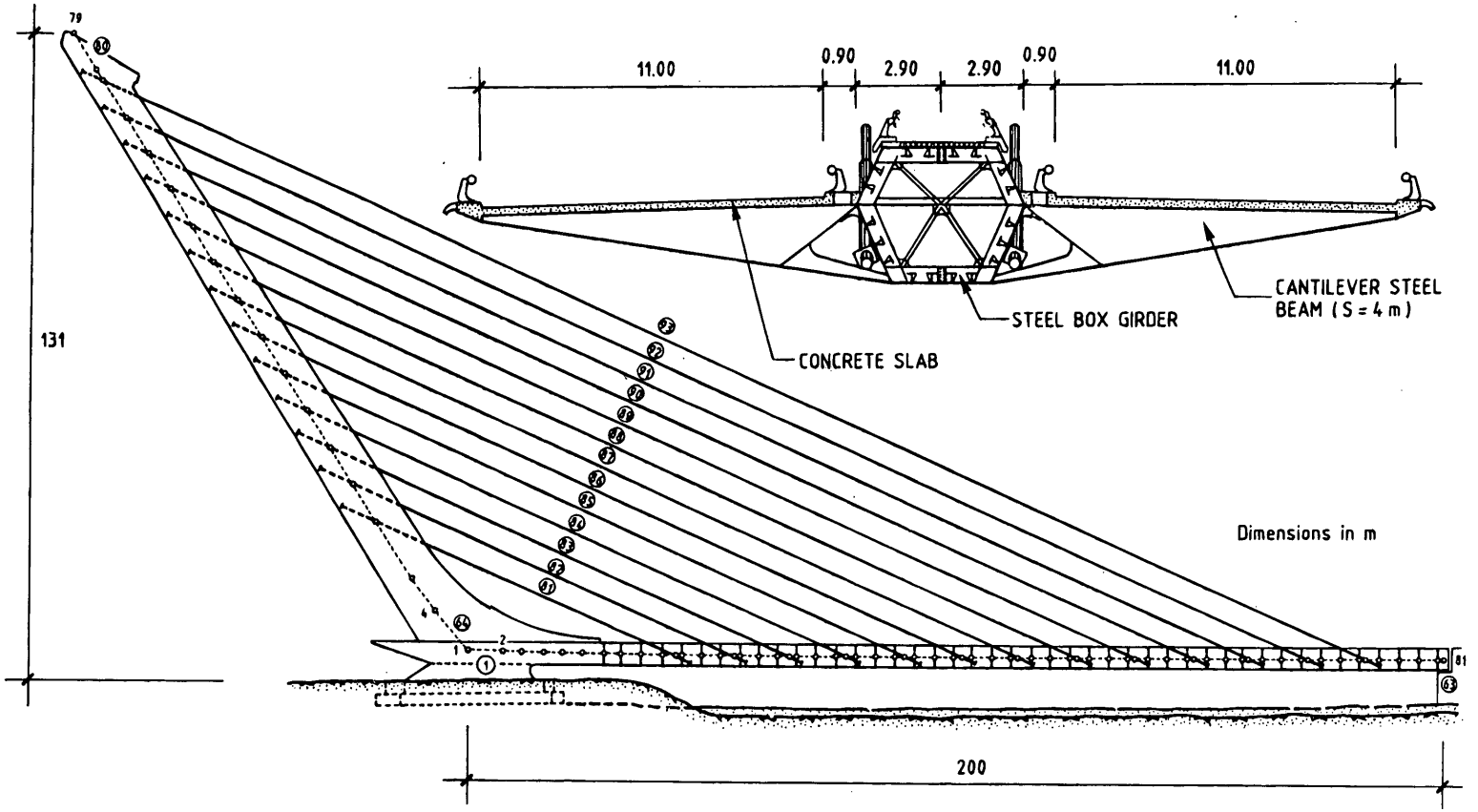

FIGURE 7. Cross section and FEM discretization of Alamillo Bridge.

TABLE 7. Natural Frequencies in Hertz of Alamillo Cable-Stayed Bridge

Mode	Theoretical		Experimental
	Linear	Non Linear	
f_1(Trans. pylon 1)	0.296	0.292	0.30
f_2(Long. pylon+deck 1)	0.375	0.373	0.40
f_3(Long. pylon+deck 2)	0.613	0.610	0.66
f_4(Trans. deck 1)	1.087	1.088	-
f_5(Long. pylon+deck 3)	1.202	1.191	1.205
f_6(Torsion deck 1)	1.219	1.235	1.155
f_7(Trans. pylon 2)	1.587	1.583	1.537
f_8(Long. pylon+deck 4)	2.190	2.196	2.155
f_9(Torsion deck 2)	2.301	2.298	2.295
f_{10}(Long. pylon+deck 5)	2.350	2.312	2.78
f_{11}(Trans. deck 2)	3.251	3.244	-

(-) Not recorded

REFERENCES

1. Clough, R. W., and J. Penzien. *Dynamics of Structures*. McGraw-Hill, New York, 1975.
2. Bathe, K. J., and E. L. Wilson. *Numerical Methods in Finite Element Analysis*. Prentice-Hall, Inc., Englewood Cliffs, N.J., 1976.
3. *NCHRP Research Results Digest 171*: Pot Bearings and PTFE Surfaces. TRB, National Research Council, Washington D.C., Sept. 1989.
4. Aparicio, A. C., and J. R. Casas. Results and Conclusions Deriving from the Tests Carried Out on the Alfonso X Flyover on the First Ring-Road in Barcelona: a Source of Relevant Data (in Spanish). *Hormigón y Acero*, No. 162, April 1987, pp. 33–141.
5. Hambly, E. C. *Bridge Deck Behaviour*, 2nd ed. Chapman & Hall, London, 1991.
6. West, R. *Recommendations on the Use of Grillage Analysis for Slab and Pseudo-Slab Bridge Decks*. Cement and Concrete Association, London, 1973.
7. Jaeger, L. G., and B. Bakht. The Grillage Analogy in Bridge Analysis. *Canadian Journal of Civil Engineering*, Vol. 9, No. 2, 1982, pp. 224–235.
8. Jaeger, L. G., and B. Bakht. *Bridge Analysis by Microcomputer*. McGraw-Hill, New York, 1989.
9. Whalter, R. *Ponts Haubanés* (in French). Presses Polytechniques Romandes, Lausanne, Switzerland, 1985.

Publication of this paper sponsored by Committee on Dynamics and Field Testing of Bridges.

Dynamic Load Spectra for Girder Bridges

HANI H. NASSIF AND ANDRZEJ S. NOWAK

The dynamic load is an important component of bridge loads. The determination of the dynamic load factor (DLF), defined as the ratio of dynamic and static responses, is essential for the development of a new generation of reliability-based bridge design codes. Field measurements are performed to determine the actual variation of the DLF with various truck as well as bridge parameters and to verify the available analytical models. The effects of various parameters, such as truck gross weight, truck speed, truck type, girder static stress, and girder position, on the DLF are presented. The field tests are carried out on four steel girder bridges. Measurements are taken using a weigh-in-motion system with strain transducers. For each truck passage, the truck weight, speed, axle configuration, and lane occupancy are determined and recorded. A numerical procedure is developed to filter and process collected data. The DLF is determined under normal truck traffic of various load ranges and axle configurations. The field measurements confirm the results of the analytical study. In absolute terms, the response caused by dynamic load is practically constant and does not depend on truck weight. However, for exterior girders the static stress is small. Therefore, the DLF should be considered on the basis of girders of maximum stress values.

The major load components include dead load, live load, and dynamic load. This paper deals with truck-induced dynamic loads in girder bridges. The dynamic load is time variant and random in nature and it depends on the vehicle type, vehicle weight, axle configuration, bridge span length, road roughness, and transverse position of a truck on the bridge. An example of the actual bridge response caused by an actual vehicle, a five-axle truck traveling at a highway speed, is shown in Figure 1. For comparison, also shown is an equivalent static response, which represents the same vehicle traveling at crawling speed.

The dynamic load is usually considered as an equivalent static live load and is expressed in terms of a dynamic load factor (DLF). There are different definitions for DLF, as summarized elsewhere (*1*) in a state-of-the-art report on dynamic testing of bridges. In this study, DLF is taken as the ratio of dynamic and static responses (*2*):

$$DLF = \frac{D_{dyn}}{D_{stat}} \tag{1}$$

where D_{dyn} is the absolute maximum dynamic response at any point (e.g., stress, strain, or deflection) measured from the test data and D_{stat} is the maximum static response obtained from the filtered dynamic response.

The measurement of static load spectra is described by Nowak et al. (*3*). An accurate dynamic load model is required for the development of rational criteria for the design and evaluation of bridges. Yet, the available data are insufficient and unclear. Analytical simulation procedures provided a basis for calculation of design provisions (*4*). However, there is a need for field verification of the results. Therefore, the objective of this study is to determine the dynamic load factor based on the field measurement data. The work is carried out on selected steel girder bridges. The obtained results are compared with DLFs calculated on the basis of the analytically simulated model (*4*).

H. H. Nassif, Civil Engineering and Construction Department, Bradley University, Peoria, Ill. 61625. A. S. Nowak, Department of Civil and Environmental Engineering, University of Michigan, Ann Arbor, Mich. 48109-2125.

CODE PROVISIONS

Most bridge codes specify the dynamic load as an additional static live load. The actual values vary from one document to another. In the current AASHTO (*5*), DLF or $(1 + I)$, is specified as a function of span length only:

$$I = \frac{50}{125 + L} \tag{2}$$

where L is the span length in feet (1 ft = 0.305 m). However, the maximum value of DLF is 0.30. This empirical equation has been in effect since 1944.

In the new load and resistance factor design (LRFD) AASHTO Code (*6*), live load is specified as a combination of HS20 truck (*5*) and uniformly distributed load of 640 lb/ft (9.3 kN/m). DLF is equal to 0.33 of the truck effect, with no dynamic load applied to the uniform loading.

PREVIOUS STUDIES

The available data on dynamic load in bridges is limited (*7*). Some measurements were taken by the Ontario Ministry of Transportation (*2*). A total of 27 bridges were tested. The structural types included prestressed concrete (girders and slabs), steel girders (rolled sections, plate girders, and box girders), steel trusses, and rigid frames. Data were recorded for test vehicles and actual traffic. The mean values are about 0.05 to 0.10 for prestressed concrete AASHTO-type girders and 0.08 to 0.20 for steel girders. The maximum observed values exceed 0.5, and some of the coefficients of variation are over 1.0. However, the correlation between DLF and truck weight is not available. On the other hand, it is expected that the largest DLFs correspond to lighter trucks. Considerable differences in DLF are observed for otherwise similar structures, which indicates the importance of factors such as surface condition.

Cantieni (*8*) tested 226 bridges in Switzerland, mostly prestressed concrete. With the exception of 11 bridges, all were loaded with the same vehicle, under the same load, and with the same tire pressure, thus minimizing the variability caused by truck dynamics. The effect of local unevenness in the pavement on the dynamic load was also investigated. The study showed that the dynamic fraction of the load was as high as 0.7 for bridges with fundamental natural frequency

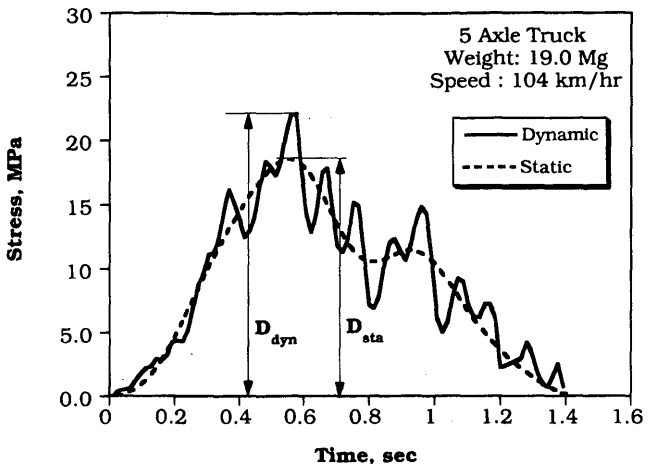

FIGURE 1. Dynamic and static response for Girder 3, Bridge 1, under a five-axle truck (1 MPa = 6.89 ksi; 1 km = 0.6 mi, 1 Mg = 1,814 lb).

between 2 and 4 Hz. However, as in the Ontario data (*2*), the static and dynamic loads were recorded separately, so that it is not possible now to determine the degree of correlation. It is also expected that the high values of DLF are associated with lighter vehicles.

O'Connor and Pritchard (*9*) found that the dynamic load is vehicle dependent and varies with the suspension geometry. They carried their tests on a short-span composite steel and concrete bridge in Australia. The results indicate that as the weight of the vehicle increases, the dynamic load decreases. Also, O'Connor and Chan (*10*) collected strain data and, using those records, determined DLFs ranging from −0.08 to +1.32. As in the previous studies, the extreme values are associated with light trucks.

Most of the theoretical studies on vibration of beams under moving loads concentrated on modeling only one of the parameters—either the vehicle, bridge, or surface roughness. The vehicle was modeled as a constant force (*11*), one degree-of-freedom system (*12*), two degrees-of-freedom system, or more realistic complex systems (*13*). The bridge was modeled as either a continuous or discrete system (*14*). Discrete models can be in the form of simple beams, simple beams with torsional degree of freedom, and orthotropic plates. The surface roughness was modeled using the so-called artificial bump on the approach method (*13*), and Honda and Kobori (*14*) used a random process to represent the random road profile as a Fourier series with random coefficients.

The development of a new LRFD code required a verification of the load model. In particular, there was a need for confirmation of the observation that the dynamic load factor decreases for heavier trucks and for multiple truck occurrence. Therefore, a computer procedure was developed previously (*4*) for simulation of the dynamic bridge behavior. The dynamic load was determined as a function of three major parameters: road surface roughness, bridge dynamics (frequency of vibration), and vehicle dynamics (suspension system). The bridge was modeled as a prismatic beam. Dynamic parameters of trucks were based on the available data. Road roughness was generated using the actual measurement records. The DLF was calculated in terms of deflections. It was found that the dynamic deflection is almost a constant, whereas static deflection is proportional to truck weight. Therefore, DLF decreases for heavier trucks. The simulations were carried out for single trucks and two trucks side-by-side. For two trucks, the DLF was smaller by about 50 percent compared with DLF for single trucks.

EXPERIMENTAL PROGRAM

The purpose of the experimental program is to measure the dynamic load amplification in simple-span steel girder bridges. Corresponding truck weights, in particular axle loads and axle spacings, are also recorded. The measurements are taken simultaneously by two systems: the weigh-in-motion (WIM) system (truck information and girder strains) and the dynamic system (accelerations) (*15*). The WIM system was developed by the bridge weigh systems. Its purpose is to measure and record all relevant truck information in addition to the strain response in each girder. The strain gauges are placed on lower flanges close to the position of the maximum moment. The dynamic system, developed by Krenz Electronics, is set up to measure accelerations simultaneously, and at the same location as, the strain gauges. Both systems are triggered by special tape switches, pasted to the pavement. The same tape switches are used to determine the truck speed, the number of axles, and axle spacings.

Four bridges are selected for the field tests. All of them are located in southeastern Michigan. The span lengths vary from 9 to 24 m (30 to 80 ft). The same procedure is used for all bridges, however, with a different equipment setup. All selected structures are multi-simple–span bridges with steel girders and concrete slabs. The basic design parameters include span length, girder spacing, slab thickness, and skewness. The basic parameters of the selected bridges are given in Table 1. Girders are labeled starting from the exterior girder in the right lane (Girder 1) to the exterior girder in the left lane (Girder 8).

The strain gauges are attached to bottom flanges of girders. The location of the strain gauge was 2 to 3 ft from midspan, depending on span length and access to the point of installation. The equipment is calibrated using trucks with known axle weights and spacings. The accuracy of calculation for axle loads is within 20 percent and for gross vehicle weight (GVW) within 10 percent (within 5 percent for three and five axle trucks). The measurements are carried out for several days at each location.

A computer program is developed for the automated data processing. Each data file contained data from six or eight channels. Each record represents the passage of a truck over the bridge in either right or left lane. The data capturing starts when the truck crosses over the first tape switch, which is about 6 m (20 ft) from the bridge support in either lane. The tape switch signal is used to trigger the system and start collecting data from the accelerometers and strain transducers. The data collection is automatically stopped after the departure of the last truck axle from the bridge. However, this synchronization works for bridges with traffic intensity not higher than normal. On bridges with trucks of certain characteristics (e.g., heavy, 11 axles), the manual trigger permits a better control of the data acquisition system.

The strain records are smoothed and filtered using the widely used fast fourier transform (FFT) technique (*16*). The FFT procedure is utilized assuming that the measured strain-time (or acceleration-time data) can be represented as the sum of all contributions from all mode shapes. FFT is also used to determine the dominant frequencies as well as the cutoff frequency in the frequency domain. The cutoff frequency is best estimated, for each individual bridge,

TABLE 1. Parameters of the Tested Bridges

Bridge No.	Location	Span (m)	No. of Girders	Girder Spacing (m)	Slab Thickness (mm)	Bridge Width (m)	Skew
1	US-23/ Huron River	24.5	6	1.90	190	11.0	14°
2	M-14/ N.Y.C. Rail Road	16.0	8	1.85	200	12.8	25°
3	I-94/ Jackson Road	16.0	9	1.70	190	14.5	25°
4	I-94/ Pierce Road	10.5	10	1.70	175	13.7	29°

by minimizing the error in estimating the total energy under the power spectrum plot in the frequency domain. After eliminating the contribution of all modes (or frequencies) above the cutoff frequency in the frequency domain, inverse FFT is then performed to obtain the time-domain equivalent static response (referred to as static response). This process is performed on various truck strain records using a computer program that was developed on the basis of available numerical routines (*15*). The dynamic and static response are then plotted and compared to determine the DLF.

The WIM measurements provided data on truck weights, axle loads, axle configurations, and vehicle speeds. Most of the trucks traveled at about 90 km/hr (60 mph). The truck traffic was a mixture of mostly 5-axle vehicles with few very heavy 11-axle trucks. The GVW ranges were above the legal limits.

MEASURED DYNAMIC LOAD

The measurements are carried out on four bridges listed in Table 1. Static and dynamic stress is determined for each girder. The resulting dynamic load factors (DLF) are plotted versus the static stress in each girder in Figures 2 through 5. The results are shown for a maximum of eight girders limited by the number of available data acquisition channels.

In general, DLF decreases as the static stress in each girder increases. However, the DLF is the ratio of dynamic and static stress, and static response varies from girder to girder, depending on the positions of the girder and truck. The variation in DLF with respect to static stress in each girder is shown in Figures 2 through 5. It is shown that the exterior girders exhibit small static stress (almost negligible), whereas the interior girders have much larger static stresses.

In general, the static stress is proportional to truck weight. However, the dynamic stress (maximum dynamic stress-maximum static stress) is practically independent of truck weight (or static stress), as shown in Figure 6. Therefore, the dynamic load factor, DLF, decreases with increasing static stress or truck weight. The variation of DLF with truck parameters is shown in Figures 7 through 9. Results for each bridge are shown corresponding to the most loaded interior girder. Observations indicate that the DLF decreases as the GVW increases for all bridges (Figure 7). Observations also indicate that among all types of vehicles (excluding light-weight two-axle vehicles), four- and five-axle trucks cause the largest DLF values (Figure 8). Additionally, the DLF decreases with an increase in truck speed (Figure 9). Moreover, to represent the variation of DLF with girder position, the mean value of DLF, for right lane girders in each bridge, is plotted versus the girder position as shown in Figure 10. On average, the most loaded girders (Girders 3 and 4) will have values of DLF below 1.20.

CONCLUSIONS

The dynamic loads under a normal highway traffic are measured for selected steel girder bridges. For each truck, the measured parameters include: axle loads, axle spacings, speed, strain record, and acceleration record. A numerical procedure is developed for data processing, filtering, and smoothing. The DLF is calculated using strain records.

Observations indicate that the dynamic component of stress (i.e., dynamic increment) is practically independent of static component. Therefore, DLF decreases with increased static stress. For very heavy trucks, DLF does not exceed the theoretical results (*4*).

Larger values of DLF are observed in exterior girders; however, this is because of a relatively smaller static load effect. Values of DLF should be based on those obtained from the most loaded interior girders.

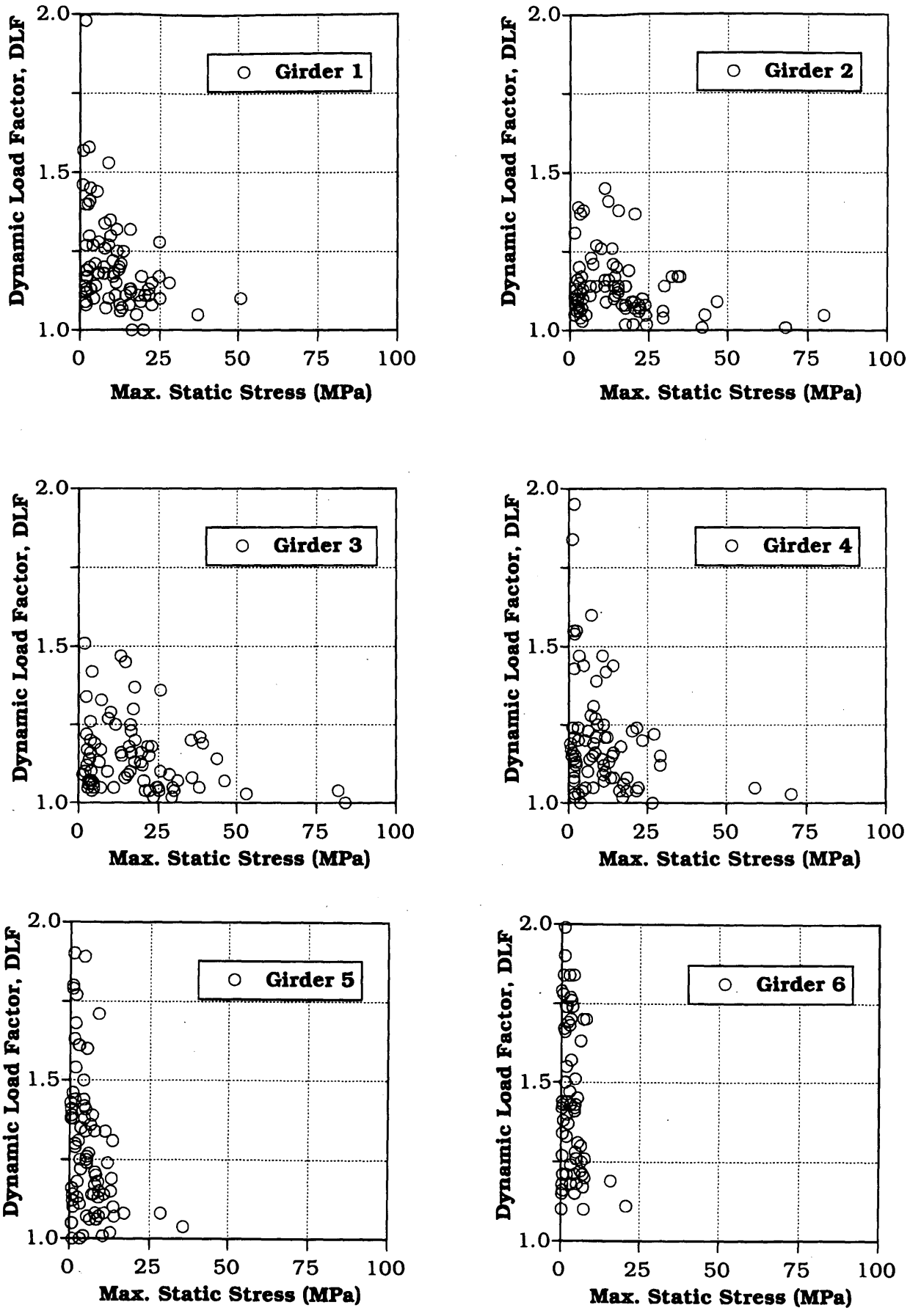

FIGURE 2. DLF versus static stress for Girders 1 through 6, Bridge 1 (1 MPa = 6.89 ksi).

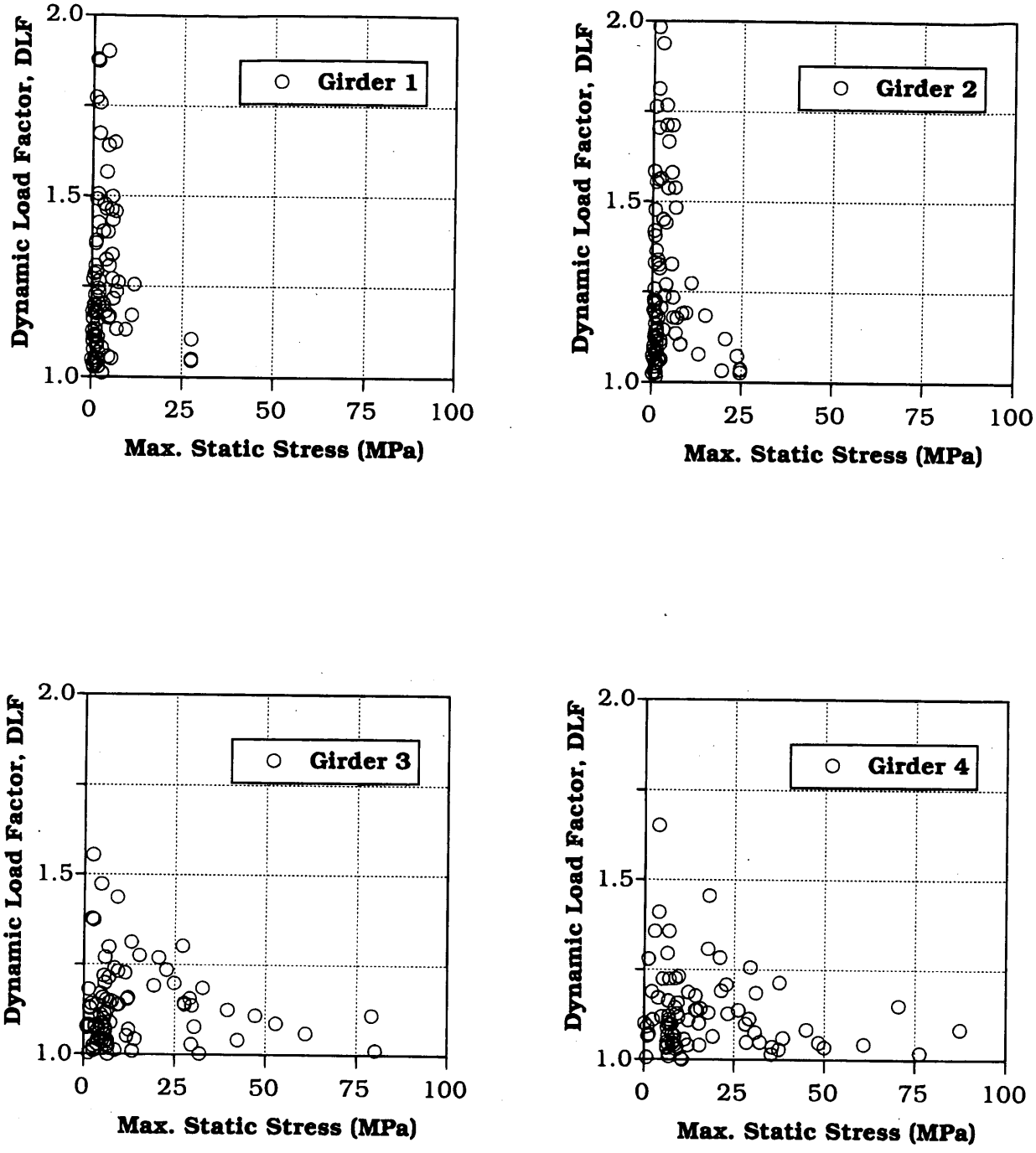

FIGURE 3. DLF versus static stress for Girders 1 through 8, Bridge 2 (1 MPa = 6.89 ksi).

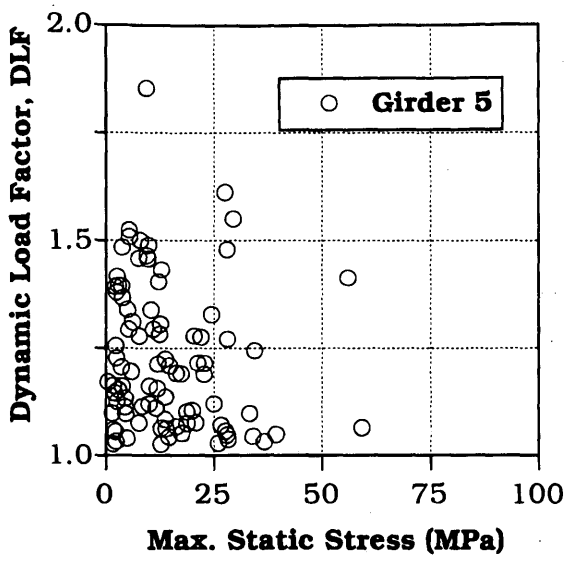

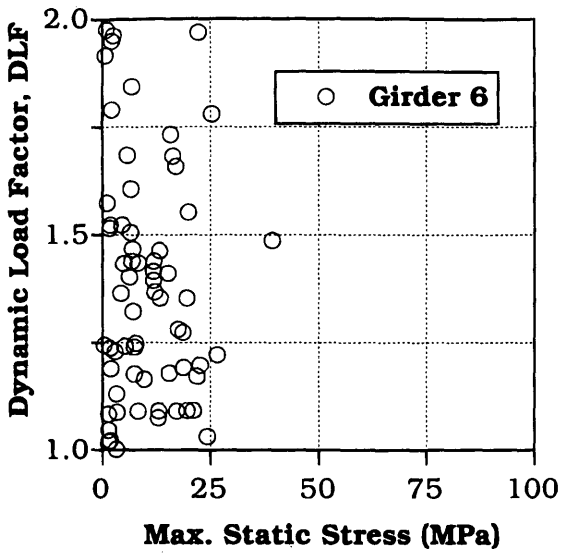

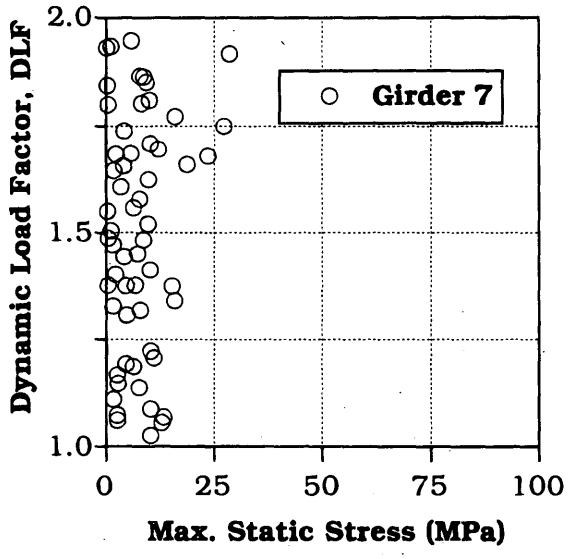

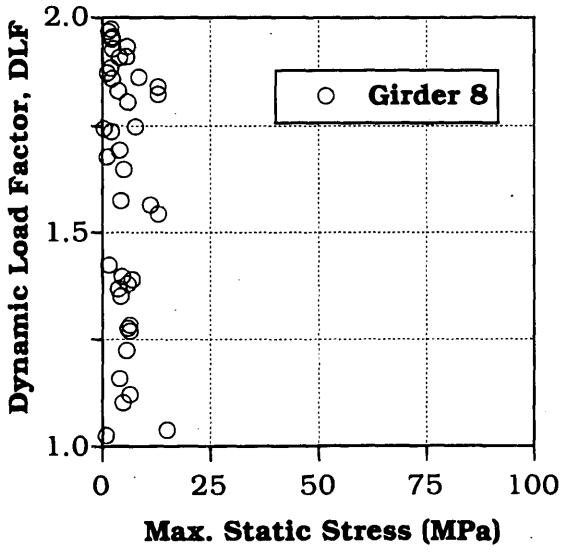

FIGURE 3. (*continued*)

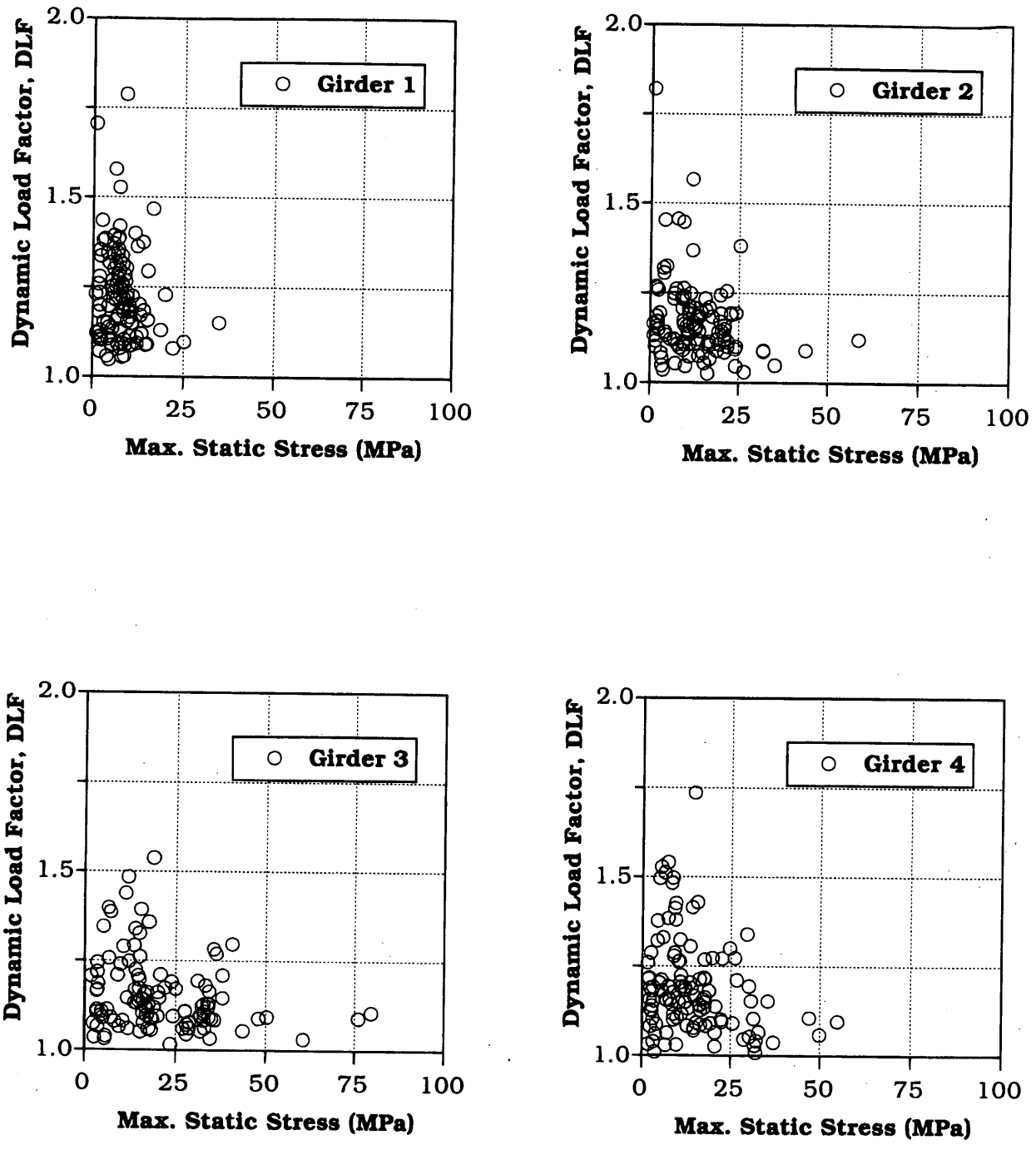

FIGURE 4. DLF versus static stress for Girders 2 through 9, Bridge 3 (1 MPa = 6.89 ksi).

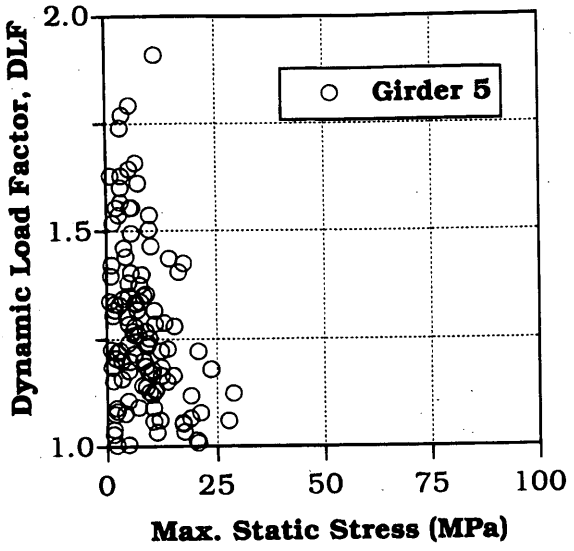

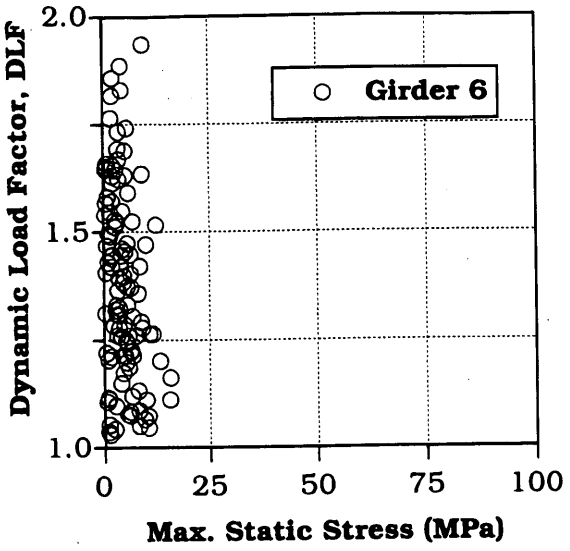

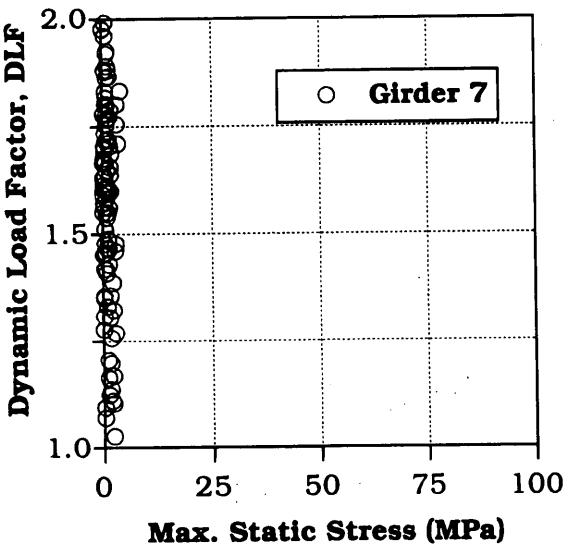

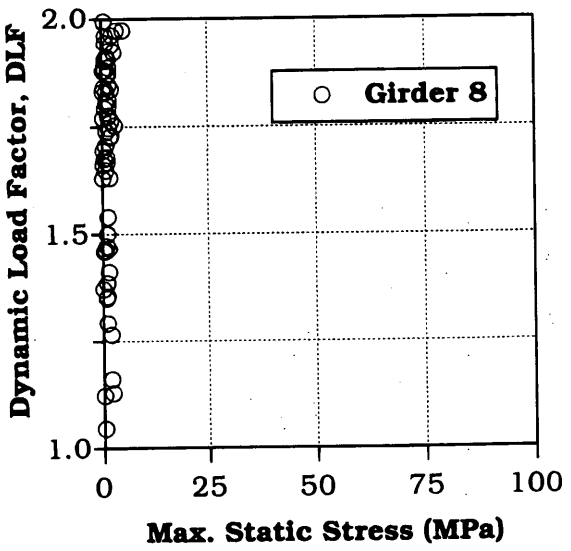

FIGURE 4. (*continued*)

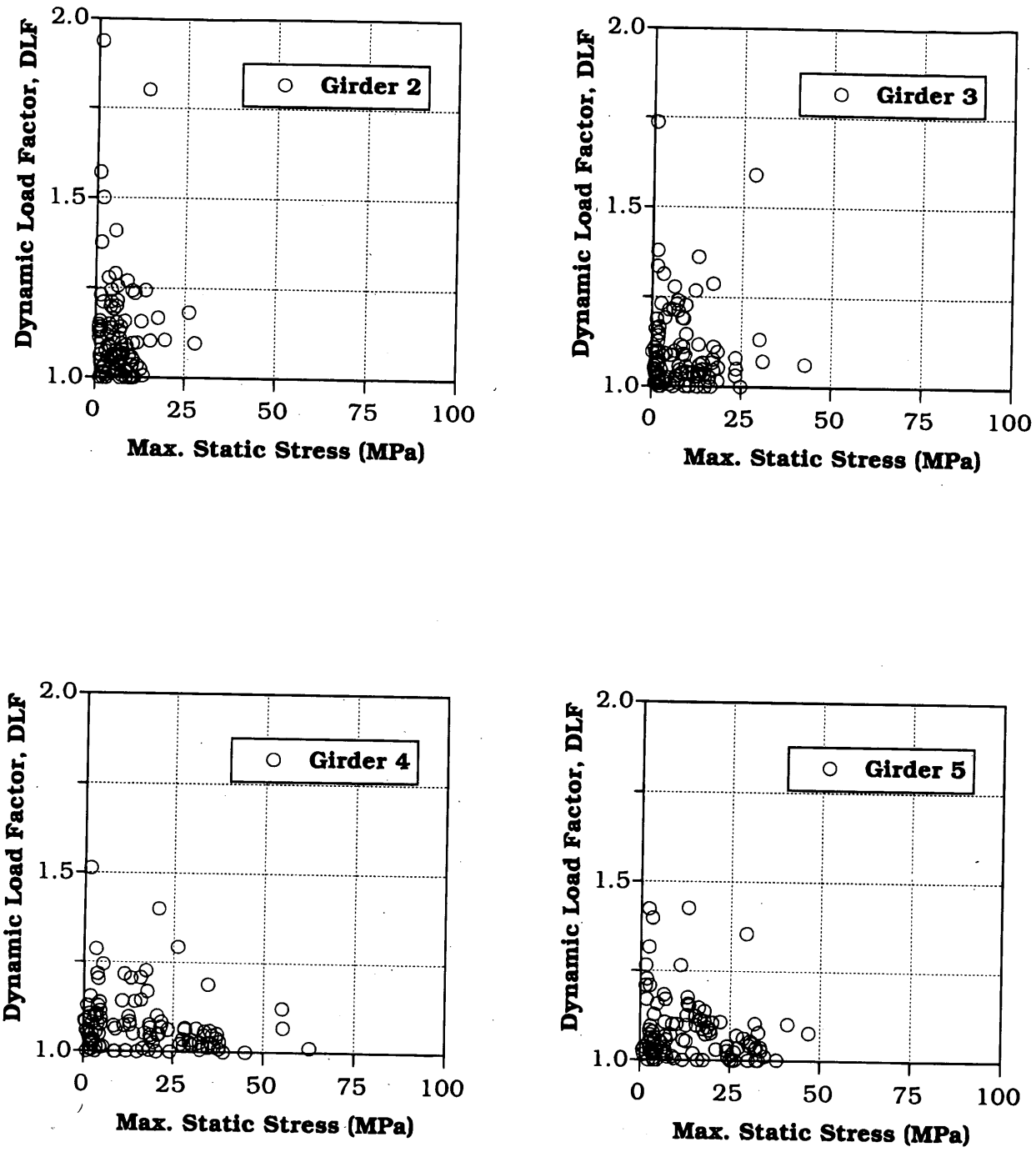

FIGURE 5. DLF versus static stress for Girders 2 through 10, Bridge 4 (1 MPa = 6.89 ksi).

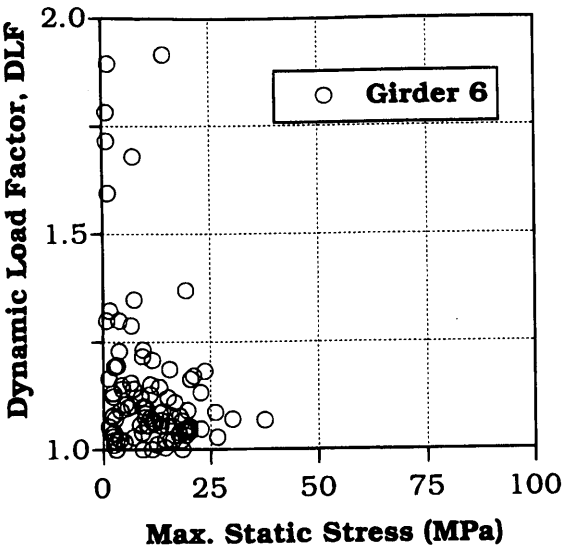

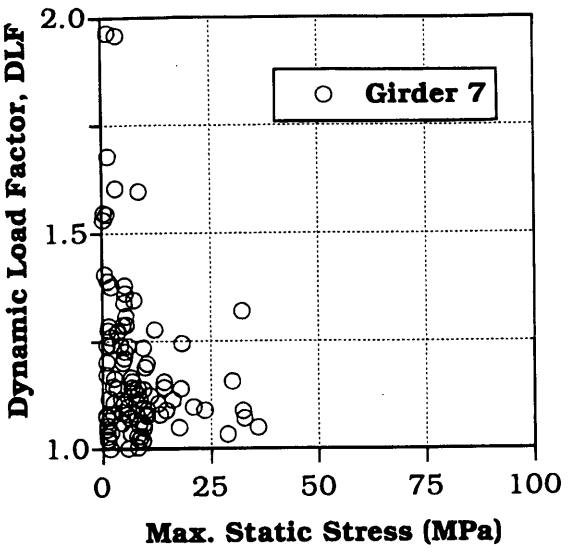

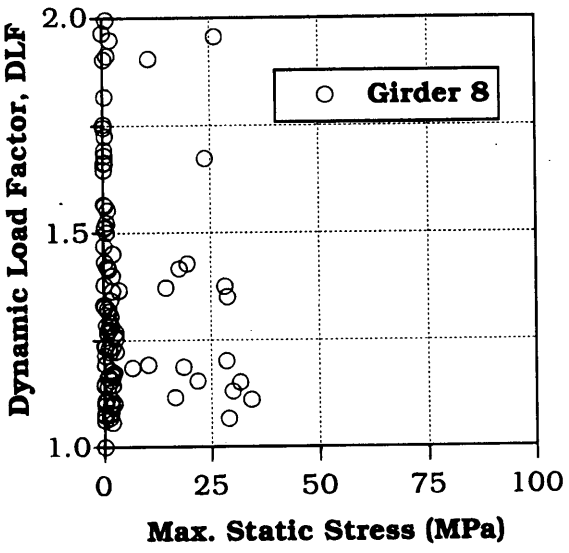

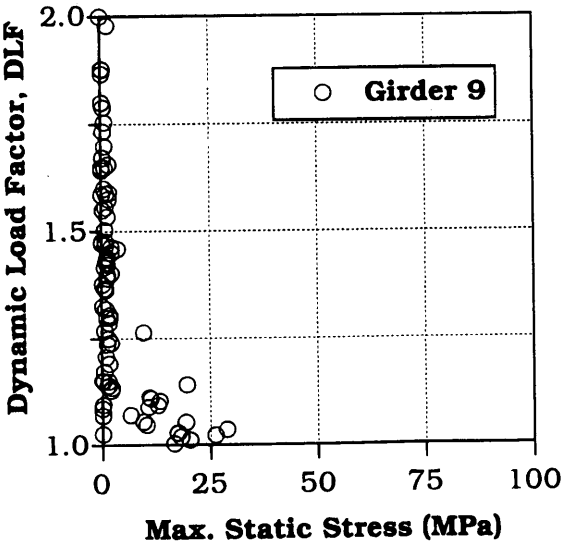

FIGURE 5. (*continued*)

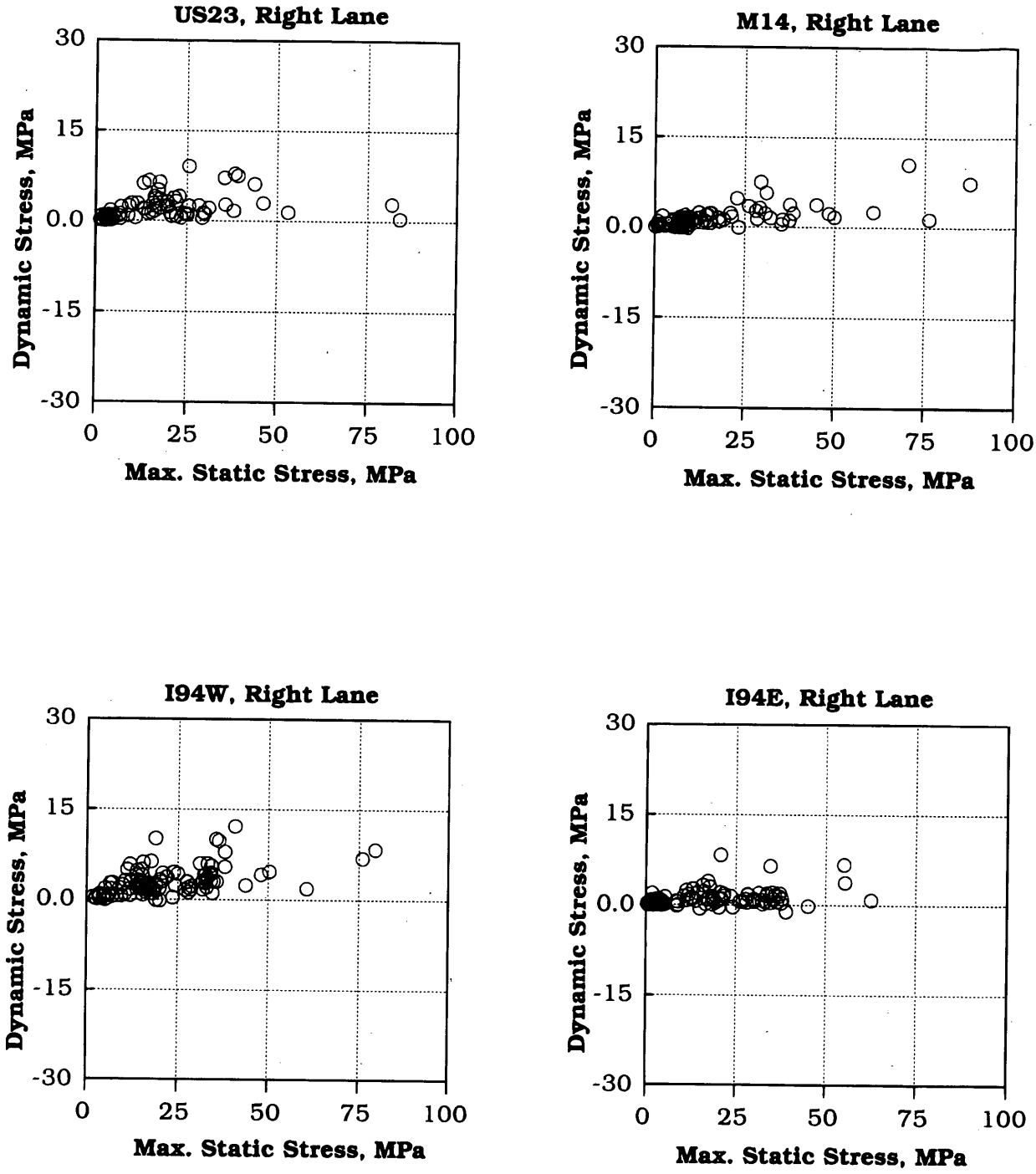

FIGURE 6. Dynamic stress versus maximum static stress (1 MPa = 6.89 ksi).

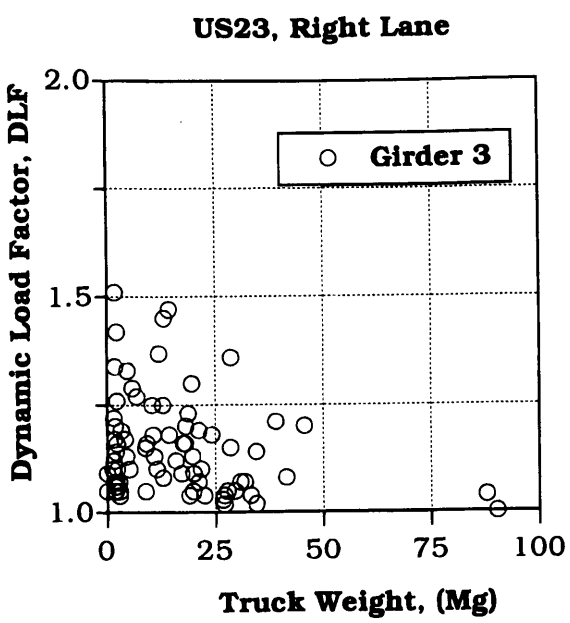

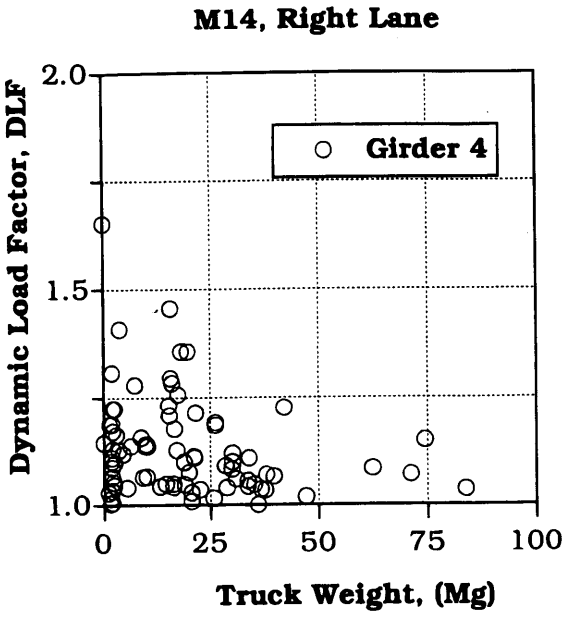

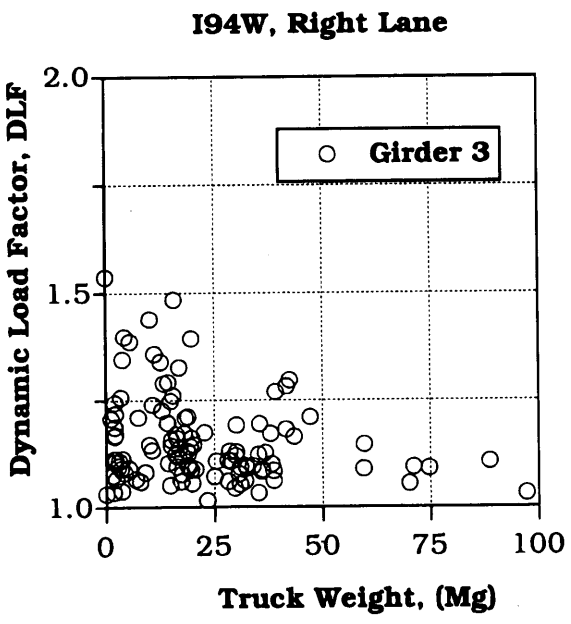

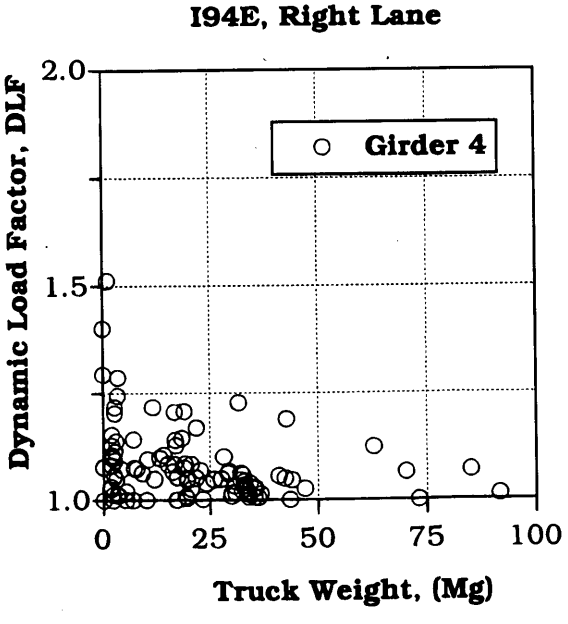

FIGURE 7. DLF versus truck weight (1 mg = 1,814 lb).

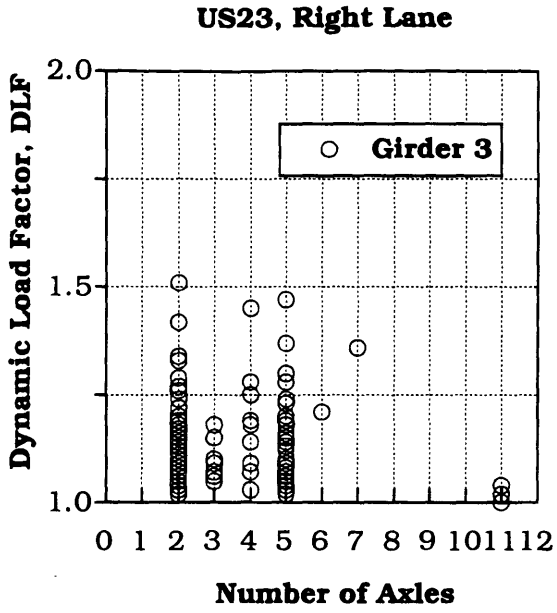

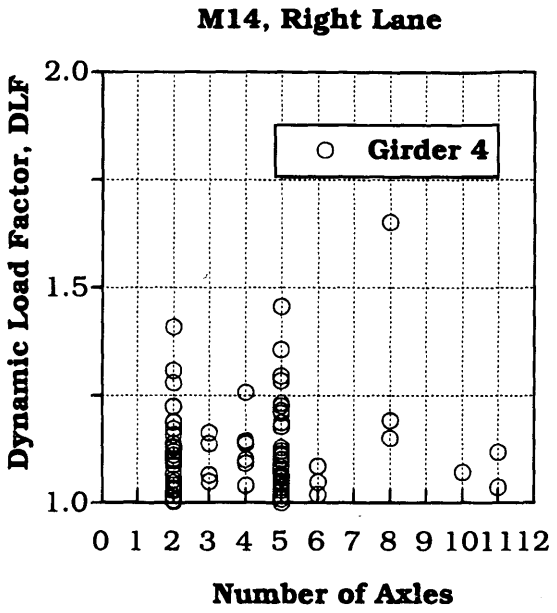

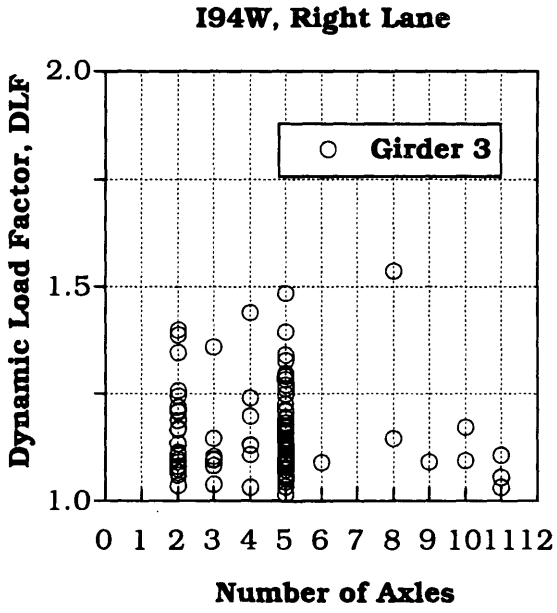

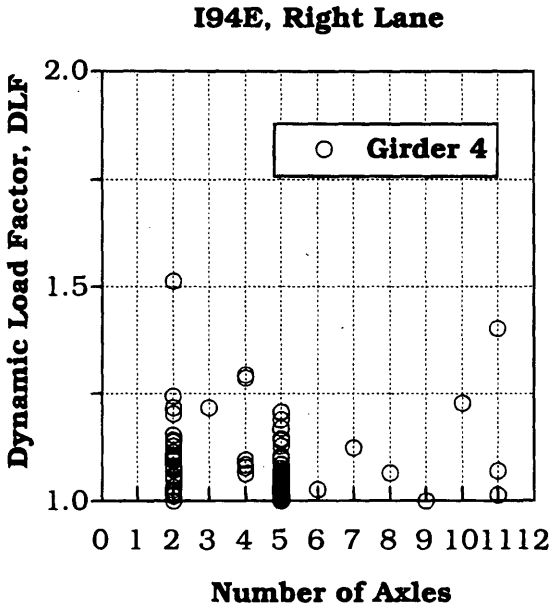

FIGURE 8. DLF versus truck type (number of axles).

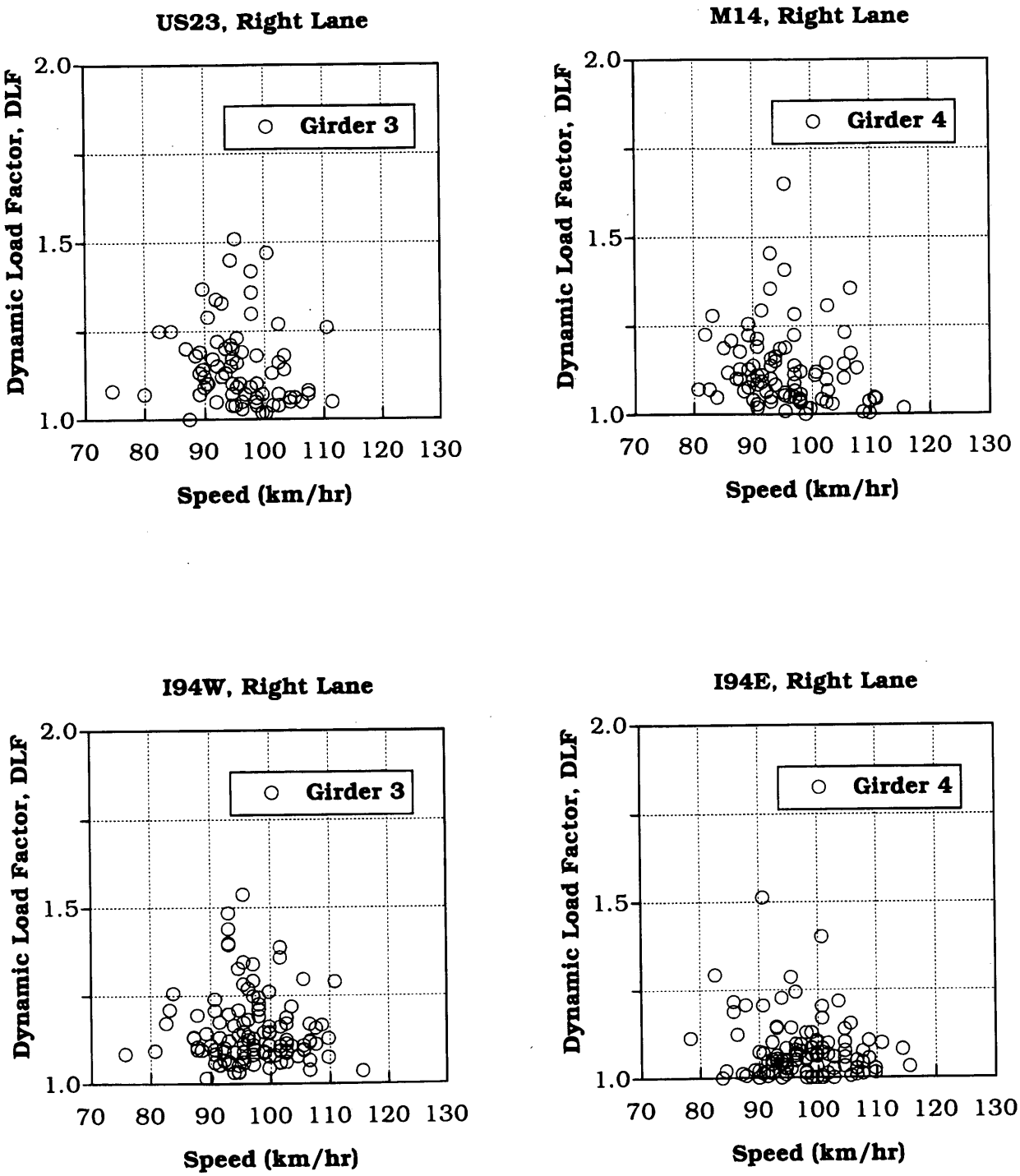

FIGURE 9. DLF versus truck speed (1 km = 0.6 mi).

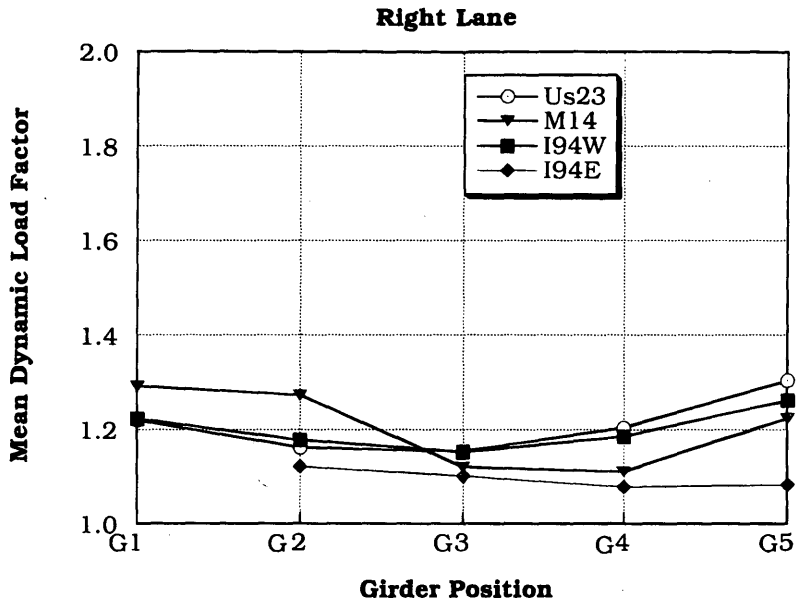

FIGURE 10. Mean DLF versus girder position.

ACKNOWLEDGMENTS

The presented research was sponsored by the Michigan Department of Transportation and Great Lakes Center for Truck Transportation research, which are gratefully acknowledged.

REFERENCES

1. Bakht, B., and S. G. Pinjarkar. Dynamic Testing of Highway Bridges—A Review. In *Transportation Research Record 1223*, TRB, National Research Council, Washington, D.C., 1989, pp. 93–100.
2. Billing, J. R. Dynamic Loading and Testing of Bridges in Ontario. *Canadian Journal of Civil Engineering*, Vol. 11, No. 4, 1984, pp. 883–843.
3. Nowak, A. S., H. H. Nassif, and L. DeFrain. Effect of Truck Loads on Bridges. *Journal of Transportation Engineering*, ASCE, Vol. 119, No. 6, 1993, pp. 853–867.
4. Hwang, E.-S., and A. S. Nowak. Simulation of Dynamic Load for Bridges. *Journal of Structural Engineering*, ASCE, Vol. 117, No. 5, 1991, pp. 1413–1434.
5. *Standard Specification for Highway Bridges*. AASHTO, Washington D.C., 1992.
6. Nowak, A. S. *Calibration of LRFD Bridge Design Code*. Report UMCE 93-22. Department of Civil and Environmental Engineering, University of Michigan, Ann Arbor, 1993.
7. Paultre, P., O. Chaallal, and J. Proulx. Bridge Dynamics and Dynamic Amplification Factors—a Review of Analytical and Experimental Findings. *Canadian Journal of Civil Engineering*, Vol. 19, 1992, pp. 260–278.
8. Cantieni, R. *Dynamic Load Tests on Highway Bridges in Switzerland*. Report 211. Swiss Federal Laboratories of Material Testing and Research (EMPA), Dubendorf, Switzerland, 1983.
9. O'Connor, C., and R. W. Pritchard. Impact Studies on Small Composite Girder Bridge. *Journal of Structural Engineering*, ASCE, Vol. 111, No. 3, 1985, pp. 641–653.
10. O'Connor, C., and T. H. T. Chan. Dynamic Wheel Loads from Bridge Strains. *Journal of Structural Engineering*, ASCE, Vol. 114, No. 8, 1988, pp. 1703–1723.
11. Wu, J. S., and C. W. Dai. Dynamic Responses of Multispan Nonuniform Beam due to Moving Loads. *Journal of Structural Engineering*, ASCE, Vol. 113, No. 3, March 1987, pp. 458–474.
12. Blejwas, T. E., C. C. Feng, and R. S. Ayre. Dynamic Interaction of Moving Vehicles and Structures. *Journal of Sound and Vibration*, Vol. 67, No. 4, Dec. 1979, pp. 513–521.
13. Gupta, R. K. Dynamic Loading of Highway Bridges. *Journal of the Engineering Mechanics Division*, ASCE, Vol. 106, No. EM2, April 1980, pp. 337–393.
14. Honda, H., and T. Kobori. Vibration Control of Loshe Girder Bridge using Design of Experiments. *Proc., Japan Society of Civil Engineers*, No. 301, Sept. 1980, pp. 37–46.
15. Nassif, H. H. *Live Load Spectra for Girder Bridges*. Ph.D. dissertation. University of Michigan, Ann Arbor, 1993.
16. Paz, M. *Structural Dynamics—Theory and Computation*, 3rd ed. Van Nostrand Reinhold, New York, 1991.

Publication of this paper sponsored by Committee on Dynamics and Field Testing of Bridges.

Effect of Varying Foundation Stiffness on Seismically Induced Loads in Bridge Bents: A Sensitivity Study

TOMMY L. COOK, EDWIN G. BURDETTE, RICHARD L. GRAVES, DAVID W. GOODPASTURE, AND J. HAROLD DEATHERAGE

Research was undertaken to assist the Tennessee Department of Transportation (TnDOT) in its analysis of bridges subjected to seismic loading. Specifically, consideration was given to the modeling of the soil-pile interface where friction piles are used in loessial soil. TnDOT uses the SEISAB bridge analysis program, developed by Imbsen and Associates, for the seismic analysis of its bridges. This program was used for all analysis of the research. Current TnDOT modeling practice is to consider that the bridge piers are fixed at the top of the pile cap rather than to assign values of stiffness to springs used to model the resistance of the soil to foundation movement. Elastic spring coefficients, developed using methods presented previously, and the traditional beam-on-elastic-foundation theory are used in the modeling of the bridges. The primary focus of this study is the sensitivity of the calculated axial loads and moments to variations in these spring coefficients. The results from this study underscore the need for more experimental data that could lead to more realistic and reliable values for spring stiffness.

In the development of any structural model, particular attention should always be given to the selection of the model's boundary conditions. In a dynamic analysis the selection of proper boundary conditions becomes increasingly more important because member forces can change by several orders of magnitude, depending on the characteristics of the model. Traditionally, engineers have had little information about techniques available for modeling a pile-supported foundation. Because the testing of a full-scale pile or pile group is both difficult and expensive, there have been limited data to supplement design assumptions, and most structural models are based largely on theoretical information. However, in recent years the destructive effects of several earthquakes on both building and highway structures have increased awareness and provided motivation to achieve a better understanding of the behavior of pile-supported foundations. As a result, several dynamic lateral testing programs on single piles and pile groups have been conducted in many different types of soils (*1–5*). However, essentially no information is available on the dynamic response of piles located in the soil type known as loess, the soil that exists in the western portion of Tennessee. Because West Tennessee is in Seismic Zone 3, this response is of considerable interest.

The Tennessee Department of Transportation (TnDOT) uses the bridge analysis program SEISAB (*6*), developed by Imbsen and Associates, for seismic analysis of bridges. Because of the lack of information on the properties of loess needed to quantify the resistance provided by the soil to the pile caps, the piers are modeled as fixed at the tops of the pile caps. Recognizing that this condition is not precisely representative of actual conditions, TnDOT is sponsoring research to determine more realistic values of stiffness to model the soil-pier interface. As a part of that research, an analytical study was done to evaluate the sensitivity of pier column moments and axial loads to the values assigned to the stiffnesses of springs used to model the soil-pier interface.

The purpose of the sensitivity study reported herein was to determine the effect of large variations in interface stiffness on the axial loads and moments in the pier columns of bridges subjected to the seismic loading used in the design of bridges in West Tennessee. Although some discussion of typical methods used to obtain stiffness coefficients is included, the emphasis is not the accurate determination of stiffness but rather the effect that variations in assumed stiffness have on the results. To accomplish the stated purpose, two actual West Tennessee bridges were modeled and analyzed using SEISAB, and the effects of varying stiffness coefficients at the soil-pier interface were studied.

BRIDGE STRUCTURES TO BE MODELED

A bridge in Madison County, Tennessee, consisting of two continuous spans (Figure 1) and a bridge in Haywood County, Tennessee, consisting of three continuous spans (Figure 2) were selected for this study because of their geographical location in an area with loess and because the structures represent the typical types of bridges used in West Tennessee by TnDOT.

The Madison County bridge consists of a two-span continuous structure with six prestressed concrete girders supporting two lanes of traffic; the girders are spaced 2.51 m (8 ft 3 in.) apart. The bridge is constructed with a 68-degree angle of skew (measured from the direction of traffic). For this analysis a 90-degree skew was considered as shown in Figure 1; however, further investigations into the effect of skew on the dynamic response were conducted by Cook (*7*) with results similar to those reported here. The foundation of the bridge is composed of two monolithic reinforced concrete abutments on either end of the road deck and a central bent pier with three columns resting on embedded footings. Each abutment is supported by a single row of 13 piles along the endwall and a single pile under each wingwall, as indicated in Figure 3. With respect to Figure 1, the piles at Abutments 1 and 2 are embedded to depths of 14 and 17 m (45 and 55 ft), respectively. The central bent pier foun-

T. Cook, Technical Engineering Consultants, P.O. Box 53221, Knoxville, Tenn. 37950. E.G. Burdette, R.L. Graves, D.W. Goodpasture, and J.H. Deatherage, Department of Civil Engineering, University of Tennessee, Knoxville, Tenn. 37996-2010.

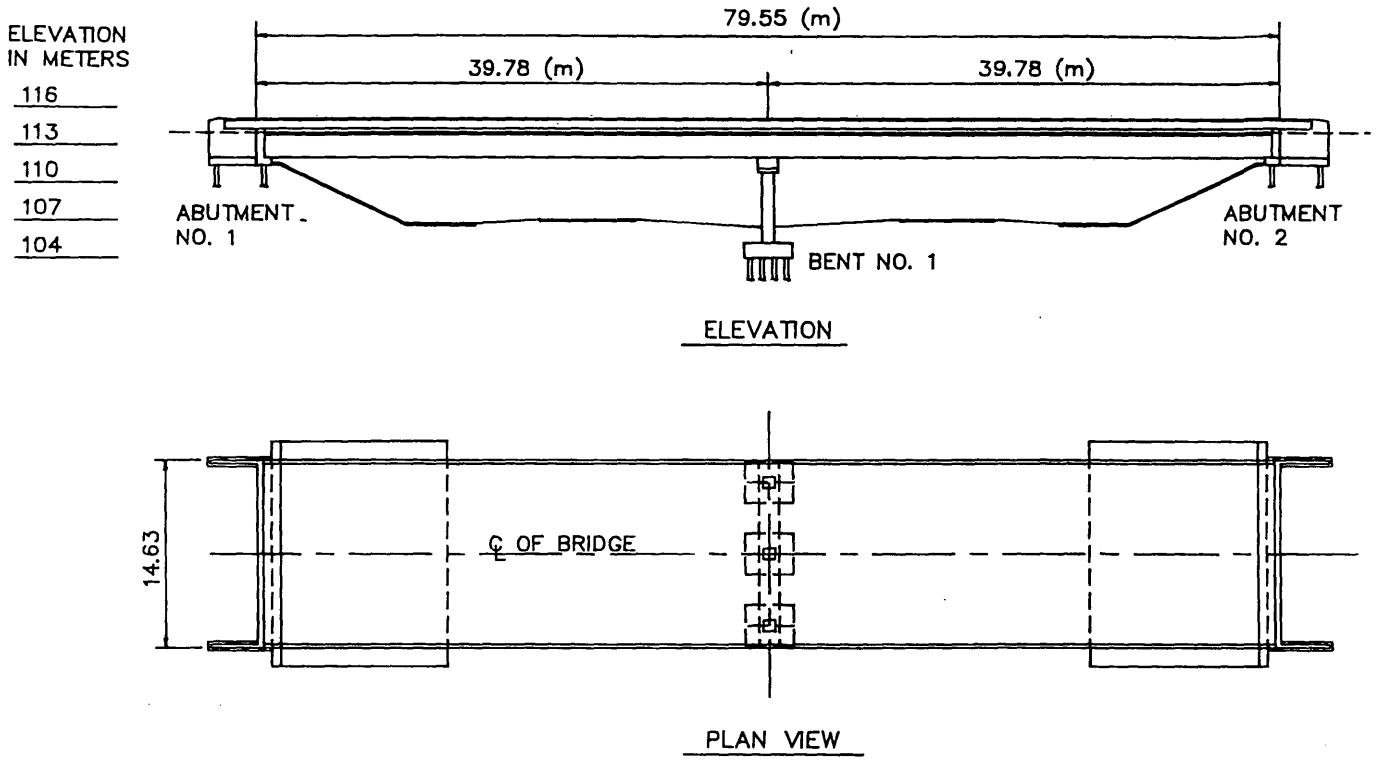

FIGURE 1 Plan and elevation of Madison County bridge (SR-233 over I-40) constructed by TnDOT in 1992 (1 m = 3.281 ft).

dation consists of a pile cap under each column supported by 12 piles embedded to a depth of 7.6 m (25 ft). Piles under both the abutments and central bent pier are precast concrete piles 356 × 356 mm (14 × 14 in.). All piles used for foundation support of the Madison County bridge are floating or friction piles and are considered to be long and flexible.

The Haywood County bridge structure consists of three continuous spans with five prestressed concrete box beams supporting two lanes of traffic; girders are spaced 2.29 m (7 ft 5 in.) apart. The abutments and bent piers were constructed with a 90-degree skew and were analyzed as such. The abutments at either end of the bridge serve primarily to provide a bearing point for the prestressed box

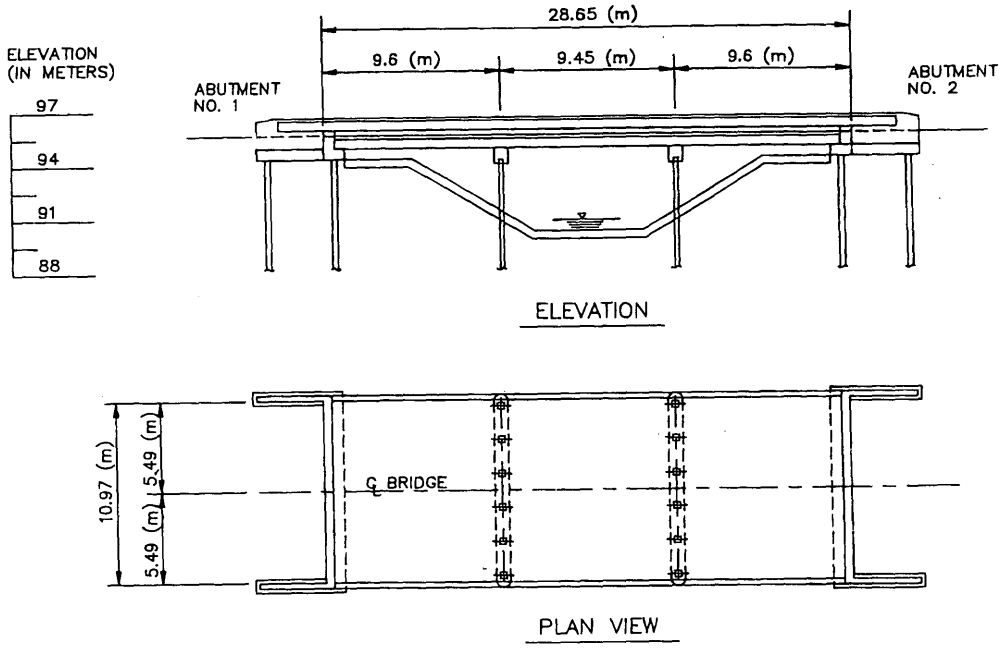

FIGURE 2 Plan and elevation of Haywood County bridge (SR-54 over Nixion Creek) constructed by TnDOT in 1992 (1 m = 3.281 ft).

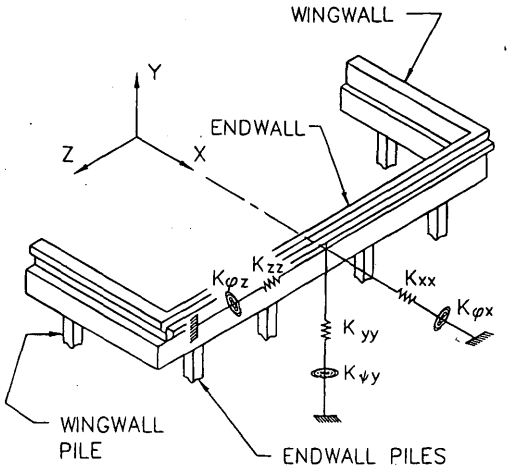

FIGURE 3 Madison County bridge abutment modeled with equivalent rotational and translational springs.

beams and retain little backfill. Each abutment is supported by six embedded piles—four along the endwall and one under each wingwall. The two bent piers are constructed with six driven piles with a portion of the pile free-standing with a cap beam at the top to allow for a bearing surface for the prestressed box beams. The piles at the abutments and bent piers are precast concrete piles 356 × 356 mm (14 × 14 in.) embedded to a depth of 16.8 m (55 ft) at the abutments and approximately 12.2 m (40 ft) at each bent pier. The piles supporting the Haywood County bridge are also friction piles, and for this analysis the piles are considered long and flexible.

SOIL PROPERTIES

No dynamic soil properties were measured at the sites of either bridge; however, geotechnical subsurface investigations were performed at both bridge locations. For the Madison County bridge site, three boreholes were drilled 15.4 m (50.5 ft) deep near the base of the pier and at each of the abutment locations. The log of the test borings indicates that the soil below the bridge is composed mostly of silt or clay terminating in dense sand or stiff clay.

An existing steel and timber bridge structure was removed completely from the site of the Haywood County bridge and replaced with the current concrete structure. The subsurface investigation consisted of two borings that were drilled 50 ft deep at each abutment location. Generally, the borings encountered interbedded layers of silts, sands, and clays with various combinations of the three soil types.

Because no dynamic soil data are available for the sites of the bridges to be modeled, data from research by Chang et al. (*8*) conducted at Memphis State University (now the University of Memphis) on dynamic soil properties for loess deposits are used in this analysis. For purposes of this study, the soil is assumed to be homogeneous along the full length of the pile.

PROPOSED MODEL FOR BRIDGE AND FOUNDATIONS

The bridge analysis program SEISAB was used to conduct response spectrum analysis on both of the aforementioned bridges. The input seismic loading in SEISAB consisted of ATC 3-06 (*9*) response spectra scaled to the maximum ground acceleration at the particular bridge location, adjusted for the prevalent soil conditions. The acceleration scaling factors used were 0.12 and 0.18 for the Madison County and Haywood County bridges, respectively. A damping value of 5 percent of critical damping was assumed for both bridges. ATC 3-06 Soil Type II was used for both bridges. Four seismic loading cases were considered for each bridge. Two cases consisted of ground motion in the longitudinal and transverse directions with respect to the bridge centerline. The other two loading cases consisted of combining 100 percent of the ground motion from one of the first two cases with 30 percent of the ground motion from the other case.

The SEISAB program allows the input of six stiffness values for modeling of the foundation elements: three for translation and three for rotation for both the bridge pier and abutments. The individual spring coefficients are defined in Figure 4 for the pile cap and pile group for the foundation elements of the Madison County bridge model. The elements of the bent pier and abutment foundations to be replaced by spring coefficients for modeling of the Madison County bridge are indicated in Figures 3 and 5 for the abutments and bent piers, respectively. The modeling of the Haywood County bridge foundation elements was similar to that of the Madison County bridge with the exception of the modeling of the bents, which are composed of free-standing piles. Figures 6 and 7 indicate how the foundations for the Haywood County bridge are modeled in this analysis.

In modeling the bridge superstructure, SEISAB "lumps" the combined cross-sectional properties of the girders and deck at the bridge centerline. The spans for both bridges were modeled as being continuous over all interior supports, with pin connections at each bent and abutment (no relative movement between superstructure and supports). Each span of the superstructure was broken into four elements by three nodes along its length, and each column was modeled with two nodes (i.e., three elements) along its height. Figure 8 shows how the model for the Madison County bridge was

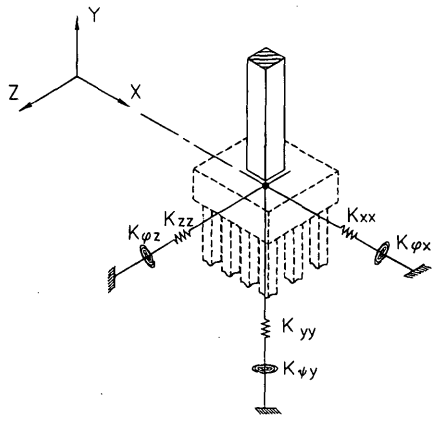

FIGURE 4 Pile group and pile cap equivalent spring model K_{xx} = translational spring along X-axis, $K_{\varphi x}$ = rotational spring about X-axis, K_{zz} = translational spring along Z-axis, $K_{\varphi z}$ = rotational spring about Z-axis, K_{yy} = vertical spring along Y-axis, and $K_{\psi y}$ = torsional spring about Y-axis.

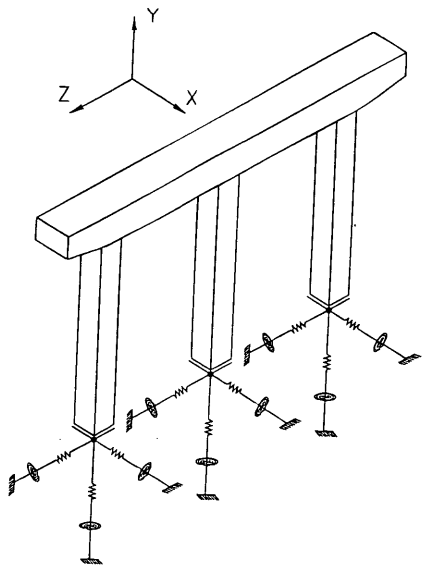

FIGURE 5 Madison County bridge central bent with pile cap and pile group modeled with rotational and translational springs.

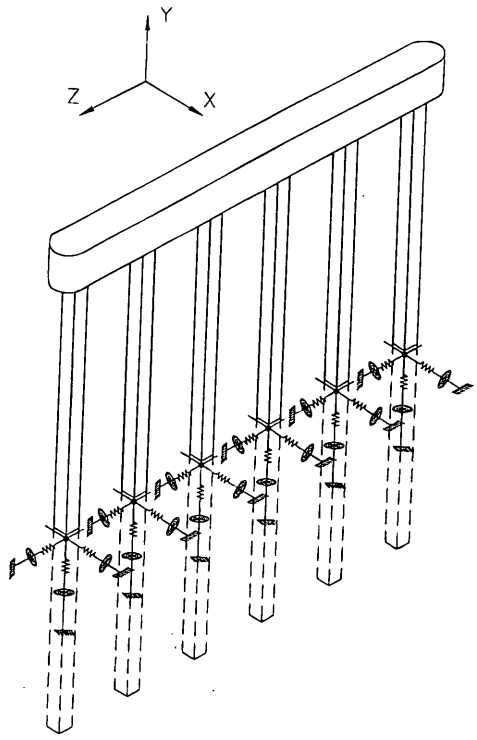

FIGURE 7 Haywood County bridge central bent modeled with rotational and translational springs.

interpreted by SEISAB. The model for the Haywood County bridge was similar to that shown in Figure 8.

DEVELOPMENT OF FOUNDATION SPRING COEFFICIENTS

A detailed account of the application of various methods to determine foundation spring coefficients is presented by Cook (*7*). A condensed description of the methodology is presented here with the note that this paper is not concerned with the precise determination of stiffness but with the effect of variations in stiffness.

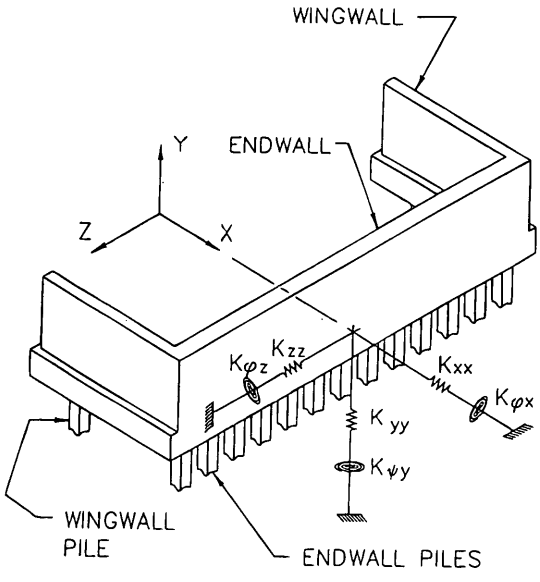

FIGURE 6 Haywood County bridge abutment modeled with equivalent rotational and translational springs.

To estimate values for the foundation spring coefficients, two methods were investigated in considerable detail. A method developed by Novak (*10*) and revised by Novak and El Sharnouby (*11*), based on the theoretical behavior of an embedded pile in an elastic medium, was used to model the stiffness of single piles. The individual spring stiffnesses were combined by methods developed by Poulos (*12,13*) to account for pile group interaction. In addition to the modeling techniques of Novak, a second method was also studied. An approach using beam-on-elastic-foundation analysis was utilized in which the pile is considered to act as a beam on an elastic half-space. The equations used in development of the elastic spring coefficients were derived from methods suggested by Scott (*14*). The individual spring stiffnesses were again combined by methods suggested by Poulos to account for pile group interaction.

The development of elastic spring coefficients to account for the stiffnesses of the abutments was derived from techniques suggested by Wilson (*15*). Wilson's model accounts for the stiffness supplied by both the abutment walls and embedded piles incorporated into elastic spring coefficients. To reduce the amount of data to be generated in this analysis, only the methods suggested by Novak and Wilson were used to model the pile foundations and abutments of the Madison County bridge. The stiffness of the pile cap, modeled as a foundation on an elastic half-space, was added to the stiffness of the pile. The beam-on-elastic-foundation theory, in addition to Wilson's techniques, was used to model the free-standing pile foundations and abutments of the Haywood County bridge. From previous modeling by Cook (*7*), the individual spring coefficients from

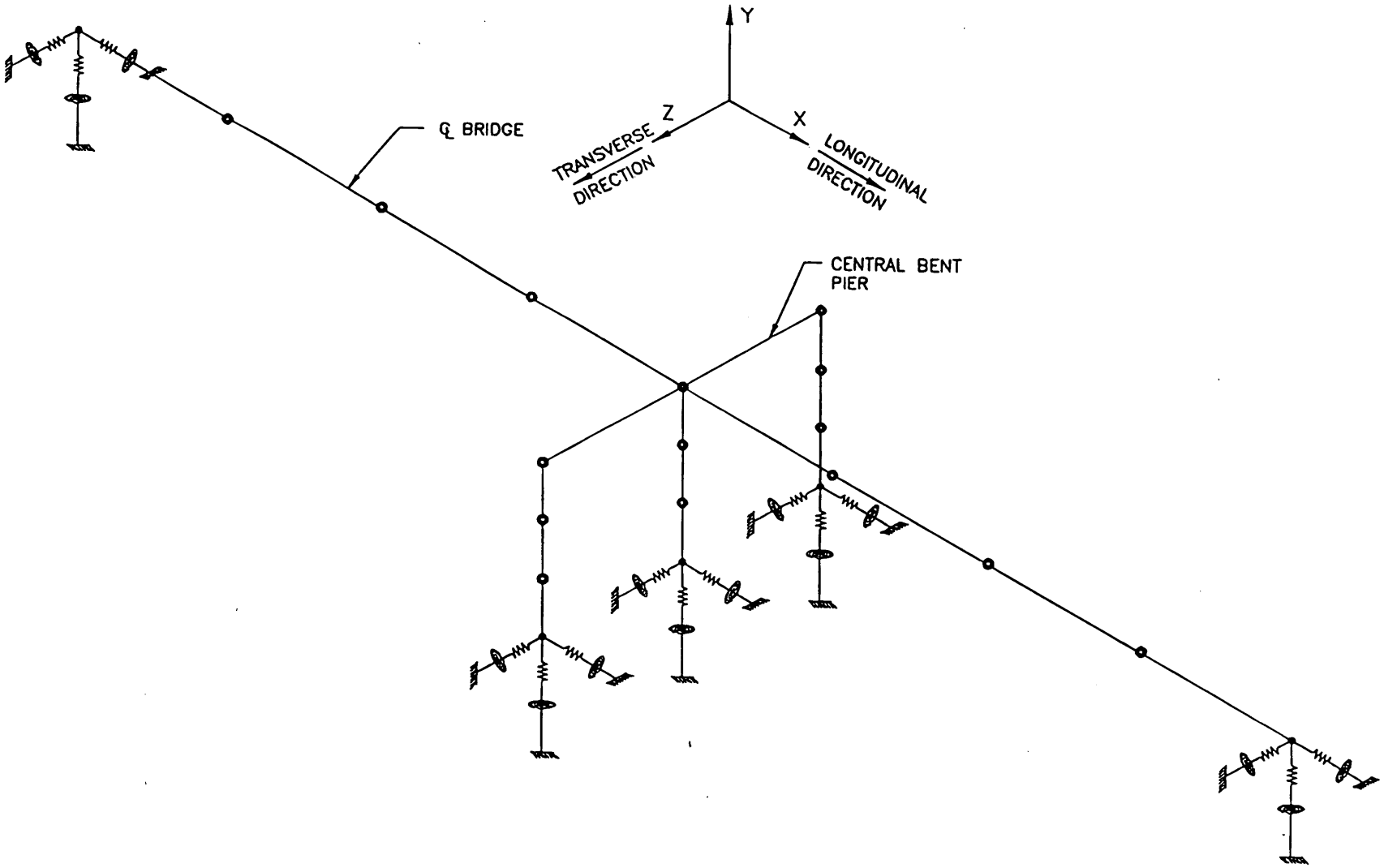

FIGURE 8 Equivalent SEISAB model for Madison County bridge structure.

the beam-on-elastic-foundation theory and Novak's method did not correlate very well, although the response of the model was not significantly affected by the use of one method versus the other.

Because the Madison County bridge is a symmetrical structure (i.e., two equal spans), the model was reanalyzed with one of the span lengths increased by 20 percent. With this model any additional effects on member forces in the substructure caused by unequal span lengths could be investigated.

The spring coefficients used for the Madison County bridge pier are shown in Table 1. These are examples of the coefficients used in the sensitivity analysis that follows.

SENSITIVITY ANALYSIS

In modeling the Madison County bridge, initially all the supports were considered "fixed" (i.e., no translation or rotation of the foundation elements). Spring coefficients were then applied at both the abutments and bent columns. From Figure 9 it is evident that modeling of the foundations with the Novak spring coefficients caused the forces in the bent columns (with the exception of the longitudinal moment) to decrease somewhat as stiffness was taken out of the foundation system. To account for the possibility of variations in the spring stiffnesses, all the spring coefficients were reduced by a factor of 10. Dividing the spring coefficients by a factor of 10 reflects a lack of confidence in the calculated values caused by a limited amount of knowledge concerning the dynamic characteristics of loess. This lack of confidence is somewhat less acute for the abutment foundation springs because the makeup and placement of backfill surrounding the abutments is controlled. For this reason the spring coefficients at the abutments were held constant as the bent column spring coefficients were reduced by a factor of 10. Finally, all spring coefficients at both the bents and abutments were reduced by 10.

The SEISAB program performs a dynamic analysis for loading in both the transverse and longitudinal directions, as well as a combination of loading in both directions simultaneously. In Figures 9 through 12, only absolute maximum moments are plotted without regard to the direction of loading, because these maximum moments are the ones used for design purposes. Figure 13 indicates

TABLE 1 Spring Coefficients for Modeling Central Bent Foundation for Madison County Bridge

DIR. OF MOTION	SINGLE PILE	PILE GROUP	PILE CAP	TOTAL
(K_{xx}) X-DIR. HORIZ. (kN/m)	2.703×10^5	1.229×10^6	4.024×10^5	1.631×10^6
(K_{zz}) Z-DIR. HORIZ. (KN/m)	2.703×10^5	1.127×10^6	4.024×10^6	1.529×10^6
(K_{yy}) Y-DIR. VERTICAL (kN/m)	7.831×10^5	1.973×10^7	3.539×10^5	2.327×10^6
($K_{\phi x}$) ROT. ABT. X-AXIS (kN-m/rad)	9.190×10^5	1.402×10^7	1.014×10^6	1.504×10^7
($K_{\phi z}$) ROT. ABT. Z-AXIS (kN-m/rad)	9.190×10^4	1.818×10^7	1.014×10^6	1.919×10^7
($K_{\phi y}$) TORSION Y-AXIS (kN-m/rad)	3.332×10^4	6.120×10^6	5.225×10^6	1.135×10^7

NOTE: To convert from kN/m to k/ft., multiply by 0.0685.
To convert from kN-m/rad to k-ft./rad, multiply by 0.735.

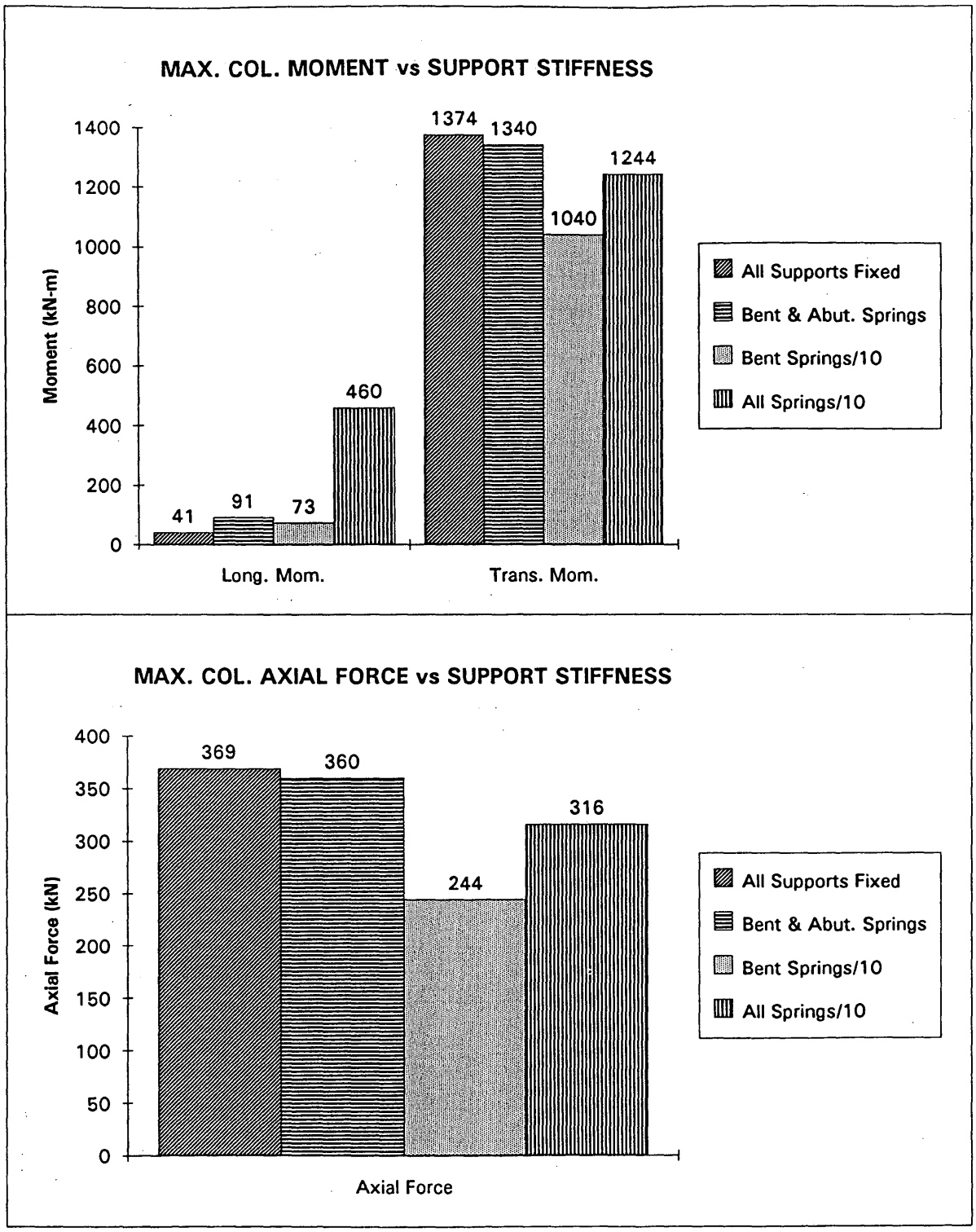

FIGURE 9 Effect of support stiffness on column moments and forces for Madison County bridge with unequal spans (1 kN = 0.225 kip; 1 kN-m = 0.735 kip-ft).

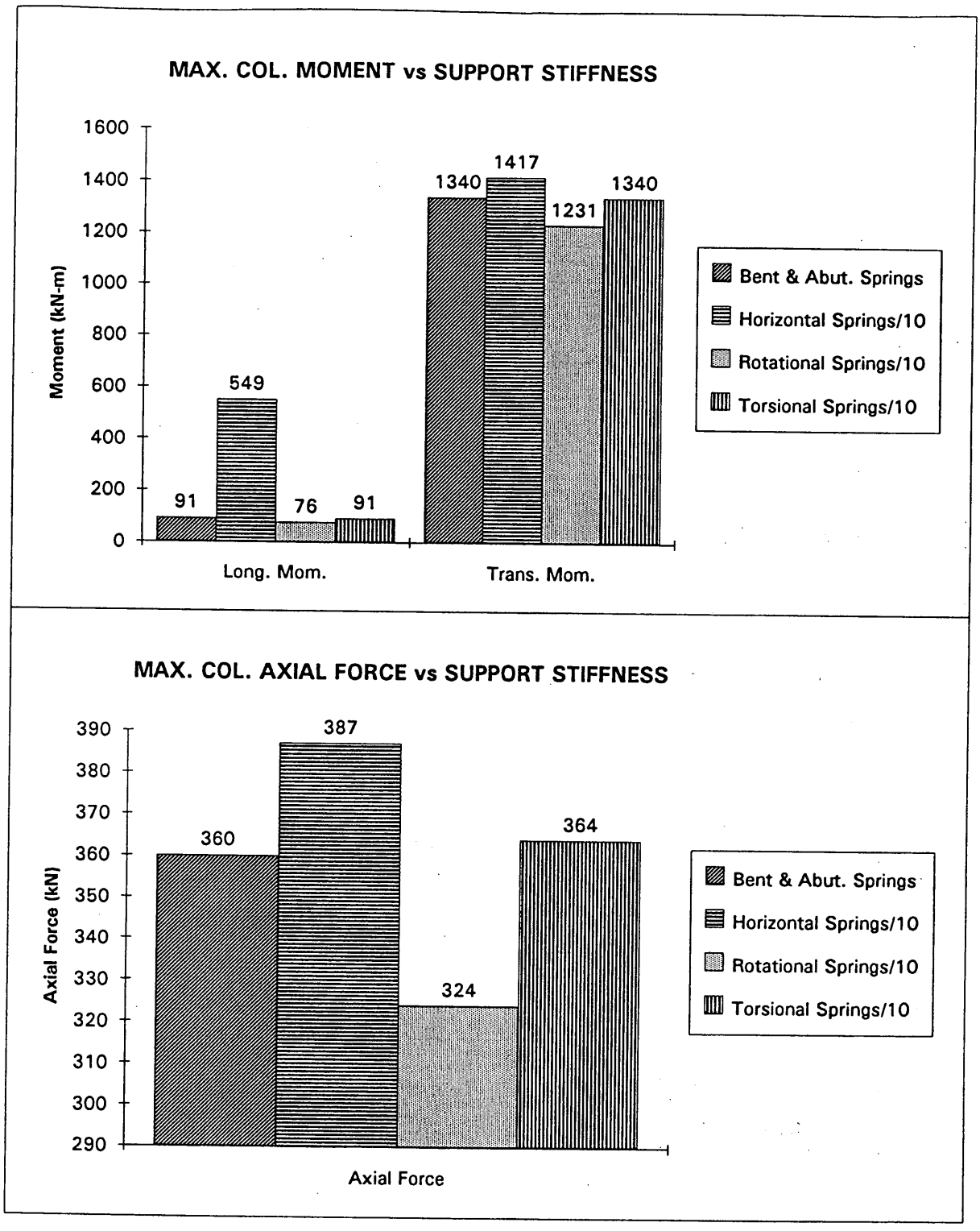

FIGURE 10 Relative effects of variations in horizontal versus rotational and torsional springs for Madison County bridge with unequal spans (1 kN = 0.225 kip; 1 kN-m = 0.735 kip-ft).

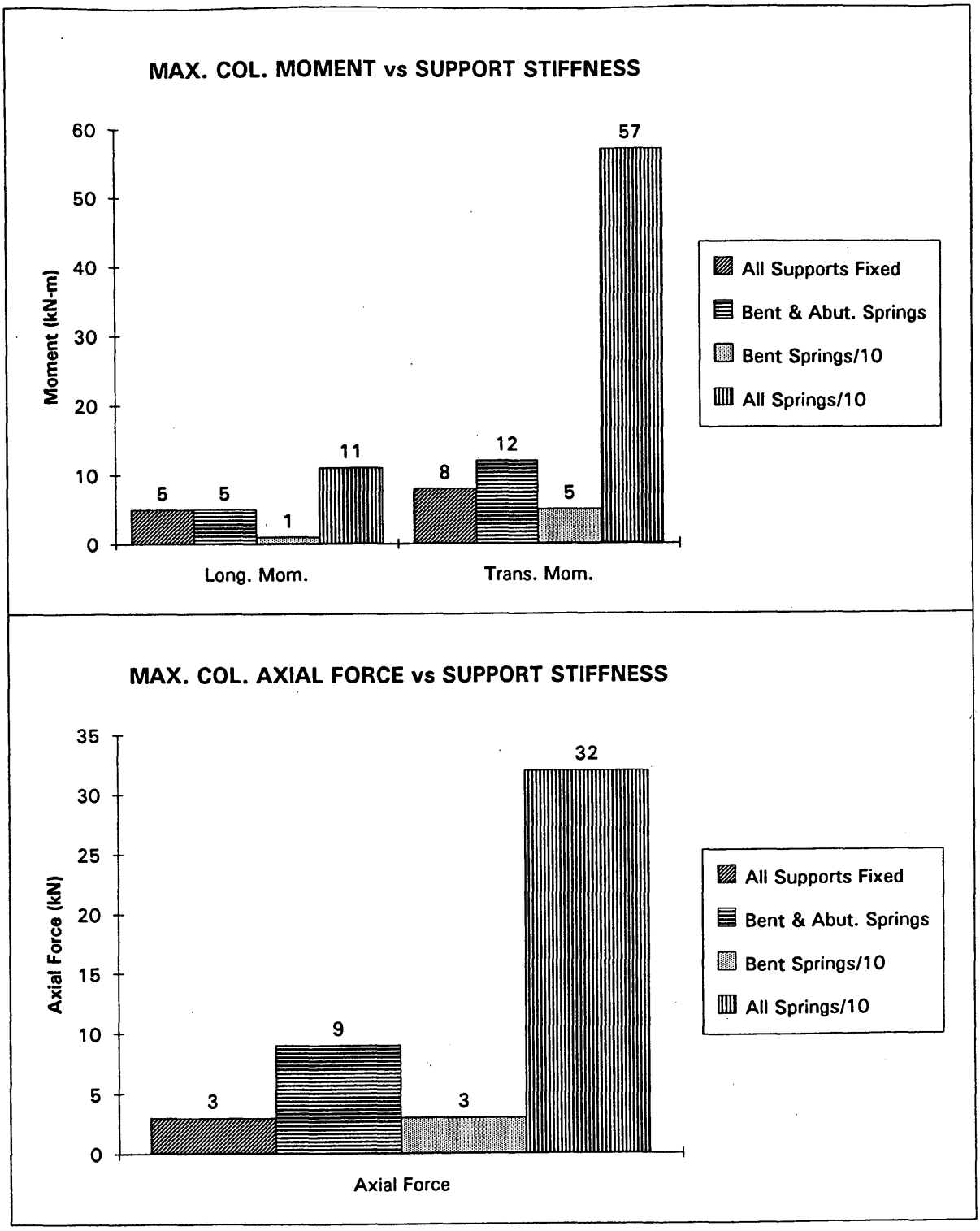

FIGURE 11 Effect of support stiffness on column moments and forces for Haywood County bridge (1 kN = 0.225 kip; 1 kN-m = 0.735 kip-ft).

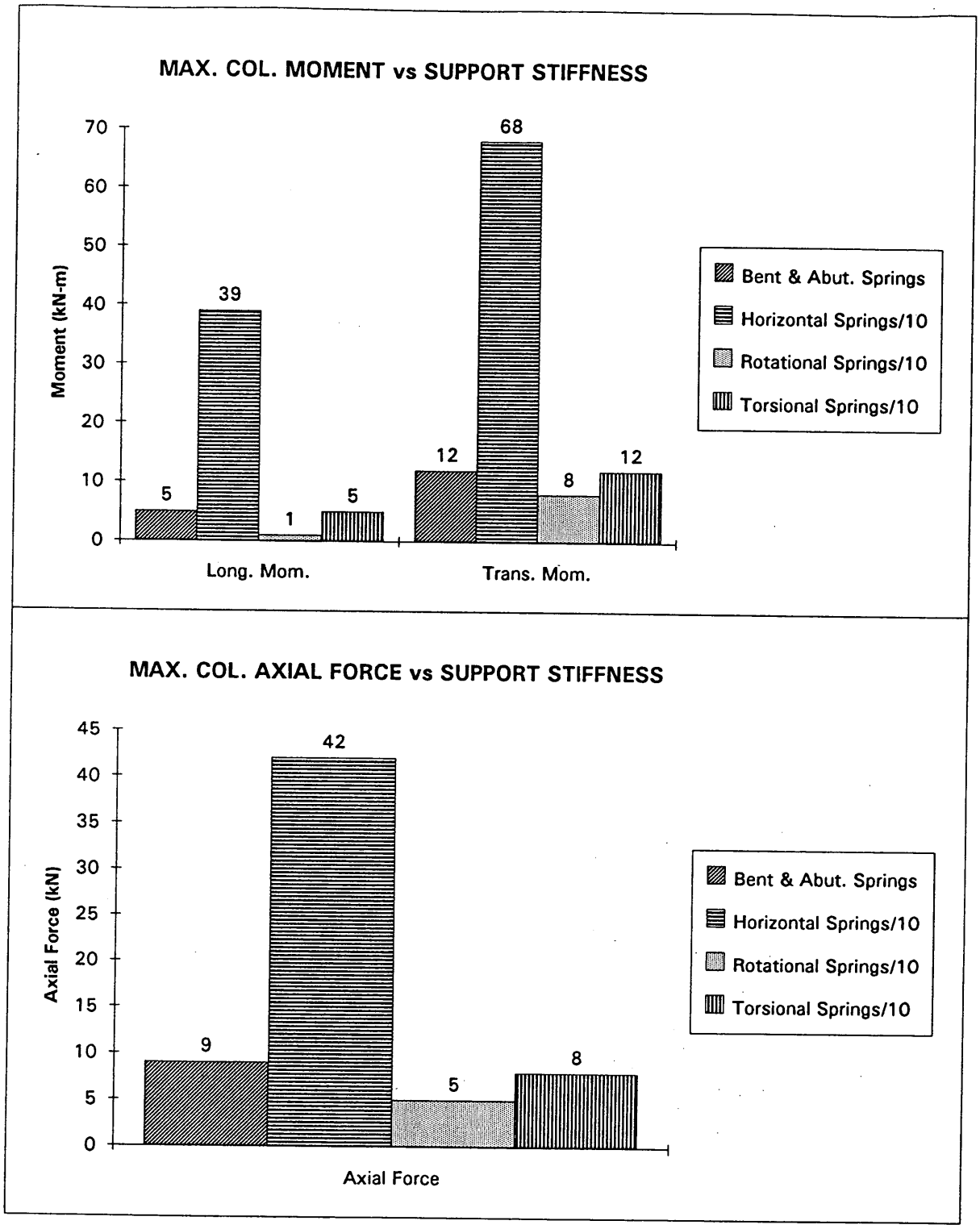

FIGURE 12 Relative effects of variations in horizontal versus rotational and torsional springs for Haywood County bridge (1 kN = 0.225 kip; 1 kN-m = 0.735 kip-ft).

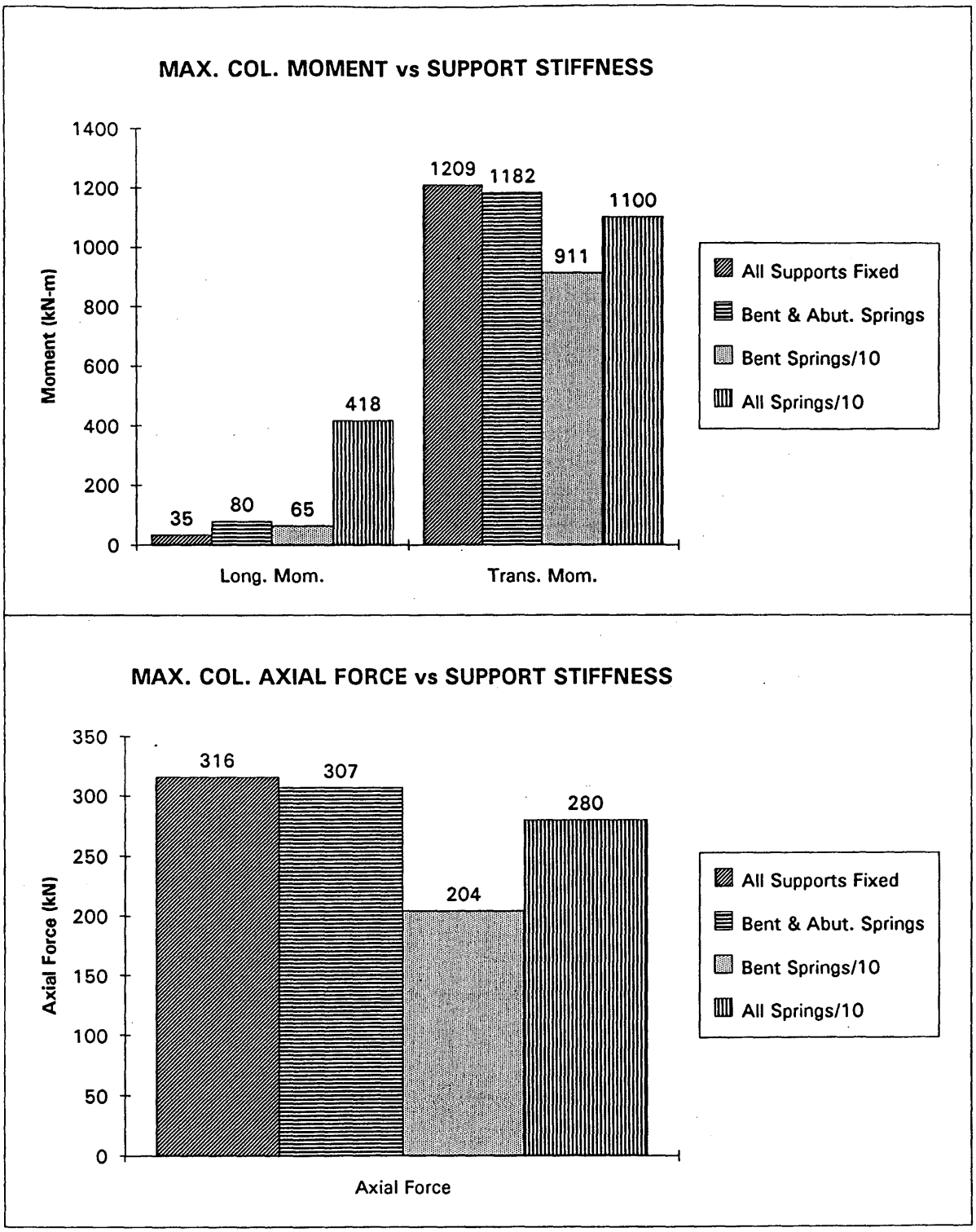

FIGURE 13 Effect of support stiffness on column moments and forces for Madison County bridge with equal spans (1 kN = 0.225 kip; 1 kN-m = 0.735 kip-ft).

that the reduction in all spring coefficients by a factor of 10 caused the transverse and axial forces to decrease somewhat; however, the longitudinal moment increased by a factor of approximately 12 from the case of a "fixed" support condition. This large increase occurred only when the structure was analyzed with loading in the longitudinal direction. As the foundation springs were reduced, the transverse moments in the bent columns were not significantly increased since the short span structure essentially acted as a deep beam laterally and any increase in dynamic effects were probably redistributed to the superstructure. When the structure was analyzed for loading in the longitudinal direction with a reduction in all spring stiffnesses, the central bent pier attracted more moment as stiffness was taken out of the foundations. This increase in column moment was not observed for the case when only the bent springs were reduced and abutment springs were held constant, indicating that the abutment stiffnesses are critical in determining bent column forces for the longitudinal direction.

To investigate the contributions of the lateral stiffness coefficients, the lateral springs were reduced by a factor of 10. From Figure 14, it appears that the most significant terms affecting an overall increase in member forces come from the contributions of the lateral (horizontal) spring coefficients. Thus, it appears that a reduction in the lateral stiffness coefficients can cause significant increases in column forces.

To confirm that the contributions of the rotational and torsional spring coefficients are minimal for both abutments and bent piers, these coefficients were investigated separately. The rotational and torsional spring coefficients were divided by a factor of 10. The torsional spring coefficient is probably the least understood and least investigated component of a pile foundation system. Although an attempt was made in the analysis described earlier to determine a value for the torsional spring coefficient, the results indicated in Figure 10 show that varying magnitudes of the torsional spring coefficient has an insignificant effect on the overall response of the foundation system. The reduction in the rotational spring coefficient from a fixed condition did not produce any increase in member forces. In all cases analyzed the member forces tended to decrease by small amounts as rotational stiffness was reduced in the foundation system.

Figures 9 and 10 reflect the results of the analysis of the unequal span modeling of the Madison County bridge. The same general trends observed in the modeling of the two-span symmetrical structure appear to be evident again. The results of the analysis with reduced lateral, rotational, and torsional stiffness coefficients are shown in Figure 10. These results again confirm that, as the lateral stiffness is reduced, member forces in the bridge substructure are increased. From the plot of the magnitude of the member forces from the reduced rotational and torsional spring coefficients in Figure 10, it is apparent that the changes in column moments and axial forces are minimal. Therefore, for the unequal-span model of the Madison County bridge, the response patterns generally follow those of the two-equal-span model with no significant changes because of geometry.

The Haywood County bridge structure was modeled using the same procedures as those used for the Madison County bridge structure. The bents and abutments were initially held fixed; then spring coefficients were applied at the abutments and bent columns. The bent spring coefficients were reduced by a factor of 10, whereas the abutment spring coefficients were held constant. Finally, all the spring coefficients were reduced by a factor of 10. As was the case for the two-span Madison County bridge structure, the longitudinal moment increased when all spring coefficients were reduced, but only by a factor of approximately 2 from the case of fixed supports, as indicated by Figure 11. The magnitude of increase in column moments for the longitudinal direction is somewhat less for the case of the three-span structure than for the case of the two-span bridge because an additional bent column is available to absorb moment.

The lateral spring coefficients were again reduced by a factor of 10 to study their effect on substructure forces. The results shown on the graphs in Figure 12 indicate that the column forces for the three-span structure were influenced by the variation of spring coefficients in a way similar to that for the two-span Madison County bridge. As the lateral spring coefficients were reduced, a significant increase in the magnitude of both column moments and axial forces was observed.

Rotational and torsional spring coefficients were also investigated for the Haywood County bridge to evaluate their significance to the overall structural response. The results shown in Figure 12 indicate that the magnitudes of the rotational and torsional spring coefficients do not significantly affect the structural response of the model.

SUMMARY AND CONCLUSIONS

No attempt was made in the study reported here to evaluate current methods of calculating foundation stiffness. Instead, the study evaluated the sensitivity of the moments and axial loads in bent columns to variations in foundation stiffness.

From the results of the sensitivity analysis, it appears that the moments and forces in the bent columns are not sensitive to small variations in spring stiffnesses. The effects of creating an unsymmetrical structure by varying a span length were minimal, with results consistent with those for a symmetrical two-span bridge. By reducing the bent spring stiffness and holding the abutment stiffness coefficient values constant, moments and forces in the substructure were somewhat reduced from the case with the bents fixed. But if lower abutment stiffness is assumed to exist concurrently with low bent stiffness, larger moments result in the longitudinal direction. As the lateral spring coefficients were reduced, significant increases in longitudinal, transverse, and axial forces were observed for all three bridge geometries. On the other hand, variations in rotational and torsional stiffnesses appear to be relatively unimportant. Therefore, it appears that, for relatively short-span structures, the forces and moments in the bent columns are most affected by variations in the lateral (horizontal) spring coefficients.

Because of the lack of information on the behavior of single piles and pile groups in loessial soil deposits, further investigation in the form of dynamic field testing is clearly needed to define a more realistic analysis model. Whether or not it is conservative to model a pile foundation simply as being a fixed support depends on the magnitude of the stiffness of the bent and abutment springs. Full-scale testing is also needed to investigate the effect of pile group interaction, especially for loess.

ACKNOWLEDGMENTS

The work that led to this paper was sponsored by TnDOT and FHWA.

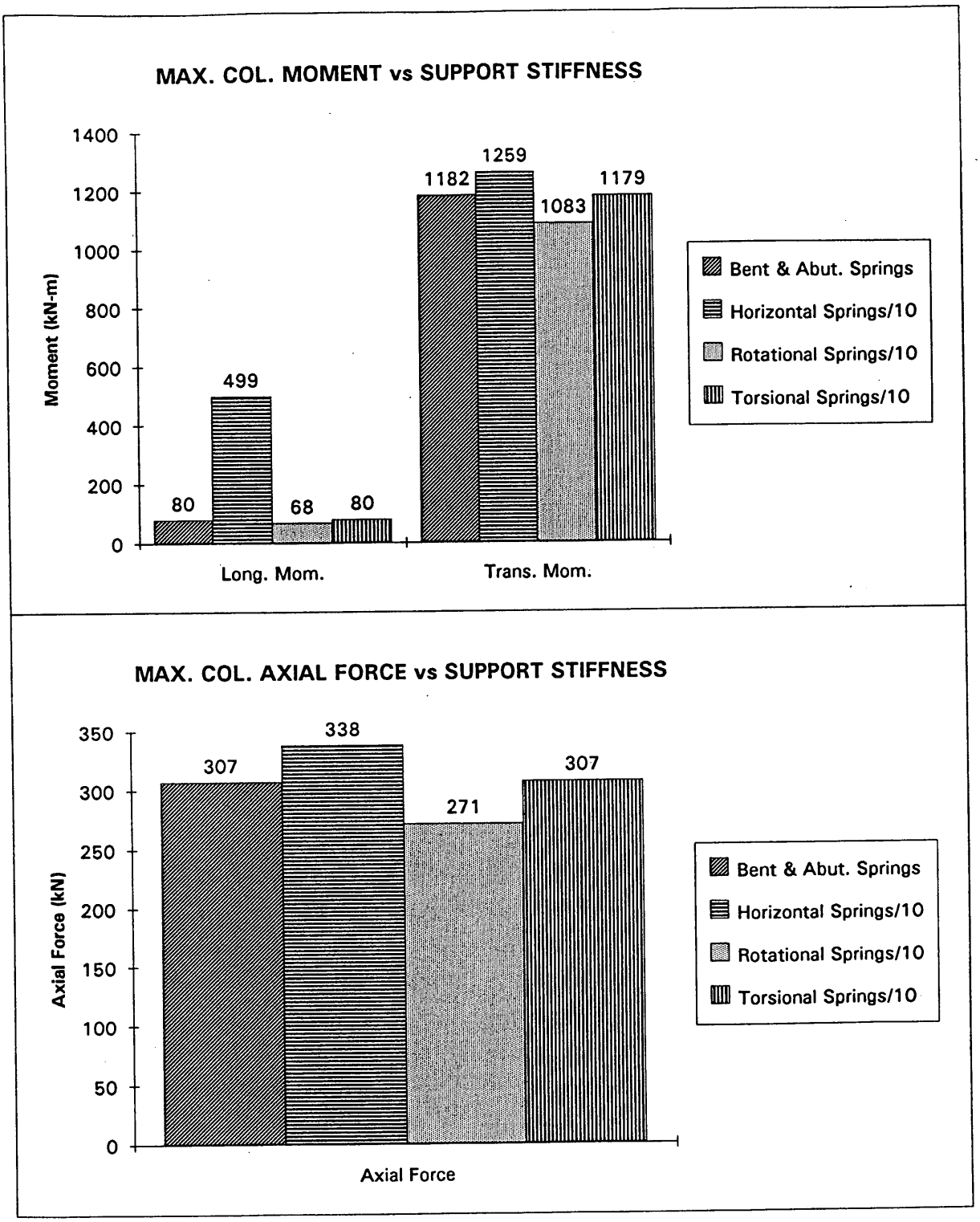

FIGURE 14 Relative effects of variations in horizontal versus rotational and torsional springs for Madison County bridge with equal spans (1 kN = 0.225 kip; 1 kN-m = 0.735 kip-ft).

REFERENCES

1. Brown, D. A., C. Morrison, and L. C. Reese. Lateral Load Behavior of Pile Group In Sand. *Journal of Geotechnical Engineering*, ASCE, Vol. 114, No. 11, Nov. 1988, pp. 1261–1276.
2. Brown, D. A., L. C. Reese, and M. W. O'Neill. Cyclic Lateral Loading of A Large-Scale Pile Group. *Journal of Geotechnical Engineering*, ASCE, Vol. 113, No. 11, Nov. 1987, pp. 1326–1343.
3. Kim, J. B., and R. J., Brungraber. Full-Scale Lateral Load Tests of Pile Groups. *Journal of the Geotechnical Engineering Division*, ASCE, Vol. 102, No. GT1, Jan. 1976, pp. 87–105.
4. Kim, J. B., L. P. Singh, and R. J. Brungraber. Pile Cap Soil Interaction From Full-Scale Lateral Load Tests. *Journal of the Geotechnical Engineering Division*, ASCE, Vol. 105, No. GT5, May 1979, pp. 643–653.
5. Douglas, B. M., and G. M. Norris. Bridge Dynamic Tests: Implications For Seismic Design. *Journal of Technical Topics in Civil Engineering*, ASCE, Vol. 109, No. 1, April 1983, pp. 1–22.
6. *SEISAB, Computer Code for Seismic Analysis of Bridge Structures.* Version 4.0. Imbsen and Associates, Inc., Sacramento, Calif.
7. Cook, T. L. *Modeling of Soil-Pile Interaction For Bridge Foundations Under Seismic Loading.* M.S. thesis, University of Tennessee, Knoxville, 1994.
8. Chang, T.-S., L. K. Teh, and Z. Yigong. *Seismic Characteristics of Sediments in the New Madrid Seismic Zone.* Memphis State University, Memphis, Tenn., Feb. 1992.
9. *ATC Publication ATC 3-06, NBS Special Publication 510, and NSF Publication 78-8*, Applied Technology Council, Associated with the Structural Engineers Association of California, June 1978.
10. Novak, M. Dynamic Stiffness and Damping of Piles. *Canadian Geotechnical Journal*, Vol. 2, 1974, pp. 574–598.
11. Novak, M., and B. El Sharnouby. Stiffness Constants of Single Piles. *Journal of Geotechnical Engineering*, ASCE, Vol. 109, No. 7, July 1983, pp. 961–974.
12. Poulos, H. G. Analysis of the Settlement of the Pile Groups. *Geotechnique*, Vol. 18, No. 4, 1968, pp. 449–471.
13. Poulos, H. G. Behavior of Laterally Loaded Piles: II—Pile Groups. *Journal of the Soil Mechanics and Foundations Division*, ASCE, Vol. 97, No. SM5, May 1971, pp. 733–751.
14. Scott, R. F. *Foundation Analysis.* Prentice-Hall, Englewood Cliffs, N.J., 1981.
15. Wilson, J. C., Stiffness of Non-Skew Monolithic Bridge Abutments for Seismic Analysis. *Earthquake Engineering and Structural Dynamics*, Vol. 16, Jan. 1988, pp. 867–883.

The opinions and conclusions expressed herein are those of the authors and not necessarily those of TnDOT or FHWA.

Publication of this paper sponsored by Committee on Dynamics and Field Testing of Bridges.

Guide Specification Strength Capacity Rating of Existing Girder Bridges

MICHAEL G. BARKER

The impact of the AASHTO Guide Specifications for Strength Evaluation of Steel and Concrete Bridges (STRENGTH method) on 40 steel and 33 concrete bridges in Missouri was investigated. The STRENGTH method is a reliability-based load and resistance factor rating procedure. The variable factors depend on levels of redundancy, deterioration, inspection, maintenance, truck volume, and weight enforcement, and selection of these factors is subjective, requiring considerable engineering judgment. The STRENGTH method considers site-specific loading and capacity characteristics to obtain consistent levels of safety over the bridge inventory. For bridges with good load and resistance characteristics, the STRENGTH method can significantly increase load ratings over current AASHTO load factor rating operating levels. However, deterioration and adverse traffic conditions can cause STRENGTH ratings to fall below load factor rating inventory levels. A method to evaluate the load capacity of concrete bridges that do not have detailed bridge plans is also investigated.

In the United States, federal law (*1*) requires that all bridges be evaluated periodically. The inspection process shall include a physical investigation of the bridge to ascertain the bridge's overall safety and operational characteristics and shall include a bridge load-carrying capacity evaluation (bridge rating). The governing authority over bridge inspections and load ratings is AASHTO. AASHTO's Manual for Maintenance Inspection of Bridges (*2*) (referred to as the maintenance manual) is used for guidance in the evaluation process and the current AASHTO Standard Specifications for Highway Bridges (*3*) (referred to as the design specs) is also used in conjunction with the maintenance manual. Although not used in this paper, there is also the new Manual for Condition Evaluation of Bridges, recently approved by AASHTO (*4*).

The process of bridge evaluation consists of two important operations: inspection and rating. Bridge inspection determines the actual condition of the bridge based on field inspection and field measurements. Results of the current inspection are compared with those of previous records to determine whether there are changes in the bridge condition. If there are substantial changes, or trends of deterioration are verified, then the load capacity is evaluated (bridge rating) for the new conditions.

Bridge rating is concerned with two major issues:

1. What vehicle, or group of vehicles, should be used for the load capacity evaluation?
2. How should the capacity of the bridge be evaluated?

Bridge rating is a mathematical exercise by which the strength of the bridge is evaluated. The specific outcome of the analysis is the rating factor (RF). The RF is the ratio of the calculated live load capacity of the bridge to the rating vehicle live load effects. Typically, the AASHTO rating vehicles, or state specific vehicles, are used to approximate the live load effects. The RF multiplied by the rating truck weight is the rating load. If RF is less than unity, then the bridge is judged to be deficient and some type of action is called for such as

1. Posting (reduce live load and/or speed),
2. Retrofitting the bridge,
3. Replacing the bridge, or
4. Closing bridge to traffic.

For most bridges, only a flexural capacity rating check is performed. However, there may be situations when a shear or bearing capacity check is warranted. Examples of these situations would be in deteriorated members with significant section loss and for older bridges. Also, fatigue rating (*5*) may be required in members with known high service load stresses. One important feature of the rating process is to subject the mathematical conclusions to the judgment of experienced bridge engineers.

With regard to structural analysis and load capacity limit states, as of 1994 there were three AASHTO methods for rating beam and girder bridges:

1. Allowable stress rating (ASR). For the ASR method, the nominal live loads on the structure and all other nominal loads shall not produce stresses in the member that exceed allowable stresses (*2*).
2. Load factor rating (LFR). For the LFR method, the criteria are that factored live loads and factored other loads must not exceed the (factored for concrete) nominal strength of the member (*2*).
3. Guide Specifications for the Strength Evaluation of Existing Steel and Concrete Bridges (STRENGTH method). The STRENGTH method is a load and resistance factor method using variable site-specific factors. Factored live loads and factored other loads must not exceed the factored member capacity (*6*).

There are also field testing rating methods where diagnostic or proof loads are physically applied to the bridge (*7*).

All three of these analytical rating methods use the maintenance manual as a guide for bridge inspection. The ASR and LFR methods are also contained in the maintenance manual. The STRENGTH method is similar to the LFR method; however, the load, resistance, and impact factors are variable and depend on site-specific characteristics. The nominal capacity is the same as the LFR maximum-strength capacity and both methods use the same level of structural usefulness (i.e., flexural hinge).

The ASR and LFR methods are direct extensions of their respective design procedures. In design, additional uncertainty needs to be incorporated in the process to meet the desired safety. Over the long design life, conservatism is warranted for changes in traffic volume and loads, deterioration, and material variabilities. Evaluating an

Department of Civil Engineering, E2509 EBE, University of Missouri-Columbia, Columbia, Mo. 65211.

existing bridge over short intervals removes many of the uncertainties inherent in the design process. When load rating an existing bridge, the uncertainty associated with the truck volume and expected weights, the level and rate of deterioration, and the as-built geometry and material properties are lower than at the design stage.

The truck volume and expected weights on individual bridges will have a large impact on the demands of the structure. For instance, a rural bridge with five trucks a day demands much less from a structure than an interstate bridge with 10,000 trucks a day. Likewise, a bridge with a 10 percent per year deterioration rate is of more concern than a bridge with virtually no deterioration rate. The ASR and LFR methods fail to fully consider these site characteristics. The methods will rate a high-volume severely deteriorating bridge and a low-volume bridge not deteriorating equally. Ignoring the differences in particular bridges leads to inconsistent safety.

An NCHRP project (*8*) was initiated in 1980 with the objective of developing improved techniques for evaluating the load-carrying capacity of reinforced concrete bridges. Another NCHRP project (*9*) was initiated in 1985 to extend and finalize the findings of NCHRP Project 10-15 (*8*) for reinforced concrete, prestressed concrete, and steel bridges. The researchers' goal was to produce "a flexible comprehensive approach to bridge evaluation that best utilizes the economic resources available and yet maintains consistent and definable criteria for ridge safety." To achieve this, a reliability framework was adopted that allowed a range of load and resistance factors (partial load factors) depending on site-specific bridge characteristics and the level of effort in the rating process. The STRENGTH method (*6*) is based on these two NCHRP projects.

The STRENGTH method yields only one rating factor corresponding to a strength limit state, whereas the LFR method has an operating rating and an inventory rating for both a maximum-strength capacity and a serviceability capacity. Ignoring serviceability limits (not including fatigue limits) for existing bridges is justified in the STRENGTH method by the fact that these bridges have survived these serviceability demands in the past.

OBJECTIVES

The AASHTO guide specs STRENGTH method (*6*) was released in 1989. However, not much is known on how the new procedures will affect the rating process. Barker et al. (*10*) investigated and compared the LFR method and the STRENGTH method with 73 steel and concrete girder bridges typical of state and rural bridges in Missouri. The study emphasized the impact of the STRENGTH method and the procedural changes from the LFR method.

This paper presents the following:

1. Comparisons of the STRENGTH method to the LFR maximum-strength operating and LFR serviceability operating ratings for 40 steel girder bridges,
2. Comparisons of the STRENGTH method to the LFR maximum-strength operating rating for 33 concrete girder bridges, and
3. An historically based method to evaluate concrete bridges with insufficient or nonexistent plans.

LOAD CAPACITY RATING EQUATION

For the LFR maximum-strength operating level and the STRENGTH method, the general load capacity rating equation is

$$\Gamma_D D_n + (RF)\Gamma_L L_n(DF)(1 + I) \leq \Phi M_n \tag{1}$$

or, solving for the rating factor,

$$RF = \frac{\Phi M_n - \Gamma_D D_n}{\Gamma_L L_n(DF)(1 + I)} \tag{2}$$

where

RF = rating factor (RF $\geq$ 1 is sufficient capacity),
Γ_D = dead load factor,
Γ_L = live load factor,
Φ = resistance factor,
M_n = nominal resistance,
D_n = nominal dead load,
L_n = nominal live load from the rating vehicle,
DF = lateral distribution factor, and
I = impact factor.

The nominal live loads are the same for both procedures. The lateral distribution factors of these loads is also identical except the STRENGTH method adjusts the factor if a method other than the AASHTO design specs S/D method is used. The nominal dead load is the same except that the STRENGTH method increases the nominal overlay thickness by 20 percent as a result of excessive uncertainty in overlay thickness estimations. The nominal resistance should consider the effects of deterioration with a reduced section analysis.

The major difference between the two methods is in the load and resistance factors and the impact factor as shown in Table 1. The STRENGTH method uses variable load, resistance, and impact factors, and the rating engineer must choose the values on the basis of site-specific information. To obtain consistent ratings, the use of engineering judgment is critical for selecting these subjective factors.

The LFR method also has a serviceability limit (excluding fatigue) for the operating level. For steel bridges the equation is

$$RF = \frac{M_s - D_n}{L_n(DF)(1 + I)} \tag{3}$$

The limit is basically a limited stress at service or nominal loads where M_s is the serviceability strength corresponding to the operating level and the other variables are defined above. The STRENGTH method has no such serviceability limit.

The LFR inventory ratings are 60 percent of the LFR operating ratings. This is simply the ratio of the operating and inventory live load factors (1.3/2.17) from Table 1.

STRENGTH METHOD LOAD AND RESISTANCE FACTORS

The following are general guidelines (*6,10*) for determining the factors for the STRENGTH method. For a more detailed explanation, and for variances to the conditions that follow, the reader is referred to the guide specs (*6*).

Dead and Live Load Factors

The dead load factor is a constant 1.2. However, the live load factor ranges from 1.30 to 1.80. A factor of 1.30 (same as LFR operat-

TABLE 1 Load and Resistance Factors

Factor	LFR	STRENGTH
Γ_D	1.30	1.20 plus 20% additional thickness on the wearing surface
Γ_L	1.30 Operating 2.17 Inventory	1.30 low volume and enforced weight limits 1.45 high volume and enforced weight limits 1.65 low volume and unenforced weight limits 1.80 high volume and unenforced weight limts
Φ	1.00 steel 0.90 concrete	0.55-0.95 based on redundancy, deterioration, inspection, and maintenance
I	50/(L+125)≤0.3 based on span length	0.10 smooth deck 0.20 significant deck roughness 0.30 major deficiency in riding surface

ing) represents a low-volume bridge with good weight enforcement. As the volume increases or enforcement decreases, or both, the live load factor increases. The volume is deterministic, but the level of enforcement is subjective. The rule that the site is considered enforced if less than 5 percent of the trucks exceed legal limits can be used if this information is available and dependable. Of course the rating agency could be conservative and categorically assume insufficient enforcement; however, this would defeat the objective of having uniform safety over the bridge inventory.

Impact Factor

The impact factor depends on the riding surface roughness. The dynamic effects range from 0.10 for smooth surfaces to 0.30 for surfaces with serious deficiencies. Inspection procedures will need to be developed and a new appraisal rating will need to be incorporated into the inspection program to determine this subjective factor. The deck appraisal did not correlate well with the perceived dynamic effects for the bridges used in this study. The engineer should consider the design specs impact factor when choosing from the STRENGTH method options. Perhaps for shorter bridges, 0.20 should be used unless there are serious deficiencies. For longer bridges with smooth conditions, a value of 0.10 could be justified.

Resistance Factor

The resistance factor has a large impact on the load rating because it can vary from 0.55 to 0.95. The basic resistance factor for a member in good condition (0.95 for steel and 0.90 for concrete) is significantly decreased if there is deterioration. If there is deterioration, the resistance factor can be increased if a careful inspection is executed and either increased or decreased, depending on whether maintenance will inhibit future section losses or deterioration is uninhibited, respectively. Although the resistance factor is subjective, there seems to be adequate information to determine the adjustments for deterioration and inspection effort (*10*).

ASSUMPTIONS USED FOR BRIDGE DATA BASE

This study used a uniform set of assumptions for determining the live load, resistance, and impact factors for the STRENGTH method. For the live load factor, all sites were assumed enforced. This was done because a high percentage of the bridges should have less than 5 percent of the trucks exceeding legal limits. However, for posted bridges this may not be true. There would be a tendency for bridges with restrictive loading to have a higher percentage of weight violators. Future studies are needed to examine weight characteristics on posted bridges. If the sites are unenforced, the STRENGTH ratings would decrease by approximately 20 percent from the ratings assuming enforced conditions.

The resistance and impact factors were chosen conservatively. Deck and superstructure appraisal ratings from inspection reports were used to determine the level of deterioration according to the STRENGTH method guidelines. The resistance factor was also decreased for intermittent maintenance, and it was assumed that there was not a careful inspection. The impact factor was based on the deck appraisal rating. Thus, the majority of the STRENGTH ratings reported herein could be increased significantly (upwards of 10 percent) with a careful inspection adjustment and a vigorous maintenance adjustment.

BRIDGE DATA BASE

This paper compares the LFR method and the STRENGTH method for 73 bridges typical of state and rural girder bridges in Missouri. Of the 40 steel girder bridges examined, 10 are simple-span composite (SC), 5 are continuous-span composite (CC), 20 are simple span noncomposite (SNC), and 5 are continuous span noncomposite (CNC). Of the sections checked for the capacity ratings for both the composite and noncomposite bridges, there is a mix of compact, noncompact, braced, and unbraced sections. The dates the bridges were built range from 1932 to 1968.

Of the 40 steel girder bridges, two have high truck volume (Γ_L = 1.45), and the remaining 38 have low truck volume (Γ_L = 1.30). Six of the bridges have slight deterioration (Φ = 0.80), whereas the rest have insignificant section loss (Φ = 0.90). Three of the bridges have lower deck appraisal ratings, which resulted in an impact factor of 0.20, whereas the remaining bridges have high deck appraisal ratings, which resulted in an impact factor of 0.10.

The 33 concrete girder (T-beam) bridges analyzed for comparison in this study are typical state bridges built between 1922 and 1961. Of the 33, five of the bridge plans have general member dimensions but do not have reinforcement details. This is a problem with many concrete bridges across the nation. However, as will be

discussed, a method to estimate the reinforcement details on the basis of limited historical data was used to determine the load capacities. This method, with future verification and refinement, could be an asset for rating concrete bridges that have no plans.

Of the 33 concrete girder bridges, 30 have low truck volume ($\Gamma_L = 1.30$) and three have high truck volume ($\Gamma_L = 1.45$). Whereas all the steel bridges in this study have good or fair structural appraisal ratings, 8 of the concrete bridges have superstructure conditions of good or fair ($\Phi = 0.85$), 16 are classified deteriorated ($\Phi = 0.75$), and 9 are heavily deteriorated ($\Phi = 0.65$). Deterioration significantly reduces the STRENGTH rating as evidenced by the wide range of the resistance factors. The concrete bridge impact factors are distributed as follows: 25 have impact factors of 0.10, 5 have impact factors of 0.20, and 4 have impact factors of 0.30 (major deficiency in the riding surface).

IMPACT OF THE STRENGTH METHOD

Table 2 shows the average rating factors for controlling vehicles and controlling spans for the steel and concrete bridges. For the steel data base, the STRENGTH method average ratings (1.33) were significantly greater than the LFR operating levels considering serviceability limits (1.19). However, when considering only the maximum-strength LFR limit, the average ratings were nearly identical (1.33 STRENGTH and 1.34 LFR). When serviceability controls, the LFR rating is lowered from what the maximum-strength limit ratings dictate and, therefore, the difference between the STRENGTH and LFR methods increases.

This difference is illustrated in Figures 1 and 2. In these figures, the ratio of the STRENGTH RF to the LFR operating RF is plotted against the controlling span length. In Figure 1, the ratio varies considerably because of the serviceability limit. All the points above the dashed line, and the two points indicated below this line, had serviceability controlling the LFR rating. It is clear that large increases in the rating could be realized if the rating agency switches from LFR serviceability limits to the STRENGTH method limits, especially for SC bridges. This would be in agreement with the STRENGTH method philosophy that these bridges have survived these serviceability demands in the past. However, if the LFR method ignores serviceability limits and uses only maximum strength limits, the ratio is much more uniform, as shown in Figure 2. Here all the points are uniform except when one or more of the factors change.

In Figure 2, the majority of the RF ratios are between 1.0 and 1.1. These points correspond to a low-volume roadway with good weight enforcement ($\Gamma_L = 1.30$), a good riding surface ($I = 0.10$), and members in good shape ($\Phi = 0.90$). As the load factors increase or the resistance factor decreases, the STRENGTH ratings will decrease and, thus, give a relatively lower rating compared with the LFR method. In summary, the STRENGTH ratings are, on average, approximately equal to or above the average LFR operating ratings.

This is not the case for the concrete bridges. For the concrete bridges shown in Table 2, the STRENGTH method average ratings (1.06) were well below the LFR operating level maximum-strength ratings (1.30). In fact, they were about midway between the LFR operating and the LFR inventory levels (0.78). This means that the STRENGTH method would require more restrictions on the concrete bridges of this data base relative to those imposed on the steel bridges.

In Figure 3, the ratio of the STRENGTH RF to the LFR operating RF is plotted against the controlling span length. There are three distinct regions that correspond to the Φ factor or the level of deterioration. With heavier deterioration, the STRENGTH method will give a low rating compared with the LFR method. Variations in the other factors affect the ratio to a lesser extent. Examination of the STRENGTH method resistance factors, live load factors, and impact factors reveals why the concrete bridges did so much more poorly than the steel bridges when LFR ratings were compared.

The concrete data base had an average resistance factor of 0.75, whereas the average was 0.89 for the steel bridges. This difference greatly exceeds the 0.05 difference for steel and concrete members in good condition. The disparity occurred because the concrete bridges had consistently lower structural appraisal ratings. Visual inspection of the bridges, however, showed no apparent condition differences. Because the STRENGTH method considers deterioration in the rating process and because of the subjective factors, an important aspect of the STRENGTH method is the inspection. This apparent discrepancy between steel and concrete bridge inspection appraisals will hinder the consistency of the STRENGTH ratings.

For example, four of the concrete bridges have structural appraisal ratings of 3. According to the inspection, these bridges

TABLE 2 Rating Factors for the 73-Bridge Data Base

RATING METHOD	STEEL BRIDGES		CONCRETE BRIDGES	
	AVG	RANGE	AVG	RANGE
Guide Spec STRENGTH Rating	1.33	0.58-3.77	1.06	0.26-2.23
LFR Operating Max. Strength & Serviceability Rating	1.19	0.63-2.99	NA	NA
LFR Operating Maximum Strength Only	1.34	0.63-3.98	1.30	0.78-2.68
LFR Inventory Max. Strength & Serviceability Rating	0.71	0.38-1.79	NA	NA
LFR Inventory Maximum Strength Only	0.81	0.38-2.39	0.78	0.47-1.61

Serviceability not Considered for Concrete Bridges

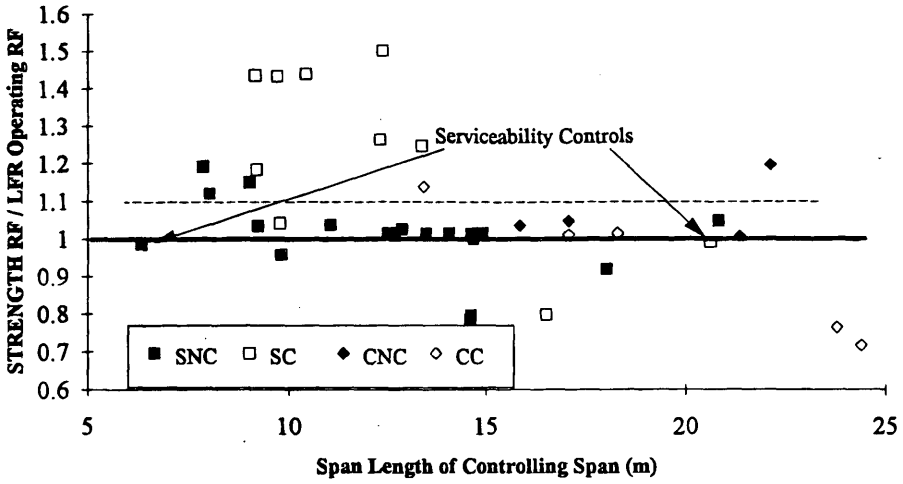

FIGURE 1 Ratio of STRENGTH and LFR operating maximum strength and serviceability rating factors for steel bridges.

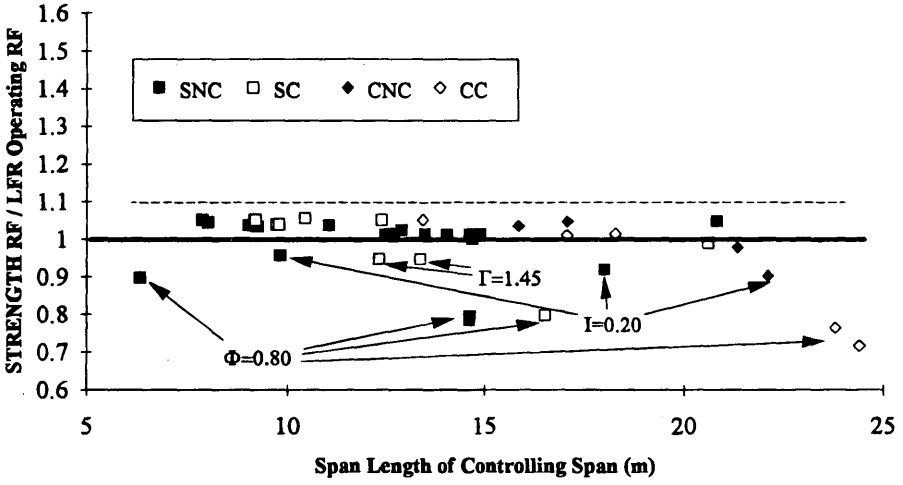

FIGURE 2 Ratio of STRENGTH and LFR operating maximum strength rating factors for steel bridges.

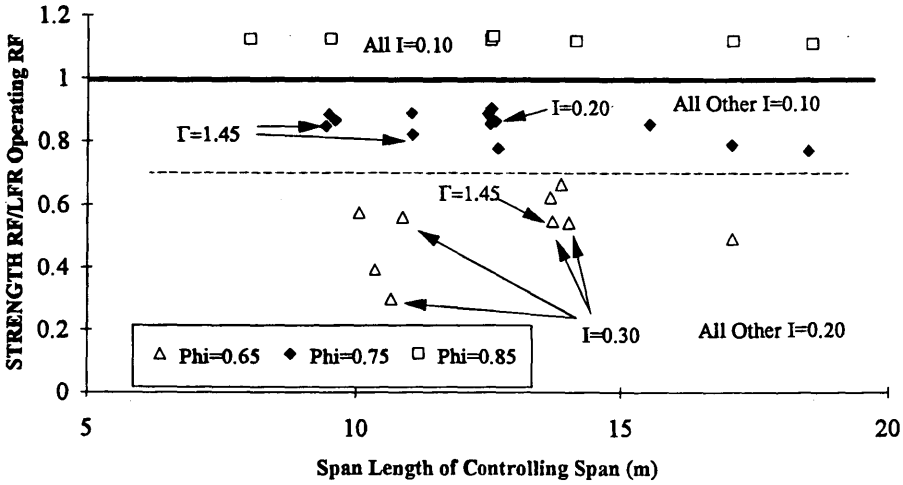

FIGURE 3 Ratio of STRENGTH and LFR operating maximum strength rating factors for concrete bridges.

are in serious condition. A superstructure appraisal of 3 means the following (*11*):

> Serious Condition: Loss of steel section, deterioration, or spalling has seriously affected primary structural components. Repair or rehabilitation required as soon as possible. Damage or disintegration of a structural support element which requires shoring, auxiliary splices, or substitute members. Severe disintegration of concrete. Diagonal shear cracks. Wide flexural cracks. Delamination from primary steel.

If these concrete bridges are truly in the shape that the appraisal ratings indicate, then the LFR method is not adequately representing the condition of the bridge or the seriousness of the deterioration. The LFR method would give nearly the same ratings to these seriously deteriorated bridges and a new bridge. However, the STRENGTH method reduces the load-carrying capacity to reflect the heavy deterioration.

The average live load factor for the concrete bridges is 1.314, and the average is 1.307 for the steel bridges. Therefore, the live load factor did not cause much difference between the steel and concrete data bases. However, the average impact factor for the concrete bridges is 0.14, whereas the average for the steel bridges is 0.108. This factor has a direct effect on the ratings and the relative differences between the steel and concrete bridges.

CONCRETE BRIDGES WITH INSUFFICIENT PLAN DETAILS

An ongoing problem for many states is how to estimate the load-carrying capacity of concrete bridges that lack reinforcement details. One solution is to field test the bridge with applied diagnostic or proof loading (*7*). However, if load testing is not feasible, the maintenance manual states that a bridge that shows no signs of distress need not be posted. This clearly is not acceptable in many situations. There is no definitive definition of distress and, if there is distress, there are no guidelines for posting limits. There are also no permitting guidelines should the situation arise.

There is a need for a more consistent strategy for making rational estimations of the load-carrying capacity for these bridges. The information required to calculate the section capacity is the structural depth (d), the area of steel, represented by the reinforcement ratio (ρ), and the concrete strength, (f'_c), which can be estimated with respect to age in the maintenance manual. Following is a method based on historical data from existing concrete bridges with known reinforcement configurations (*10*). Figure 4 plots the normalized depth against the age for the 28 concrete bridges in the data base that had full plans including reinforcement details. The normalized depth is simply the structural depth divided by the overall depth (d/H). Figure 5 is a similar plot for the normalized reinforcement ratio (ρ/ρ_{max}) where ρ_{max} is 75 percent ρ_{bal}.

The normalized depth shows little scatter for the 28 bridges. The normalized reinforcement ratio shows more scatter. The averages and standard deviations for the two variables are shown on the figures. The proposed strategy for selecting the reinforcement area and effective depth is based on these statistical values. To incorporate a margin of safety, target values lying roughly 1.3 standard deviations below the mean values were selected. This distance from the mean corresponds roughly to a probability that the assumed value will be conservative 90 percent of the time.

The results of these calculations yield the following target values: $d/H = 0.84$, and $\rho/\rho_{max} = 0.66$. These numbers are rounded to convenient values to produce the following recommended strategy for bridges with unknown reinforcement details: $d = 0.85\ H$, and $\rho = 2/3\ \rho_{max} = 0.5\ \rho_{bal}$. Although this procedure does not in any way ensure the actual reinforcement configuration, it does provide the rating engineer with a consistent and rational method for selecting reinforcement properties and dimensions for bridges without reinforcement details.

Before implementing the specific values in the above example, a larger data base should be surveyed. Further refinement of the target values could also be obtained by examining the data with respect to design-specific factors such as year built, material properties, and span length.

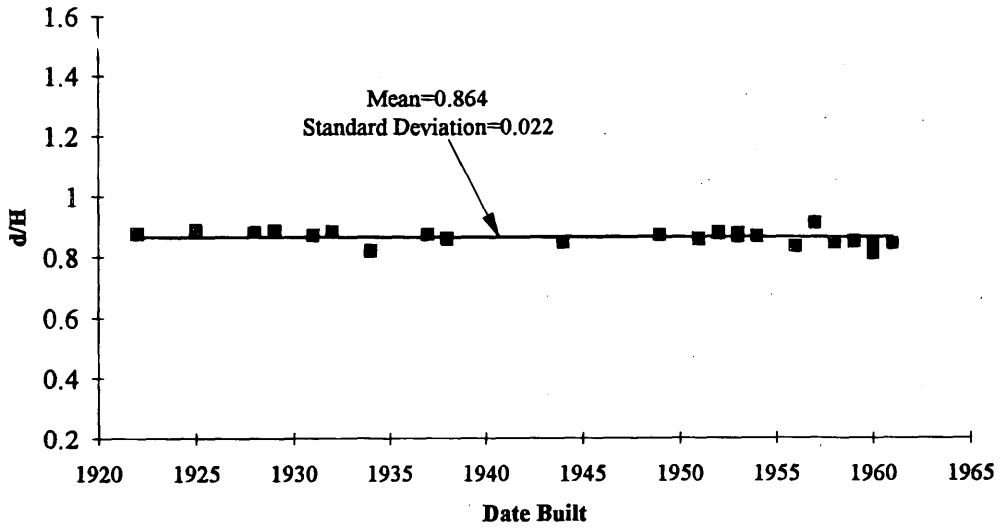

FIGURE 4 Normalized structural depths (d/H) for concrete bridges.

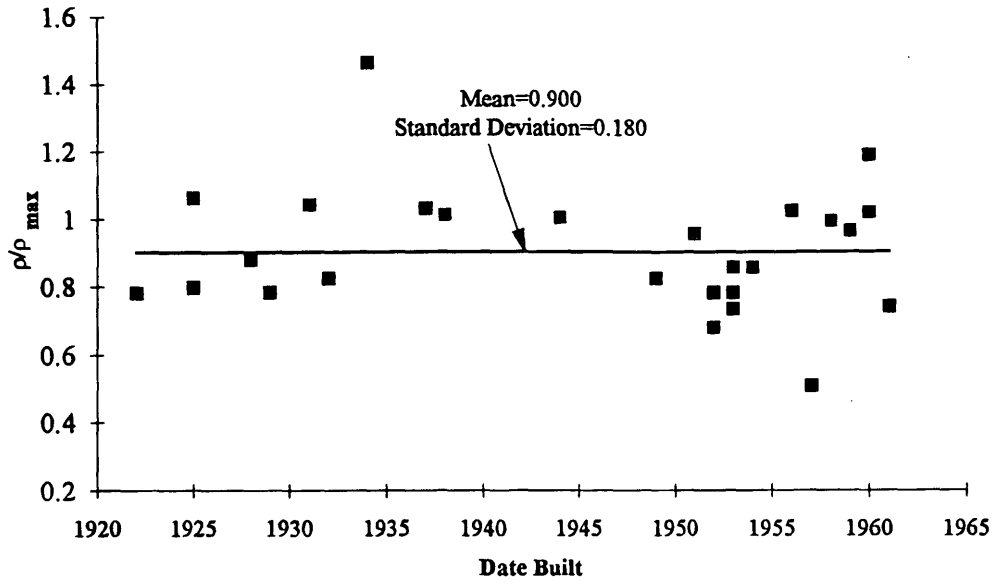

FIGURE 5 Normalized reinforcement ratios (ρ/ρ_{max}) for concrete bridges.

SUMMARY AND CONCLUSIONS

The STRENGTH method is a reliability-based load and resistance factor method that uses variable site-specific live load, impact, and resistance factors. The procedure considers redundancy, weight enforcement, and truck volume, deterioration, inspection effort, and level of maintenance in the rating. The STRENGTH method has several advantages over the current LFR method, including the following (*9,10*):

1. Implicitly recognizes the difference between design and evaluation,
2. Provides consistent level of safety for all bridges,
3. Uses site-specific load and resistance characteristics,
4. Incorporates engineering judgment in the rating process,
5. Uses familiar form—similar to LFR method,
6. Permits potential improvements in ratings through extra efforts in inspection and maintenance,
7. Encourages better inspection and maintenance programs, and
8. Eliminates much of the variation in state posting practices.

Unfortunately, the STRENGTH method also has disadvantages (*10*):

1. Load, impact, and resistance factors are subjective;
2. Some terms, such as "careful," "estimated," "vigorous," and "intermittent," are subjective;
3. States may choose to categorically use conservative factors, defeating the purpose of the STRENGTH method;
4. Additional inspection information is required; and
5. It changes established bridge rating programs.

The STRENGTH method is similar to the LFR maximum-strength method in form. For bridges in good shape with reasonable traffic enforcement, the STRENGTH ratings will be similar to LFR maximum-strength operating levels. The STRENGTH method can greatly improve ratings when serviceability limits control the LFR. With increased impact, deterioration, and truck volume, the STRENGTH method ratings decrease significantly and can fall below LFR inventory levels.

The concrete data base definitely shows the effect of deterioration (Figure 3). With 16 out of 33 bridges classified as slightly deteriorated and 9 classified as heavily deteriorated, many of the STRENGTH ratings fell below LFR inventory level. Although the results may seem startling, if these bridges are in this much disrepair, the LFR method does not indicate the seriousness of the situation. In other words, if the STRENGTH method yields consistent levels of safety for these bridges, the LFR method is not achieving desirable safety levels. It is suggested that, since the deterioration was based on appraisals, inspection procedures should be reviewed to determine if these bridges are truly in such poor structural condition.

Unlike the LFR method, the STRENGTH method uses variable load and resistance factors depending on site-specific information. This creates subjectivity in the rating process, and the inspection and rating personnel must use judgment in choosing values. The consistency and accuracy in which these personnel choose the factors determines the success of the STRENGTH method in meeting its objective of consistent reliability in rating.

RECOMMENDATIONS

It is first recommended that the AASHTO Guide Specification for the Strength Evaluation of Existing Steel and Concrete Bridges (*6*) be used to determine alternative posting ratings for girder bridges that are currently posted according to ASR or LFR methods. The STRENGTH method has the potential to increase or remove posted limits on many bridges, and an effort by the state Department of

Transportation (DOT) will quickly determine the usefulness of the procedure. To apply the STRENGTH method consistently, there will need to be modifications to the current inspection procedures to collect additional information. This will inherently require better communication between inspectors and bridge rating engineers. This study examined only reinforced concrete and steel girder bridges. The STRENGTH method also applies to prestressed girder and truss bridges. These types of bridges should be examined in conjunction with concrete and steel girder bridges.

Once states establish application procedures and gain confidence in the STRENGTH method with these posted bridges, the provisions should be applied to all girder bridges for a consistent evaluation over the bridge inventory.

During routine rating of concrete bridges, the state DOT should keep a tally of reinforcement ratios and structural depths to build a data base for implementing a strategy for concrete bridges without reinforcement details similar to the limited strategy shown in this paper.

ACKNOWLEDGMENTS

This research was supported by the Missouri Highway and Transportation Department and FHWA as a Highway Planning and Research Program project. The author gratefully acknowledges this support and the people who helped coordinate the Bridge Rating Workshop associated with the project.

REFERENCES

1. National Bridge Inspection Standards, *Code of Federal Regulations*, Vol. 23, Section 650.3. Government Printing Office, Washington, D.C., 1988.
2. *Manual for Maintenance Inspection of Bridges*. AASHTO, Washington, D.C., 1983.
3. *Standard Specifications for Highway Bridges*. AASHTO, Washington, D.C., 1989.
4. *Manual for Condition Evaluation of Bridges*. AASHTO, Washington, D.C., 1994.
5. *Guide Specifications for Fatigue Evaluation of Existing Bridges*. AASHTO, Washington, D.C., 1990.
6. *Guide Specifications for Strength Evaluation of Existing Steel and Concrete Bridges*. AASHTO, Washington, D.C., 1989.
7. Lichtenstein, A. G. *Bridge Rating Through Nondestructive Load Testing*. Draft Report. NCHRP Project 12-28(13A). TRB, National Research Council, Washington, D.C., 1993.
8. Imbsen, R., W. Liu, R. Schamber, and R. Nutt. NCHRP *Report 292; Strength Evaluation of Existing Reinforced Concrete Bridges*. TRB, National Research Council, Washington, D.C., 1987.
9. Moses, F., and D. Verma. *NCHRP Report 301: Load Capacity Evaluation of Existing Bridges*. TRB, National Research Council, Washington, D.C., 1987.
10. Barker, M. G., D. M. Koenig, and L. M. Magruder. Load Rating Steel and Concrete Girder Bridges in Missouri. Missouri Cooperative Highway Research Program Report 91-1. Missouri Highway and Transportation Department, Jefferson City, 1994.
11. Minor, J., K. White, and R. Busch. *NCHRP Report 312*: Condition Surveys of Concrete Bridge Components Users Manual, TRB, National Research Council, Washington, D.C., 1988.

Publication of this paper sponsored by Committee on Dynamics and Field Testing of Bridges.

Controlled Load Tests on a Four-Girder Steel Bridge

J. HAROLD DEATHERAGE, MICHAEL DAVID SANDERS, DAVID W. GOODPASTURE, AND EDWIN G. BURDETTE

A fatigue investigation of the I-40 bridge over the Holston River provided an excellent opportunity to measure and analyze the response of an actual structure to applied loads. During the course of the project, responses to both actual traffic loadings and controlled loadings were measured. In this paper the data collected during the controlled load tests are examined and the means by which the data were collected are outlined. Methods currently used to distribute applied loads to the main structural members have been found to produce conservative results in several cases. This project made it possible to compare actual measured load distributions with the load distributions calculated by various means. The measured responses were compared with AASHTO values and values calculated by a method developed by the authors in 1987. The latter, an extension of the Guyon-Massonnet method, was found to produce less conservative and more accurate results than the AASHTO method. Full-speed and crawl test data were analyzed in order to calculate dynamic impact factors for this structure. These values were also compared with the AASHTO design impact factors.

The Holston River Bridge carries Interstate-40 over the Holston River just east of Knoxville, Tennessee. The bridge supports six lanes of traffic, three in each direction. Four continuous steel girders support a concrete deck 7½ in. (19 cm) thick that acts compositely with the girders. The roadway shoulder is supported by cantilever extensions that frame into the web of the exterior girders (Figure 1). The girders vary in depth throughout the length of the bridge but are identical at any given cross section. The bridge is 363.8 m (1,193 ft) in total length and consists of seven spans ranging in length from 41.2 m (135 ft) to 73.2 m (240 ft) (Figure 2). Within the single 73.2-m span, the girders are connected laterally by cross trusses at 6.7 m (22 ft) on center (Figure 3, *top*). In all other spans, floor beams run between the girders (Figure 3, *bottom*). Both the trusses and floor beams support two wide flange sections each that serve as stringers for the bridge deck.

In January 1992, the Tennessee Department of Transportation discovered a fatigue failure in the outside girder on the eastbound lane. The fracture was located near the one-third point of the 73.2-m span between Piers 1 and 2 directly over the main channel of the river (Figure 4). The fracture extended almost the entire depth of the member. A large gap was present at the bottom flange of Girder 4. The two outside lanes of the bridge were immediately closed to traffic on each side, and measures were taken to repair the damaged girder. A retrofit of the cantilever-to-girder-web connection was also implemented that was intended to eliminate the out-of-plane distortion of the girder web, which had initiated the failure. In January 1993, a research project was begun by the University of Tennessee Transportation Center to investigate the Holston River Bridge fatigue failure. This project had four basic objectives: (a) determine the effectiveness of the retrofit repairs, (b) estimate the portion of the bridge fatigue life expended at the time of failure, (c) estimate the remaining life of the bridge on the basis of current and estimated future use and identify controlling fatigue detail locations, and (d) study critical details of the bridge structure for potential fatigue problems resulting from dynamic response of the structure. In order to accomplish these objectives, extensive field testing was required. First, careful inspection of the bridge plans and the bridge itself revealed the location of several critical points. Members at these locations were then instrumented with strain gauges. Strain gauge data were collected under both normal traffic and controlled loads. The information from these gauges was used to determine the response of the structure under these loads. Details of this investigation and results of the fatigue study will be reported in other papers. The focus of this paper is limited to a consideration of (a) dynamic load factor and (b) lateral distribution of loads.

This paper provides a summary of the controlled load tests performed on the Holston River Bridge. The structural behavior of the bridge when subjected to a controlled load was examined in detail. Lateral distribution of these loads to the four longitudinal girders was examined, and the measured distributions were compared with distributions obtained by analytical methods (*1*) and those recommended by AASHTO. The results of both the dynamic and static controlled load tests were analyzed and the data were compared in order to determine a dynamic impact factor for the structure. These values were also compared with AASHTO values.

REVIEW OF LITERATURE

Dynamic Impact Factors

Data including dynamic impacts and girder distributions were collected and incorporated into a system to evaluate bridge safety by Ghosn et al. (*2*). Dynamic impact factors calculated from these data were compared with AASHTO values; the AASHTO values were found to be conservative.

Dynamic impact factors were considered in NCHRP Report 301 (*3*). Impact factors taken from a data base of previous studies are given for various sites. It was determined that impact was directly related to roadway roughness. Instructions are provided in the report for selecting categories for a given roadway.

J. H. Deatherage, D. W. Goodpasture, and E. G. Burdette, Department of Civil Engineering, University of Tennessee, Knoxville, Tenn. 37996-2010. M. D. Sanders, Forcum-Lannom, Dyersburg, Tenn. 38025-0768.

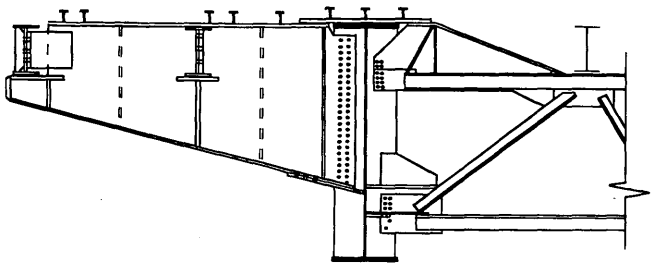

FIGURE 1 Cantilever-to-girder connection.

The effect of truck weight on the dynamic impact factor was examined by Nowak (*4*). It was found that as truck weight increased, the dynamic impact factor decreased.

Lateral Load Distribution

Present AASHTO distribution factors have been found to be conservative by many researchers (*5–7*). This research has encompassed different means, including analytical methods, computer models, scale models, and actual field measurements. The work by Sanders and Elleby referenced Guyon and Massonnet extensively in developing the current AASHTO load distribution factors. Deatherage (*5*) extended the Guyon-Massonnet theory to develop a series of influence coefficients that more accurately represent the effects of a load applied laterally on the cross section of a beam-slab bridge. In Deatherage's work, a torsional parameter, α, and a flexural stiffness parameter, Θ, are used to determine the appropriate influence coefficients to be used with a particular structure.

The effect of different variables on lateral distribution was examined by Hays et al. (*6*) through the use of a computer program, Structural Analysis for Load Distribution (SALOD). AASHTO factors were found to produce conservative results when compared with the results from SALOD.

An experimental test program was used to evaluate the behavior of a 4/10-scale model of a two-span continuous plate girder bridge (*7*). Distribution factors computed using AASHTO procedures were found to be quite conservative for the interior girder and less so for the exterior girders.

Field data were collected using strain gauges and weigh-in-motion (WIM) equipment. These data were used to calculate lateral distribution factors and dynamic impact factors. When these values were compared with AASHTO values, the AASHTO values were again found to produce conservative results.

Nowak et al. (*1*) also used strain gauges and WIM equipment to evaluate a structure's response to traffic. The structure was a multispan bridge supported by four steel plate girders. In addition to evaluation of the bridge details with respect to fatigue damage, measured girder moment distribution factors are presented for the structure.

CONTROLLED LOAD TESTS

On August 5, 1993, control tests were performed on the Holston River Bridge using a truck of known weight and axle spacing under controlled traffic conditions. The test vehicle, a tandem-axle dump truck, was provided by the Tennessee Department of Transportation. The total weight of the truck was 341.6 kN (76,760 lb). The weight on the front axle was 67.9 kN (15,260 lb). The two rear axles combined to support 273.7 kN (61,500 lb). The wheel base of the truck was 4.27 m (14 ft 11 in.) from the front to the first rear axle and 5.87 m (19 ft 4 in.) from front to the second rear axle (Figure 5). The width measured 2.36 m (7 ft 9 in.) from outside to outside of the rear tires. The tests were conducted in the early morning hours to minimize the disruption of traffic flow. Tests were begun at 1:00 a.m. and no other traffic was allowed on the bridge when data were being taken. During all test runs an observer from the research team was in the truck to ensure that the driver was in the proper lane and traveling at the proper speed.

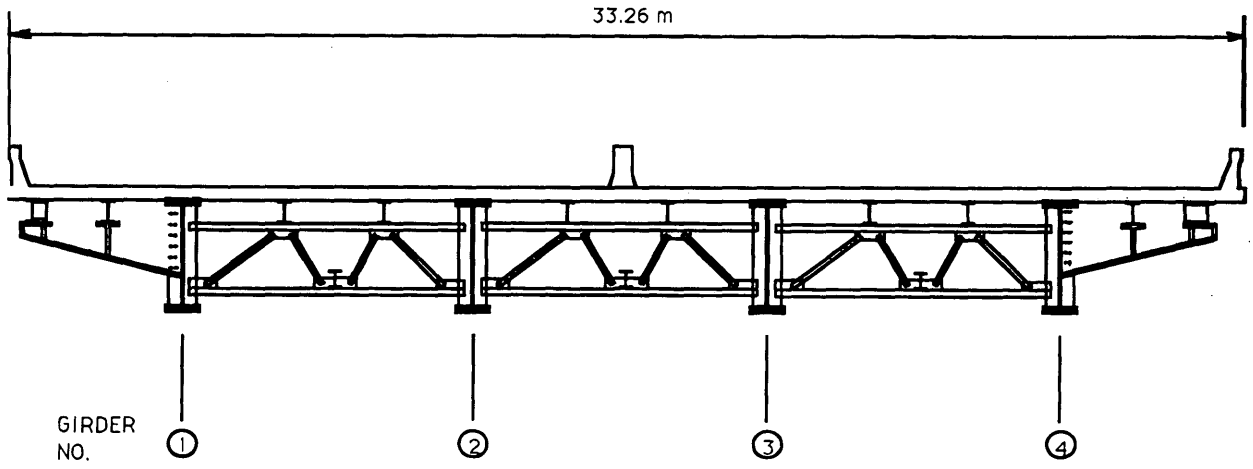

FIGURE 2 Typical cross section.

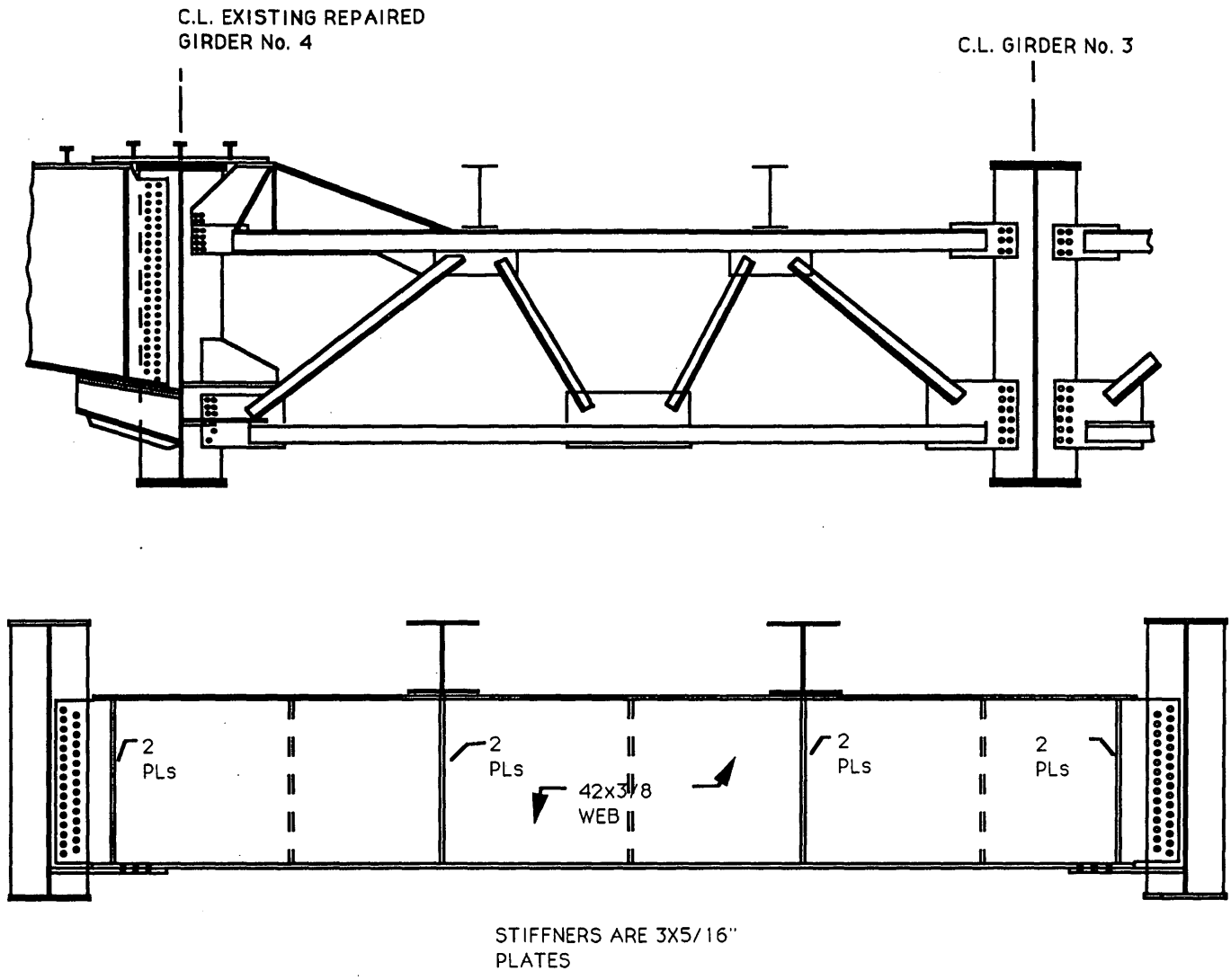

FIGURE 3 *Top*, typical floor truss; *bottom*, typical transverse floor girder.

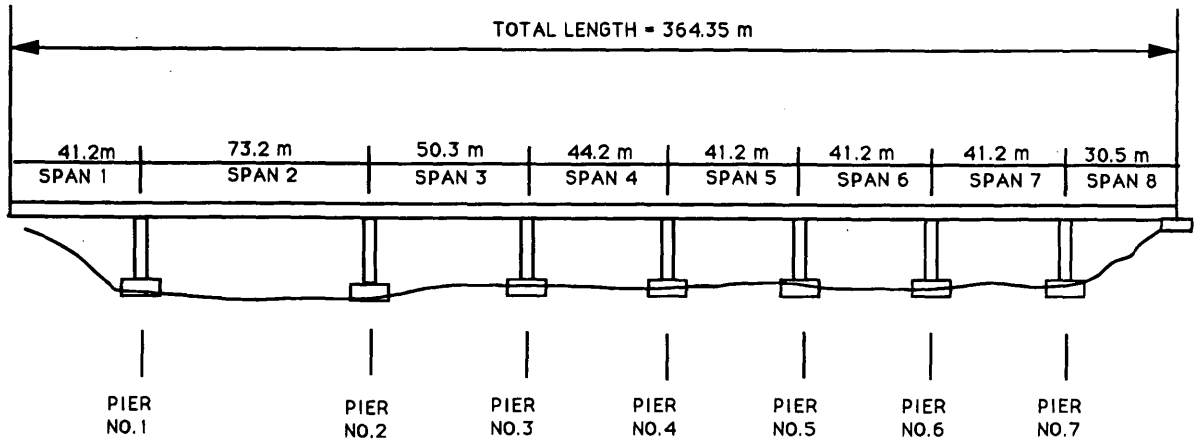

FIGURE 4 Elevation looking north.

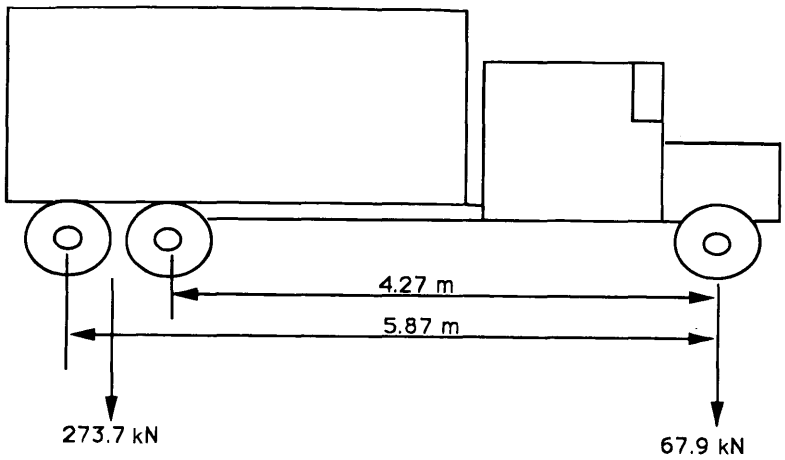

FIGURE 5 Test vehicle for controlled load test.

Tests were conducted at crawl speeds to determine the structure's response to a static load moving along the length of the bridge. A constant speed of 8.05 km/hr (5 mph) was maintained. Data collection for the eastbound crawl tests was begun when the truck reached the west abutment and was stopped when the truck reached the fourth span. All gauge locations were in the first and second spans. The effect of the load on these locations was therefore negligible by the time the truck reached the fourth span. The westbound tests were begun with the truck at approximately the center of the fourth span and ended when it crossed the west abutment. Crawl test data were taken for all six traffic lanes and for both shoulders. Data were also collected when the truck was returning from the end of each run. This allowed two data-collection passes in each lane.

Dynamic tests were also conducted with the truck at speeds ranging from 80.5 km/hr (50 mph) to 104 km/hr (65 mph). The tests with lower speeds were in the eastbound lanes because of the proximity

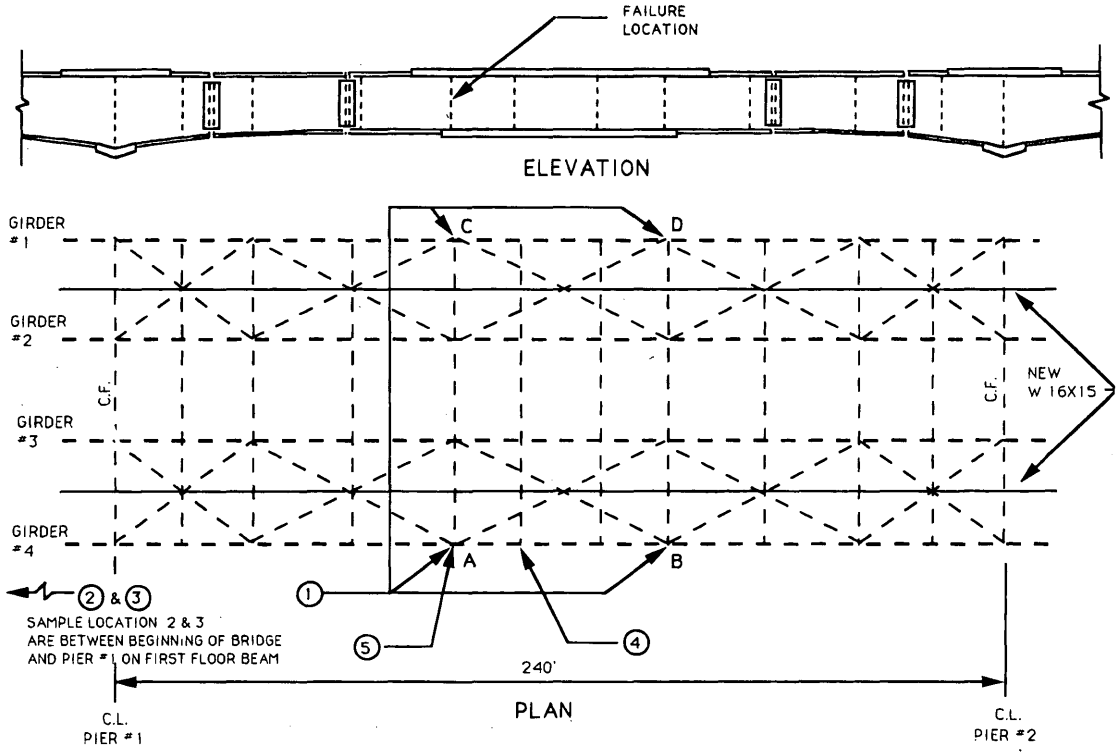

FIGURE 6 Data sample locations.

of the nearest exit west of the bridge. The truck was only able to obtain a speed of around 80.5 km/hr (50 mph) in this relatively short distance. Data were collected for passes with the truck in all six traffic lanes. No dynamic data were taken for the shoulder lanes. The dynamic test data were also collected only when the truck was in the first three spans.

Thirty-one gauges were monitored during these tests. Gauges on the top and bottom flanges of the girders were monitored at locations 1A, 1B, 1C, and 1D (Figure 6). Gauges on the two interior girders at the cross section where the failure occurred were also monitored. Balancing problems prevented obtaining data on the flange of Girder 2. Gauges at the coped ends of the floor girders in Span 1 were also chosen to be monitored. However, only data from the bottom gauge were obtained because of a problem with the top gauge just before the test.

TEST RESULTS

Strains recorded using the MegaDec and the TCS 3000 software were analyzed using an electronic spreadsheet program. The ability to manipulate large amounts of numerical data quickly and easily made the spreadsheet program ideal for analyzing the controlled load test data. To utilize the spreadsheet, data from TCS 3000 had to be converted to a format compatible with the spreadsheet program. This was done by exporting the data into a Data Interchange File (DIF) within the TCS 3000 program. Once converted, the file was transferred to the spreadsheet program where manipulation of the data was possible.

Strain gauge readings were taken at a rate of 60 Hz. Although the spreadsheet was capable of handling any of the test files transferred from TCS 3000, the files were quite large and required a great deal of memory. A lower sample rate would have adequately reflected the structure's behavior during the controlled load tests. Once the data were transferred to the spreadsheet, they were reduced to reflect a sample rate of 10 Hz by creating a macro within the spreadsheet that automatically deleted the appropriate data from each test file.

The spreadsheet program also allowed the creation of plots for any given gauge in any given test (Figure 7). Data from each test were reduced and analyzed. Maximum stresses at gauge locations of interest were determined for each of the test runs. Tables 1 and 2

TABLE 1 Maximum Main Girder Stresses for Crawl Tests (MPa)

		EAST BOUND			
GIRDER #		SHOULDER	RIGHT LANE	MIDDLE LANE	LEFT LANE
1	POS	0.71	1.42	1.19	1.42
	NEG	-2.84	-1.18	-0.48	-1.65
	RANGE	3.55	2.60	1.65	3.07
3	POS	4.26	6.16	9.47	9.94
	NEG	-3.31	-2.13	-2.13	-2.84
	RANGE	7.57	8.29	11.60	12.78
4	POS	17.52	170.51	10.65	5.45
	NEG	-5.44	-37.85	-3.32	-3.32
	RANGE	22.96	20.84	13.97	8.76

		WEST BOUND			
GIRDER #		SHOULDER	RIGHT LANE	MIDDLE LANE	LEFT LANE
1	POS	14.44	13.73	9.23	5.21
	NEG	-4.26	-3.32	-2.84	-2.36
	RANGE	18.71	17.05	12.07	7.58
3	POS	1.65	2.36	3.79	5.45
	NEG	-1.18	-2.13	-1.42	-1.42
	RANGE	2.84	8.29	5.21	6.87
4	POS	1.42	0.94	1.19	2.84
	NEG	-2.84	-1.65	-0.71	-0.94
	RANGE	4.26	2.60	1.90	3.79

Divide stresses by 6895×10^{-3} to convert to psi.

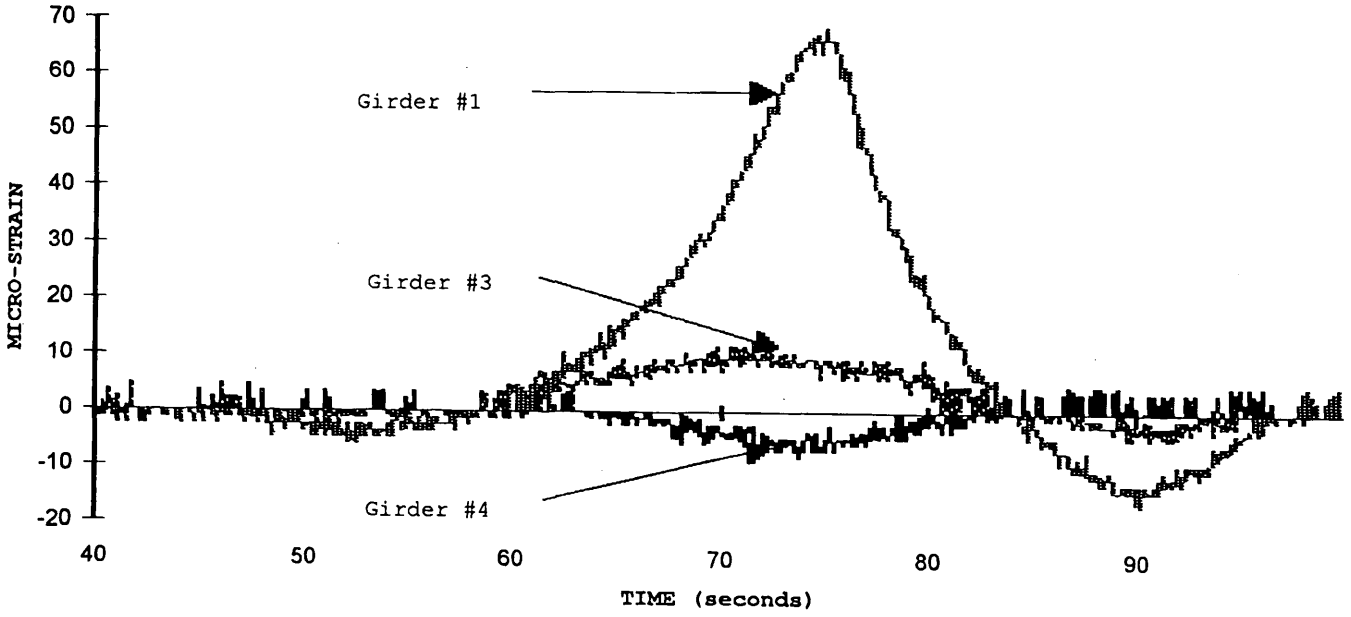

FIGURE 7 Typical gauge outputs for controlled load crawl test data, westbound right lane.

TABLE 2 Maximum Measured Main Girder Stresses for Dynamic Tests (MPa)

GIRDER #		EAST BOUND			
		SHOULDER	RIGHT LANE	MIDDLE LANE	LEFT LANE
1	POS	N/A	2.61	1.19	2.14
	NEG	N/A	-1.19	-1.19	-0.71
	RANGE	N/A	3.79	2.36	2.84
3	POS	N/A	6.38	10.18	13.25
	NEG	N/A	-2.85	-2.36	-1.65
	RANGE	N/A	9.23	12.55	14.92
4	POS	N/A	16.81	10.65	6.86
	NEG	N/A	-5.21	-4.10	-2.60
	RANGE	N/A	22.02	14.68	9.47

GIRDER #		WEST BOUND			
		SHOULDER	RIGHT LANE	MIDDLE LANE	LEFT LANE
1	POS	N/A	14.92	8.76	5.68
	NEG	N/A	-3.07	-4.02	-2.36
	RANGE	N/A	17.99	12.78	8.05
3	POS	N/A	1.35	3.075	4.97
	NEG	N/A	-1.59	-1.42	-1.42
	RANGE	N/A	2.95	4.49	6.39
4	POS	N/A	1.65	0.94	2.36
	NEG	N/A	-1.89	-1.18	-1.65
	RANGE	N/A	3.55	2.13	4.02

Divide stresses by 6895×10^{-3} to convert to psi.

show the maximum stresses at the main girder bottom flange for the crawl tests and the dynamic tests, respectively, Figure 8 shows a typical plot of static versus dynamic test data. Data from two other areas of interest were also examined. These two areas were believed to be locations of high stress and susceptible to fatigue damage. Table 3 shows maximum stress ranges at the web gap on Girder 1. The values for the test runs with the truck in the westbound lanes are given. Test runs with the truck in the eastbound lanes had little effect on this location. Table 4 shows the maximum stress ranges for the floor beam in the area of the termination of its bottom flange near its connection to the interior girder.

TABLE 3 Maximum Stress Ranges at Web Gap on Girder 1 (MPa)

TRUCK POSITION	MAXIMUM STRESS RANGE (MPa)	
	STATIC	DYNAMIC
WEST BOUND LEFT LANE	14.44	16.09
WEST BOUND MIDDLE LANE	21.54	23.67
WEST BOUND RIGHT LANE	26.51	28.64

Divide stresses by 6895 x 10^{-3} to convert to psi.

ANALYSIS OF DATA

It has been shown by several other researchers that the approximations commonly used for design to predict stresses in members produce conservative results (*1,6,7*). The Holston River Bridge project provided an excellent opportunity to measure the response of an actual structure to applied loads. Data collected during the controlled load tests provide a means of evaluating the accuracy of assumptions and simplifications made during the design of this and other bridges. The data were analyzed and compared with results obtained using analytical methods developed by other researchers (*5*) in an attempt to verify the results of these methods. The actual measured responses were also compared with values obtained using AASHTO values.

Deatherage (*5*) attempted to provide engineers with a simplified means of evaluating load distributions for beam-slab bridges. He extended the Guyon-Massonnet theory and developed a series of influence coefficients that can be used to predict the effect of a load applied laterally at any point on the cross section of a bridge. The values of these influence coefficients depend on a flexural parameter, Θ, and torsional parameter, α, which are specific to the particular structure being evaluated. Curves representing influence coefficients versus the relative lateral location of loads for the Holston River Bridge were developed (Figures 9 and 10). From these curves, distribution coefficients for interior and exterior girders for test trucks in all six lanes were calculated.

AASHTO uses a distribution factor based on the girder spacing divided by a constant for a particular type of structure. An AASHTO distribution coefficient obtained by dividing the girder spacing by 5.5 was calculated.

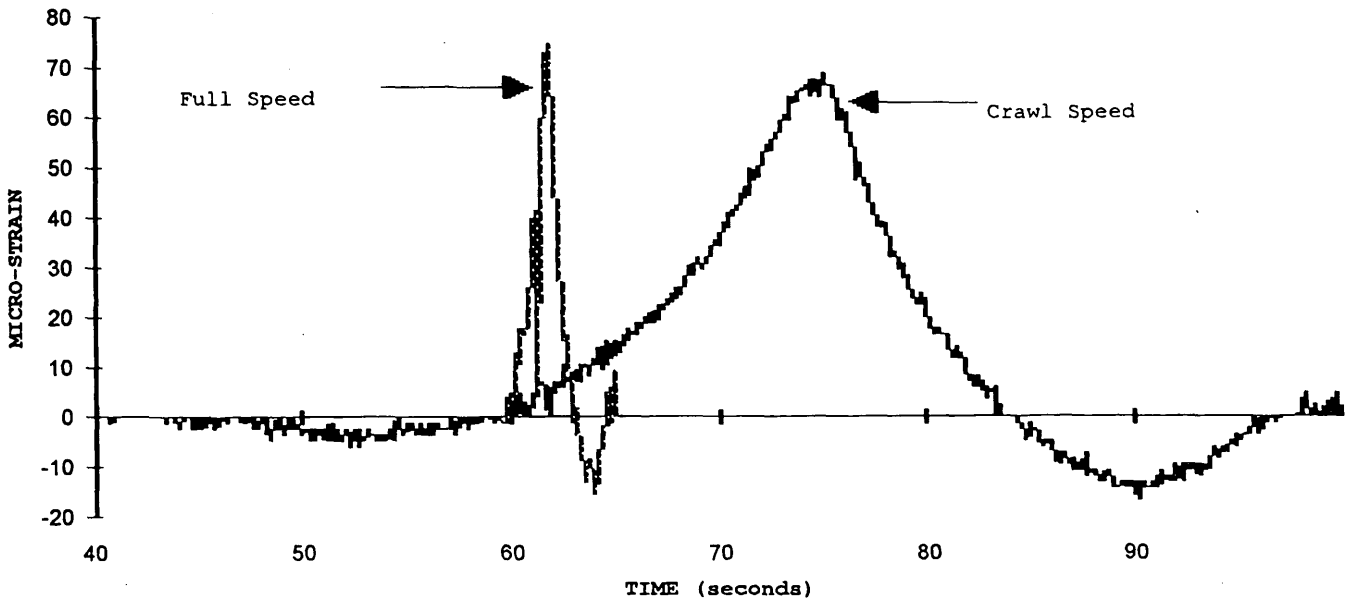

FIGURE 8 Typical gauge outputs for controlled load crawl and fullspeed test data, westbound right lane.

TABLE 4 Maximum Stress Ranges at Floor Beam Bottom Flange Termination (MPa)

TEST RUN	STRESS RANGE (MPa)	
	STATIC	DYNAMIC
EAST BOUND SHOULDER	15.63	N/A
EAST BOUND RIGHT LANE	12.78	13.96
EAST BOUND MIDDLE LANE	7.81	12.54
EAST BOUND LEFT LANE	21.31	28.41
WEST BOUND LEFT LANE	5.21	10.18
WEST BOUND MIDDLE LANE	6.63	7.81
WEST BOUND RIGHT LANE	10.89	12.54
WEST BOUND SHOULDER	13.25	N/A

Divide stresses by 6895 x 10^{-3} to convert to psi.

By superimposing measured maximum stresses for each pass of the test truck, maximum stresses equivalent to those that would be produced with a truck in all six lanes could be obtained for each girder. These stresses were used to determine an actual distribution factor, which was then compared with both calculated distribution factors.

Computer models for exterior and interior girders were developed using GTSTRUDL. With the aid of these models and the calculated distribution factors, moments for each girder were determined at the bottom flange strain gauge locations. The stresses for the bottom flange of each girder were then calculated using the section properties at strain gauge locations. These stresses were compared with the actual measured stresses at the bottom flanges of the main girders.

Table 5 summarizes the distribution factors and stresses from both methods and actual measurements.

Another important variable in determining design forces in bridge members is the dynamic impact factor. Other researchers have found that the AASHTO allowance for dynamic impact is usually higher than that measured during tests (*1*). AASHTO uses the value

$$I = 50/L + 125)$$

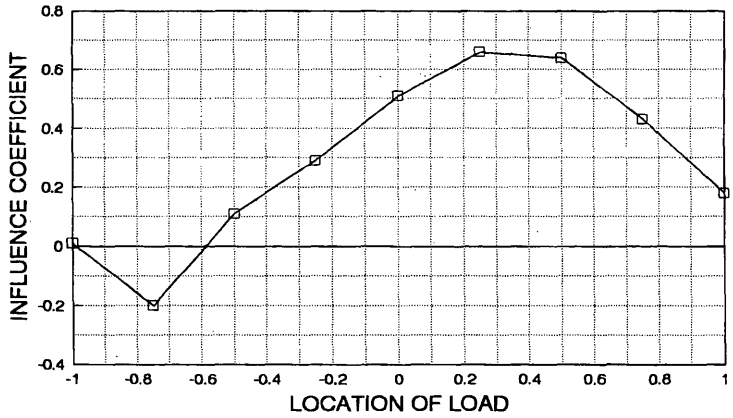

FIGURE 9 Influence coefficients for interior girder at 0.33 (α = 0.132; θ = 1.06).

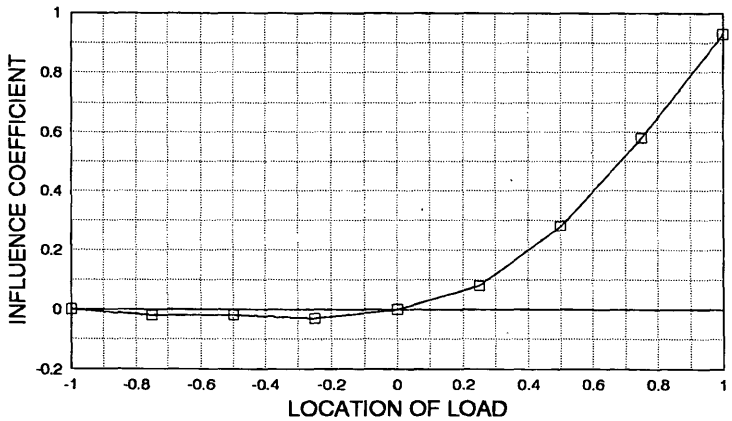

FIGURE 10 Influence coefficients for exterior girder at 1.0 (α = 0.132; θ = 1.06).

TABLE 5 Calculated and Measured Maximum Stresses (MPa)

GIRDER NUMBER	AASHTO		CALCULATED		MEASURED	
	DISTRIBUTION FACTOR	MAX STRESS MPa	DISTRIBUTION FACTOR	MAX STRESS MPa	DISTRIBUTION FACTOR	MAX STRESS MPa
3(interior)**	4.72	79.29	3.38	56.67	2.28	37.16
1(exterior)	4.72	79.29	2.36	39.57	1.92	32.19
4(exterior)	4.72	79.29	2.36	39.57	2.27	38.12

**Stresses were not measured for interior girder #2
Divide stresses by 6895 x 10^{-3} to convert to psi.

TABLE 6 Dynamic Impact Factor for Girders

TEST RUN	GIRDER #	MAX STRESS RANGE		MEASURED IMPACT FACTOR
		STATIC	DYNAMIC	
RIGHT	1	2.60	3.78	N/A*
LANE	3	8.28	9.23	1.11
E. BOUND	4	20.83	22.02	1.06
MIDDLE	1	1.65	2.36	N/A*
LANE	3	11.60	12.54	1.08
E. BOUND	4	13.96	14.67	1.05
LEFT	1	3.07	2.84	N/A*
LANE	3	12.78	14.92	1.17
E. BOUND	4	8.76	9.47	1.08
RIGHT	1	17.05	17.99	1.06
LANE	3	3.31	2.95	N/A*
W. BOUND	4	2.60	3.55	N/A*
MIDDLE	1	12.07	12.79	1.06
LANE	3	5.21	4.49	N/A*
W. BOUND	4	1.89	2.13	N/A*
LEFT	1	7.57	8.05	1.06
LANE	3	6.86	6.39	N/A*
W. BOUND	4	3.78	4.02	N/A*

Divide stresses by 6895 x 10^{-3} to convert to psi.

for the increase in live load due to dynamic impact. This equation takes the span length as its only variable. However, research has shown that the dynamic impact factor is directly controlled by road surface roughness (*2,4*).

During the controlled load tests on the Holston River Bridge, data were taken for both crawl and full-speed tests. Comparing the maximum stresses in the two sets of tests allowed the determination of an actual impact factor. Impact factors were calculated for three locations on the bridge, including the bottom flange of the main girders in Span 2, the web gap on Girder 1 in Span 2, and the floor beam in Span 1. The test runs that produced maximum stresses below 6.89 MPa (1,000 psi) were not included in the calculations because of the more pronounced effect of outside interference on these readings. These factors were then compared to the AASHTO value of $50/(L + 125)$. Tables 6, 7, and 8 show the dynamic impact values for each location along with the AASHTO values.

TABLE 7 Dynamic Impact Factors for Web Gap on Girder 1

TEST RUN	MAX STRESS RANGE		MEASURED IMPACT FACTOR
	STATIC	DYNAMIC	
WEST BOUND LEFT LANE	14.44	16.09	1.11
WEST BOUND MIDDLE LANE	21.54	23.67	1.10
WEST BOUND RIGHT LANE	26.51	28.64	1.08

Divide stresses by 6895 x 10^{-3} to convert to psi.

TABLE 8 Dynamic Impact Factors for Floor Beam

TEST RUN	MAX STRESS RANGE		MEASURED IMPACT FACTOR
	STATIC	DYNAMIC	
EAST BOUND SHOULDER	15.63	N/A	N/A
EAST BOUND RIGHT LANE	12.78	13.96	1.09
EAST BOUND MIDDLE LANE	7.81	12.54	1.61
EAST BOUND LEFT LANE	21.31	28.41	1.33
WEST BOUND LEFT LANE	5.21	10.18	N/A
WEST BOUND MIDDLE LANE	6.63	7.81	1.18
WEST BOUND RIGHT LANE	1580	1820	1.15
WEST BOUND SHOULDER	1923	N/A	N/A

Divide stresses by 6895 x 10^{-3} to convert to psi.

CONCLUSIONS

AASHTO provides a simple method for determining the lateral distribution of loads on a particular girder. This method, however, has been shown to produce very conservative results in the case of the Holston River Bridge as well as for others (*5–7*). The AASHTO factors led to the calculation of stresses that were in excess of two times the actual measured stresses for both interior and exterior main girders. Although sophisticated computer modeling techniques can potentially provide much more accurate results, the time involved and level of expertise required may outweigh the benefits of a more precise solution. The need for a methodology that quickly and accurately predicts the portion of applied load carried by a single member is evident. Even when a more sophisticated computer model is to be used, a method accurate enough to verify its results is useful. Deatherage (*5*) attempted to provide such a method; his method accounts for both bending and torsional stiffness in laterally distributing the loads. When applied to the Holston River Bridge, this method produced results that, although still conservative, were less conservative than the AASHTO values for both the interior and exterior girders. The method proved to be extremely accurate for the exterior girders and less so for the interior. However, this method does provide a simple and quick procedure for determining the appropriate amount of applied loads to assign to longitudinal members.

The dynamic impact factor used by AASHTO has been shown by several researchers to be higher than that actually measured in some cases (*4*). The AASHTO equation for the dynamic impact factor takes only one variable into consideration, span length. A review of the recent research on the effect of variables on the dynamic impact factor shows that roadway roughness rather than span length is the controlling factor.

The values measured on the Holston River Bridge varied depending on the location being considered. The measured impact factors for the main girders in Span 2 compared relatively well with the AASHTO value (*8,3*). Although one test run produced a value above the AASHTO value, the measured values were consistently lower than calculated. The measured values at the floor beam in Span 1, however, do not compare well with the AASHTO value (*8,1*). The AASHTO value to be used for this location was calculated using the span length of the main girders in Span 1 41.2 m (135 ft), as is believed to be normal practice. There was evidence that this value when applied to the floor beams is unconservative.

REFERENCES

1. Nowak, A. S., H. Nassif, and K. H. Frank. Fatigue Load Spectra for Steel Girder Bridge. In *Transportation Research Record 1393*, TRB, National Research Council, Washington, D.C., 1993.
2. Ghosn, M., F. Moses, and J. Gobieski. Evaluation of Steel Bridges Using In-Service Testing. In *Transportation Research Record 1072*, TRB National Research Council, Washington, D.C., 1986.
3. Moses, F. and D. Verma. *NCHRP Report 301: Load Capacity Evaluation of Existing Bridges*. TRB, National Research Council Washington, D.C., 1987.
4. Nowak, A. S., Y. K. Hong, and E. S. Hwang. Modeling Live Load and Dynamic Load for Bridges. In *Transportation Research Record 1290*, TRB, National Research Council, Washington, D.C., 1991.
5. Deatherage, J. H. *Investigation of Variables Affecting Beam-Slab Bridge Load Capacity*. Ph.D. dissertation. University of Tennessee at Knoxville, June 1987.
6. Hays, C. O., L. M. Sessions, and A. J. Berry. Further Studies on Lateral Load Distribution Using a Finite Element Method. In *Transportation Research Record 1072*, TRB, National Research Council, Washington, D.C., 1986.
7. Moore, M., K. A. Strand, M. A. Grubb, and L. R. Cayes. Wheel-Load Distribution Results from AISI-FHWA Model Bridge Study. In *Transportation Research Record 1275*, TRB, National Research Council, Washington, D.C., 1990.
8. *Standard Specifications for Highway Bridges*, 13th ed. American Association of State Highway and Transportation Officials, Washington, D.C., 1983.

Publication of this paper sponsored by Committee on Dynamics and Field Testing of Bridges.

Field Study of Longitudinal Movements in Composite Bridges

HERODOTOS A. PENTAS, R. RICHARD AVENT, VIJAYA K.A. GOPU, AND KEITH J. REBELLO

Bridge deck expansion joints often develop serious problems requiring extensive and expensive maintenance. This has become a nuisance to users and to bridge engineers, and many states have been involved in investigations aiming to alleviate this problem. Results reported by various states about the behavior of specific joint sealing systems have been contradictory, indicating that the problems may not be inherent to the particular system. Rather, the problems may stem from a failure to properly access actual joint movements, inadequate design criteria, improper installation procedures, or other factors such as differences in environmental conditions. In recognition of these problems, a comprehensive experimental investigation was conducted to obtain thermally induced movements of a newly constructed bridge in central Louisiana. The instrumentation, field monitoring, and analysis of long-term longitudinal movements are described. The primary causes of movements obtained were thermal changes. The bridge experienced unsymmetrical and irreversible movements, and these were attributed to restraints associated with the neoprene-bearing pads at the expansion joints. The bent movements and the effects of traffic were small compared with the thermal movements.

Highway bridges generally require expansion joints between sections of the deck or at the approach roadway. The standard practice is to specify a sealed joint to prevent debris and water from passing through the joint and causing deterioration of the bridge. Frequently the joint seals have leaked, ruptured, or fallen out of position. Once the seals fail, debris can lodge within the joint and road salts, can penetrate the failed seals, causing deterioration of the structural components. In short, joint seals have proved a continual and expensive maintenance problem for highway departments. Because various states have reported contradictory performance of specific joint sealing systems, the problems may not be inherent to the systems. Rather, the problems may stem from improper design criteria, poor installation practices, differences in bridge type or environmental conditions, and failure to determine actual joint movements.

To assess the importance of these factors, an experimental study was conducted on a newly constructed bridge located in central Louisiana to determine longitudinal movements. The purpose of this paper is to describe the field monitoring procedures and report on the general behavior of the bridge and its movements.

Trends in modern highway bridge construction such as the use of precast, prestressed concrete girders and creation of multiple continuous spans for live loads, complicate the prediction of joint movements. The current practice for the design of expansion joints for Louisiana highway bridges (*1*) is based on elementary strength of materials formulas, which may not accurately predict the joint movements. Systematic, detailed studies are required to properly assess actual joint movements, which will lead to the development of rational design methodologies for joints in modern bridges.

H. A. Pentas, Forte and Tablada, Inc., Baton Rouge, La. 70809. R. R. Avent and V. K. A. Gopu, Department of Civil Engineering, Louisiana State University, Baton Rouge, La. 70803. K. J. Rebello, Gulf Engineers and Consultants, Inc., Baton Rouge, La. 70809.

RELATED STUDIES

In a broad sense, highway bridge joints can be classified as open or closed (waterproof). Common types of open joints are plate bearing, butt, or toothed. Closed joints are composed of compression seals, membrane seals, or cushion seals. Purvis and Berger (*2*) give a brief description of joint seals along with their applications and associated problems. Several studies have been conducted to develop the best joint sealing system that would minimize bridge joint problems (3–7). These studies focused primarily on the performance specifications and evaluation of bridge joint systems.

The most significant bridge movements and the ones that by far cause most of the joint seal problems are the longitudinal across-the-joint thermal movements. Reynolds and Emanuel (*8*) have written a concise summary of prevalent research conducted in this area between 1957 and 1970. They concluded that relating environmental conditions to bridge movements is extremely complex. Dillon and Kissane (*9*) summarized the movements of prestressed concrete girders located throughout New York State over a 2-year period. Abdul-Ahad (*10*) developed a theoretical method of calculating thermally induced stresses and movements in continuous bridge structures. The experimental and analytical results were close; however, the experimental data were limited and no generalized conclusions could be drawn. Moulton and Kula (*11*) analyzed pier and abutment movement data obtained from 180 bridges through questionnaires. The surveys suggested that abutment movements occurred more frequently than pier movements and that horizontal movements caused much greater damage than vertical movements.

Mortlock (*12*) investigated various types of instruments used to obtain bridge movements. He concluded that the following should be used: (*a*) copper constantin thermocouples to obtain the temperature variation through the slab depth; (*b*) linear variable differential transformers (LVDTs) to measure the joint movements; and (*c*) a Kipp solarimeter to measure the solar radiation of the slab. Emerson (*13*) used a combination of these devices on seven bridges located in England.

OBJECTIVES AND SCOPE

The purpose of this paper is to describe the experimental procedures of instrumentation and monitoring and to discuss the general behavioral characteristics of the bridge with respect to long-term move-

ments. Reported here are also the results of the systematic study of the bridge joint movements. The reader is referred to Pentas et al. (*14*) for an analysis of the bridge temperatures and thermal distributions. The study was focused on a newly constructed bridge on US-190 over the Atchafalaya River at Krotz Springs, Louisiana. Specific objectives of this research were to

1. Instrument the designated bridge for field monitoring using LVDTs, thermocouples, and optical devices;
2. Field monitor the appropriate bridge movements through a program of instrumentation and periodic measurement;
3. Analyze the experimental data obtained and evaluate the bridge joint movements;
4. Compare the experimental data with current procedures predicting longitudinal bridge movements.

BRIDGE DESCRIPTION

The bridge to be investigated is the east approach of US-190 over the Atchafalaya River at Krotz Springs, Louisiana. It consists of cast-in-place concrete slabs acting compositely with either Type IV AASHTO prestressed concrete girders or steel plate girders. This superstructure is supported by 12 bents as shown in Figure 1. The abutment is labeled Bent 1 and the rest of the bents are numbered in ascending order from east to west. Five expansion joints are provided to allow for bridge movements. Joints 1 through 4 are membrane seals, whereas Joint 5 is a toothed type. The bridge continues over the river as a steel through truss.

Unit 2 is the longest single span of the approach at 42.7 m. (140 ft). It consists of a cast-in-place slab 21.6 cm (8-½ in.) thick slab acting compositely with four steel plate girders 183 cm (72 in.) deep. The other three sections of the approach (Units 1,3, and 4) consist of a slab 19 cm (7½ in.) thick acting compositely with five Type IV AASHTO prestressed concrete girders.

The supporting Bents 2 through 5 consist of concrete caps poured at the top of precast concrete piles 194 cm^2 (30 $in.^2$). Bents 2 and 3 each have four precast concrete piles supporting a level cap. Bents 4 and 5 each have five piles supporting the cap. The cap is stepped to allow the top of the steel girders to match flush at the same level as the top of the concrete girders. Bents 6 through 11 consist of level concrete caps supported by two concrete columns 137 cm (54 in.) in diameter. Bent 12 consists of two concrete columns 76 cm (30 in.) in diameter anchored to a bridge pier that also supports the end rocker bearings of the river crossing truss.

At continuous joints, the girders were connected to the bent cap by imbedding a dowel into the cap extending into the continuous joint. At some expansion joint locations, the girders were pinned to the bent cap, whereas at others the girders were allowed to slide. Pinned joint connections are denoted by the letter F, whereas joints allowed to move are denoted by the letter E, as shown in Figure 1. The ends of the girders at the expansion joints and at the continuous joints over the bents were placed on neoprene bearing pads of the standard type used in Louisiana. The reader is referred elsewhere (*15*) for more information and bridge design details.

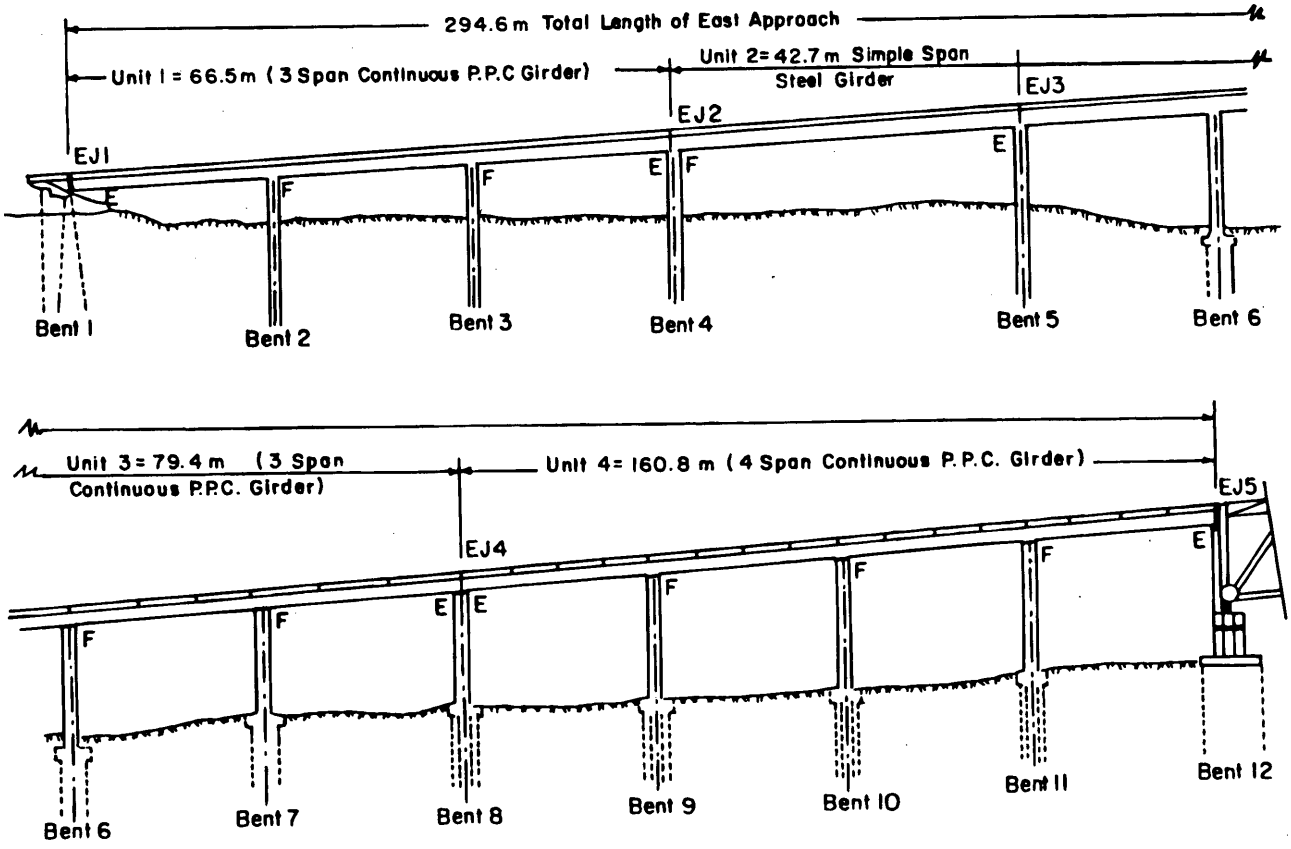

FIGURE 1 North elevation of east approach, US-90 bridge at Krotz Springs, Louisiana.

The bridge was already under construction at the beginning of this research (October 1986). The bents had been erected and the girders were already in place. It was during that period of construction when the first instrumentation was installed. At that time the decks were also constructed. On October 27, 1988, construction was completed and the bridge was opened to traffic.

BRIDGE MEASUREMENTS AND INSTRUMENTATION

Measurements were taken near the top and bottom of the girders at the expansion joints to obtain the relative longitudinal movements between the two adjoining girder sections. Measurements were also taken between the bent cap and one of the sections at the expansion joints, to obtain the movement of each section with respect to the cap. The sway of the bents at the expansion joints was also measured. The temperatures through the depth of the sections and ambient temperatures also were measured. The time was also recorded, thereby giving a time reference.

LVDTs were chosen to obtain the joint movements. A theodolite was chosen to obtain the bent sway, and thermocouples were used to measure the temperatures. The LVDT's and thermocouples were wired to the monitoring station where they would be connected to a Hewlett Packard microcomputer and data acquisition system that would store the readings for later processing. Electrical power was supplied through a portable generator. The theodolite readings were taken and recorded in a field book and later transcribed into the computer for processing.

Combined with a data acquisition system and a microcomputer, all LVDTs placed on the bridge could be read nearly simultaneously. Furthermore, the rugged construction of the LVDTs permitted them to function properly even after exposure to substantial shock loads. The LVDTs, however, could be used only to establish local relative movements of the girders at the expansion joints. In the case of the Krotz Springs Bridge, the LVDTs were used to obtain the measurements at the locations shown in Figure 2. The label at each location indicates the expansion joint number and the side on which it lies (north or south). Because of construction delays

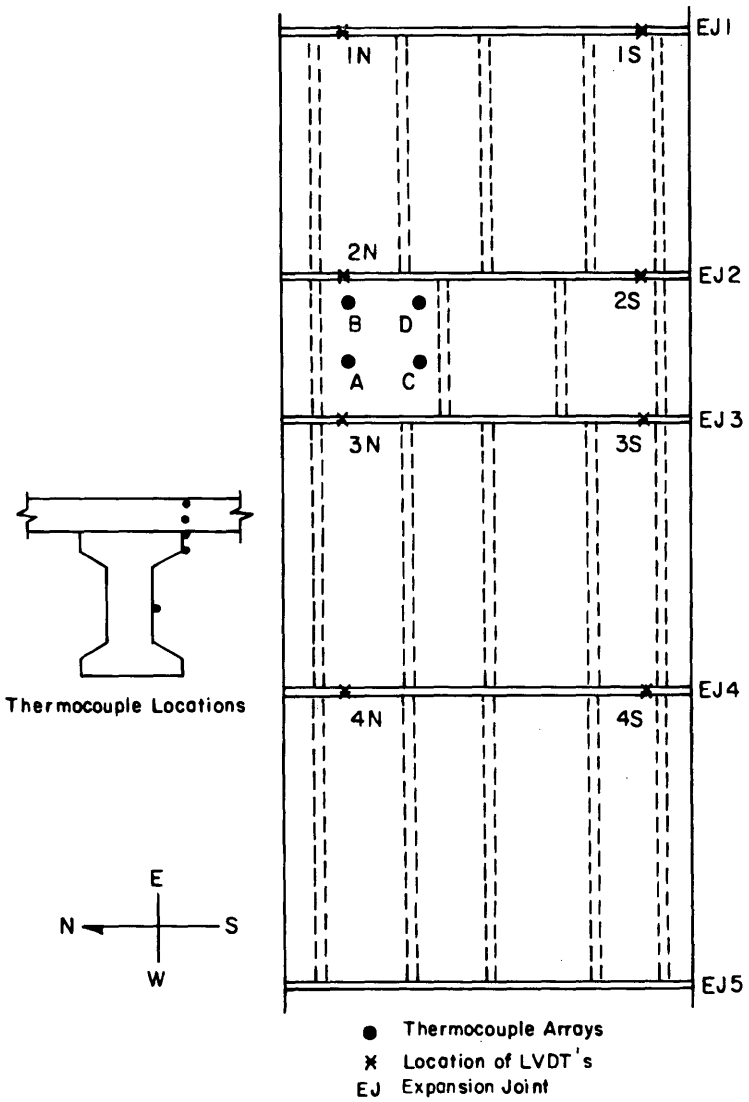

FIGURE 2 Plan view of bridge showing locations of LVDTs and thermocouples.

Joint 5 was not instrumented. The LVDTs were placed at the inner sides of the exterior girders to protect them from the outer environment. They were mounted on aluminum brackets and attached on the flanges of the girders using epoxy.

A side view of a typical section at an expansion joint is shown in Figure 3. An arbitrary positive displacement is denoted by the dashed line. LVDT A was placed near the top of the girder at a distance *a* from the neutral axis. The body was secured to the girder, and the core was fixed to an angle iron anchored vertically on the bent cap. LVDT B was placed near the bottom of the girder at a distance *b* from the neutral axis in a similar manner. LVDTs C and D had their bodies secured to the westward section and their cores secured to the eastward section. The distances labeled DA, DB, DC, and DD are the readings recorded by LVDTs A, B, C, and D, respectively. The required movements were calculated using geometric relations. The movements at the other expansion joints were obtained in a similar manner. The assumption was made that the abutment would remain stationary and was later proved to be correct by theodolite measurements. It was therefore necessary to install only two LVDTs at the abutment to calculate the joint movements.

A Pentax total station theodolite was used to obtain the bent sway of the Krotz Springs Bridge. A setup point was constructed for each of the 12 bents. A central reference point was constructed on the levee to allow for visibility from all setup points. The setup and reference points are made up of cast-in-place concrete benchmarks reinforced with three No. 4 bars. Each benchmark is 1.5 m (5 ft) in length with 1.2 m (4 ft) in the ground. The top of the setup points is marked by a brass plate embedded in the concrete.

Thermocouple wires type PP20TX were used to measure the temperatures of the Krotz Springs Bridge. They presented the following advantages: first, the temperature range was such that both ambient and slab temperatures could be accurately measured. Second, the thermocouples could be connected to the data acquisition system, allowing all temperatures to be measured at the same time as LVDT measurements. Finally, the thermocouple wire was fairly inexpensive, and preparation of the wire was very simple. The thermocouples were placed along the depth of the sections to detect the temperature variation. Each array consists of six thermocouples located on both slab and girder, as shown in Figure 2. The slab thermocouples were placed near the top, center, and bottom of the slab at the time of pouring. The girder thermocouples bonded on the outer surface of the concrete girders using epoxy and a layer of hydraulic cement. Two additional thermocouples were placed hanging under the slab to record the ambient temperature. All thermocouples were run under the bridge to the data acquisition system at the monitoring station.

BRIDGE MONITORING SCHEDULE

The theodolite readings began on January 1987. Each full set of readings required approximately 5 hr. As the effects of creep and

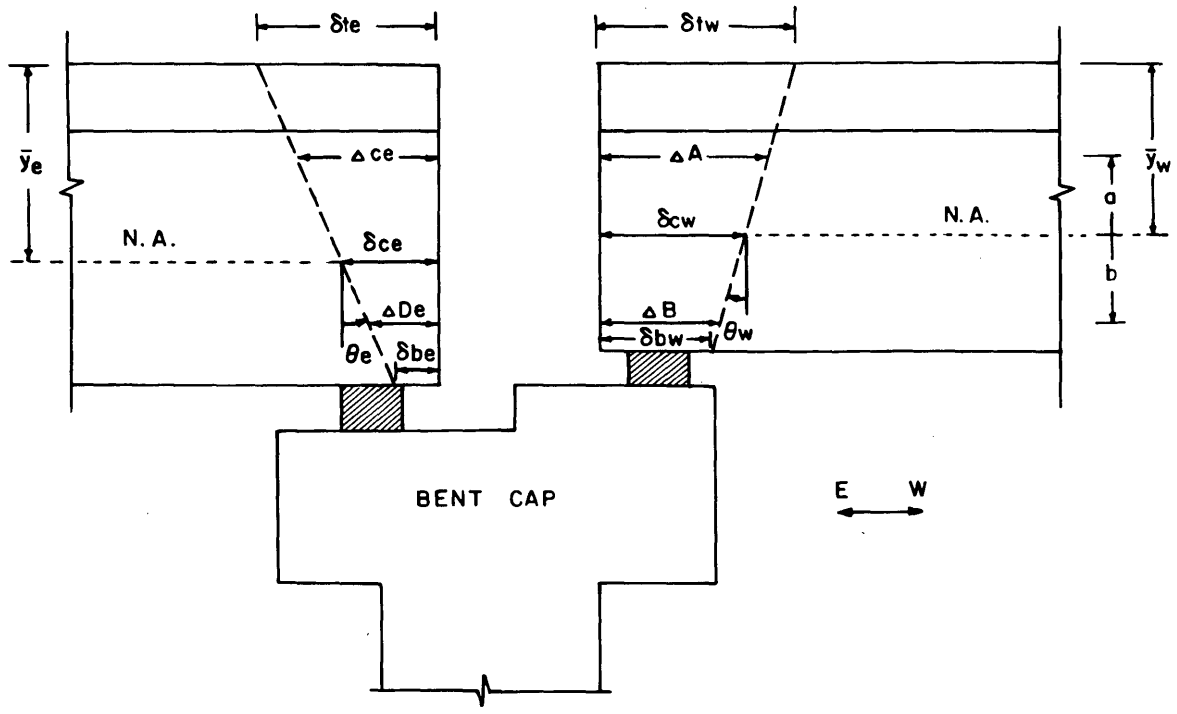

FIGURE 3 North elevation of typical expansion joint other than abutment, showing movements and LVDT measurements required to calculate movements.

shrinkage were anticipated to decrease, the frequency of data collection was gradually changed to a 6-week schedule. The LVDTs were on line at 8:00 a.m. on October 22, 1987. The LVDT readings were taken approximately every month. Alternate LVDT readings were taken for either 12 or 24 hr continuously. The thermocouple readings were recorded at the same time as the LVDT readings. During the days of data collection with the LVDTs, the theodolite was also used to obtain the sway of the bent caps at the expansion joints. Monitoring continued on schedule except for some minor interruptions. Five of the bridge markers were destroyed, either accidentally by the construction crew or by vandals. Also, one LVDT at location 4S was found to be defective, and the data collected at the joint were discarded.

MAXIMUM JOINT MOVEMENTS

A large amount of data was collected, but only the data required to evaluate the long-term expansion joint movements are presented in this paper. A complete analysis of the bridge temperatures is presented by Pentas et al. (*14*), in which a model to predict thermal distributions in bridges was developed.

The movements obtained were caused by dead loads and thermal changes only. Because the LVDTs were not in place until 9 months after the slabs were poured, creep and shrinkage effects had dissipated and could not be monitored. Traffic had not begun on the bridge until October 27, 1988; therefore the effects of traffic loads are not considered until after that time. The extreme values of movements recorded at the four expansion joints are summarized in Table 1. The following observations can be made:

1. The maximum closing of the top of the joint occurred during the warmer days of May 16 and June 10, 1988.
2. The maximum opening of the top of the joint occurred during the colder days of December 16, 1987, and February 21, March 17, and December 1, 1988.
3. The maximum joint movements at the north and south sides of the bridge do not necessarily occur during the same day.
4. The maximum joint movements of the north and south sides of the bridge have different magnitudes.

Possible factors affecting the inconsistencies of joint movement behavior include joints reaching maximum value allowed by mechanical connection; defective truss-bearing pins, construction crew and equipment; and bent movements, connection performance, and orientation of the bridge with respect to the sun path. No specific correlation related to these movements was identified. However, it is most likely that the build-up of stresses at the defective truss pins, as well as friction in the neoprene bearing pads, had the more pronounced effects on the bridge movements.

EFFECTS OF TRAFFIC

As indicated earlier, the bridge was opened to traffic on October 27, 1988. With the exception of December 1988, when the traffic loads may have aided in releasing stresses built up at joint supports, the movements obtained over the 9-month period after the bridge was opened to traffic did not show any deviation from previous movements. The observed behavior indicates that the traffic effects on the bridge joint movements were small compared to the effects of ther-

TABLE 1 Maximum Values of Expansion Joint Movements Obtained from LVDTs

Joint Location	Max. Closing (cm)	Date	Max. Opening (cm)	Date	Total Range (cm)	Ambient Temp. Differential (degrees C.)	Slab Temp. Differential (degrees C.)
1 North	-1.78	May 16	+0.25	Dec 16	2.03	28	39
(1 South)	(-0.38)		(+0.13)		(0.51)		
1 South	-0.38	May 16	+0.89	Dec 01	1.27	17	28
(1 North)	(-0.78)		(-0.38)		(1.52)		
2 North	-1.52	June 10	+0.89	Mar 17	2.41	19	31
(2 South)	(-1.78)		(+1.40)		(3.18)		
2 South	-1.91	May 16	+1.40	Mar 17	3.30	22	33
(2 North)	(-1.27)		(+0.89)		(2.16)		
3 North	-2.03	June 10	+1.52	Feb 21	3.56	11	14
(3 South)	(-1.27)		(+0.25)		(1.52)		
3 South	-1.52	May 16	+0.51	Mar 17	2.03	22	33
(3 North)	(-1.52)		(+1.52)		(3.05)		
4 North	-1.27	June 10	+0.127	Feb 21	1.40	19	31

2.54 cm = 1 inch

Numbers in ( ) represent movement on opposite side of joint corresponding to the maximum value listed.

mal changes. However, to more fully evaluate these effects, monitoring over a more lengthy period is required.

DATA DISCONTINUITIES

The movements obtained from the LVDT readings showed some discontinuities. An examination of the instrumentation was conducted to ensure that these changes were not a result of a system operation error. All electronic impulses were filtered and surge protected, shielding the instruments from improper power fluctuations. The sudden changes were not present throughout the whole set of data on the particular day, indicating that electronic malfunction was not the cause of this abnormal behavior. The exact causes of these movements have not been determined; however a possible explanation might be the sudden release of stresses built up at the pins of the steel truss. Shock waves caused by release of stresses at the truss pins act as an external force causing the release of stresses built up at joint supports, which results in sudden movements. The pins were replaced in January 1988, after which time the bridge movements did not show any discontinuities. It is important to note that the exact times of occurrence of the shock waves were not recorded and that the shock waves were not proved to be directly associated with the sudden bridge movements.

ANALYSIS OF LONG-TERM JOINT MOVEMENTS

To identify long-term movements caused by temperature changes from other movements, the behavior of the bridge can be studied using the data obtained over the 24-hr monitoring days. Because of space limitations, only selected data are presented in this paper. The reader is referred elsewhere for more information (*15*). The long-term movements obtained from the LVDTs on October 22, 1987, and February 21, 1988, are shown schematically in Figures 4 through 8. Figures 5 and 7 show the movements obtained from the LVDTs located at the south side of the bridge, and Figure 8 shows the plan view movements of the deck units. Each of Figures 4 through 8 shows the movements of the bridge sections at the expan-

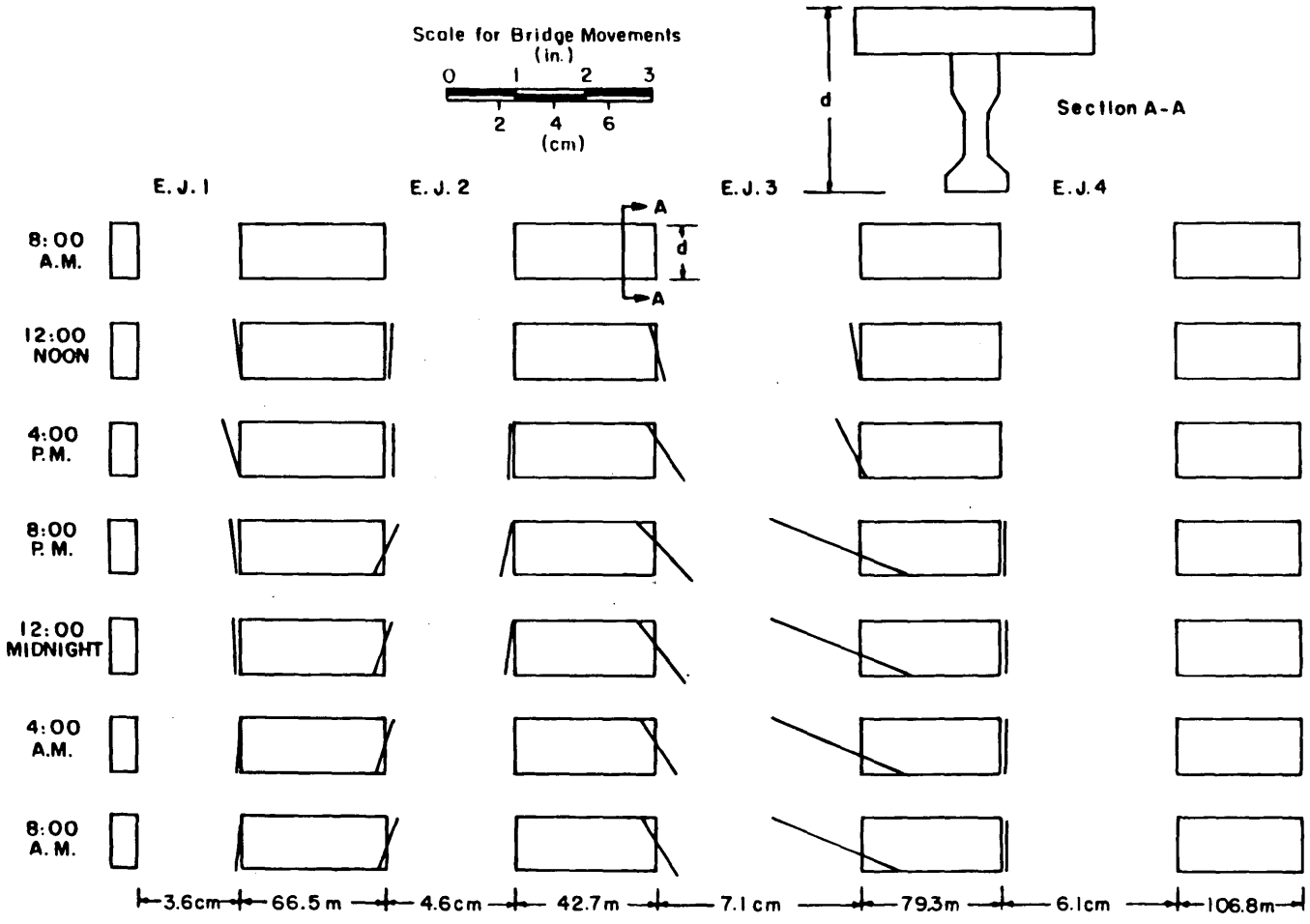

FIGURE 4 Elevation of north side girders showing 24-hr movements with respect to cap for October 22, 1987. (Note: Longitudinal dimensions of girders and joint spacings are not to scale, but actual end movements are to the scale indicated.)

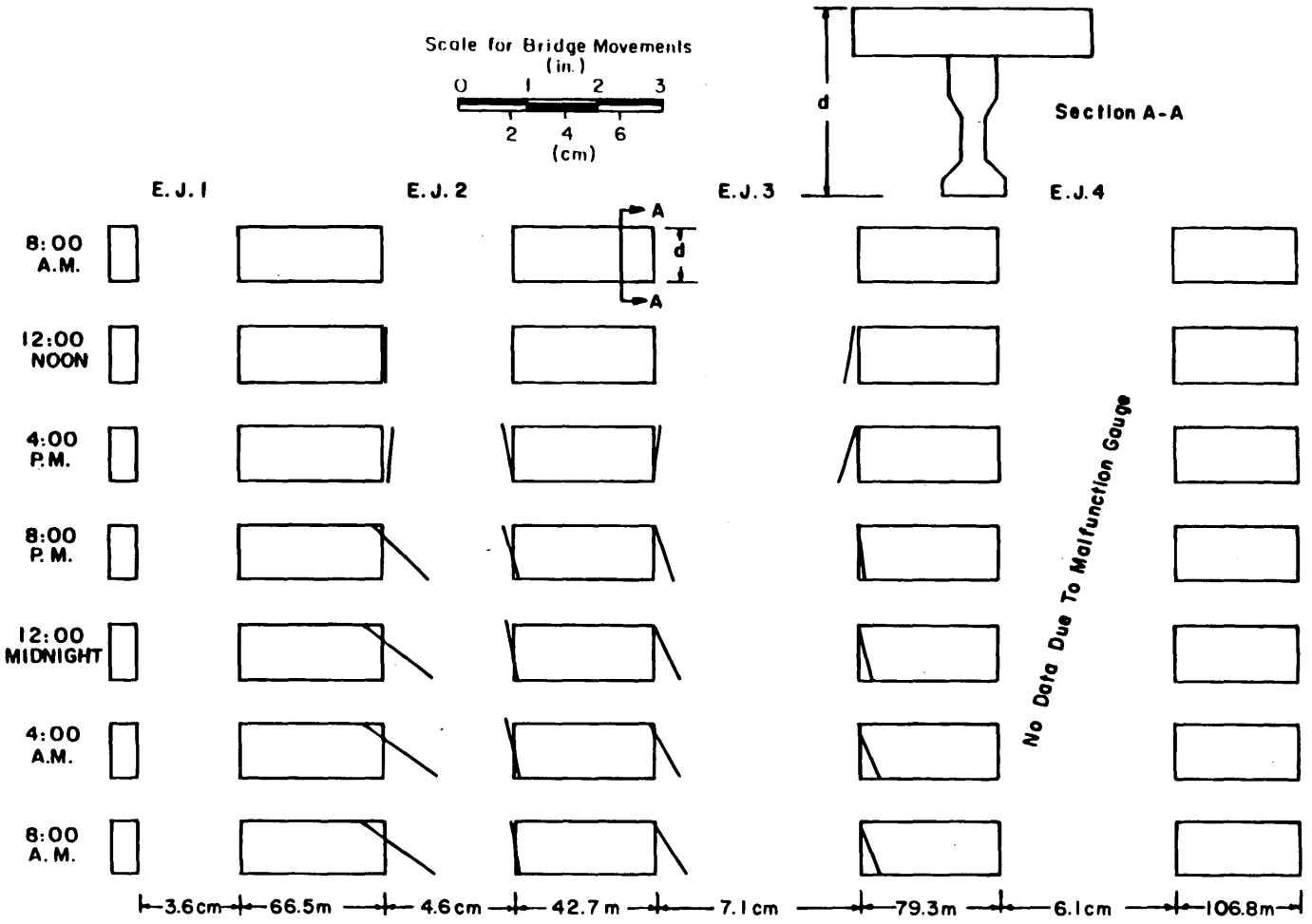

FIGURE 5 Elevation of south side girders showing 24-hr movements with respect to cap for October 22, 1987. (Note: Longitudinal dimensions of girders and joint spacings are not to scale, but actual end movements are to the scale indicated.)

sion joints for a 24-hr period. These movements are relative to the bent caps and are referenced to the first day of monitoring, which is October 22, 1987. The rectangles shown in Figures 4 through 8 represent, from left to right, the abutment and Bridge Units 1 through 4. The top row represents the initial position of the bridge units, and the subsequent rows represent the position of the bridge units at 4-hr intervals. The straight lines shown at the ends of each rectangle represent the movement of the unit for the given time. The scaled data shown in the figures can be easily used to compare with and verify the results of finite element programs or procedures predicting longitudinal bridge movements. The following observations can be made from 24-hr movements:

1. The bridge sections exhibit nonsymmetrical and nonreversible joint movements. This behavior can be attributed to restraints associated with the neoprene bearing pads;
2. There is a general seasonal repetitiveness of joint movements associated with seasonal temperature trends; and
3. There is no indication of rigid body translation.

The effects of support restraints on joint movements may be identified by comparing the joint movements obtained on two different days of similar bridge temperatures. The monitoring days of October 22, 1987, and February 21, 1988, were chosen for this comparison. The change in length at the top of the bridge units is obtained from the bridge movements shown in Figure 6 at 8:00 a.m. and adding the corresponding bent cap movements at each end of the units. Computations performed for Units 1 and 2 showed a shortening of 0.76 cm (0.3 in.) for Unit 1 and 0.51 cm (0.2 in.) for Unit 2.

The long-term movements of the expansion joints are summarized in Figure 9. The horizontal axis of the figure represents the time (day of monitoring). The vertical axis of the figure includes the ambient temperature and the movements of the expansion joints. The solid line represents the maximum opening of the joint, and the dashed line represents the minimum opening of the joint. The difference of the two lines represents the movement of the adjacent girders with respect to each other. The arrangement utilized in Figure 9 clearly shows the joint opening at each joint location relative to its position on October 22, 1987.

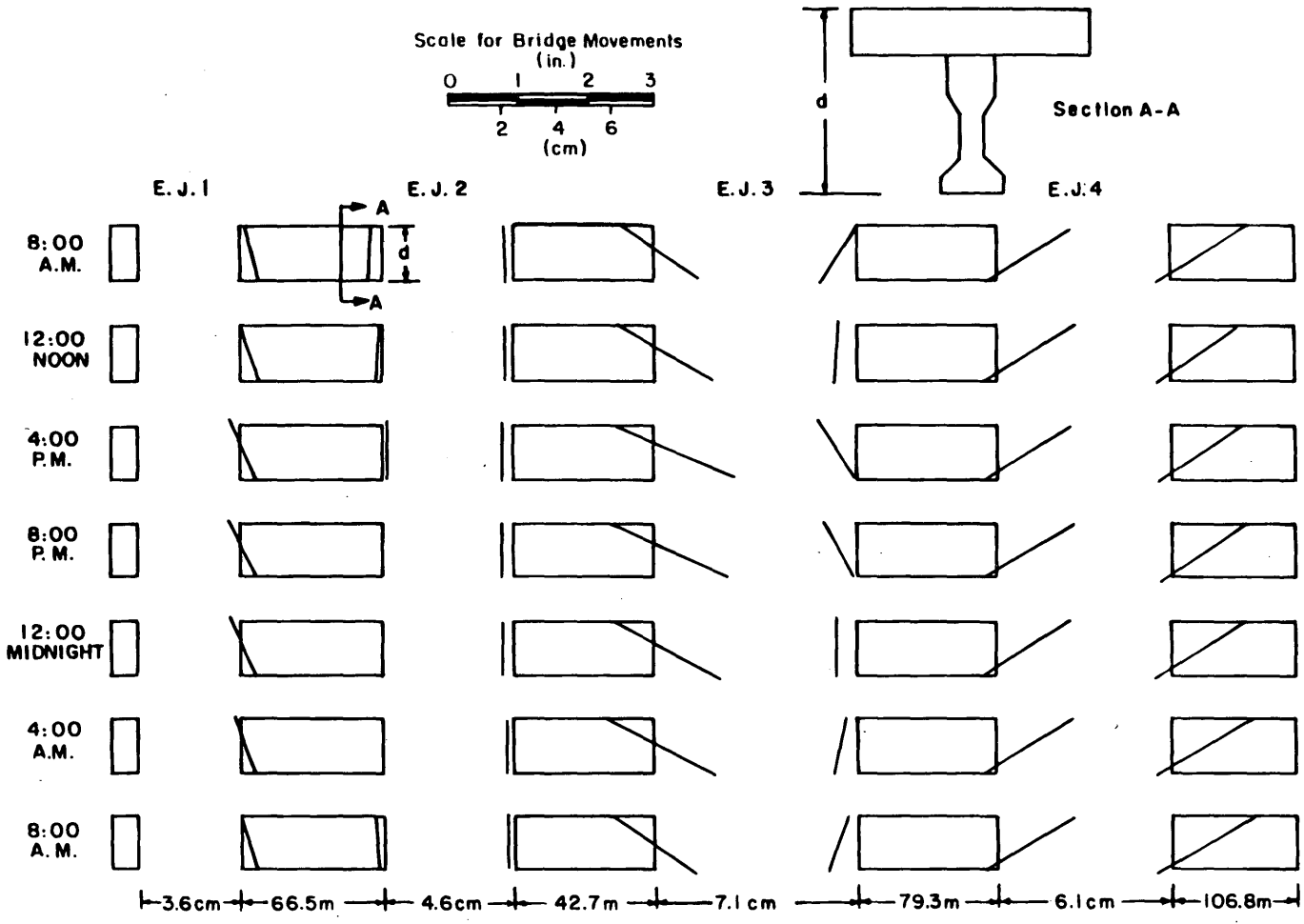

FIGURE 6 Elevation of north side girders showing 24-hr movements with respect to cap for February 21, 1988. (Note: Longitudinal dimensions of girders and joint spacings are not to scale, but actual end movements are to the scale indicated.)

The theodolite readings began early in the construction phase, before the LVDTs were placed on the bridge, to observe the long-term behavior of the bents. From the study of the bent behavior conducted the following were found: (*a*) The bents experienced negligible vertical movements; (*b*) the bent rotations were small and considered insignificant, and (*c*) the maximum longitudinal movements of the bents were smaller than the maximum movements of the girders.

COMPARISON OF MEASURED MOVEMENTS TO ESTIMATED MOVEMENTS

The 1983 AASHTO specifications provide guidelines for expansion of bridge members from temperature changes. These guidelines are generally adopted by the Louisiana Department of Transportation Bridge Design Manual, [LaDOTD (*1*)] where the design of expansion devices is based on bridge joint movements. The prediction of movement caused by thermal effects is obtained by multiplying the coefficient of thermal expansion by the length of the member and by the range of temperature (rise and fall). The movement caused by creep and shrinkage is estimated by multiplying the shrinkage coefficient by the length of the member.

These criteria were applied to estimate the movements of the Krotz Springs Bridge. These estimated joint movements are tabulated and presented in Table 2 along with the measured joint movements given previously in Table 1. It can be seen from Table 2 that the measured movements at Expansion Joints 1 and 2 have either reached or exceeded the estimated values, although they were obtained at temperature ranges approximately 30 percent lower than the ones used for the estimated movements. The movements of

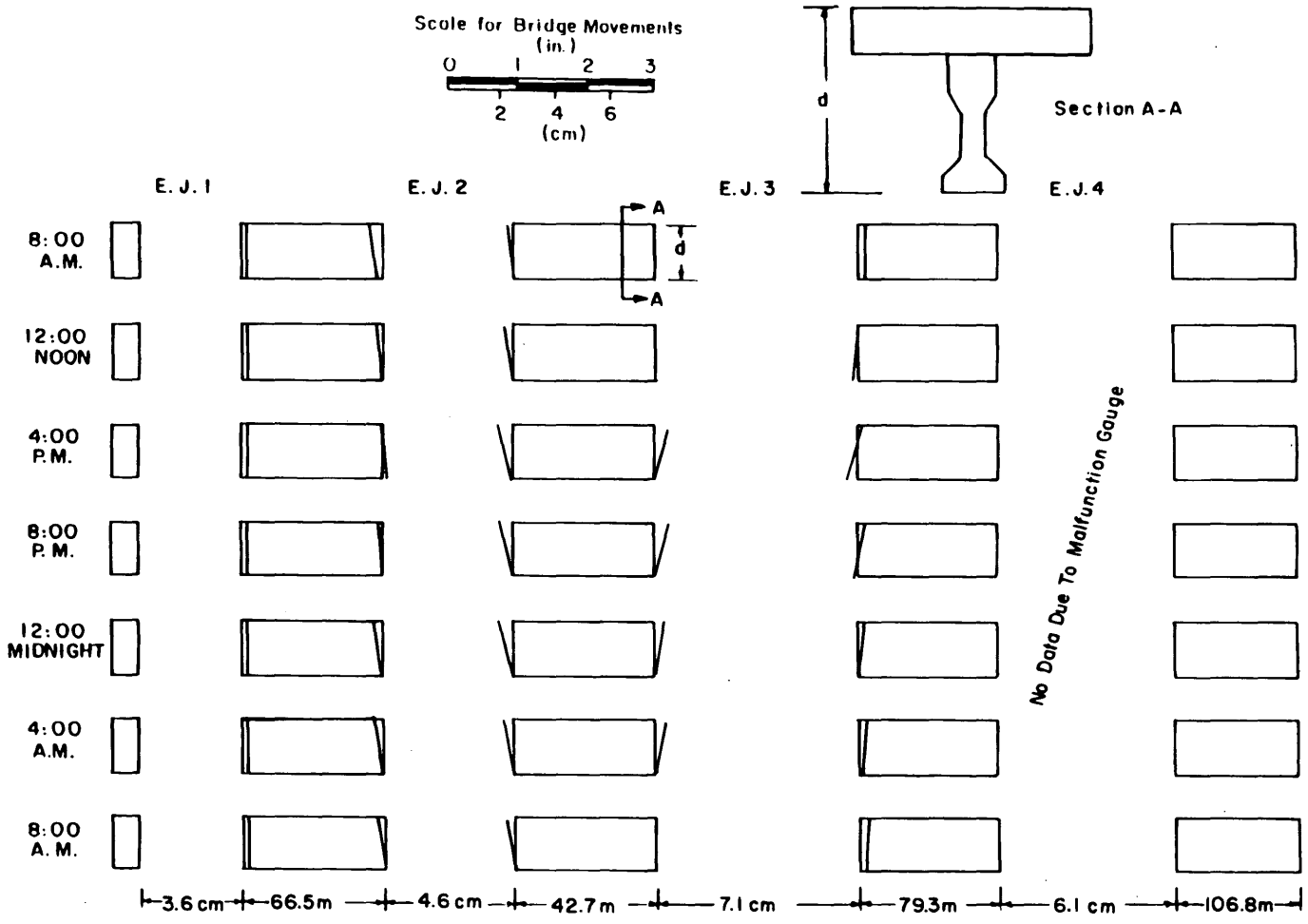

FIGURE 7 Elevation of south side girders showing 24-hr movements with respect to cap for February 21, 1988. (Note: Longitudinal dimensions of girders and joint spacings are not to scale, but actual end movements are to the scale indicated.)

Expansion Joints 3 and 4, however, are well below the estimated values.

CONCLUSIONS

A comprehensive experimental field study of longitudinal movements of bridge components was performed. Actual field monitoring extended over a 3-year period. Bridge movements were monitored from pouring of the bridge decks through 1 year of exposure to normal traffic. As a consequence bridge engineers have available to them data on the long-term longitudinal bridge behavior. These data can be utilized to test and verify computer models and procedures predicting longitudinal movements in bridges. The data gathered have significant implications on the future development of expansion joint design for bridges. In this regard the principal conclusions are as follows:

1. The primary causes of movements in the bridge decks obtained during the period of monitoring were caused by thermal effects. Since most instrumentation was not in place until 9 months after span construction, creep and shrinkage effects could not be monitored. The range of movements over the 21 months of monitoring with LVDTs was on the order of 1.3 to 3.6 cm (0.5 to 1.4 in.). Expansion joints at steel-to-concrete girder locations experienced approximately twice the movements of the concrete-to-concrete girder joints.

2. The results of the experimental study revealed the presence of restraining effects at the expansion joint supports. Stresses built up at the neoprene bearing pads as a result of thermal expansion were suddenly relieved when a certain stress level was reached or when an external force was applied. An example of this behavior was demonstrated when the release of thermal stresses built up at the pins of the steel truss river crossing section caused shock waves in the structure and aided in relieving stresses built up at the joint supports. This behavior was also seen during one of the days of traffic usage.

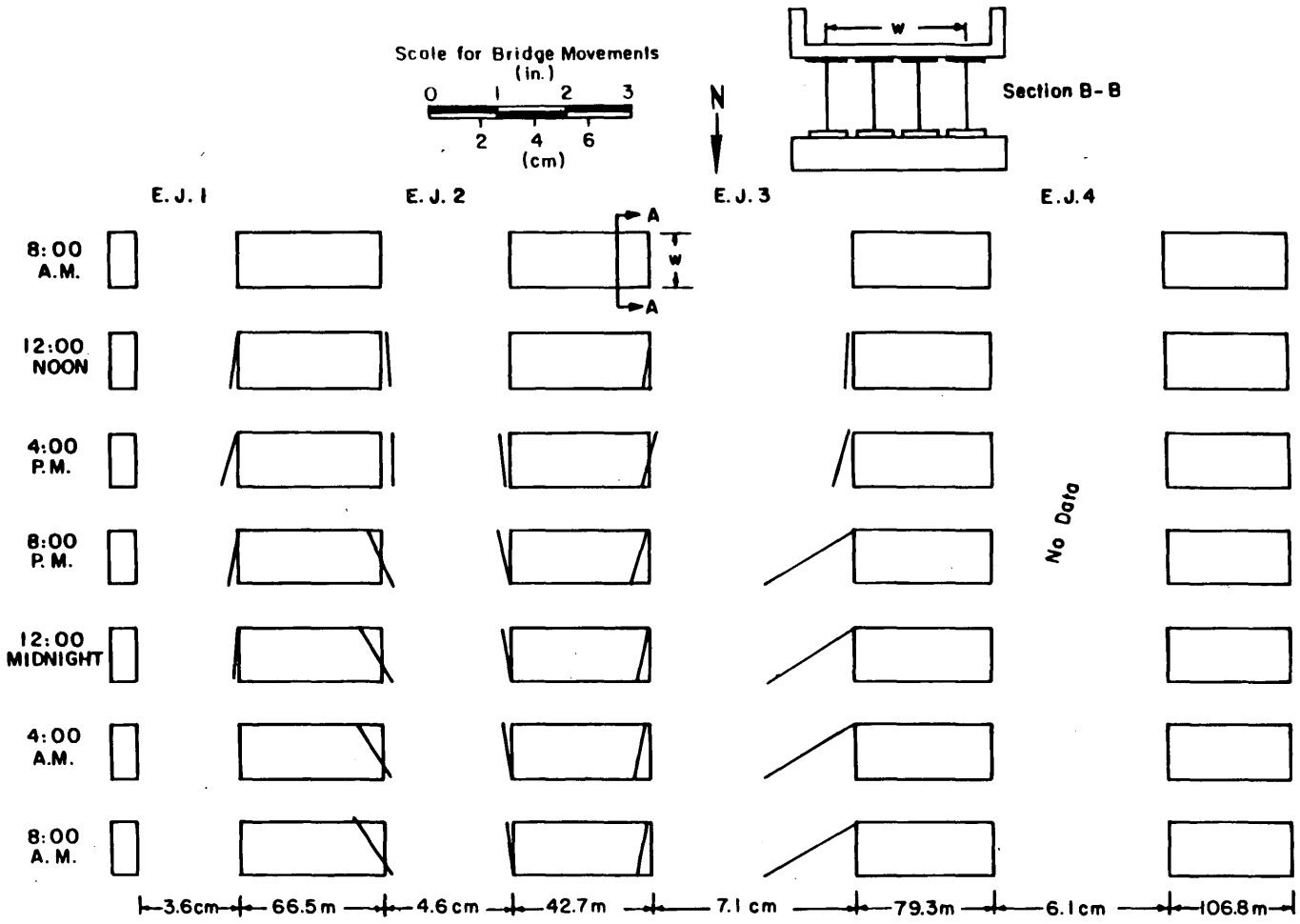

FIGURE 8 Plan view of bridge showing 24-hr movements of deck units with respect to cap for October 22, 1987. (Note: Longitudinal dimensions of girders and joints are not to scale, but actual joint displacements are to scale as shown.)

3. The bridge sections experienced unsymmetrical joint movements with the north side displaying larger movements. This unsymmetrical deformation can be attributed to restraints associated with the neoprene bearing pads. Measurements showed that the bridge temperatures on the north and south sides of the bridge were similar and thus did not contribute to the unsymmetrical deformation. This pattern further supports the previous conclusion that significant restraints exist at the joint supports.

4. The bridge underwent nonreversible joint movements. It was observed that in many cases the bridge sections did not return to their initial positions as temperatures rose and fell to their initial values. This behavior was evident over the 24-hr monitoring cycles as well as over the long-term seasonal period. The nonreversible movements are attributed to the restraining effects present at the joint supports. There was no consistent pattern in this behavior, further substantiating the preceding two conclusions.

5. Although nonreversible behavior was observed, a general seasonal repetitiveness of joint movement behavior occurred, which was in agreement with the seasonal temperature trends.

6. The bridge sections showed no signs of rigid body translation. There was no tendency of the bridge to move downhill over time.

7. Bents under expansion joints responded to, but did not contribute to joint movements. The bents experienced negligible vertical movements and small rotations. In addition, the maximum longitudinal movements of the bents were smaller than the movements of the girders, which indicates that the bents were moving along with the girders during thermal expansion and contraction.

8. The data acquired over the 9-month period after the bridge was opened to traffic indicated no discernable effects caused by traffic loads. However, to more fully evaluate these effects, monitoring over a longer period of time is required.

9. A comparison of measured joint movements with those estimated by the current LaDOTD procedures did not indicate a consistent pattern. In some cases the LaDOTD recommendations overestimated the movements but in other cases under-estimated them.

10. Measurements with LVDTs proved to be the appropriate method for investigating joint movements. Theodolite measurements had limited value and proved inefficient.

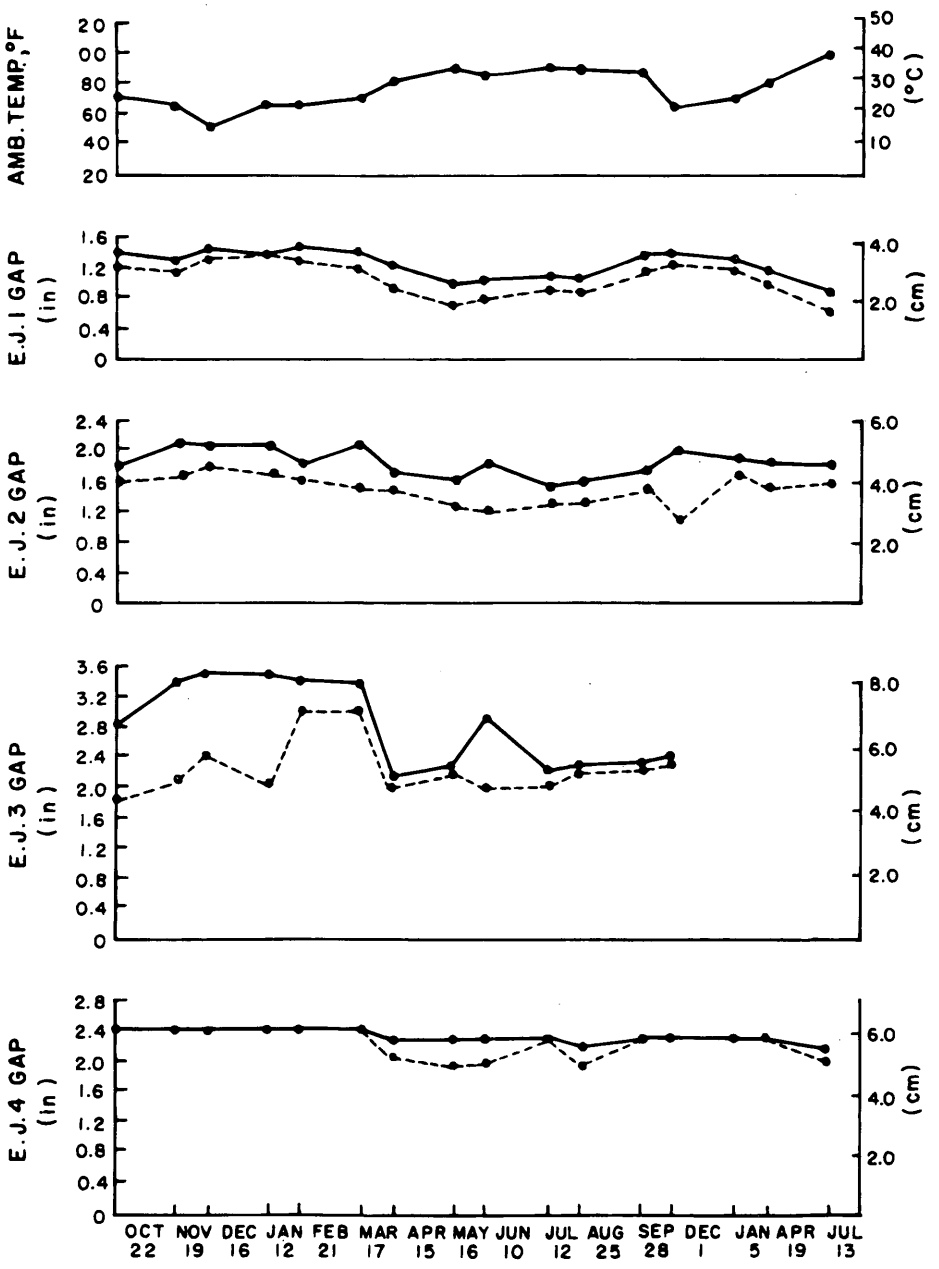

FIGURE 9 Summary of long-term movements obtained from LVDTs at north side of Joints 1-4.

TABLE 2 Comparison of Measured and Estimated Movements in Centimeters

Joint Location	Measured Movements (with LVDT's)	Estimated Movements*	
		Thermal	Total
E.J. 1	2.03	1.40	2.06
E.J. 2	2.41	1.40	2.06
E.J. 3	3.56	5.00	6.22
E.J. 4	1.40	3.91	5.77

2.54 cm = 1 inch

*Estimated movements based on LDOTD procedures which include creep & shrinkage as well as Thermal (shown separately).

REFERENCES

1. *Bridge Design Manual*, 3rd ed. LaDOTD, Baton Rouge, 1987.
2. Purvis, R. L., and Berger, R. H. Bridge Joint Maintenance. In *Transportation Research Record 899*, TRB, National Research Council, Washington, D.C., 1983, pp 1–10.
3. Kinchen, R. W., W. H. Temple, W. T. Burt III, and D. G. Azan. Evaluation of Joint Sealant Materials. Research Report 105. Louisiana Department of Transportation and Development, Baton Rouge, 1977.
4. Kozlov, G. S. Preformed Elastomeric Joint Sealers for Bridges-Phase II: Compression Sealers for Joints. Report FHWA/NJ-80/003, New Jersey Department of Transportation, 1978.
5. Howard, Needles, Tammen, and Bergendoff. *NCHRP Report* 204: Bridge Deck Joint Sealing Systems, Evaluation and Performance Specifications, TRB, National Research Council, Washington, D.C., 1979.
6. Kozlov, G. S., and B. Kosaboom. Preformed Elastomeric Joint Sealers for Bridges. In *Transportation Research Record 651*, TRB, National Research Council, Washington, D.C., 1983, pp. 53–64.
7. Price, R. Expansion Joints Using Elastomeric Concrete Nosing Materials—Texas Experience. *Proc., 2nd World Congress on Joints and Bearings*. ACI Special Publication SP-94. San Antonio, Texas, 1986, pp. 747–764.
8. Reynolds, J. C., and J. H. Emanuel. Thermal Stresses and Movements in Bridges. *Journal of Structural Division, ASCE*, Vol. 100, No. 1, 1974, pp. 63–78.
9. Dillon, E. W., and R. J. Kissane. Annual End Movements of Prestressed Concrete Bridges. Final Report. FHWA, U.S. Department of Transportation, New York, 1978.
10. Abdul-Ahad, R. B. Effects of Restrained Thermal Movement in a Continuous, Prestressed Concrete Bridge Without Interior Expansion Joints, Ph.D. Dissertation. Department of Civil Engineering, University of Tennessee, Nashville, 1981.
11. Moulton, L. K., and J. R. Kula. Bridge Movements and Their Effects. *Public Roads*, Vol. 44, No. 2, 1980, pp. 62–75.
12. Mortlock, J. D. *The Instrumentation of Bridges for the Measurement of Temperature and Movement*. TRRL Laboratory Report 641. U.K. Transport and Road Research Laboratory, Crowthorne, Berkshire, England, 1974.
13. Emerson, M. Thermal Movements of Concrete Bridges: Field Measurements and Methods of Prediction. *Joint Sealing and Bearing Systems for Concrete Structures*. ACI Special Publication SP-70. Vol. 1, Detroit, 1971, pp. 77–102.
14. Pentas, H. A., R. R. Avent, V. K. A. Gopu, and K. J. Rebello, Field Study of Bridge Temperatures in Composite Bridges. In *Transportation Research Record 1460*, TRB. National Research Council, Washington, D.C., 1994, pp. 45–52.
15. Pentas, H. A. Experimental Investigation of the Longitudinal Movements Associated with Highway Bridge Joints. Ph.D. Dissertation. Department of Civil Engineering, Louisiana State University, Baton Rouge, 1990.
16. *Standard Specifications for Highway Bridges*, 13th ed. AASHTO, Washington, D.C. (with Interim Specifications, 1984, 1985, 1987–1988), 1983.

Publication of this paper sponsored by Committee on Dynamics and Field Testing of Bridges.

Issues in Rating Steel-Stringer Bridges

A.E. AKTAN, D.N. FARHEY, AND V. DALAL

Nondestructive dynamic field testing and structural identification studies on three steel-stringer bridges (2, 20, and 43 years old) are presented. The bridges were rated by code procedures and by field-calibrated comprehensive three dimensional finite element models developed by structural identification. Experimentally measured and analytically simulated modal flexibilities were correlated with bridge deflections obtained under proof-load level truck load tests. Test results indicated that all three bridges, although constructed as noncomposite, exhibited composite action between the slab and girders. Although the composite action was nearly perfect in the 2-year-old bridge, the older bridges exhibited partially composite behavior caused by deterioration of the chemical bond and friction. The rating factors obtained by field-calibrated models exceeded the corresponding operating rating factors by about 2.5 to 4 times for the three test bridges. The rating process and the resulting factors helped to identify and conceptualize a number of unresolved important issues that influence bridge rating and management. Serviceability aspects that emerged as critical were studied through the relative contributions of various mechanisms to bridge deflections.

The AASHTO manual (*1,2*) guides most state Department of Transportation (DOT) operations related to the routine biannual inspection and rating of bridges. Consequently, condition indexes assigned by visual inspection influence critical bridge management decision about repairs, posting, rehabilitation, and replacement. In 1994, FHWA officials estimated a financing need of $90 billion to repair the bridges deemed deficient on the basis of visual inspection results.

Recent related NCHRP research projects (*3–8*) have led to the AASHTO guide (*9*) and the draft Load and Resistance Factor Design (LRFD) specifications (*10*). Others, such as Lichtenstein (*8*) and Galambos et al. (*11*), have recommended significant revisions and modifications to the AASHTO manual (*1,2*) and AASHTO guide (*9*) with respect to condition assessment and rating. A new Manual for Condition Evaluation of Bridges has been issued by AASHTO (*12*).

The AASHTO guide (*9*) encourages the use of facility-specific information in rating a bridge as well as experimentally calibrated analytical models. However, organizational and technical consensus methods need to be established for (*a*) generating bridge-specific objective information to adequately document a bridge's structural and loading conditions; and (*b*) modeling and simulation to reflect the actual loading environment, existing structural conditions, and all the critical structural response mechanisms of a bridge.

A. E. Aktan and D. N. Farhey, Department of Civil and Environmental Engineering, Cincinnati Infrastructure Institute, 741 Baldwin Hall, P.O. Box 210071, University of Cincinnati, Cincinnati, Ohio 45221-0071. V. Dalal, Bureau of Research and Development, Ohio Department of Transportation, Columbus, Ohio 43216-0899.

CONDITION ASSESSMENT AND RATING OF STEEL-STRINGER BRIDGES

Appreciation of bridge behavior has evolved through allowable stress design (ASD), load factor design (LFD), and alternate load factor design (ALFD) (*11*). The corresponding rating provisions for ASD, LFD, and ALFD are respectively based on an evaluation of the ratio of the maximum stresses to their allowable counterparts, the cross-sectional force demands to the corresponding cross-sectional strength capacities, and the structural load demands to the capacity of a plastic mechanism. The recently issued draft LRFD specifications (*10*) require an explicit check of capacity and performance at all the critical limit states, including serviceability, fatigue, stability, deterioration, and collapse.

Hence, according to the spirit of the draft LRFD code provisions (*10*) and the AASHTO guide (*9*), it is desirable to use field-calibrated models and to evaluate performance at all of the critical limit states, including serviceability. The issue remains in the development of field-testing methodology and field-calibrated models that will allow rating a bridge and checking its serviceability. The main obstruction to objective condition assessment and rating has been lack of complete understanding of how bridges actually respond to many different external and intrinsic loading effects, actual contributions of different load-resisting mechanisms, their relative variation at different loading stages, and effects of aging and deterioration on both the load demands and capacities. The lack of a clear understanding of a bridge response also makes it difficult to formulate realistic and precise definitions for the structural limit states and the performances expected at these limit states.

OBJECTIVES AND SCOPE

Integrated analytical-experimental structural identification research has been conducted on a number of highway bridges in Ohio (*13–19*), on the basis of dynamic modal and truck load tests, development of field-calibrated finite-element models, and rating of bridges by a variety of linear and nonlinear analyses and limit-state definitions. Observations and findings from such research raise the need to review some concepts and applications proposed by the recent NCHRP reports (*8,11*).

The first objective of this paper is to discuss the characteristic problems in condition assessment of steel-stringer highway bridges with their specific resistance mechanisms. The second objective is to review the critical issues in rating steel-stringer bridges. The discussion focuses on steel-stringer bridges because this type composes the largest segment of the bridge population in the nation and more than one-third of nearly 40,000 bridges in Ohio.

Three steel-stringer bridge test specimens were evaluated and rated by field-calibrated models. The nondestructive tests conducted for structural identification included modal tests by impact

as well as vertical and lateral forced excitation, followed by truck load tests for measuring global and local bridge response under different static loading patterns. The results of these experiments helped improve an understanding of some obscure local response mechanisms that significantly influenced bridge behavior at the service limit states.

STRUCTURAL IDENTIFICATION METHODOLOGY FOR INTEGRATING CONDITION ASSESSMENT AND RATING

The comprehensive bridge research project has been organized to solve the following issues before new inspection and rating tools are developed: (*a*) identification of the most important mechanisms that affect bridge behavior at different limit states and their proper incorporation into design, inspection, evaluation/rating, and maintenance management; (*b*) investigation of age and deterioration effects on these mechanisms; (*c*) verification of the possibilities to measure short-term and long-term bridge behavior in the field accurately and completely, and to develop experimental condition-assessment techniques that would help to reliably establish the global state of health of a bridge; (*d*) integration of rating with such an experimental condition-assessment procedure; and (*e*) development of analytical techniques that would reliably project the existing capacities of a bridge and its remaining service life from the results of experimental condition assessment.

The important issue is to design a comprehensive methodology that would integrate an objective condition assessment with bridge rating and life-cycle maintenance management. This research has led to an attempt to develop a bridge structural-identification methodology that integrates analytical modeling, experiment, damage diagnostics, and rating into a rational framework. A schematic of the methodology is given in Figure 1, entailing the following steps:

1. For a particular bridge, researchers first compile all of the information that exists on the original design, fabrication/shop and as-built drawings, and construction details, followed by maintenance records. The current conditions of the structure are documented and a preliminary finite element model is constructed.
2. The researchers use the a priori analytical model to design a modal test and conduct a pilot modal test labeled to calibrate the experiment. The pilot test typically does not require traffic control.
3. A rigorous modal test follows. This test is generally conducted by impact; however, in the case of flexible bridges, such as long span through truss or suspension bridges, forced excitation may be needed. Moreover, in case the lateral response characteristics of the

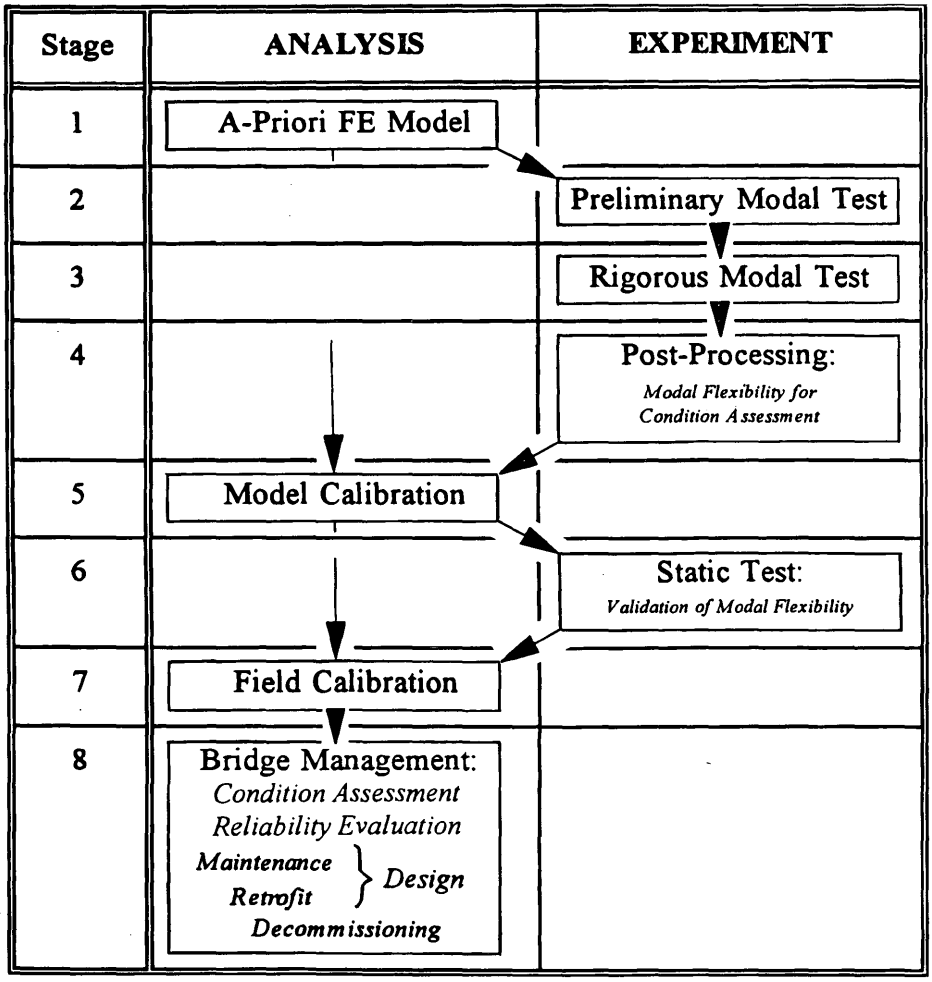

FIGURE 1 Structural identification method for bridge management applications.

bridge are included in the evaluation, forced excitation may have advantages over impact. The rigorous test requires traffic control; however, if impact is used the bridge may be tested in parts so that one or more lanes may be continuously kept open to traffic.

4. Post-processing the modal test data provides a wealth of information about the mechanical characteristics of the bridge: frequencies, damping coefficients, mode shapes, and most importantly, bridge flexibility. The flexibility from the modal test serves as a reliable objective bridge signature that is sensitive to damage and is typically more than 90 percent reliable if testing and post-processing are properly planned and carried out by experienced engineers.

5. and 6. After a complete evaluation of the bridge conditions by studying the flexibility, if needed, an improved understanding of local bridge behavior is gained by additional instrumentation and measurement under truck loads. The researchers calibrate the finite element model such that the existing state and all the critical global and local behavior mechanisms are captured and simulated accurately.

7. The field-calibrated model then serves for reliable rating, projections of capacities, and design of effective maintenance, rehabilitation, or retrofit. The researchers have tested several bridges to damage and failure to demonstrate the reliability of the projected behavior and rating coefficients obtained by the methodology (*15–17,19*).

This methodology is intended as a research tool and is not for routine implementation on every bridge. Once the researchers test a sufficient number of samples from a recurring bridge type, a considerable amount of generic information is gained. This helps to design more practical experiments on other samples for routine applications. The generic bridge- and type-specific knowledge obtained from the applications of the methodology to a selected number of bridges provides an invaluable understanding of behavior fundamentals.

STEEL-STRINGER BRIDGE TEST SPECIMENS

The three steel-stringer bridge specimens, shown in Figure 2, were the HAM-42-0992, CLE-50J-0080L, and HAM-128-1006, which were, respectively, 2, 20, and 43 years old at the time of testing. Table 1 describes the main features of the three specimens, which represent a wide variety of continuous steel-stringer bridge design parameters related to girder spacing, spans, bearings, and abutments. All of the bridges were designed as noncomposite, that is, mechanical connectors were not provided between the steel girders and the concrete deck. None of the bridges had been rehabilitated for maintenance after construction or maintained with deck overlay.

STRUCTURAL IDENTIFICATION AND CONDITION ASSESSMENT OF TEST BRIDGES

The bridge structural identification methodology described earlier was applied to each of the three specimens, resulting in a field-calibrated three-dimensional (3-D) finite element model specific to each bridge. HAM-42-0992 was subjected to truck load testing after installing 64 channels of local strain and displacement instrumentation to verify the modal test results and to better understand the complex bearing pad and integral abutment response mechanisms. The structural identification results for HAM-42-0992 were reported earlier (*18*). An important finding from the structural identification of HAM-42-0992 and CLE-50J-0080L was related to composite behavior. Bridge displacements found by applying a uniform load to the measured flexibility were correlated with the resulting deflections simulated by the calibrated finite element model. Because the deflections from the finite element models, simulating rigid connections between the deck and the girders, closely correlated with those obtained from the experimentally measured flexi-

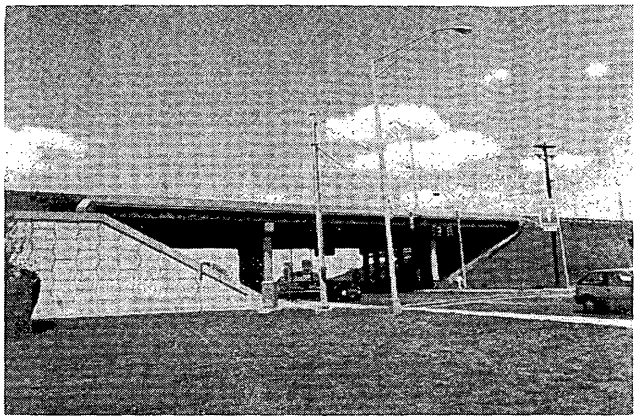

(*a*)

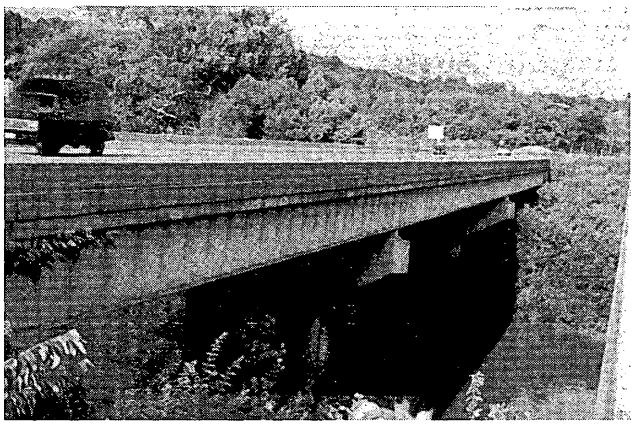

(*b*)

(*c*)

FIGURE 2 Steel-stringer test bridges: (*a*) HAM-42-0992; (*b*) CLE-50-J-0080L; (*c*) HAM-128-1006.

TABLE 1 Important Attributes of Tested Steel-Stringer Bridges

Bridge Features	HAM-42-0992 Cross County Highway	CLE-50J-0080L Little Miami River	HAM-128-1006 Paddy's Run
Construction year	1986	1970	1950
Design code	1983 AASHTO	1969 AASHTO 10th Ed.	N/A
Design loads	HS20-44	HS20-44	S-15-46
Number of Spans	3 (continuous)	3 (continuous)	3 (continuous)
Span lengths ft (m)	55, 78, 55 (16.8, 23.8, 16.8)	100.5, 125.5, 100.5 (30.6, 38.3, 30.6)	40, 50, 40 (12.2, 15.2, 12.2)
Roadway width ft (m)	42 (12.8)	50 - 55 (15.2 - 16.8)	33' 4" (10.2)
Skew	15° 11' 16"	32° 30' 00"	25°
Type of steel	ASTM A-36	ASTM A-36	N/A
No. of steel girders	6	7	5
Girder spacing (m)	7' 9" (2.36)	9' 6" - 10' 11.5" (2.90 - 3.34)	7' 4" (2.24)
Girder depth in. (m)	36 (0.91) W-flange beam	62 (1.57) plate girder	30 (0.76) W-flange beam
Capacity design	Noncomposite	Noncomposite	Noncomposite
Deck thickness in. (m) included surface layer	8.5 (0.216) 1.25 (0.032) latex modified	9 (0.229) 1 (0.025) monolithic	7.25 (0.184) 3/4 (0.019) monolithic
Design f_c' psi (MPa)	4500 (31)	4000 (28)	4000 (28)
Transverse reinforcement (%)	top = 0.71 bottom = 0.50	top & bottom = 0.74 to 0.83	top = 0.53 bottom = 0.71
Longitudinal reinforcement (%)	top = 0.24 bottom = 0.52	top = 0.28 bottom = 0.61	top = 0.24 bottom = 0.38
Pier support	elastomeric pads	rocker & bolster	sliding plate
Abutment support	full integral	rocker & bolster	sliding plate

bilities of HAM-42-0992 and CLE-50J-0080L, it was inferred that these two bridges were exhibiting perfect composite behavior. This inference was verified by measuring the strain profiles along the girders and deck-girder interfaces of HAM-42-0992 under truck loads that confirmed the composite behavior (*18*).

The finite element model for HAM-128-1006 and the simulated deflections along one of the girders under uniform loading of the measured and analytical model flexibilities are shown in Figure 3. The field-calibrated model is partially composite. It is observed that the measured and analytical flexibilities of this bridge correlate when a partial continuity between the deck and the girders is simulated in the analytical model, that is, a partial composite behavior. Moreover, at the northeast (right) end span, the measured flexibility is larger than the simulated one, whereas in the other spans the correlation is better. This reveals that the northeast end span has retained a lesser chemical bond and friction between the girder and slab relative to the other two spans. Figure 3 illustrates that one could discern regions that may have deteriorated more than others. It is important to note that the measured flexibility is about 10 percent more than in the case of simulated perfect composite action and 10 percent less than when no composite action is simulated. This characteristic is shown to have a significant effect on the serviceability and rating of the bridge.

NCHRP RECOMMENDATIONS FOR NONDESTRUCTIVE TESTING AND RATING

Lichtenstein, in the draft final report of an NCHRP paper (*8*), proposed a general scheme for diagnostic and proof testing of bridges together with expressions that would be used for arriving at a test-based rating factor. The recommendations in the report are applicable to truss bridges as well as others. Lichtenstein (*8*) defines diag-

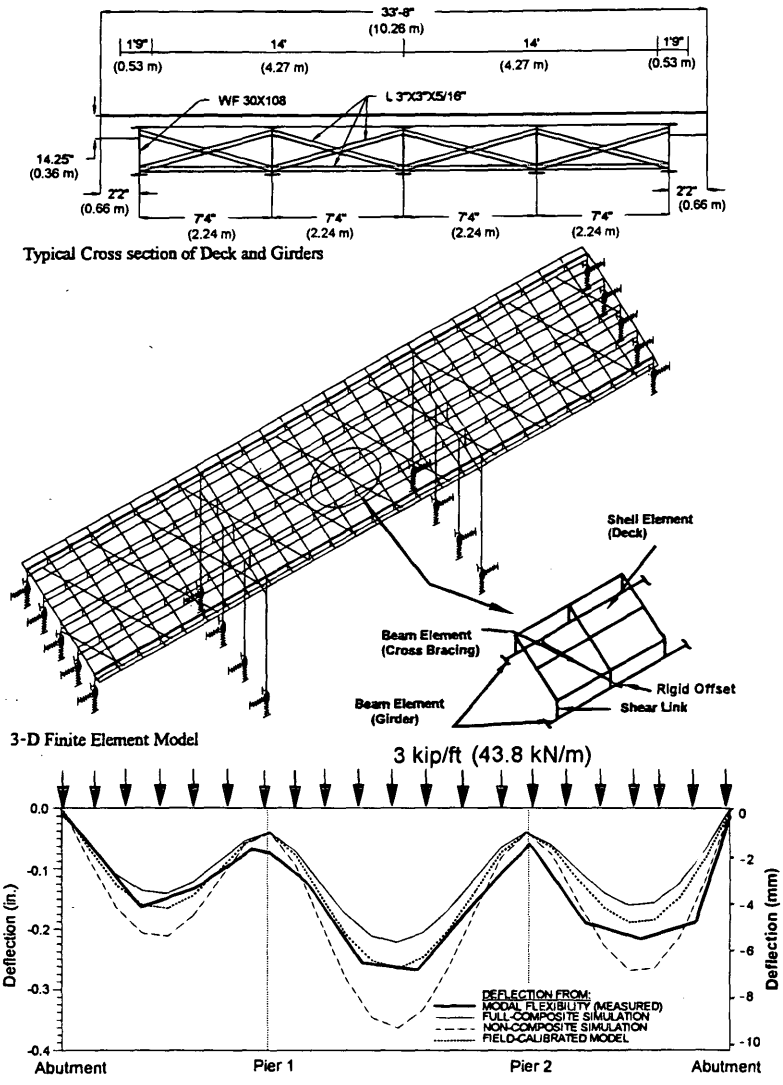

FIGURE 3 Finite element model and simulated deflections for HAM-128-1006.

nostic tests as those conducted to verify predicted or nominal load effects. These tests are recommended for validating a model to rate a structure under design, legal, permit, or rating loads. Assumptions about material properties, boundary conditions, cross-section contributions, effectiveness of repair, impact of damage, and deterioration, among others, may be validated by diagnostic tests. Diagnostic testing is acknowledged to be much more elaborate than proof testing because both an analytical model and more stringent field measurements are required.

The load placement and load levels in a diagnostic test may be less than those at service load levels. However, the test should be conducted to rule out any possible nonlinearities at the service load level. After the test, the theoretical rating factor, which would be obtained prior to the diagnostic test, is multiplied by a factor K, which is larger than or equal to unity. This factor is based on the comparison of measured test behavior with the analytical model adjusted for site-specific considerations.

Lichtenstein's formulation (*8*) for making the best use of a diagnostic test for bridge rating is a significant contribution to the state of the practice. However, a large number of example applications and verifications are needed before the method is fully calibrated and the details of practical and meaningful applications can be streamlined. For example, suppose rating is based on an extremely idealized analytical model that ignores a number of relevant mechanisms that affect load distribution and the resistance of the critical element. Can this type of analytical deficiency be rectified by a diagnostic load test?

The following are some additional questions that come to mind: What if the critical element of the bridge is not properly identified or if the instrumentation is not properly designed and installed to capture the critical stress in the critical element? How should the load be placed to activate the most critical actions in the most critical element, particularly if the bridge has damage or deterioration or both? How would the bias and variance errors in the experimental results be evaluated? Obviously, the minimum qualifications and experience of a test team that can be entrusted with a diagnostic test should be clearly established and certified before a theoretical rating factor may be legally modified.

The experience of the authors based on the research reported here is that the strains measured during a diagnostic test have to be reli-

able within 20 με (the authors' truck load tests on reinforced concrete slab, steel-girder, and truss bridges have revealed that the critical strains in most bridges under legal trucks will correspond to 20 to 100 με). Typically, a temperature change of several degrees may lead to comparable strains. Further specifications are needed for bridge instrumentation and diagnostic testing to benefit from NCHRP recommendations (*8*).

RATING OF TEST BRIDGES

The three test bridges were rated by the procedures followed by the Ohio Department of Transportation (ODOT) bridge bureau and based on the AASHTO Manual (*1,2*). The bridges were also rated by using the field-calibrated analytical models that were developed by structural identification. The field-calibrated finite element models simulated the 3-D geometry and incorporated all of the structural and nonstructural elements, as shown in Figure 3: reinforced concrete deck, cover plates, cross braces, parapets, abutments, piers, support and continuity including the composite action, flexibility at the interface with the integral abutment, flexibility at the pads, soil-pile interaction flexibility, and flexibility characteristics of each individual element of the bridges.

As the test bridges were rated by bridge-specific models, a number of important issues had to be resolved. Table 2 provides an overview of the issues in demand and capacity computation that are needed for rating. In computing demands, the main issues are analytical modeling, selection of linear or nonlinear analysis options and the corresponding software, simulation of live load, and interpretation of the results from analysis. In the case of capacity computation, the issues have to do with the approach, that is, whether ASD, LFD, or ALFD are to be adopted; incorporation of actual material properties and existing state of damage or deterioration or both; selection of linear or nonlinear analysis to compute capacity of materials, sections, or the complete structure; and interpretation of the results.

Clearly, there are many possible options and decisions to make in the rating process, and the analytical aspects of the process are complex in the case of bridge-specific rating on the basis of field-calibrated models. The field calibrated rating factors given in Table 3 were obtained by using linear analysis of the field-calibrated 3-D finite element models in conjunction with the load factor approach recommended by the AASHTO guide (*9*). Critical trucks and their positions were established on the basis of 3-D influence lines generated by using the 3-D finite element models. In computing capacity, nominal material properties were used. For calculating the flexural capacity of the composite or semicomposite girder-slab sections, a 3-D nonlinear section analysis software 3-DRCSA (*20*) was used.

IMPLICATIONS OF RATING FACTORS

The rating factors obtained for all the three test bridges (Table 3) reveal that those that are based on field-calibrated models exceed the corresponding rating factors obtained by ODOT procedures by

TABLE 2 Issues in Rating Steel-Stringer Bridges

Definition of Limit State and Analysis Approach (ASD,[a] LFD,[b] ALFD,[c] or LRFD[d])	
DEMAND COMPUTATION	**CAPACITY COMPUTATION**
(1) Analytical Modeling (a) Dimensional idealization (1-D, 2-D, or 3-D) (b) Member discretization (c) Boundary conditions (d) Continuity conditions (e) Analytical elements (f) Actual material properties (g) Existing damage and deterioration	**(1) Analytical Approach** (a) Local stress (b) Section capacity (c) Structural capacity (d) Actual vs. nominal material properties (e) Existing damage and deterioration
(2) Selection of Analysis Package (a) Linear or (b) Nonlinear	**(2) Selection of Analysis Package** (a) Nonlinear Cross-Sectional Analysis vs. (b) Finite-element analysis for different actions and failure modes
(3) Simulation of Live Load (a) Critical trucks (b) Truck configurations on the bridge (c) Truck loading and impact (d) Fatigue effect	**(3) Interpretation of Analytical Results** (a) Limit state considered for defining capacity (b) Localized stresses (c) Effective cross-section resultants (d) Structural strength capacity (e) Serviceability and fatigue considerations
(4) Interpretation of Analytical Results (a) Nodal forces/stresses (b) Localized stresses (c) Effective cross-section resultants (d) Structural demands and limit states considered	

Notes:
[a] Allowable Stress Design;
[b] Load Factor Design;
[c] Alternate Load Factor Design;
[d] Load and Resistance Factor Design.

TABLE 3 Rating Results for Test Bridges

Bridge	HAM-42-0992 Cross County Highway			CLE-50J-0080L Little Miami River			HAM-128-1006 Paddy's Run		
Procedure	M^+	M^-	M^-/M^+	M^+	M^-	M^-/M^+	M^+	M^-	M^-/M^+
AASHTO *Manual* (1983) BARS 1-D Model	1.64	2.14	1.30	1.27	1.62	1.28	1.57	1.63	1.04
AASHTO *Guide* (1989) Identified 3-D FEM	6.00	5.39	0.90	5.14	5.24	1.02	4.93	5.19	1.05
Ratio: *Guide/Manual*	**3.66**	**2.52**	0.69	**4.05**	**3.23**	0.80	**3.14**	**3.18**	1.01

Notes:

(1) All procedures consider Strength Limit State;

(2) Impact Factors specified according to AASHTO *Manual* are used in computing all of the rating factors.

about 2.5 to 4 times. It is important to note that if an inelastic rating approach such as one proposed by Galambos et al. (*11*) was adopted, the level of conservatism in the rating factors obtained from typical DOT practice would be even larger. From another perspective, whether inelastic rating would lead to more accurate rating factors, if it is not based on a field-calibrated model that incorporates all the critical elements of the bridge, is questionable.

The extreme conservatism in the rating factors based on typical DOT practices would have an important implication in permit load requests, which may be presently denied. Table 3 further reveals a lack of balance in positive and negative moment rating factors from the 1-D models other than for HAM-128-1006, whose negative and positive moment factors are closest to each other, as indicated by their ratios. In the rating factors based on field-calibrated models, all the structural and nonstructural elements were incorporated, including the cover plates provided for the splices over the bearing plates for the negative moment. The actual balance ratios of negative-to-positive moment capacities from the field-calibrated models are much closer than those from 1-D models.

Other observations from this bridge-specific rating research are (*a*) damage or deterioration, or both, as a result of aging affect demand and capacity and, more importantly, the failure mode; (*b*) the reinforced concrete deck affects both demand and capacity by its two-way flexural and shear capacities and, more importantly, by the compressive membrane forces that develop as a result of composite or partial composite action; (*c*) cross braces significantly affect demand, particularly in the negative moment regions; (*d*) composite action caused by chemical bond or friction, or both, between slab and girders, even without mechanical connectors, affects demand and capacity; (*e*) abutment fixity affects demand; and (*f*) deck parapets, beam cover plates, and size and flexibility of bearing elements are mechanisms that affect demand and capacity.

Present rating methods use analytical models that typically omit the reinforced concrete slab and the parapets as well as the lateral load distribution provided by the brace system. The composite action is also neglected if mechanical connectors are not provided. Bridge engineers generally justify omitting the composite action in noncomposite designs on the basis of the argument that the chemical bond and friction would be lost over time. On the other hand, this research has shown that a considerable level of composite action has been maintained even 40 years postconstruction. In fact, there is evidence that in the case of complete loss of composite action, stringer bridges lose a considerable amount of stiffness and the decks become unserviceable. More importantly, by omitting the slab, the interface of the slab with the girders, and the cross braces in the rating models, the DOTs are not evaluating the actual performance of these components, which are emerging as important as the girders for serviceability in conjunction with lifetime-cost management considerations. Clearly, the uncertainties in the rating factors and a lack of addressing serviceability in rating is affecting the reliability in bridge management.

Serviceability Versus Strength

Table 4 compares the critical deflections of the three test bridges (calculated by their field-calibrated finite element models, which represent the actual behavior of the bridges) normalized with the code-permitted deflection, showing that the actual deflections are far smaller than code-permitted values. The actual deflections under both lanes loaded by a T-3 truck at midspan were observed to be less than 50 percent of the deflection expected in design.

One may also observe an order of magnitude difference in the actual deflections of the three test bridges, although their rating factors, that is, expected strength capacities, are comparable (4.93 to 6.00).

The field-calibrated finite element models were used to further evaluate the contributions of two-way action of reinforced concrete deck, composite action, cross braces, and girders to the midspan deflection flexibilities of the test bridges. This was accomplished by simulating each one of these elements or mechanisms not to contribute to the stiffness of the bridge; that is, the stiffness provided by each mechanism was set to 0 in the field-calibrated finite element model, as indicated in Figure 4.

TABLE 4 Comparison of Deflections and Mechanisms Contributing to Stiffness of Stringer Bridges

Bridge	HAM-42-0992 Cross County Highway		CLE-50J-0080L Little Miami River		HAM-128-1006 Paddy's Run	
	Middle span L=78 ft (23.77 m)		Middle span L=126 ft (38.41 m)		Middle span L=50 ft (15.24 m)	
3-D FE Model	Deflection D in. (mm)	D / (L/800) (L/800=1.17" ≈29.7mm)	Deflection D in. (mm)	D / (L/800) (L/800=1.17" ≈29.7mm)	Deflection D in. (mm)	D / (L/800) (L/800=0.75" ≈19.1mm)
Calibrated	0.67 (17.0)	57%	0.88 (22.4)	46%	0.20 (5.1)	27%
Full Composite	0.67 (17.0)	57%	0.88 (22.4)	46%	0.13 (3.4)	18%
Noncomposite	1.19 (30.2)	102%	1.50 (38.1)	80%	0.27 (6.8)	36%
w/o RC deck	1.71 (43.4)	146%	1.67 (42.4)	88%	0.4 (10.1)	53%
w/o RC deck & X-braces	2.00 (50.8)	171%	1.69 (42.9)	90%	0.58 (14.6)	77%

Note: Deflections are for both lanes loaded by truck T-3 at midspan.

The calculated deflections (Table 4) of the different models reflect the importance of composite action and other bridge mechanisms under service loads. Figure 5 quantifies the significance and the relative contribution of different elements or resistance mechanisms participating in the global stiffness of the three test bridges. For each bridge, the contribution of each mechanism can be different, depending on span and other attributes. For example, in the case of CLE-50J-0080L, the girders are dominating the complete superstructure stiffness. For HAM-42-0992, which is on pads, the cross braces seem to have a much more significant contribution than in the case of CLE-50J-0080L. For HAM-128-1006, the effect of composite action dominates the stiffness, in spite of its 43-year-long service life at the time of testing, showing the contribution that saved the bridge from deck replacement and emphasizing the significance of this mechanism.

The implication of the observations from Table 4 and Figure 5 is significant because it enables one to infer, objectively, the actual contribution of each critical component to the total stiffness of the superstructure. Currently, the contribution of components is not controlled in an objective quantified manner because the deck and cross braces are empirically designed. Present codes and design traditions in bridge engineering have successfully ensured safety against inadequate strength. However, an evaluation of Table 4 indicates that relative flexibility and serviceability of typical highway bridges may not have been properly controlled in bridge design and evaluation practice.

It is now emerging that bridge evaluation should include an objective quantitative assessment of serviceability in addition to strength and safety. The related issues that should be taken into consideration are long-term performance, durability, toughness, or resistance to mechanisms that cause deterioration or aging, and damage caused by environmental attack. New codes, such as the Draft LRFD (*10*), have recognized that existing design processes may not be successful in providing long-term serviceability. This research showed the significance of quantifying serviceability in terms of critical deflection mechanisms in bridges possessing large reserves of strength. The research further demonstrated a structural-identification-developed integrated condition assessment and performance evaluation method to objectively quantify both the safety and serviceability.

CONCLUSIONS

It appears rational to emphasize, in the design, evaluation, and retrofit procedures, composite action over the longer term. In addition, evaluating a bridge by properly recognizing the contributions of the slab system as well as the cross braces would be important for understanding the state of force in these bridge components and their contribution to stiffness. This may help develop a uniform distribution of safety for all the critical components that transfer load. For example, although the evaluation of the steel girders of a stringer bridge may be conservative, the evaluation of the concrete deck or the braces may be unconservative. Moreover, ignoring some of the important mechanisms that govern the actual load distribution and structural stiffness does not permit controlling all of the attributes that lead to desirable safety and serviceability performance during a retrofit design.

All three steel-stringer test bridges had comparable strength rating factors, whereas their live-load deflection and vibration characteristics varied greatly. Current rating methods completely ignore serviceability performance as affected by deflection and vibration. The L/800 deflection limit does not reflect the serviceability performance of bridges.

In general, design, construction, inspection, and evaluation of steel-stringer bridges, because of their complexity, are particularly difficult to implement objectively, and these bridges make up the largest segment of the National and Ohio Bridge Inventories. The

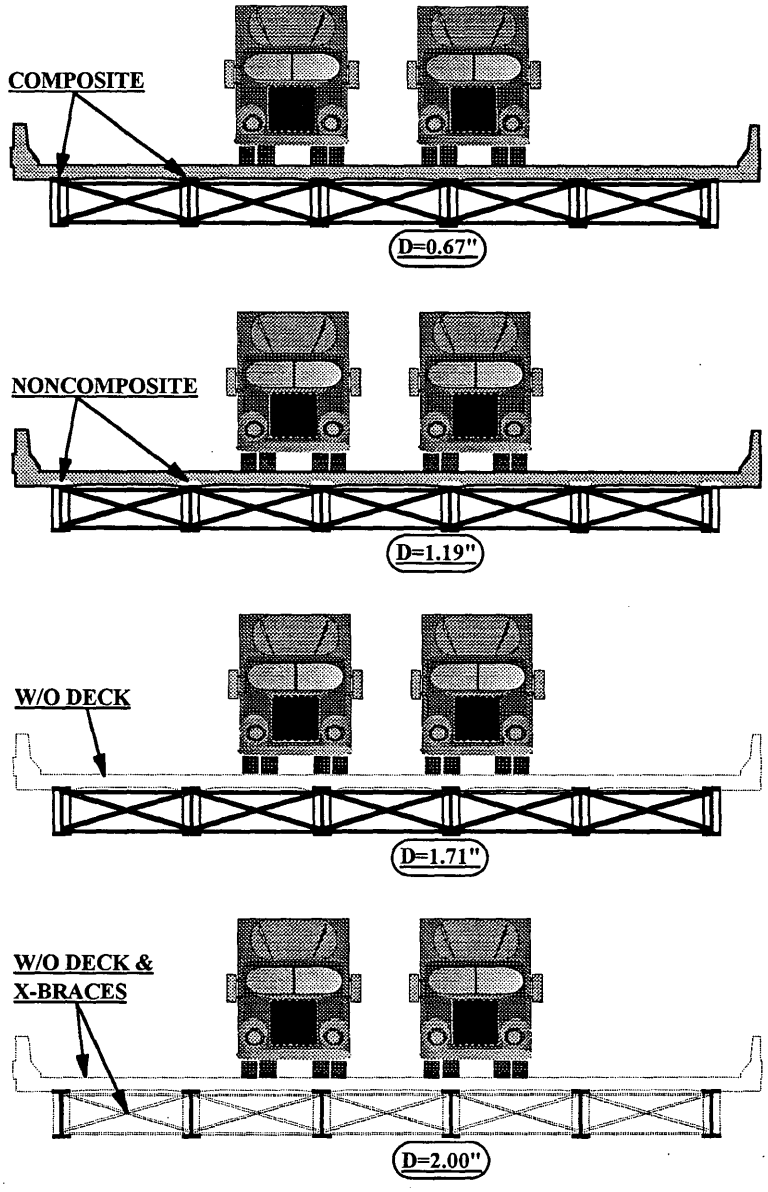

FIGURE 4 Comparison of deflections of HAM-42-0992.

replacement value of the 15,830 steel-stringer bridges in Ohio's inventory would exceed $2.5 billion, and more knowledge of their actual behavior is needed.

It is helpful to determine contribution by slab, girder, and cross braces to understand flexibility and safety and determine ways to improve rating.

RECOMMENDATIONS

As a result of the research reported here, the following recommendations are made:

1. For starting the design, selection of the dimensions and spacing of the steel stringers, assuming a stiffness based on noncomposite action at the interface with the concrete deck, provides excellent serviceability and redundancy in design. However, it is more desirable to use a complete 3-D model in design, incorporating the girders, cross braces, and the reinforced concrete deck, to arrive at a more reasonable estimate of resistance/capacity. It is also important to check for deflection and vibration problems with more rational procedures than just checking individual girders. Research demonstrated that L/800 is not an adequate measure of serviceability. Unfortunately, there are many reports of excessive deflection and vibration in the case of new bridges designed by incorporating composite action.

2. Mechanical girder-slab interface connectors provided during construction as well as other proven local details at the interface may facilitate long-term maintenance of composite action. This has been determined as a very desirable mechanism for performance at service and at ultimate limit states.

3. Cover plates that provide additional negative moment capacity at regions where negative moments are critical may lead to a

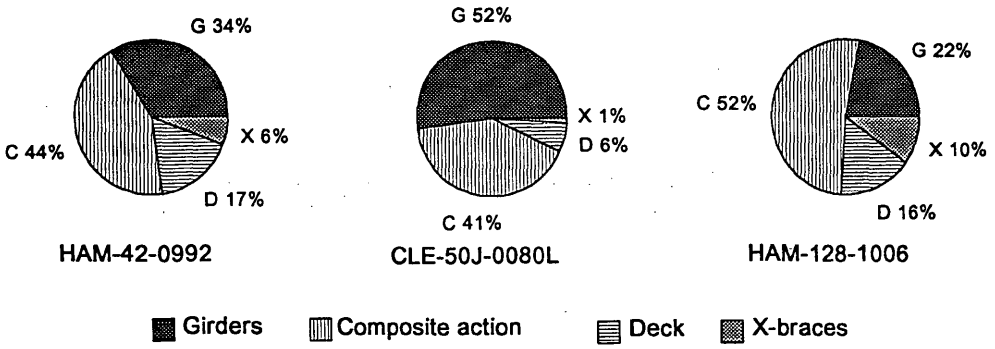

FIGURE 5 Contribution of mechanisms participating in stiffness.

more balanced design between negative and positive moments. Currently, designs based on AASHTO and conducted by analyzing 1-D models without incorporating the cover plates may appear not to be well balanced for different senses of moment.

4. This research revealed that integral abutments do significantly decrease positive moments in the end spans and increase the stiffness and serviceability by providing rotational stiffness. Some states permit integral abutment designs up to 800 ft. Their use in retrofit should be encouraged.

5. Provision of mechanical connections between the pads and the pier caps are recommended for lateral stability in the case of accidents. The flexibility provided by the pads at the supports regulated the negative moment demands.

6. Lateral cross-braces should be explicitly designed and incorporated in the global design. The stiffness provided by these braces was found to significantly enhance lateral redistribution of negative moment demands. Some of these recommendations on evaluation and rehabilitation are already incorporated into the Ontario Highway Bridge Design Code (*21*).

ACKNOWLEDGMENT

This research was funded by ODOT and FHWA. The support and encouragement extended by W. F. Edwards, D. Hanhilammi, J. Barnhart, L. Welker, R. Eltzroth, and A. Waheed of ODOT are greatfully acknowledged. The confidence extended by S. Chase and M. Shamis of FHWA and K. P. Chong of the National Science Foundation to the researchers is deeply appreciated.

REFERENCES

1. *Manual for Maintenance Inspection of Bridges*. AASHTO, Washington, D.C., 1983.
2. *Manual for Maintenance Inspection of Bridges*. AASHTO, Washington, D.C., 1989.
3. Imbsen, R. A. *NCHRP Report 108: Bridge Weight Limit Posting Practice*. TRB, National Research Council, Washington, D.C., 1984.
4. Moses, F., C. G. Schilling, and K. S. Raju. *NCHRP Report 299: Fatigue Evaluation Procedures for Steel Bridges*. TRB, National Research Council, Washington, D.C., 1987.
5. Moses, F., and D. Verma. *NCHRP Report 301: Load Capacity Evaluation of Existing Bridges*. TRB, National Research Council, Washington, D.C., 1987.
6. Burdette, E. G., and Goodpasture, D. W. *NCHRP Report 306: Correlation of Bridge Load Capacity Estimates with Test Data*. TRB, National Research Council, Washington, D.C., 1988.
7. Pinjarkar, S. G., O. C. Guedelhoefer, B. J. Smith, and R. W. Kritzler. *NCHRP Report 12-28 (13): Nondestructive Load Testing for Bridge Evaluation and Rating*. TRB, National Research Council, Washington, D.C., Feb. 1990.
8. Lichtenstein, A. G. *NCHRP Report 12-28(13) A: Bridge Rating Through Nondestructive Load Testing*. TRB, National Research Council, Washington, D.C., Aug. 1992.
9. *Guide Specifications for Strength Evaluation of Existing Steel and Concrete Bridges*. AASHTO, Washington, D.C., 1989.
10. *Development of Comprehensive Bridge Specifications and Commentary. Draft LRFD Bridge Design Specifications and Commentary*. Report NCHRP 12-33. TRB, National Research Council, Washington, D.C., March 1993.
11. Galambos, T. V., R. T. Leon, C. W. French, M. Barker, and B. Dishongh. *NCHRP Report 352: Inelastic Rating Procedures for Steel Beam and Girder Bridges*. TRB, National Research Council, Washington, D.C., Aug. 1993.
12. *Manual for Condition Evaluation of Bridges*. AASHTO, Washington, D.C., 1994.
13. Aktan, A. E., and M. Raghavendrachar. *Nondestructive Testing and Identification for Bridge Rating*. Report FHWA/OH-90/005. FHWA, U.S. Department of Transportation, 1990.
14. Aktan, A. E., C. Chuntavan, T. Toksoy, and K. L. Lee. Bridge Nondestructive Evaluation by Structural Identification: 1. Description of the Methodology and 2. Applications. *Proc., 3rd NSF Workshop on Bridge Engineering Research in Progress*. Department of AMES, University of California at San Diego, Nov. 1992.
15. Aktan, A. E., R. Miller, B. M. Shahrooz, M. Zwick, M. Heckenmueller, I. Ho, W. Hrinko, and T. Toksoy. *Nondestructive and Destructive Testing Of A RC Slab Bridge and Associated Analytical Studies*. Report FHWA/OH-93/017. FHWA, U.S. Department of Transportation, Dec. 1992.
16. Aktan, A. E. A Summary of Important Findings Resulting From University of Cincinnati's Bridge Research for ODOT. Presented at AASHTO Meeting, Denver, 10–14 May 1993.
17. Aktan, A. E., M. Zwick, R. Miller, and B. Shahrooz. Nondestructive and Destructive Testing of Decommissioned Reinforced Concrete Slab Highway Bridge and Associated Analytical Studies. In *Transportation Research Record 1371*, TRB, National Research Council, Washington, D.C., 1993, pp. 142–153.
18. Aktan, A. E., C. Chuntavan, K.-L. Lee, and T. Toksoy. Structural Identification of a Steel Stringer Bridge. In *Transportation Research Record 1393*. TRB, National Research Council, Washington, D.C., 1993, pp. 175–185.
19. Aktan, A. E., K. L. Lee, C. Chuntavan, and T. Aksel. Modal Testing for Structural Identification and Condition Assessment of Constructed Facilities. *Proc., 12th International Modal Analysis Conference*, Honolulu, Hawaii, 1994.
20. Huria, V., M. Raghavendrachar, and A. E. Aktan. 3-D Characteristics of RC Wall Response. *Journal of Structural Engineering*, ASCE, Vol. 117, No. 10, Oct. 1991, pp. 3149–3167.
21. *Ontario Highway Bridge Design Code*. Code and Commentary, 3rd ed., MTO, Publications Management Office, 1991, Sections 11 and 12, pp. 333–370.

Publication of this paper sponsored by Committee on Dynamics and Field Testing of Bridges.

Systematic Evaluation of Structural Deterioration in Underwater Bridge Substructures

MARK D. FUGLER, R. RICHARD AVENT, AND MOHAMED ALAWADY

A comprehensive statistical analysis was performed on the condition data generated by a statewide underwater inspection of bridges in Louisiana. The research defined pertinent underwater structural decay characteristics and established a method for determining a bridge's propensity for underwater deterioration on the basis of those relevant factors. The inspection results were reviewed to ascertain the impact of human bias on consistency in the bridge condition ratings. Using a set of importance factors obtained through a questionnaire submitted to a group of inspectors, the fuzzy set theory was employed to assist in the removal of data incongruities. A combination of pure fuzzy set theory and classical binary weighing was found to produce optimal results. Bridge age, material type, and location were found to be significant in defining the rate of deterioration in Louisiana bridges. Linear least-squares, piecewise linear least-squares, and polynomial regression curves were matched to the overall underwater condition ratings. Comparisons of regression curves for neighboring states indicated reasonable consistency in results for differential inspection programs if similar inspection methodologies are employed. The correlation between above-water and subsurface inspection ratings was found to be poor for concrete and steel bent bridges but acceptable for timber bent bridges within a given age group. Additionally, a poor correlation was found between water quality data and underwater bridge deterioration rates. A methodology for determining the frequency and detail of future underwater inspection projects was developed on the basis of the de-terioration trends and available bridge decay-defining characteristics discovered in this research.

With over half of the United States' 600,000 bridges now over 50 years old, there is growing interest in discovering new and more efficient methods for maintaining and rehabilitating the existing bridge network at the least possible cost. Performance prediction curves based on archived bridge inspection data traditionally have provided graphic evidence of the behavior of a system of bridges. The performance curves allow transportation officials to comparatively examine each bridge to find those structures that show regression rates that are significantly greater than expected. The engineer may then choose to grant priority for future inspections to any bridge that shows a propensity for unusually high deterioration, thus assuring that the structure does not unexpectedly enter a critical condition state. Traditionally, scheduling of future inspections has relied on an informal decision-making process that is based on the experience of the bridge maintenance engineer. Today, the popularity of computerized bridge inspection data storage and retrieval allows greater optimization in scheduling future inspections.

M. D. Fugler, Figg Engineering Group, Tallahassee, Fla. 32301-1298. R. R. Avent and M. Alawady, Department of Civil and Environmental Engineering, Louisiana State University, Baton Rouge, La. 70803.

The purpose of this paper is to introduce a procedure for assigning an inspection priority value for a given bridge element on the basis of the element's past conditional behavior and other decay-defining parameters. The methodology will be illustrated by a study of pile bents taken from the data of a statewide underwater bridge inspection program initiated in 1991 in Louisiana.

DATA SET DEVELOPMENT

In 1991 and 1992, the Louisiana Department of Transportation and Development (LDOTD) initiated its first statewide underwater inspection of bridge structures. Divers were required to subjectively rate each of 10 to 19 items (depending on material type) for every bent, pier, and abutment of over 600 bridges across the state as well as to give an overall bent or pier rating. The condition ratings for these items ranged from 1 to 7 and were based on a list of descriptive guidelines listed by Avent and Whitmer (*1*).

Numbering over 2,400, bridge bents constituted the largest type of structure investigated in the Louisiana inspection program. Additionally, bents with imperfect ratings for scour and erosion were excluded from the data base because the presence of these conditions would have influenced the assessment of the condition of the element itself. The remaining 2,200 bents served as the source for the material degradation relationships described in this paper.

The most important rating was the overall underwater condition rating (OVR), a single value representing the general condition of the bent that was based on the individual ratings. Because divers may consider the importance of each of the items differently when casually formulating an OVR in their minds, this method of assigning the OVR is inconsistent. Because the OVR is the most important single indicator of the condition of the structural element, the lack of consistency in determining the OVR hinders any comparative analysis within the set of underwater bridge condition appraisals. This obstacle was overcome by employing a factoring routine that computes the element's OVR using a weighted average for each of the important values of the element's 10 to 19 observations. In this study, a group of ten inspectors and experienced engineers were surveyed to determine the relative importance each of the 10 to 19 items should be allotted when formulating the element's OVR.

One-to-one comparisons of the field-assigned overall ratings (OVRs) and the corresponding computer-generated factored overall condition ratios (FOVRs) showed a general agreement between the values for the bent population. Summary statistics indicate comparable mean values (6.12 versus 6.21) and standard deviations (0.82 versus 0.94) for the OVRs and FOVRs, respectively. Only

seven of the bridge elements (0.3 percent of the data set) were found to have differences greater than one-half point between the OVRs and the FOVRs.

FACTORS INFLUENCING UNDERWATER DECAY

Because the underwater portions of a bridge structure typically do not receive periodic maintenance, the condition can be assumed to regress (and never improve) from the date of construction. Thus, the average rate of underwater decay can be defined as

$$ADR = 7 - \frac{FOVR}{T} \quad (1)$$

where

ADR = average annual deterioration rate,
$FOVR$ = factored overall underwater condition rating on a seven-point scale, and
T = bridge age in years.

To predict the behavior of a structure, the conditions that influence the ADR must be identified and investigated for their contribution to the structure's rate of decay. From the list of available data and descriptive parameters for each bent, the average daily traffic (ADT), climate region (local environmental effects), and material type were thought to be potentially significant factors in describing the ADR of a given bent in Louisiana. An analysis of variance (ANOVA) was performed on each of these factors to numerically assess the significance of the factor at a 95 percent confidence level.

The ANOVA performed to study the effects of ADT on the regression rate was conducted using the continuous relationship described by the third-order polynomial curve:

$$QVR\,(T_i A_i) = \beta_0 + \beta_1 T_i A_i + \beta_2 T_i A_i^2 + \beta_3 T_i A_i^3 + \epsilon_i \quad (2)$$

where $FOVR(T_i,A_i)$ is the factored overall condition rating of bent I as a function of the bent age (T_i) and the ADT carried by the bent (A_i). The beta values (β_0, β_1, β_2, β_3) are constants generated when the equation is fitted to the data, and ϵ_i is the term describing the error between the equation and the actual FOVR for bent I.

From the results indicated in Table 1, the effect of ADT on the rate of change in the FOVR is insignificant for each of the terms of the polynomial at the 95 percent confidence level, as witnessed by the P-values greater than 0.05.

In processing the ANOVA of the influence of climate region on the rate of regression in the overall underwater condition, the definition of the climate region itself proved a difficult task. Generally speaking, Louisiana is climatically homogeneous; however there are small differences in weather and terrain between the northern and southern portions of the state defined by a line of latitude running through Alexandria. An ANOVA processed to investigate the influence of this two-region climate zone on the ADR indicated that the climate was an insignificant factor with a P-value = 0.109. However, reprocessing the model with nine regional climate zones (in which each region is identically the same as the LDOTD district in which the bent was located) improved the P-value to 0.068.

Further detailed analysis revealed that, although southern Louisiana bents had marginally greater ADRs compared with northern Louisiana bents (20 percent higher in the north), those bents located along the Gulf Coast were witnessing regression rates up to 60 percent greater than the remaining bent population in the same southern district. Table 2 details the ADRs of item observations for concrete bents in a region located in a particular southwestern Louisiana region in which saltwater intrusion has been measured several miles inland from the coast.

Finally, the material of construction was investigated as a potential factor in describing the propensity for underwater decay. An ANOVA performed on a categorical model relating the material type (concrete, steel, or timber) to the ADR produced a P-value = 0.001, a value that is highly significant at a confidence level of 95 percent. The high level of significance results both from the superiority in underwater performance of one material over another and variations in the depth and type of observations recorded for bents of different material types. In light of the significance of the material of construction in determining the propensity for decay, material type must be considered when determining the bent's conditional regression characteristics.

CORRELATION OF ABOVE SURFACE AND SUBSURFACE EVALUATIONS

According to LDOTD guidelines for determining the frequency of underwater inspections, every bridge in the state that crosses rivers over 4 ft deep must undergo an underwater inspection once every 5 years and more frequently if conditions indicate a potential underwater problem. Following similar FHWA criteria, every bridge in the state undergoes a routine above-surface inspection at least once every 2 years. During these biennial surveys, the condition of the bridge substructure (at least those portions visible from above the surface of the water) are rated on a nine-point scale. The possibility

TABLE 1 ADR ANOVA Data Summary Table

Factor	Factor Definition	P-Value
Average Daily Traffic:		
Factor 1	Ti * (Ai)	0.278
Factor 2	Ti * $(Ai)^2$	0.091
Factor 3	Ti * $(Ai)^3$	0.054
Climate Zone:		
Two Regions	North/South La.	0.109
Nine Regions	Region = DOT Dist. #	0.068
Material Type:	Concrete/Steel/Timber	0.001

TABLE 2 Coastal Effects on ADRs for Southwestern Louisiana

Item Rated	ADR X 1000	
	SW La. Coastal Region	All SW La.
Cracks	6.053	5.544
Spalls	27.78	17.36
Exposed Reinforced Concrete	0.0	0.0
Laitance	0.0	0.0
Sulphate Attack	0.0	0.0
Honeycombing	[0.355]	[0.273]
Rustspots	14.21	9.411
Grout Loss	62.50	41.90

Bracketed values indicate less than 5 percent (5%) of the bents within the region were assessed at a rating less than 7 (new) for that item. Zero (0.0) values indicate all bents within the region had ratings of 7 for that item.

that the above-surface substructural rating (SSR) might predict the underwater condition (FOVR) was investigated using a Pearson product-moment correlation analysis, the results of which are given in Table 3.

The greatest degree of correlation between the SSR and FOVR for a given bent is found for bent elements constructed of timber. For these structures the Pearson product-moment coefficient (ρ) ranged from $0.746 < \rho < 0.877$ across all the age groups ($\rho = 1$ indicates linear correlation). In contrast, steel and concrete bents could not generate a ρ-coefficient greater than 0.5 for any age group. The high degree of correlation between the SSR and FOVR for timber bents is likely the result of two characteristics of timber structures: first, timber bridges generally cross smaller, shallower, slow-moving rivers or bayous where much of the substructure is above the water surface and, second, timber piles will generally exhibit the greatest amount of deterioration at or just above the water surface. In this area (easily seen from above the surface) repeated cycles of wetting and drying have been proven to accelerate the mechanisms of timber decay (2). Consequently, for timber bents, the SSR may serve as an indicator of the underwater condition.

METHODOLOGY FOR NUMERICALLY DEFINING INSPECTION PRIORITIES

Although the National Bridge Inspection Standards require that all bridges with at least part of their structure located in water receive periodic inspections of those submerged elements, there exists no federal requirement that precisely dictates the frequency and level of underwater inspection, as long as each applicable structure is routinely investigated at least once every 5 years (3). FHWA recommends that nonscheduled inspections, that is, inspections more frequent than once every 5 years, should be conducted on the basis of the local transportation officials' assessment of certain known conditions, including incidence of flooding, debris build-up, vessel impact, and bridge importance within the system (3). However, for any given bridge system, a prioritization of the underwater inspections for the system elements can be numerically established by considering all applicable factors and applying the numerical assessment of those factors to each element.

Before summation, however, the factors should be weighted by a value indicative of the degree of correlation between each individual factor and the anticipated rate of underwater deterioration attributable to that factor. The relationship is simply the summation of weighted terms and, using the terminology of bridge inspection, is hereby proposed to be described by the basic mathematical operation

$$P_e = \sum_{m=1}^{n} C_m * R_{m,e} \tag{3}$$

where

P_e = inspection priority ranking for element e;
C_m = weighting value for factor m; and
$R_{m,e}$ = assessment or rating for factor m of a total of n factors, for element e.

Not all bridges will be subject to the same rating factors because those rating factors are dependent on such characteristics as material type. Normalization of Equation 3 is necessary for comparison

TABLE 3 Pearson Product-Moment Coefficients for SSR-to-FOVR Correlations

Age Group (years)	All Materials	Concrete	Steel	Timber
[0 to 20]	0.151	0.285	0.720	0.746
[20 to 40]	0.396	0.436	[-][1]	0.858
[40 to 60]	0.229	0.270	[-][1]	0.783
[60 to 80]	0.360	0.325	[-][1]	0.877

1: Insufficient data to establish correlation.

across categorical boundaries. Thus, the prioritization ranking process proposed in Equation 3 becomes

$$P_e = \sum_{m=1}^{n} \frac{C_m * R_{m,e}}{(C_m)_{\max} * (R_{m,e})_{\max}} \quad (4)$$

for all applicable ratings m for the given element,

where

$(C_m)_{\max}$ = maximum weighting coefficient for each factor m of n factors; and
$(R_{m,e})_{\max}$ = the maximum assessment or rating for each factor m of element e.

The value of the rating matrix, $R_{m,e}$, may be extracted from inspection data or other sources supplying element particular condition information and may be either continuous or categorical in nature. Evaluation of the weighting factor C_m might be dependent on an elemental categorical definition, and the rating scale may be peculiar to a given observation or measurement as well. For example, the correlation of decay to a geographical factor may be different for steel or concrete bents on the basis of past experiences; hence the weight given to that factor may be dependent on the material-type category.

Some factors apply to all elements of a given type or location. For subcategorical weighting and the application of these broad-based factors, Equation 4 may be modified to include one or more general beta-weighting factors:

$$P_e = \sum_{m=1}^{n} \frac{C_m * R_{m,e}}{(C_m)_{\max} * (R_{m,e})_{\max}} * \beta_1 * \beta_2 \ldots \quad (5)$$

where β_1, β_2, and soon are the subcategorical weights or general factors.

The development of an inspection priority algorithm will generally involve two basic steps. First, the factors that may drive the frequency and level of inspection must be determined, and the available $R_{m,e}$ values must be collected; second, the weighting factors, C_m, associated with the $R_{m,e}$ values must be assembled. For calculating the underwater inspection priority for Louisiana bents, the list of physical parameters and ratings to be considered included bent age, material type (concrete, steel, timber), structure type (bent, pier, etc.), overall underwater condition rating (FOVR), subcomponent ratings (i.e., the ratings given to the items that contribute to the FOVR), location (latitude and longitude), above-water assigned substructural rating, and the criticality of the element to bridge network, listed by LDOTD as "state priority points." These terms can be simply extracted from the LDOTD data base for each bridge and, with the exception of the criticality factor, are known to influence conditional regression.

The C_m factors are not necessarily constants; instead, they take on a predetermined value, depending on the interpretation of its associated $R_{m,e}$ term. For example, although age is of high importance in establishing a propensity for deterioration, it has been shown that the typical regression of concrete bents in Louisiana is not constant over the bent's lifespan. Consequently, the priority for conducting underwater inspections, as well as the level of the inspections themselves, should optimally be indexed in some manner to the age of the structure. In effect, the weighting matrix will be populated by a collection of functions that establish a particular R_e (the ratings assigned to a given element e) contribution to the overall priority rating, P_e, based on the relative value of R_e. It can be seen, then, that each rating term has a general categorical importance as well as a particular significance based on the magnitude of the term.

To differentiate the importance of a factor with the significance of the value assigned to that particular factor, it will be beneficial to consider the weighting value as the product of two weights: (*a*) the importance weight (I_m); and (*b*) the value significance weight (S_m). This operation will allow the weight allotted to any rating value used to establish the structure's inspection priority to be a function of both the general importance of that factor in determining the rate of underwater deterioration and the relative magnitude of that particular value.

Modifying Equation 5 to reflect the concept of importance and significance matrixes results in the following:

$$\sum_{m=1}^{n} \frac{I_m * S_m * R_{m,e}}{(I_m)_{\max} * (S_m)_{\max} * (R_{m,e})_{\max}} * \beta_1 * \beta_2 \quad (6)$$

where, in addition to the previously defined terms, I_m is the assemblage of importance values associated with each factor, R, of m factors, and S_m is the significance function associated with each factor, R, of m factors. The subscript max indicates the maximum values possible for each factor or rating. The interpretation of the importance weight must consider the degree of correlation between that factor and the rate of decay of the corresponding bridge element. To simplify the resolution of I_m consider five categories of importance:

0: Not applicable or not important;
2: Of minor importance in establishing the rate of underwater deterioration;
4: Average importance. The factor is known to be a general indicator of the rate of underwater deterioration;
6: High importance. The factor has been proven to be a strong representative of the rate of conditional regression; and
8: Extremely important. The factor is entirely representative of the current underwater condition or the rate of change in the underwater condition of the element, or both.

In a similar manner, S_m may be objectively or subjectively determined. In establishing a decision hierarchy for significance, two elements must be considered: Does the magnitude of the factor indicate that the structure is experiencing conditions that are conducive to accelerated decay? and Does the magnitude of the factor reflect a reasonable probability that the structure will enter a condition requiring repair or maintenance before the next normal inspection cycle (5 years)? Applying the levels of significance to a five-point scale results in the following delineation of S_m:

1: The magnitude of this factor (relative to the range of values expected for that factor) indicates that the factor is insignificant in establishing a critical rate of decay or the probability that the structure will enter a state of disrepair within the following 5-year period, or both;
3: The magnitude of this factor (relative to the range in values expected for that factor) indicates that the factor holds average significance in establishing a critical rate of underwater decay or the probability that the structure will enter a state of disrepair within the following 5-year period, or both; and
5: The magnitude of this factor (relative to the range in values expected for that factor) indicates that the factor is highly significant in establishing a critical rate of decay or the probability that the structure will enter a state of disrepair within the following 5-year period, or both.

For both I_m and S_m, the scale is continuous, with the intermediate (even) values used to describe value significance levels that fall between those specifically outlined.

The importance, significance, and β-factors generated in the remainder of this paper are based on the subjective as well as objective statistical interpretation of the inspection results from the latest survey of underwater structures in Louisiana. The discussion that follows is best viewed as a structured methodology for developing a priority equation incorporating user-defined input and requisite output data.

The importance of age (hereafter denoted as the factor AGE) as a determinant of underwater condition is logically of high importance, given the time-dependent nature of deterioration in any form. Previous regression investigations have graphically illustrated the relationship between condition and AGE for underwater substructures; therefore, the importance factor for AGE will receive an importance weight of 8 for all material types:

$$I_{AGE} = 8.0 \tag{7}$$

As the structure ages, of course, the significance of AGE in determining the probability that repair is (or soon will be) required increases by some degree. This understanding is supported by the values indicated in Table 4, which describe the percentage of bents awarded an FOVR less than 5—the point at which maintenance action is suggested or required. With the percentage of bents increasing by a factor of 10 or more from the earliest to the latest age groups (depending on material type), the following chart is presented as a proposed breakdown of S_{AGE} by age group:

- Concrete bents

$$S_{AGE} = 1.00 \quad (\text{Age} < 20) \tag{8}$$

$$S_{AGE} = 2.00 \quad (20 \leq \text{Age} \leq 40) \tag{9}$$

$$S_{AGE} = 5.00 \quad (\text{Age} > 40) \tag{10}$$

- Steel bents

$$S_{AGE} = 1.00 \quad (\text{Age} < 20) \tag{11}$$

$$S_{AGE} = 4.00 \quad (20 \leq \text{Age} \leq 40) \tag{12}$$

$$S_{AGE} = 5.00 \quad (\text{Age} > 40) \tag{13}$$

- Timber bents

$$S_{AGE} = 3.00 \quad (\text{Age} < 20) \tag{14}$$

$$S_{AGE} = 3.00 \quad (20 \leq \text{Age} \leq 40) \tag{15}$$

$$S_{AGE} = 5.00 \quad (\text{Age} > 40) \tag{16}$$

Although the factor AGE could serve as an indicator of the probability that a structure is in need of short-term maintenance, the ADR should serve as a measure of how the in situ environment will dictate the probability that the structure will soon enter such a condition.

Similar to AGE, the factor explicitly describes the rate of change of the overall underwater condition rating; thus ADR will receive the highest importance weight for all material-type designations:

$$I_{ADR} = 8.0 \tag{17}$$

The degree of significance allotted to the ADR will be indexed to the magnitude of the term with the understanding that the value describes the likelihood that the condition will change before the following inspection cycle. For the given 5-year standard cycle, a structure would need to demonstrate an average annual deterioration rate of 0.200 points per year to drop one point in overall rating before the next inspection cycle. For the results of the latest underwater survey in Louisiana, 5.6 percent of the bents exceeded this in the factored ADR. A further breakdown shows that 9.0percent of the bents exceeded 0.150 points per year in ADR, 17.6 percent exceeded 0.100, and 43percent exceeded 0.050. The median ADR for Louisiana bents was 0.042 points per year.

The significance factor must assign a proportionately higher weight to the appraisals of those bents that are experiencing characteristically high deterioration rates, particularly those in excess of 0.200 points per year. Obviously, to achieve this goal, the significance value must be indexed to a category of ADR:

$$S_{ADR} = 1.00 \text{ for ADR} < 0.010 \tag{18}$$

$$S_{ADR} = 2.00 \text{ for } 0.010 \leq \text{ADR} \leq 0.030 \tag{19}$$

$$S_{ADR} = 3.00 \text{ for } 0.030 < \text{ADR} \leq 0.075 \tag{20}$$

$$S_{ADR} = 4.00 \text{ for } 0.075 < \text{ADR} \leq 0.200 \tag{21}$$

$$S_{ADR} = 5.00 \text{ for ADR} > 0.200 \tag{22}$$

When establishing an inspection priority based on overall underwater condition ratings, an effort should be made to ensure that single critical subcomponent ratings are not lost in the production of the general priority. The subcomponent ratings are considered in establishing the overall rating, as discussed earlier, but the ADR of the structure will not wholly depict the deterioration rate in any particular subcomponent rating. The inspection priority must ensure that a "weak link" in the structural system does not develop over the normal inspection cycle. To account for this potential oversight, the deterioration rate in the subcomponent, or SDR, shall be considered a factor in establishing an inspection priority for the structure.

The SDR is a strong indicator of the rate of deterioration but is not wholly indicative of the condition of the overall structure and thus will receive an importance value of:

TABLE 4 Percentage of Bents Requiring Maintenance

Age Group	All Materials	Concrete	Steel	Timber
All Ages	9.67	5.92	5.63	12.1
[0 to 20]	5.95	2.67	0.00	10.7
[20 to 40]	7.22	3.45	16.7	10.3
[40+]	20.6	21.7	*	19.7

* Insufficient data.

$$I_{SDR} = 5.00 \quad (23)$$

Following the same rationale as with the ADR factor, the significance of SDR will follow the breakdown:

$$S_{SDR} = 1.00 \text{ for SDR} < 0.010 \quad (24)$$

$$S_{SDR} = 2.00 \text{ for } 0.010 \leq \text{SDR} \leq 0.030 \quad (25)$$

$$S_{SDR} = 3.00 \text{ for } 0.030 < \text{SDR} \leq 0.075 \quad (26)$$

$$S_{SDR} = 4.00 \text{ for } 0.075 < \text{SDR} \leq 0.200 \quad (27)$$

$$S_{SDR} = 5.00 \text{ for SDR} > 0.200 \quad (28)$$

The high concentration of bridges experiencing much-higher-than-average deterioration within the coastal regions will be considered in the general β_1 factor. Coastal structures will be defined as elements which, according to LDOTD data base latitude and longitude descriptions, fall at a latitude of less than 30 degrees north latitude for longitudes between 91 degrees 30 min west and 94 degrees west, or at a latitude of less than 29 degrees 30 min north for longitudes between 89 degrees west and 91 degrees 29 min 59 sec west.

The relative increase in the deterioration of structures along the coast is substantial (ten times larger in some cases) compared with similar structures located inland, which should, on average, require a decrease in inspection cycle and greater inspection priority. Consequently, the β-factor for coastal structures will increase the priority by 25 percent for all applicable factors such that

$$\beta_1 = 1.25 \text{ for coastal structures} \quad (29)$$

Similarly, the β_2-factor will incorporate the correlation between the substructural rating assigned by the inspector performing the biennial above-surface bridge evaluations (SSR) and the factored overall underwater condition rating (FOVR) derived from the diver evaluation of the same timber bent. The ratio of SSR and FOVR may thus be utilized to determine the β_2-factor, such that

$$\beta_2 = \frac{FOVR}{SSR} \text{ for age-grouped timber} \quad (30)$$

The β_2-factor should be applied only if it increases the priority rating (i.e., is greater than 1.0) and, since the correlation between SSR and OVR was marginally significant (recall $0.746 > \rho > 0.877$), the factor should be limited to a reasonable value of 1.2:

$$1.0 \leq \beta_2 \leq 1.2 \quad (31)$$

The contribution of a single structure to the integrity of a bridge system is established by transportation officials on consideration of the bridge's traffic volume, physical dimensions and alignment, load rating, detour length, district priority, functional classification, age, and prior appraisal ratings. Utilizing a weighted point system, LDOTD engineers determine the bridge replacement priority and record the four-digit numerical evaluation on the Structure Inventory and Appraisal (SIA) sheet maintained for each bridge in the state system.

Because all bridge structures undergo the same replacement priority policy, there is no need to normalize the DOTD rating; thus the value itself will define the β_3-factor representing bridge criticality to the bridge network. To allow for the comparison of relative priorities independent of the bridge replacement priority, however, the routine will output priority rankings inclusive and exclusive of replacement priority (P_e and P_e', respectively). Retrieving the state priority point rating from the SIA sheet, the β_3-factor may be simply established as

$$\beta_3 = \text{state priority rating} \quad (32)$$

BRIDGE INSPECTION PRIORITIES: DECISION FLOW PROCESS

A sequence of operations used to develop importance, significance, and β-factors and the resulting bent inspection priorities for Louisiana bridges is outlined in Figure 1. The decision flow followed a basic four-step prioritization process:

1. Retrieval of electronically stored bridge inspection data/descriptive information;
2. Division of the data set by age/material/structure-type subsets;
3. Internal computation of bridge regression behavior and the logical assignment of pertinent weighting factors; and
4. Generation of a singular underwater bridge inspection priority value with and without the replacement priority considerations (referred to as the "priority rating" and "priority factor," respectively).

During the computational process, the system searched for and flagged unusually low rating values in addition to calculating priority rankings. The actual value of P_e is of little significance in itself but it does provide a standardized measurement for comparing the deterioration of a mixed population of bridge bents. In combination with the listing of critical subcomponent ratings, the priority value will allow bridge maintenance planners to plan both the level and interval of future underwater inspections.

CONCLUSIONS

The use of computers to store bridge inspection results has allowed meaningful statistical comparisons of the data thanks to the ease of data retrieval and mathematical manipulations. In the preceding discussion of deterioration in underwater bridge bents in Louisiana, computerized analysis has shown the rate of underwater decay to vary during the structure's lifespan and to be related to one or more of a set of bridge descriptive parameters.

Timber bents have demonstrated a strong correlation between the substructural condition assessed during biennial above-surface surveys and the underwater condition rating assigned by the diver. The strong correlation between these ratings can allow bridge engineers to use the frequent above-water surveys as a tool for determining the possible existence of subsurface deterioration in bridges using timber bents.

In Louisiana, bridge location must be considered when determining a bent's propensity for underwater deterioration. Environmental conditions found along the coastal regions of the state were shown to adversely affect the rate of change in underwater condition rating.

Taking all these observations into account, a decision flow process has been presented that permits the numerical assessment of underwater bridge inspection priorities given the results of the underwater inspections along with certain bridge descriptive param-

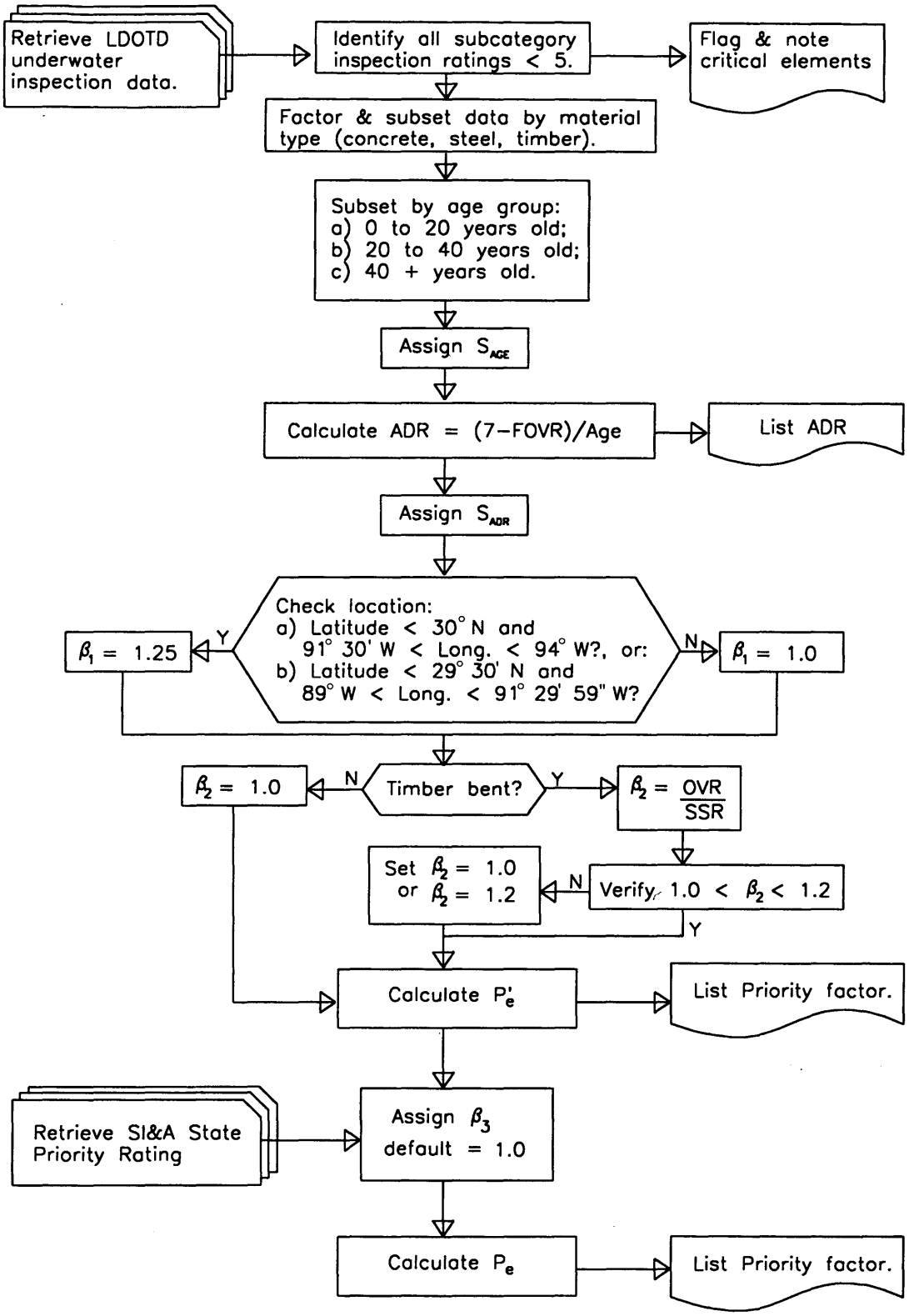

FIGURE 1 Decision flow process for establishing underwater bridge inspection priorities.

eters. The use of such a process, in conjunction with the current experienced-based method of determining inspection priorities, will allow the limited funding for future inspections to be allocated in the most effective manner.

Still, further investigations using the results of future underwater inspection programs on the same bridge population are warranted to support the relationships presented in this paper. The methodology followed in determining the structural decay characteristics for bents should also be applied to both piers and abutments to ascertain the variations in behavior based on structure type. Moreover, future investigations using the results of underwater inspections need not be limited to the area of structural decay. The same research methodology can be applied to develop a scour propensity rating based on known parameters that can be proven to affect the structures' scour condition rating.

This study provides a framework for a subset of a bridge management system related to underwater bridge components. Using the Louisiana inspection ratings and focusing on material degradation of bents only, all bridges in this subset were prioritized. With only minor changes in the type of data considered, the same methodology can be used to include all bent and pier types, as well as the effects of stream bed scour.

REFERENCES

1. Avent, R. R., and M. D. Whitmer. Underwater Inspection of Bridges—Overview of a Statewide Program. In *Transportation Research Record* 1268, TRB, National Research Council, Washington, DC, 1990, pp. 118–129.
2. Gobie, C. H. The Chemical Resistance of Timber. *Wood*, Vol. 19, 1954, pp. 322–325.
3. *Underwater Inspection of Bridges*. Report FHWA-DP-80-1. FHWA, U.S. Department of Transportation, 1988.

Publication of this paper sponsored by Committee on Dynamics and Field Testing of Bridges.

Creep Analysis of Hybrid Integral Bridges

K. A. SIROS AND C. C. SPYRAKOS

A state-of-the-art three-dimensional (3-D) model is developed and utilized for nonlinear creep analysis of composite (steel stringer-concrete slab) integral bridges. The results of the analysis are evaluated and compared with results of an equivalent two-dimensional (2-D) linear creep analysis. The rate of creep method and the age-adjusted effective modulus method are employed for the 3-D and the 2-D analysis, respectively. Two typical structural systems are analyzed: a single-span bridge (15.24 m) and a two-span bridge (2 × 34.75 m). Change of stresses with time at critical points of the bridges are shown and comparisons of the 2-D and the 3-D analyses are included. Evaluation of the results with respect to the behavior of integral bridges is presented.

Comparison between the two major forms for highway bridges, integral (or jointless) versus jointed, has shown that the former present several important advantages, including reduced construction and maintenance cost, as a result of elimination of joints. This is because bridge joints are expensive to purchase and install, and continuous maintenance is needed to keep them working properly (*1*).

The first integral bridges were designed after 1956. At the beginning, they were short in length and designed with precautions. Until 1985, the maximum length for integral concrete bridges had increased to 282 m and for those with steel superstructure to 127 m. In Tennessee it has become policy that "all bridges shall be continuous from end to end, and there shall be no intermediate joints introduced in the bridge deck other than cold joints required for construction" (*2*).

Bridges are subjected to various loading conditions, such as self-weight, temperature, and creep. The stresses caused by such loadings result in different total stresses for the jointed and the integral bridges. For example, a simply supported bridge develops higher stresses at midspan than does an indeterminate frame-type structure caused by dead and live loads, whereas stresses caused by thermal expansion or contraction in a simply supported bridge are much smaller (if at all) than those developed in the indeterminate system.

Several integral bridges have been built during the last few years in many states. Nevertheless, there is still no final and complete answer to what makes those bridges work efficiently and survive the high stresses that are supposed to develop. In a comparison of integral and jointed bridges Siros and Spyrakos (*3*) have shown that the change of bending moments because of creep in an integral bridge can be up to three times smaller than that in a jointed bridge. This fact, possibly being part of the answer, was the motivation for further investigation of creep stresses that develop in an indeterminate composite bridge.

A three-dimensional (3-D) model was developed and the rate of creep method (RCM) formulation was utilized in a step-by-step computer analysis. The age-adjusted effective modulus method (AEMM) was also used in a linear two-dimensional (2-D) analysis. Stresses at the top of the concrete slab and at the bottom of the steel stringer were calculated for several critical points along the bridges. Stress versus time plots are shown, and comparisons are presented between the 3-D and the 2-D analysis.

Department of Civil Engineering, Constructed Facilities Center, West Virginia University, Morgantown, W.Va. 26505-6103.

STRESS-STRAIN RELATIONSHIP

A concrete member that is subjected to a constant load exhibits continuous change of strain over time at each point because of creep. The creep law that describes this behavior is a function of time, strength of the material, and stress at each time.

One of the most widely accepted methods (*4*) for the calculation of creep in concrete, the RCM, is utilized here for the 3-D analysis. This method is mathematically attractive because it formulates the creep problem as a simple first-order differential equation, and therefore a step-by-step analysis can be easily carried out.

Gilbert (*5*) has utilized both the RCM and the AEMM to calculate creep stresses for a composite cross section, when the internal forces acting on the section at a certain time are known. When the structure is indeterminate, however, creep causes change of the reactions and the internal forces in the structure with time. Ghali (*6*) presents a methodology for 2-D creep analysis of indeterminate structures, which is also employed here for the 2-D analysis.

Bazant (*7*) discusses the multiaxial stress case for the AEMM. The analysis of bridges as 3-D structures is performed with the RCM. The formulation as it is given in the literature cannot be used directly with FEM analysis packages, and therefore a conversion is required.

In finite element analysis, the 3-D state of stress is taken into account by calculating the equivalent total strain at each time step as follows (*8*):

$$\varepsilon_{el} = \frac{1}{(1+\nu)\sqrt{2}}\left[\left(\varepsilon_x-\varepsilon_y\right)^2+\left(\varepsilon_y-\varepsilon_x\right)^2+\left(\varepsilon_z-\varepsilon_x\right)^2+\frac{3}{2}\left(\gamma_{xy}\right)^2+\frac{3}{2}\left(\gamma_{yz}\right)^2+\frac{3}{2}\left(\gamma_{zx}\right)^2\right]^{1/2} \quad (1)$$

where ε_x, ε_y, and ε_z are the axial strains in the x, y, and z directions, respectively, and γ_{xy}, γ_{yz}, γ_{zx} are shear strains in the respective planes and directions.

According to the RCM, the rate of creep strain at time t is a function of the stress, $\sigma(t)$, the creep coefficient derivative, $\phi'(t,t_o)$, and the modulus of elasticity of concrete at the present time, $E_c(t_o)$, that is

$$\varepsilon'_{cr}(t,t_o) = \phi'(t,t_o)\frac{\sigma(t)}{E_c(t_o)} \quad (2)$$

In this creep formulation, the aging of the concrete is ignored. Therefore creep may be overestimated for old concrete, but when the load starts acting soon after casting the concrete, the method gives good results.

The modulus of elasticity $E_c(t)$ of concrete varies also with time according to Equation 3 but should be taken as constant equal to $E(28)$ to arrive at a procedure that is computationally manageable. Note that in 28 days the concrete has gained about 90 percent of its strength. $E_c(t)$ is computed from

$$E_c(t) = E(28)\sqrt{\frac{t}{(4 + 0.85t)}} \tag{3}$$

The American Concrete Institute (*9*) Committee 209 suggests that $\phi(t)$ for $t_o = 7$ days be taken as

$$\phi(t) = \phi_u\left[\frac{t^{0.6}}{10 + t^{0.6}}\right] \tag{4}$$

with $\phi_u = 2.35g_c$ and $g_c = g_{la}\, g_h\, g_{vs}$

where g_{la}, g_h, and g_{vs} are constants that depend on age of loading, humidity, and ratio of volume to surface of the member, respectively. For constant humidity of 40 percent, age of loading of 7 days, and ratio of volume to surface of 1.5, g_c is equal to 1 For practical applications the estimation of this factor involves many uncertainties because humidity and temperature in the air change continuously with time.

NONLINEAR ANALYSIS

The analysis starts with the application of the self-weight or any equivalent sustained load on the structure. The time of application of the load t_o is assumed to be at 7 days. The duration of the loading is taken as 100,000 days. This time is required until the creep coefficient reaches the assumed ultimate value $\phi_u = 2.5$.

According to Equation 4, $\phi = 2.4$ for $t = 10{,}000$ and $\phi = 2.475$ for $t = 100{,}000$. From Figure 1 it is clear that the change of ϕ after the 100,000 days is slow and therefore the predicted creep will be small. From the same figure it can be seen that the change of strain is fast during the first 500 days and consequently a small time step is needed for the first period to reach convergence.

In finite element analysis, the creep formulation is based on the constitutive law (*10*):

$$\varepsilon'_{cr} = c_1\sigma^{c_2}t^{c_3} \tag{5a}$$

where c_1, c_2, and c_3 are constants. Therefore, Equation 2, corresponding to the RCM, must be converted into this form.

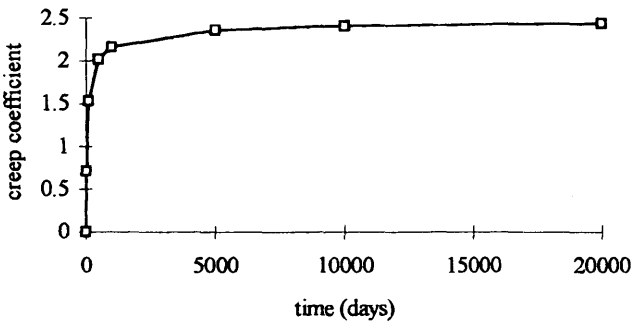

FIGURE 1 Creep coefficient versus time.

For each interval, as defined between the squares in Figure 1, Equation 4 can be expressed as

$$\phi = at^N \tag{5b}$$

where a and N are constants calculated by linear regression analysis (*11*). The constants N and a depend on the duration of each interval, which should be small enough so that the coefficient of variation r^2 is close to 1 (*12*).

The first derivative of this equation with respect to time is given by

$$\phi' = Nat^{N-1} \tag{6}$$

Substituting Equation 6 into Equation 2 the following is obtained:

$$\varepsilon'_{cr}(t,t_o) = \frac{\sigma(t)}{E_c(t_o)}\, Nat^{N-1} \tag{7}$$

or

$$\varepsilon'_{cr}(t,t_o) = \frac{Na}{E_c(t_o)}\, \sigma(t)t^{N-1} \tag{8}$$

and finally,

$$\varepsilon'_{cr} = c_1\sigma^{c_2}t^{c_3} \tag{9}$$

where

$$c_1 = \frac{Na}{E_c(t_o)} \qquad c_2 = 1 \qquad c_3 = N - 1 \tag{10}$$

The constants c_1, c_2, and c_3 describe the creep low for a given ϕ, t_o, and $E_c(t_o)$ and can be incorporated into well-documented finite element analysis programs such as ANSYS (*13*) and ABACUS (*14*).

The creep strain increment $\Delta\varepsilon_{cr} = \varepsilon'_{cr} * \Delta t$ is then calculated and added to the elastic strain. The new stress level is calculated at each point, and the procedure is repeated by calculating the next creep strain change. At each step the $\Delta\varepsilon_{cr}/\varepsilon_{ei}$ is calculated and the time step size is increased when the ratio is smaller than a predefined criterion, which for most practical applications can be taken as 0.25 (*8*). During the initial period though, when the creep strain rate is high, this ratio should be kept below 0.10 by increasing the number of iterations or decreasing the time step size.

THREE-DIMENSIONAL ANALYSIS

In the process of developing the 3-D model, many modeling aspects were considered, such as size and aspect ratio of elements, and combination of various types of elements (*15*). The model utilizes four node isoparametric plate elements with 6 degrees of freedom (dof) per node to simulate the concrete deck and the bridge abutments. Beam elements with six dof per node model the steel stringers and are connected to the plate elements of the slab with small and stiff fictitious beam elements (Figure 2). Close to the abutments and intermediate supports, more elements are used as a result of the anticipated higher stress gradient. At those regions, triangular elements are also used for gradual element size increase. A model with the minimum number of elements is essential in nonlinear analysis because of the substantial processing time. Therefore modeling

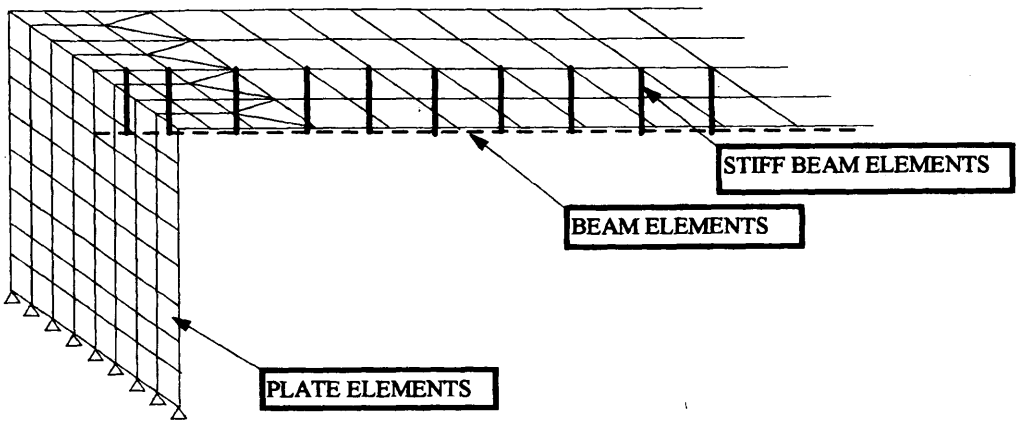

FIGURE 2 Detail of the 3-D model: abutment and deck.

rules and various alternative modeling schemes were employed toward this goal with minimum loss of computational accuracy. The number of the stiff fictitious connectors as well as their stiffness had to be kept at a minimum to avoid numerical instability. The size of the elements was also properly chosen at each point to satisfy size and aspect ratio requirements. A detailed discussion of the modeling considerations is given by Spyrakos (*16*). Special emphasis has been given to proper modeling of the boundary conditions. Simulation of the boundary conditions that is not accurate may result in small errors in a linear analysis. However, in nonlinear analysis caused by the multiple steps the error is accumulated.

A small creep (practically 0) was given for the time 0 to 7 days because nonzero values are required by the iterative algorithm.

The ultimate creep coefficient varies from 1.35 to 4.15 (*9*), but for most practical applications it ranges from 2 to 2.5. The aging coefficient (χ) varies from 0.774 to 0.8 for $\phi = 2.5$ and variable E_c and from 0.839 to 0.899 for constant E_c (*7*).

EXAMPLES

Example 1

A single-span bridge is analyzed first. Figure 3 shows the geometry of the structure. The material and geometric properties corresponding to one stringer are given as follows:

Steel:
E_{st} = 200 GPa I_{st} = 0.00278 m^4 A_{st} = 0.02806 m^2

Concrete:
E_c = 30 GPa I_{ocol} = 0.03487 m^4 Abutment thickness = 0.5677 m

$\phi(\infty,7)$ = 2.5 $\chi(\infty,7)$ = 0.8 Self-weight = 18919 N/m

The 2-D analysis is carried out according to Ghali and Favre (*6*), and the results are shown in Table 1. Results from the 3-D analysis are shown in Figure 4*a* and *b*. Stresses are calculated at midspan and the end of the deck. Negative stresses are compressive, whereas positive ones are tensile.

Example 2

The second example is a two-span bridge built in Iowa. The middle support is simulated here as a hinge. The total self-weight of the structure per stringer is 21 315 N/m. The dimensions and the geometry of the bridge are shown in Figure 5. The material and geometric properties are as follows:

E_{st} = 200 GPa I_{st} = 0.008625 m^4 A_{st} = 0.03129 m^4

E_c = 23.255 GPa I_{col} = 0.28525 m^4 Abutment thickness = 1.0668 m

$\phi(\infty,7)$ = 2.5 $\chi(\infty,7)$ = 0.8 Self-weight = 21 315 N/m

Results for three sections are listed for the first span of the bridge, the end of the deck, the midspan, and the center of the bridge (hinge location). Because the structure is symmetric the results are identical for the second span (see Figure 6 and Table 2).

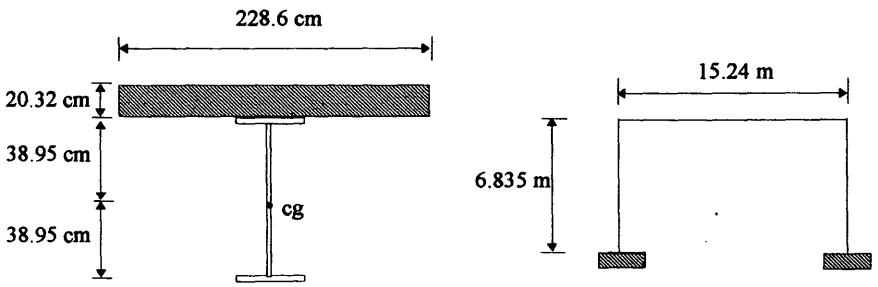

FIGURE 3 Geometry of the single-span bridge.

TABLE 1 Creep Analysis for Single-Span Bridge: 2-D versus 3-D

LOCATION	CREEP 2D (MPa)	CREEP 3D (MPa)	DIFFER. (MPa)	DIFFER. (%)
TOP OF CONCRETE				
ABUTMENT	-0.4207	-0.5724	0.1517	26
MIDSPAN	0.6138	0.6965	0.0827	12
BOTTOM OF STEEL				
ABUTMENT	-5.6827	-5.4689	0.2138	4
MIDSPAN	0.4483	0.5931	0.1448	24

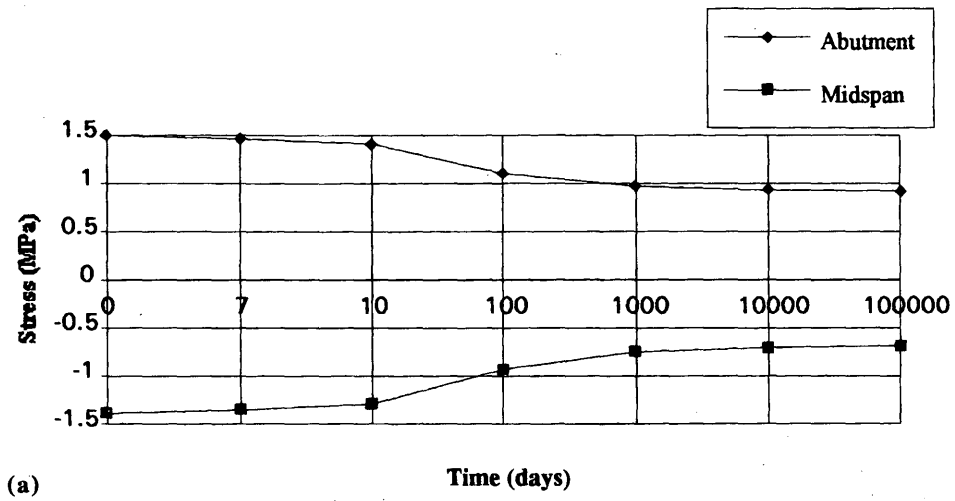

(a)

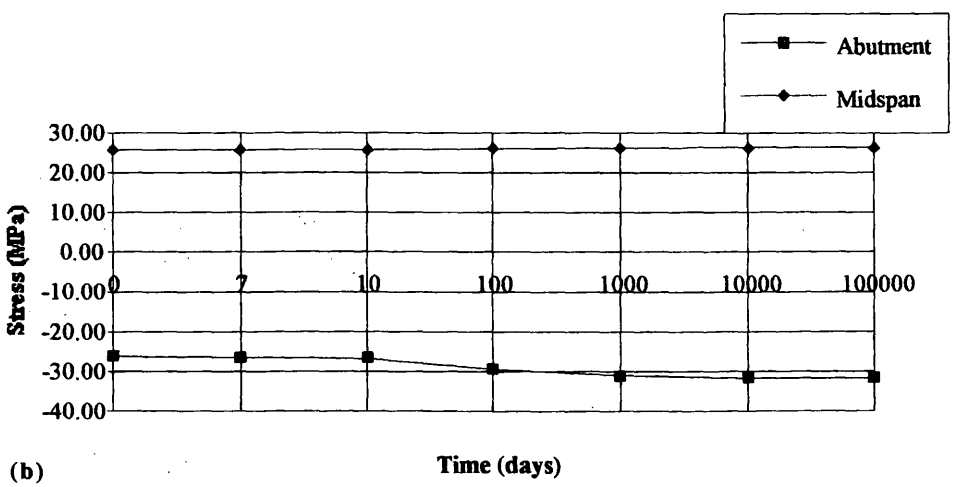

(b)

FIGURE 4 Stresses versus time, single-span bridge: (*a*) at the top of the concrete slab; (*b*) at the bottom of the steel beam.

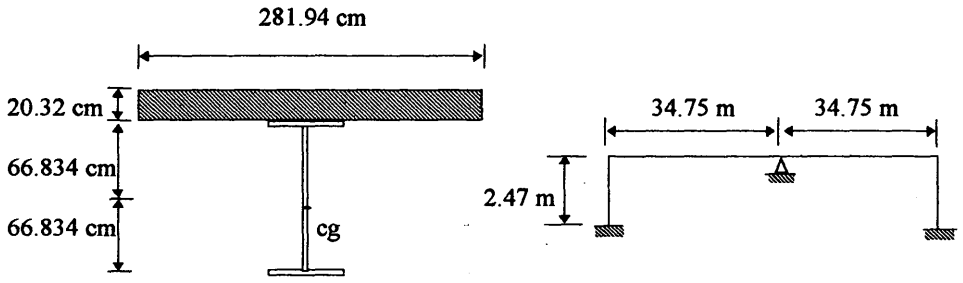

FIGURE 5 Geometry of the two-span bridge.

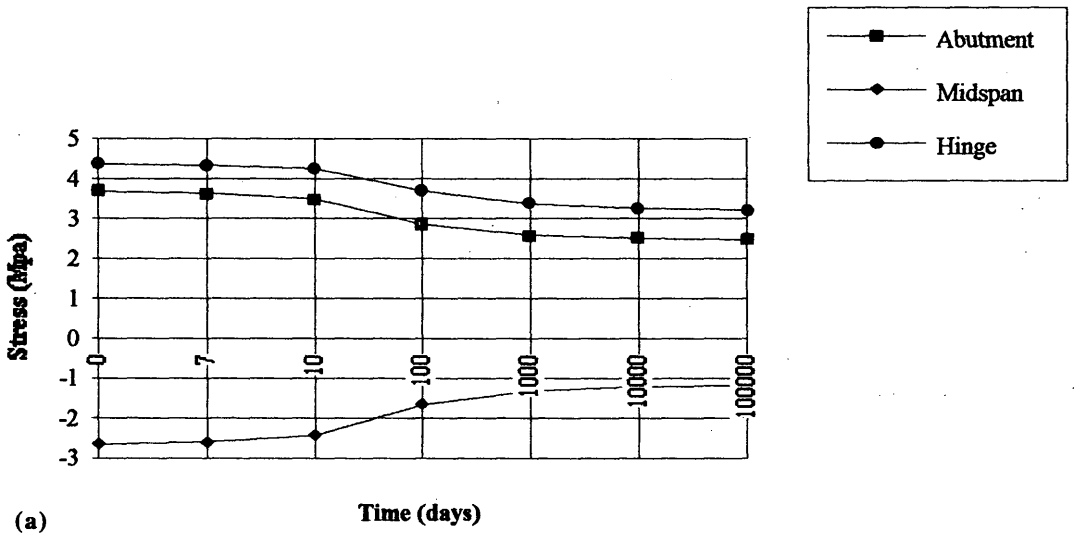

(a)

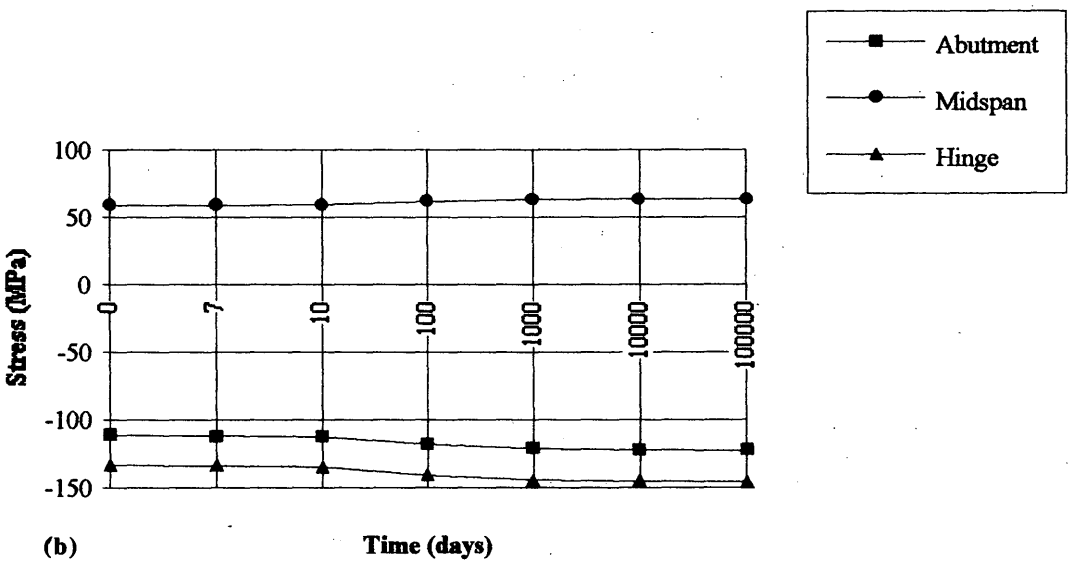

(b)

FIGURE 6 Stresses versus time, two-span bridge (*a*) at the top of the concrete slab; (*b*) at the bottom of the steel beam.

TABLE 2 Creep Analysis for Two-Span Bridge: 2-D versus 3-D

LOCATION	CREEP 2D (MPa)	CREEP 3D (MPa)	DIFFER. (MPa)	DIFFER. (%)
TOP OF CONCRETE				
ABUTMENT	-0.9724	-1.2000	0.2276	19
MIDSPAN	1.1655	1.4552	0.2897	20
HINGE	-1.3379	-1.1517	0.1862	14
BOTTOM OF STEEL				
ABUTMENT	-13.3034	-11.3172	1.9862	15
MIDSPAN	6.0620	5.1103	0.9517	16
HINGE	-12.4414	-12.3517	0.0897	1

RESULTS AND DISCUSSION

Two indeterminate composite structural systems are analyzed for creep: a single-span bridge (15.24 m) and a two-span bridge (2 × 34.75 m). The geometric and material properties are varied. Static and creep analysis are carried out with 2-D and 3-D models. Two creep analysis methods are used: the RCM and the AEMM. For the nonlinear analysis with the 3-D models the time step is varied. At the beginning, when creep was large, the step was small but was increased with time.

Tables 1 and 2 show that despite the various approaches used (RCM and AEMM), the differences between the 3-D and 2-D analysis range from 4 to 26 percent for the first example and from 15 to 20 percent for the second example. Usually the concrete stresses show higher differences because the comparison is between small numbers. From the results it is obvious that when the high stresses of steel are compared, the difference in percentage is smaller.

Results from 3-D analysis are not always smaller than those from the 2-D analysis. Tables 3 and 4 show the relative significance of creep with respect to dead load stresses. Creep stresses in concrete are as high as 26 to 55 percent of the dead load stresses and in steel creep stresses are as high as 2 to 21 percent.

In bridge design, dead load, live load, differential settlements, temperature, shrinkage, creep, and other effects are considered. It is understood that a fraction of the allowable stress of the material should be assumed to withstand the creep stresses. Therefore, a comparison of the creep stresses with the allowable stresses of steel and concrete provide an insight into how important creep is for jointless bridges. The creep stresses are only 1 to 9 percent of the allowable for the steel and 3 to 42 percent for the concrete (Tables

TABLE 3 Relative Significance of Creep With Respect To Dead Load Stresses: Single-Span Bridge

LOCATION	DEAD LOAD 3D (MPa)	CREEP 3D (MPa)	CREEP/DL (%)
TOP OF CONCRETE			
ABUTMENT	1.4965	-0.5724	38
MIDSPAN	-1.4069	0.6965	49
BOTTOM OF STEEL			
ABUTMENT	-26.3586	-5.4689	21
MIDSPAN	25.6689	0.5931	2

TABLE 4 Relative Significance of Creep With Respect To Dead Load Stresses; Two-Span Bridge

LOCATION	DEAD LOAD 3D (MPa)	CREEP 3D (MPa)	CREEP/DL (%)
TOP OF CONCRETE			
ABUTMENT	3.6827	-1.2000	32
MIDSPAN	-2.6483	1.4551	55
HINGE	4.3724	-1.1517	26
BOTTOM OF STEEL			
ABUTMENT	-111.1448	-11.3172	10
MIDSPAN	58.9724	5.1103	9
HINGE	-133.1931	-12.3517	9

5 and 6). It is clear that the steel stresses caused by creep are insignificant, but the concrete stresses can be large. Notice though that the concrete stresses decrease as a result of creep.

As discussed by Siros and Spyrakos (*3*), the moment change caused by creep is negative at all points along the deck, which implies that negative moments (supports) as a result of dead load will increase, but positive moments (midspans) will decrease. This was further verified with the present work, although moments are not shown but rather stresses are presented in the tables and figures. Also, the axial forces caused by creep should not be overlooked because they contribute to the formation of the total stresses at each point.

The results in Tables 1 and 2 demonstrate that stresses at the bottom of the steel stringers increase as a result of creep, but stresses at the top of the concrete slab decrease. It should be noticed that this happens at all points along the superstructure—for example at points of negative moment (support) and at points of positive moment (midspan).

Consequently, we can summarize that creep is additive to the dead load effect for the bottom of the steel but is acting beneficially at the top of the concrete by reducing both negative and positive stresses. Sometimes, however, the reduction of negative (compressive) stresses can be large enough to even change the sign and eventually produce tensile stresses (*17*). In such cases reinforcing of the top surface of the concrete deck would be necessary. Even though creep stress in concrete can be as high as 49 percent of the dead load stress and theoretically may cause reversal of the sign of the initial stress, it has not been observed in the analysis of several bridges of various span lengths and geometries (*18*).

SUMMARY AND CONCLUSIONS

Three-dimensional and two-dimensional analyses are performed to assess the creep effect on hybrid bridges with integral abutments. Two typical bridges with different dimensions and geometric and material properties are analyzed. Creep stresses at the top of the concrete slab and the bottom of the steel stringer are calculated for various ages with a 3-D nonlinear analysis. The results can be summarized as follows:

1. The two types of analysis (2-D and 3-D) arrived at results that differ by 1 to 29 percent. Comparisons of steel stresses usually show smaller differences (1 to 24 percent) than do concrete stresses (11 to 29 percent).
2. Creep stresses as a fraction of the dead load stresses range from 2 to 21 percent for the steel and 26 to 49 percent for the concrete.
3. Compared with the allowable stresses of the materials, creep stresses consist of 1 to 9 percent for steel and 3 to 42 percent for concrete.
4. Creep causes a small increase in positive and negative stresses at the bottom of steel stringers and a reduction in the tensile and compressive stresses at the top of the concrete deck. Designers should be alert because such reduction of compressive stresses may reverse them to tensile, in which case steel reinforcement is necessary.

ACKNOWLEDGMENT

This work is sponsored by the West Virginia Department of Highways and FHWA.

TABLE 5 Creep Stresses Versus Allowable Stress of Each Material: Single-Span Bridge

LOCATION	CREEP 3D (MPa)	ALLOWABLE (MPa)	CREEP/ALL. (%)
TOP OF CONCRETE			
ABUTMENT	-0.5724	3.6827	16
MIDSPAN	0.6965	18.0689	4
BOTTOM OF STEEL			
ABUTMENT	-5.4689	140	4
MIDSPAN	0.5931	140	1

TABLE 6 Creep Stresses Versus Allowable Stress of Each Material: Two-Span Bridge

LOCATION	CREEP 3D (MPa)	ALLOWABLE (MPa)	CREEP/ALL. (%)
TOP OF CONCRETE			
ABUTMENT	-1.2000	2.8552	42
MIDSPAN	1.4552	10.8621	13
HINGE	-1.1517	2.8552	40
BOTTOM OF STEEL			
ABUTMENT	-11.3172	140	8
MIDSPAN	5.1103	140	4
HINGE	-12.3517	140	9

REFERENCES

1. Wasserman, E. P. Jointless Bridge Deck. *Engineering Journal*/AISC, 3rd Quarter, 1987.
2. Loveall, C. L. Jointless Bridge Decks. *Civil Engineering*, Nov. 1985.
3. Siros, D. A., and C. C. Spyrakos. A Study of Jointless Bridge Behavior. Proc., 12th Structures Congress, Atlanta, Ga., Vol. 1, ASCE April 1994, pp. 485–490.
4. Bazant, Z. P. Comparison of Approximate Linear Methods for Concrete Creep. *Journal of the Structural Division*, ASCE, Vol. 99, Sept. 1973, pp. 1851–1874.
5. Gilbert, I. R. Time-Dependent Analysis of Composite Steel-Concrete Sections. *Journal of Structural Engineering*, ASCE, Vol. 115, No. 11, Nov. 1989, pp. 2687–2705.
6. Ghali, A., and R. Favre. *Concrete Structures: Stresses and Deformations*. Chapman and Hall, London, 1986.
7. Bazant, Z. P. Prediction of Concrete Creep Effects Using Age-Adjusted Effective Modulus Method. *ACI Journal*, Vol. 69, April 1972, pp. 212–217.
8. *Theoretical Manual Volume*, Revision 4.4. ANSYS.
9. Prediction of Creep, Shrinkage and Temperature Effects in Concrete Structures, In *Manual of Concrete Practice*. American Concrete Institute, 1988. pp. 209R-1-209R-60.
10. Bathe, K. J. *Finite Elements Procedures in Engineering Analysis*. Prentice-Hall, Englewood, N.J. 1982.
11. Walker, R. D. Numerical Methods for Engineers and Scientists. TAB Professional and Reference Books, 1st ed., 1987, pp. 245–251.
12. Meyer, S. L. Data Analysis for Scientists and Engineers. Wiley, 1975.
13. *ANSYS User's Manual*, Vol. 1, Revision 4.4.
14. *ABAQUS Standard User's Manual, version 5.3*. Sections 4.6.9 and 7.6.9, 1993.
15. *ALGOR User's Manual*, 1994.
16. Spyrakos, C. C. *Finite Element Modeling in Engineering Practice*. West Virginia University Press, Morgantown, 1994.
17. McHenry, D. A New Aspect of Creep in Concrete and its Applications to Design. *Proc., ASTM*, Vol. 43, 1943, pp. 1069–1086.
18. Siros, K. A. *Three Dimensional Analysis of Integral Bridges—Loading and Behavior*. Dissertation, West Virginia University, Morgantown, 1995.

Publication of this paper sponsored by Committee on Dynamics and Field Testing of Bridges.

Field Evaluation of Concrete Bridge Decks Reinforced with Epoxy-Coated Steel in Indiana

HENDY O. HASAN, JULIO A. RAMIREZ, AND DOUGLAS B. CLEARY

A field evaluation of a representative sample of six bridges in terms of traffic and environmental and salt exposure conditions was conducted to assess the in-service condition of concrete bridge decks reinforced with epoxy-coated steel in Indiana. The field condition assessment included (*a*) identification of any delaminated and spalled areas; (*b*) detailed mapping of the observed cracking; (*c*) identification of the concrete cover and the underlying reinforcement; (*d*) core sampling with and without reinforcement to determine the compressive strength and unit weight, and (*e*) concrete powder sampling to determine chloride concentration at various depths. No signs of steel corrosion were found in the bar samples extracted from cores in the six bridges evaluated. The chloride concentration levels at the level of the reinforcement for all but two of the bridges were well above the commonly accepted threshold value at the level of the reinforcement. Evaluation of the field data revealed that, to date, the combination of adequate concrete cover and epoxy coating has provided a good corrosion protection system in Indiana. The sample included the first bridge in Indiana on which epoxy-coated reinforcement was used (1976).

This paper presents the field phase findings from a research study sponsored by the Indiana Department of Transportation (INDOT) and FHWA. The field phase of this research study was aimed at the condition assessment of a representative sample of concrete bridge decks and slabs reinforced with epoxy-coated steel in Indiana.

A total of six bridges throughout Indiana were selected for the evaluation. The bridges selected represent a cross section of environmental conditions, traffic, and intensity of salt application. The sample included the first bridge deck in Indiana reinforced with epoxy-coated steel. This bridge was built in 1976. The field study addresses the performance of decks supported on a more flexible system (steel girder) as well as more rigid support conditions (precast, prestressed girders) and concrete slabs. None of the bridge decks included in the sample had been overlayed. The site selection was fully coordinated with personnel from INDOT. Evaluation of concrete core samples for compressive strength and concrete powder samples for chloride content was conducted by the Materials and Testing Division of INDOT.

BRIEF DESCRIPTION

The location of the bridges selected is shown in Figure 1. The first bridge selected for evaluation was built in 1985. The bridge is located in downtown Indianapolis over the White River. The structure is a six-span continuous composite steel box-girder bridge with a maximum span length of 62.8 m (206 ft). This bridge represents the case of a deck on a flexible superstructure in the central part of the state subjected to heavy urban traffic and severe deicing and salt exposure. The second bridge is located in downtown South Bend. The structure was built in 1983 and has a maximum span length of 27.4 m (90 ft). The structure is a four-span continuous composite bridge deck supported on precast, prestressed AASHTO girders (Type IV). It represents a case of concrete bridge deck built on a more rigid support system. This structure is subjected to significant urban traffic and severe salt application. The third structure is located a few miles south of the city of South Bend. It was built in 1980 and consists of a three-span continuous welded girder bridge with composite deck subjected to heavy truck traffic and heavy salt exposure condition. The maximum span length is 18.9 m (62 ft). The fourth structure is a three-span skewed continuous reinforced concrete slab bridge built in 1985. The maximum span length is 14 m (46 ft). The structure is subjected to moderate traffic and moderate deicing salt application. The fifth structure is a three-span continuous bridge deck supported on continuous steel girders located in the city of Gary in the northern part of the state. This bridge was built in 1980 with a maximum span length of 19.7 m (64 ft 6 in.). The concrete deck was built using stay-in-place metal forms. The bridge is subjected to heavy industrial traffic with heavy deicing salt application. The sixth bridge deck selected is continuous for live load and supported on prestressed concrete I-beams (Type III). The bridge was built in 1976, has three spans with a maximum span length of 22.5 m (73 ft 9 in.), and is subjected to light to moderate truck traffic and moderate salt exposure. A summary of the bridge information and traffic data is presented in Tables 1 and 2, respectively.

FIELD EVALUATION PROCEDURES

The field evaluation included the following procedures:

1. Identification of any delaminated and spalled areas by close visual inspection and the use of the chain drag procedure;
2. Detailed mapping of the observed cracking on the top of the deck, as well as delaminated and spalled areas on the selected lane;
3. Evaluation of the concrete cover using an *R*-meter (focused electromagnetic field) to ascertain concrete cover and to locate the underlying reinforcement;
4. Core samples taken with or without reinforcement for evaluation of concrete compressive strength, concrete cover, unit weight, and visual inspection of the conditions of the epoxy coating; and
5. Concrete power sampled at selected points and at various depths for laboratory determination of chloride content.

School of Civil Engineering, Purdue University, West Lafayette, Ind. 47907.

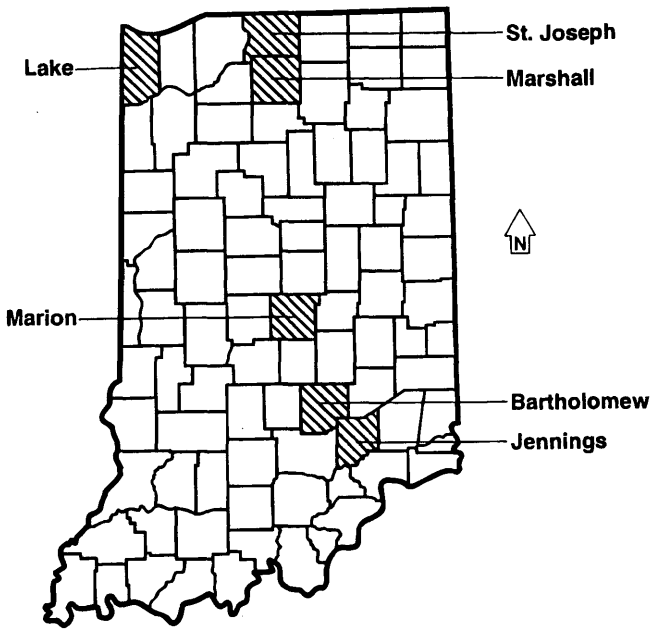

FIGURE 1 Bridge locations.

TABLE 1 Summary of Bridge Information

Bridge No.	Location	County	Bridge Type	Span Max (m)	Traffic	Deicing Salt Exposure
40-49-7032	US-40	Marion	Six-span continuous composite steel box girder bridge	62.8	Heavy urban	Severe
20-71-6538	US-2	St.Joseph	Four-span continuous composite precast pre-stressed AASHTO girder	27.4	Significant urban	Severe
31-50-2540	US-31	Marshall	Three-span continuous welded girder bridge with a composite concrete deck	18.9	Heavy truck	Heavy
7-03-6797	SR-7	Bartholomew	Three-span skewed continuous reinforced concrete slab bridge	14.0	Moderate truck	Moderate
912-45-6599	SR-912	Lake	Three-span continuous composite steel girder bridge	19.7	Heavy industrial	Heavy
7-40-6527	SR-7	Jennings	Continuous prestressed concrete I-beam (Type III)	22.5	Light to moderate truck	Moderate

Conversion Factors: 1 m = 3.281 ft.

TABLE 2 Traffic Data

Bridge	A.D.T. (V.P.D.)	A.D.T. Projected (V.P.D.)	D.H.V. (V.P.D.)	Trucks	Design Speed km/h	Access Control
40-49-7032	27,530 (1982)	44,390 (2002)	3,995 (2002)	D.H.V. 4% A.D.T. 5%	64	None
20-71-6538	11,015 (1976)	19,825 (1996)	1,190 (1996)		64	None
31-50-2540	17,080 (1978)	29,480 (1996)	-	D.H.V. 10% A.D.T. 17%	64	None
7-03-6797	5,680 (1983)	9,770 (2004)	977 (2004)	D.H.V. 7% A.D.T. 12%	113	-
912-45-6599	14,800 (1975)	25,250 (1995)	3,170 (1995)	-	97	Full
7-40-6527	2,200 (1972)	4,420 (1992)	-	D.H.V. 7% A.D.T. 17%	80	None

A.D.T. = Average Daily Traffic
D.H.V. = Design Hourly Volume
V.P.D. = Vehicles Per Day
- Data Not Available
Conversion factors: 1 km/h = 0.622 mph

During the field inspection, detailed mapping of delaminated and spalled areas as well as crack patterns were made. Crack widths were measured using a crack width comparator card. The delaminated and spalled areas were identified by close visual inspection and with the aid of chain drag procedure. Positions of reinforcement were identified by using an *R*-meter. Core samples with or without elements from the top layer of reinforcement were then taken for laboratory investigation. The chloride contents were determined through the laboratory analysis of pulverized concrete samples taken from the deck. The method used to determine chloride content approximated the automated titrator method duplicating ASTM-C114. Concrete powder samples were taken at various levels: Level A from 0 to 25.4 mm (0 to 1 in.); Level B from 25.4 to 50.8 mm (1 to 2 in.); Level C from 50.8 to 76.2 mm (2 to 3 in.); and Level D from 76.2 to 100.6 mm (3 to 4 in.). Diameters of the holes for each depth are 31.75 mm (1 1/4 in.), 25.4 mm (1 in.), 19.1 mm (3/4 in.), and 19.1 mm (3/4 in.), and 19.1 mm (3/4 in.), respectively.

RESULTS

Figures 2 through 5 show the crack patterns and the core and concrete powder sample locations for one of the decks surveyed, Bridge 7-40-6527. Similar information for the other bridges evaluated can be found elsewhere (*1*). The test results of core strength, calculated cylinder strength, unit weight, concrete cover, maximum crack width, and chloride content for all the samples of each individual bridge can be found elsewhere (*1*). A summary of the average value of these results for each bridge is indicated in Table 3.

The average concrete cover ranged from 61 to 97 mm (6.1 to 3.82 in.), and the maximum crack width ranged from 0.64 mm to 1.52 mm (0.025 to 0.060 in.). Inspections of the conditions of steel extracted from cores show no indication of rusting or debonding on any of the bars. The coating was difficult to remove with a knife. From visual inspection of samples from which the coating was stripped mechanically, no sign of under-film corrosion was observed.

DISCUSSION OF RESULTS

At the level of top reinforcement, except for the Marion and Bartholomew County bridges, the chloride content was found to be above the threshold value of 1.2 kg/m^3 (2.0 lb/yd^3) (*2*). This indicates that a potentially active corrosive environment was present. Inspection of the steel samples from coring showed no signs of corrosion or debonding of coating. The chloride content substantially decreased with every inch of increment in depth. This finding confirms the importance of concrete cover in reducing the risk of steel corrosion. Similar results were reported by Mckeel (*3*). From the evaluation during construction and through 13 years of service of two bridges in Virginia, it was concluded that the combination of cover and epoxy-coated reinforcement provided excellent protection against corrosion. In Mckeel's study, no signs of significant corrosion and debonding of the coating were found despite the poor initial state of the coating and its exposure to the elements from the onset of construction until placement of the deck concrete.

In addition to the concern over reduced bond to concrete of epoxy-coated steel, other significant issues concerning epoxy-

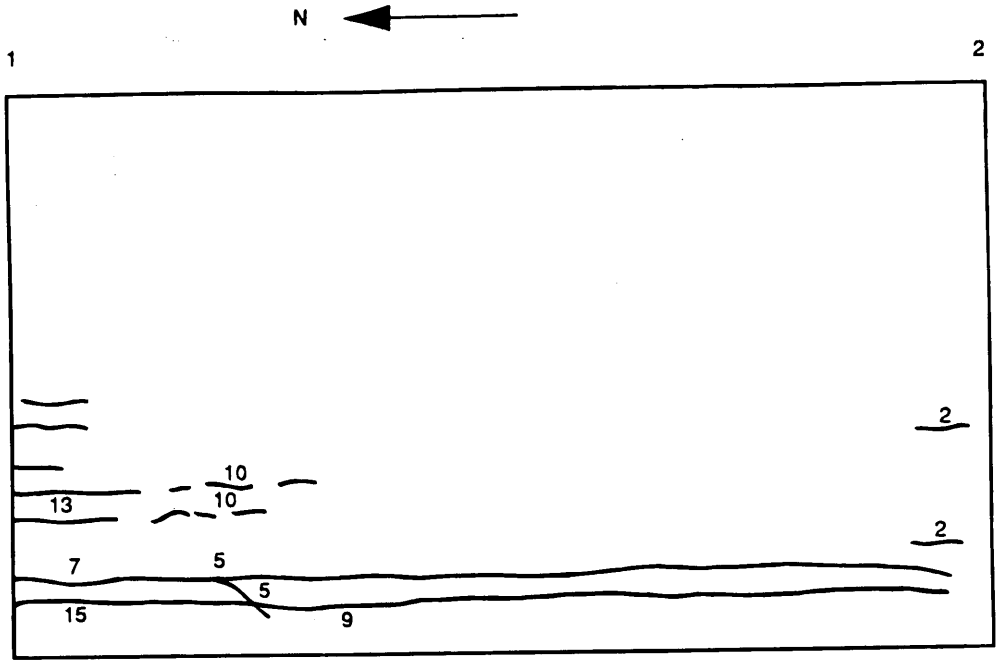

Span 1-2, East

FIGURE 2 Crack patterns, Bridge 7-40-6527, Span 1-2 east (crack widths shown $\times 10^{-3}$ in. 1 in. = 25.4 mm).

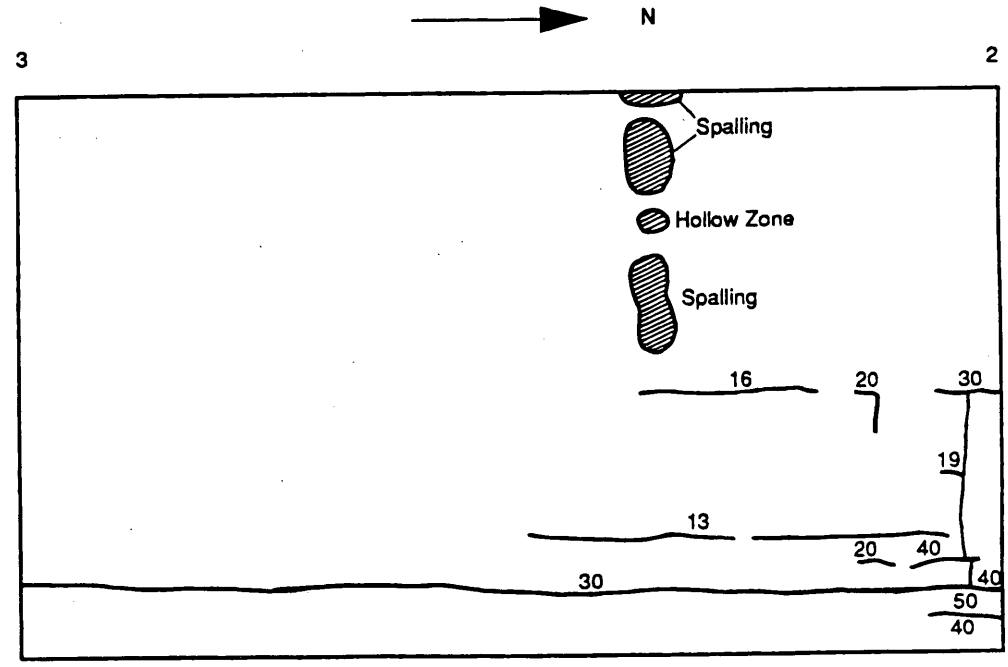

Span 2-3, West

FIGURE 3 Crack patterns, Bridge 7-49-6527, Span 2-3 west (crack widths shown $\times 10^{-3}$ in. 1 in. = 25.4 mm).

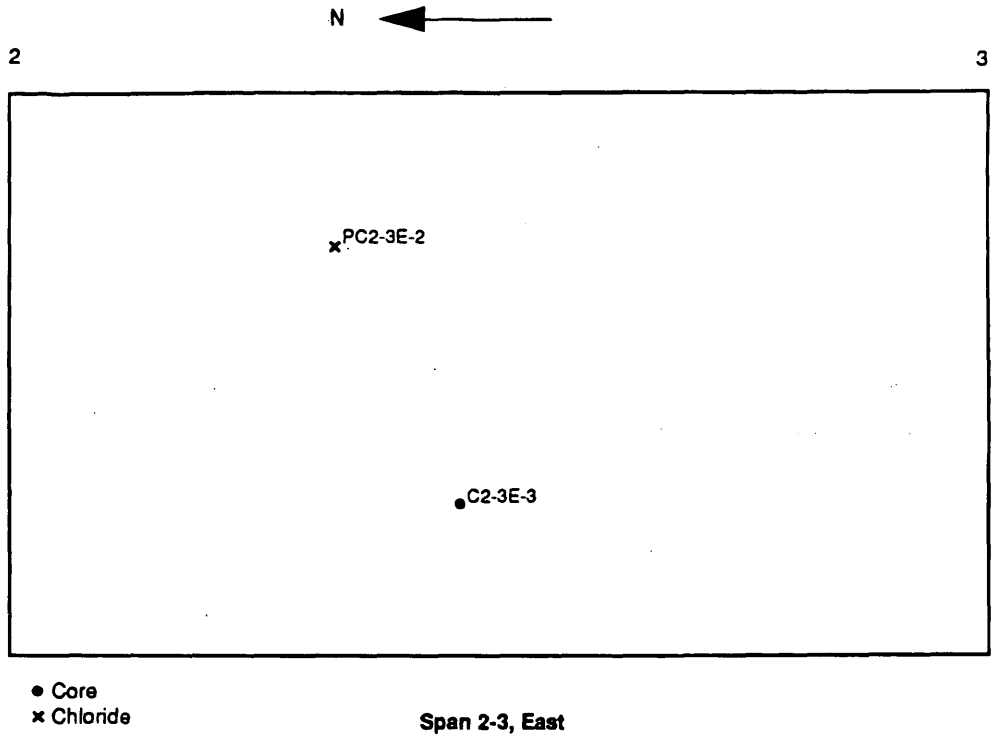

FIGURE 4 Core and chloride sampling, Bridge 7-40-6527, Span 2-3 east.

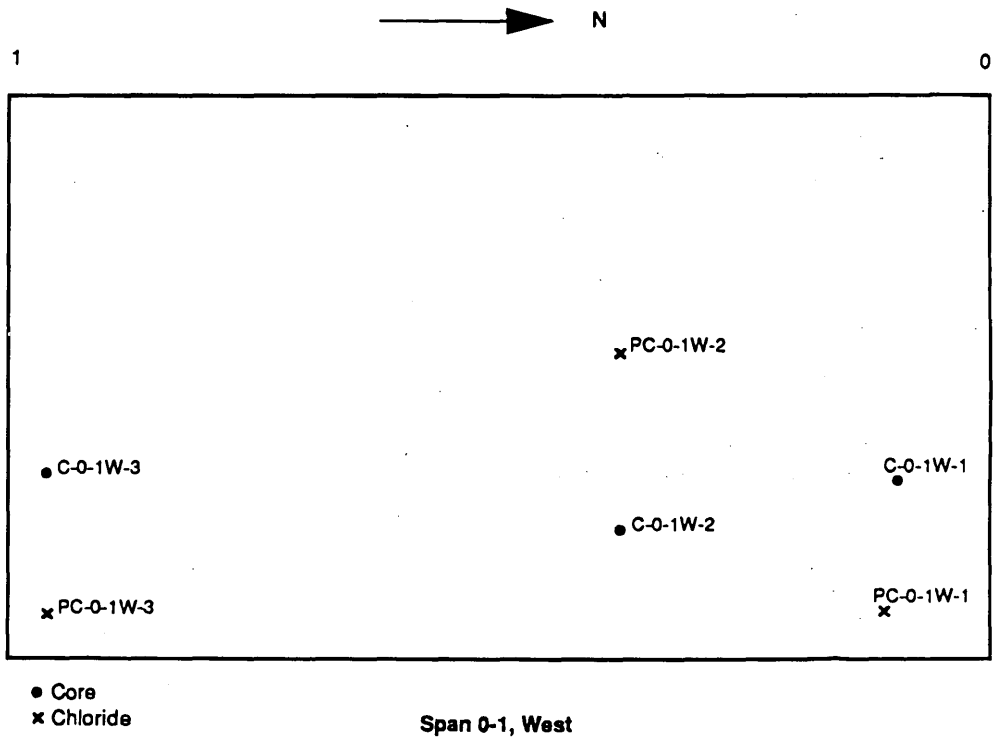

FIGURE 5 Core and chloride sampling, Bridge 7-40-6527, Span 0-1 west.

TABLE 3 Summary of Results

Bridge No.	Average Values of								Max
	Core Strength	Calculated Cylinder Strength	Unit Weight	Concrete Cover	Chloride Content kg/m³ Level				Crack Width
	MPa	MPa	kg/m³	(mm)	A	B	C	D	(mm)
40-49-7032	41.64	35.39	2341	61	3.52	1.29	0.88	0.70	0.76
20-71-6538	51.60	43.86	2423	32	8.41	4.22	2.21	2.36	0.64
31-50-2540	44.99	38.24	2387	62	10.54	7.21	1.91	0.96	0.76
7-03-6797	45.76	38.90	2483	97	4.24	1.66	0.65	0.47	0.89
912-45-6599	39.14	33.27	2328	74	7.18	2.90	1.94	1.66	1.52
7-40-6527	37.90	32.21	2384	77	8.96	5.04	2.96	1.63	1.27

Note: Level A: 0 - 2.54 cm Level B: 2.54 - 5.08 cm
Level C: 5.08 Level D: 7.62 - 10.06 cm

Conversion Factors: 1 MPa = 145 psi, 1 mm = 0.0394 in
1 kg / m³ = 1.685 lb / cu.yd.
1 kg / m³ = 0.0624 lb / cu.ft.

coated steel are related to its durability. In the last few years, there has been serious concern about the effectiveness and long-term durability of the epoxy-coated steel as a corrosion protection system. Smith et al. (*4*) investigated seven bridge structures in the Florida Keys. Significant corrosion of the epoxy-coated rebars was observed in four of the five major bridge substructures. It was found that corrosion occurred both in fabricated and straight epoxy-coated rebars. Furthermore, coating after fabrication did not significantly improve corrosion resistance. Disbondment occurred in "perfect" condition bars and in the bars coated after fabrication. It was concluded that epoxy-coated rebar will not provide suitable long-term protection against corrosion in the marine splash zone.

In 1990, Clear (*5*) stated that epoxy-coated rebar technology is flawed and will not ensure adequate long-term field performance in severe chloride environments, especially those involving continuous or frequent wetting of the concrete. The failure of the epoxy coating through means such as cathodic disbondment and the loss of the epoxy's insulative properties also have been reported. Clear concluded that the system "can no longer be considered a viable primary protective system for North American bridge structures in corrosive environments with expected maintenance-free lives in excess of about 15 years in northern environments or more than 5 years in hot, salty and moist southern exposures." Furthermore, he recommended against the continued usage of epoxy-coated reinforcing steel as the primary protection in adverse environments for structures for low-maintenance lives in excess of 5 years (southern) or 15 years (northern). Because of the controversy and the broad implications of the issue, the effectiveness and long-term durability issues of epoxy-coated bars have gained the attention of numerous researchers. Efforts are being made to gain a better understanding of the long-term durability and effectiveness of epoxy-coated bars (*3,6,7*).

SUMMARY

A field evaluation of a representative sample in terms of traffic and environmental and salt exposure conditions of six bridges in Indiana has been carried out. The bridges in the sample ranged in length of service from 6 to 18 years. Data gathered in this field study provided useful information with respect to the important issue of durability of structures with epoxy-coated steel. The following are important findings:

1. Chloride content is significantly decreased with increases in concrete cover.
2. Except for two of the bridges, all of the other bridge decks surveyed were under exposure to chloride contents well above the commonly accepted corrosion threshold value at the level of the reinforcing steel.
3. No sign of disbondment of the coating or corrosion was observed in the reinforcement extracted from the bridge decks surveyed.

On the basis of the findings of this study, it can be concluded that, even after 18 years, epoxy-coated steel has had a satisfactory performance to date in Indiana bridge decks surveyed. Currently, Indiana follows AASHTO Specification M284 for epoxy-coated bars. The concrete used in bridge decks is a Class C concrete with cement content of 391 kg/m³ and a maximum water-cement ratio of 0.443. Wet curing for at least 96 hrs is required beginning immediately after initial set.

RECOMMENDATIONS

1. Adequate concrete cover should always be ensured. The chloride content is substantially reduced with a small increase in cover, hence the corrosion risk substantially decreases. In addition, extra cover also provides improvement in the anchorage of the bars. Larger diameter ratios of cover to bar are recommended in harsh environments to reduce the crack opening and should not be reduced with the expectation that the epoxy coating will be the sole corrosion protection system.
2. Good construction practices, such as adequate inspection, and good finishing and curing techniques should be emphasized because they will lead to durable concrete. The use, proper manufacturing,

and handling of epoxy-coated bars are but a few of the aspects related to durable concrete bridge decks.

3. More research is needed to clarify the long-term effectiveness and durability issues of epoxy-coated steel as a corrosion protection system for highway and bridge structures. In particular, the close inspection of bridge structures in the field should be continued to effectively assess the long-term performance of coated bars as a corrosion protection system.

ACKNOWLEDGMENT

The work described is part of a research study funded by INDOT and FHWA as a 3-year HPR-Part II Research Study.

REFERENCES

1. Hasan, H. O., and J. A. Ramirez. *Behavior of Concrete Bridge Decks and Slabs Reinforced with Epoxy-Coated Steel.* Draft Final Report. FHWA/IN/JHRP-94-9. Purdue University, 1994, pp. 172–243.
2. Mindess, S., and J. F. Young. *Concrete.* Prentice Hall, Inc., Englewood Cliffs, N. J., 1981, pp. 544–578.
3. Mckeel, W. T., Jr. *Evaluation of Epoxy-Coated Reinforcing Steel.* Report FHWA/VA-94-R5. Virginia Transportation Research Council, Dec. 1993.
4. Smith, L. L., R. J. Kessler, and R. G. Powers. Corrosion of Epoxy-Coated Rebar in a Marine Environment. In *Transportation Research Circular 403*, TRB, National Research Council, Washington, D.C., March 1993, pp. 36–45.
5. Clear, K. C. *Effectiveness of Epoxy Coated Reinforcing Steel.* Kenneth C. Clear, Inc., Sterling, Va., Jan. 10, 1992.
6. Pfeifer, D. W., R. Landgren, and P. Krauss. Performance of Epoxy-Coated Rebars: A Review of CRSI Research Studies. In *Transportation Research Circular* 403, TRB, National Research Council, Washington, D.C., March 1993.
7. Chase, S. B. *Structural Effects of Epoxy-Coating Disbondment.* Publication FHWA-RD-93-055. FHWA, Nov. 1993.

The opinions, findings, and conclusions expressed in this paper are those of the authors and do not necessarily represent the views of the sponsors.

Publication of this paper sponsored by Committee on Dynamics and Field Testing of Bridges.

Analysis of In-Service Jointless Bridges

HEMANTH K. THIPPESWAMY AND HOTA V. S. GANGARAO

Jointless bridge systems are designed currently for primary loads only: for example, live load and dead load. The only secondary load that is considered while designing a jointless bridge is the temperature load. With respect to other secondary loads, such as creep and shrinkage of the superstructural material, it is assumed that the effects of creep and shrinkage are opposite in nature and cancel out each other. Designers have different opinions on earth pressure and settlement loads. To develop a proper explanation for jointless bridge behavior, a better insight into the performance of jointless bridges is needed in terms of primary as well as secondary loads. Five in-service jointless bridges were analyzed for primary and secondary loads by the state-of-the-art methods. The analytical data generated for one bridge are synthesized and presented. The discussion includes effect of primary and secondary loads, effect of secondary loads with respect to primary loads, and effect of different systems (boundary conditions) on stresses at various locations. The results reveal that the combination of integral stub abutment and a single row of piles makes the substructure flexible, thereby reducing the stresses at superstructure and abutment joint. The weak axis orientation of piles further reduces stresses at superstructure and abutment joint. The major contributor to total stresses is the temperature load. Creep of superstructural material is helpful in reducing the stresses at some locations. Shrinkage relieves creep to some extent but not completely. Earth pressure causes negligible stresses at all locations in the bridge. Settlement stresses are considerable in multispan jointless bridges.

Jointless bridge systems are designed currently for primary loads only, such as live loads and dead loads (*1,2*). The only secondary load that is considered while designing a jointless bridge is the temperature load. Typically, a single row of piles with an integral stub abutment is used to accommodate horizontal expansion or contraction as a result of temperature load. With respect to other secondary loads, such as creep and shrinkage of the superstructural material, it is assumed that the effects of creep and shrinkage are opposite in nature and cancel out each other. Designers have different opinions about earth pressure and settlement loads. However, there is no literature available that addresses the effect of primary and secondary loads in terms of magnitude of stresses and deformations induced in jointless bridges. Although jointless bridges operate under very high secondary stresses, they are found to function extremely well, and the distress has been nominal (*3*). To develop an appropriate explanation for jointless bridge behavior that would fit field data, a better insight into the performance of jointless bridges is needed under temperature, creep, shrinkage, settlement, and other forces.

OBJECTIVES

The objectives of this paper are to (*a*) identify the state-of-the-art methods of analysis for in-service jointless bridges; (*b*) prioritize loads for analysis of in-service jointless bridges; (*c*) present synthesized analytical data that aid in understanding the behavior of jointless bridges; and (*d*) study the effects of primary and secondary loads, boundary conditions, and system flexibility on the stresses at various locations in the jointless bridge system.

Constructed Facilities Center, West Virginia University, Morgantown, W.Va. 26506-6103.

SCOPE

Five in-service jointless bridges (Table 1) were analyzed by state-of-the-art methods of analysis. Because of space limitations, the results for only one bridge (Lone Tree Road Bridge, Iowa) are presented here (Tables 2 through 5). The structural details were extracted from the drawings supplied by various state highway departments. The loads considered in the analysis were (*a*) dead load or self-weight (DL); (*b*) dead load plus creep of the superstructural material (DL + C); (*c*) live load (LL); (*d*) temperature gradient across the depth of the superstructure (TG); (*e*) uniform temperature across the depth of the superstructure; (*f*) uniform shrinkage of the superstructural material (SH); (*g*) differential settlement (SE); and (*h*) earth pressure (EP). These loads are schematically represented in Figure 1. After a thorough study, it was found that uniform temperature was unrealistic because it rarely exists in practice; because of this, uniform temperature load was omitted in later analyses. For each bridge and for each load case, several boundary conditions were considered. The boundary conditions were considered in such a manner that minimum to maximum system flexibility was achieved. The bridge superstructures considered for analysis were made of concrete deck stiffened with steel stringers. The abutments were of stub type. Four bridges were symmetrical and one bridge was unsymmetrical. Four bridges were skewed and one bridge was straight. The maximum skew occurred for a single-span bridge, and it was 20 degrees 29 minutes. In the analyses, the skew was ignored. More details about these five bridges appear elsewhere (*4*). Furthermore, the results in terms of internal forces and corresponding stresses were tabulated and evaluated.

ANALYSIS METHOD

In the past, two-dimensional frame models (*5*) included the flexural stiffness of piles, the axial and flexural stiffnesses of the deck and girders, and the axial and flexural stiffnesses of the integral abutment. Girton et. al. (*b*) reported that excellent correlation was obtained between the results predicted by the two-dimensional (2-D) frame models and the values measured in the field. The 2-D frame models are simpler in the sense that they use ordinary beam elements, and the preparation of the model is faster than for three-dimensional (3-D) models requiring higher-order elements. Another advantage of 2-D models is their suitability for parametric study. In this paper, the jointless bridges are idealized and analyzed as 2-D frame models. The age-adjusted effective modulus method was used for creep and shrinkage analysis. Thermal stress

TABLE 1. Details of In-Service Jointless Bridges Analyzed (1 ft = 0.3 m; 1 in. = 2.5 cm; 1 psi = 6.89 kPa)

Serial No.	Name of the Bridge	Location of the Bridge	Bridge Details
1	Short Creek Road Bridge	Brooke and Ohio ounty, West Virginia	Span: Single span of 110 ft.; Width: 40 ft.; No. of stringers and spacing: 6 with 106 in.; Skew angle: 20^0-29'; Abutment height: 98 in.; Piles: Single row of HP 12x53; Pile orientation: Strong axis bending; Design live load: HS 25-44; Concrete strength: 3.122 million psi for superstructure and 3.605 million psi for substructure.
2	Lone Tree Road Bridge	Black Hawk County, Iowa	Span: Two-span of 114ft.-114 ft.; Width: 40 ft.; No. of stringers and spacing: 5 with 111 in.; Skew angle: 8^0; Abutment height: 96 in.; Piles: Single row of HP 10x42; Pile orientation: Weak axis bending; Design live load: HS 20-44; Concrete strength: 3.37 million psi for superstructure and substructure.
3	South Saturn Parkway	Maury County, Tennessee	Span: Two-span of 132.5 ft.-117.5 ft.; Width: 40 ft.; No. of stringers and spacing: 6 with 120 in.; Skew angle: 18^0; Abutment height: 88 in.; Piles: Single row of HP 10x42; Pile orientation: Weak axis bending; Design live load: HS 20-44; Concrete strength: 3.12 million psi for superstructure and substructure.
4	Over Creek Road Bridge	Jones County, South Dakota	Span: Three-span of 68 ft.-87 ft.-68 ft.; Width: 46 ft.; No. of stringers and spacing: 5 with 102 in.; Skew angle: 0^0; Abutment height: 73.5 in.; Piles: Single row of HP 10x42; Pile orientation: Weak axis bending; Design live load: HS 20-44; Concrete strength: 3.6 million psi for superstructure and substructure.
5	Bridge Over Little Kanawha River	Upshur County, West Virginia	Span: Three-span of 45 ft.-60 ft.-45 ft.; Width: 22 ft.; No. of stringers and spacing: 4 with 96 in.; Skew angle: 20^0; Abutment height: 77.2 in.; Piles: Single row of HP 10x42; Pile orientation: Weak axis bending; Design live load: HS 25-44; Concrete strength: 3.8 million psi for superstructure and 3.12 million psi for substructure.

Note: The superstructure of all bridges is made of concrete slab composite with steel stringers.

TABLE 2. Stresses at Superstructure and Abutment Joint in Various Systems (1 ksi = 6890 kPa)

Load Case	Stresses (ksi)					Remarks
	System A	System B	System C	System D	System E	
DL	0.382 -13.16	0.353 -13.15	0.353 -13.15	0.0033 -0.094	0.00113 -0.0323	The dead load stresses in Systems D and E are negligible because of the flexibility of the substructure. These Systems behave like simply supported structures.
DL+C	0.272 -14.67	0.219 -14.61	0.219 -14.61	0.00304 -0.145	0.00104 -0.0497	The effect of creep is to decrease the top tensile stresses and to increase bottom compressive stresses. Creep effect is smaller in flexible Systems D and E when compared to stiffer Systems A through C.
LL	0.301 -10.65	0.286 -10.65	0.239 -8.4	0.00236 -0.0674	0.00081 -0.0231	The live load stresses in Systems D and E are negligible because of the flexibility of the substructure. These Systems behave like simply supported structures.
TG	0.123 -8.29	0.934 -8.58	0.914 -8.58	0.480 7.56	0.479 7.58	The top tensile stresses due to temperature gradient are lower in Systems D and E. The bottom stresses in Systems D and E which are tensile in nature are within allowable stress values for steel.
SH	0.239 1.04	0.0791 1.23	0.0791 1.23	0.0765 1.38	0.0759 1.41	Stresses due to shrinkage are negligible in Systems D and E.
SE	0.136 -4.37	0.117 -4.36	0.117 -4.36	0.00119 -0.034	0.00119 -0.0342	Settlement causes negligible stresses in Systems D and E.
EP	0.0006 -0.0027	0.0024 -0.0074	0.0052 -0.1121	0.057 -1.43	0.0567 -1.43	Earth pressure causes negligible stresses in all Systems.
TOTAL	1.07 -36.93	1.62 -36.97	1.57 -34.82	0.62 7.31	0.62 7.46	The total stresses are lower in Systems D and E compared to other Systems. During winter these stresses are further reduced due to opposite nature of stresses caused by temperature gradient.

Note: Positive stresses indicate tensile stresses.
Total is the sum of DL+C, LL, TG, SH, SE and EP.

TABLE 3. Stresses at Midspan of First Span in Various Systems (1 ksi = 6890 kPa)

Load Case	Stresses (ksi)					Remarks
	System A	System B	System C	System D	System E	
DL	-0.335 6.42	-0.357 6.22	-0.357 6.22	-0.342 9.34	-0.343 9.35	Top compressive stresses are nearly same in all Systems and bottom tensile stresses are higher in Systems D and E. Though, Systems D and E behave like simply supported structures, the intermediate support moment effect the midspan stresses.
DL+C	-0.188 6.93	-0.221 6.11	-0.221 6.11	-0.218 10.24	-0.219 10.26	The effect of creep is to decrease top compressive stresses and to increase bottom tensile stresses.
LL	-0.365 7.52	-0.376 7.43	-0.399 8.51	-0.390 10.65	-0.390 10.65	Top compressive stresses are nearly same in all Systems and bottom tensile stresses are higher in Systems D and E. Though Systems D and E behave like simply supported structures, the intermediate support moment effect the midspan stresses.
TG	-0.278 2.59	0.309 7.91	0.309 7.91	0.318 12.00	0.317 12.01	The top tensile stresses due to temperature gradient are almost same in Systems B through E and the bottom stresses due to temperature gradient are higher in Systems D and E compared to other Systems.
SH	0.281 -0.714	0.181 -2.99	0.181 -2.99	0.181 -2.92	0.180 -2.91	Stresses due to shrinkage are almost same in Systems B through E.
SE	-0.0394 0.513	-0.0559 0.362	-0.0559 0.362	-0.054 1.46	-0.054 1.46	Settlement causes negligible stresses in all Systems.
EP	0.00037 0.00373	0.0015 0.017	0.0028 -0.04833	0.033 -0.785	0.033 -0.786	Earth pressure causes negligible stresses in all Systems.
TOTAL	-0.586 16.85	-0.161 18.83	-0.182 19.85	-0.131 30.64	-0.132 30.68	The total bottom stresses are higher in Systems D and E, and exceed allowable limits of steel. However, these stresses are reduced during winter due to opposite nature of temperature stresses.

Note: Positive stresses indicate tensile stresses.
Total is the sum of DL+C, LL, TG, SH, SE and EP.

TABLE 4. Stresses at Pier in Various Systems (1 ksi = 6890 kPa)

Load Case	Stresses (ksi)					Remarks
	System A	System B	System C	System D	System E	
DL	0.462 -11.2	0.447 -11.39	0.447 -11.39	0.753 -15.41	0.754 -15.43	The top tensile and bottom compressive stresses are higher in Systems D and E.
DL+C	0.269 -12.26	0.256 -13.14	0.256 -13.14	0.401 -16.72	0.402 -16.75	The effect of creep is to decrease top tensile stresses and to increase bottom compressive stresses.
LL	0.325 -7.51	0.315 -7.67	0.311 -7.89	0.517 -10.58	0.518 -10.59	The top tensile and bottom compressive stresses are higher in Systems D and E.
TG	0.044 9.68	0.452 14.49	0.452 14.95	0.812 10.24	0.813 10.24	The top tensile stresses are higher and bottom tensile stresses are lower in Systems D and E.
SH	0.329 -1.58	0.287 -4.01	0.287 -4.01	0.288 -4.02	0.289 -4.02	Shrinkage stresses are almost same in Systems B through E.
SE	-0.168 3.08	-0.179 2.93	-0.178 2.93	-0.082 1.68	-0.082 1.67	Settlement cause negligible stresses in System D and E.
EP	-0.00007 -0.0011	0.00031 -0.0055	0.00055 0.0075	0.0078 -0.084	0.0078 -0.084	Earth pressure causes negligible stresses in all Systems.
TOTAL	0.799 -8.59	1.13 -6.93	1.13 -7.14	1.94 -19.48	1.94 -19.53	The total stresses are higher in Systems D and E. The pier section of jointless bridges have to be carefully designed for higher top tensile stresses.

Note: Positive stresses indicate tensile stresses.
Total is the sum of DL+C, LL, TG, SH, SE and EP.

TABLE 5. Stresses at Abutment Bottom in Various Systems (1 ksi = 6890 kPa)

Load Case	Stresses (ksi)					Remarks
	System A	System B	System C	System D	System E	
DL	-0.127 0.0937	-0.0164 -0.0164	-0.0164 -0.0164	-0.0155 -0.0963	-0.0135 -0.115	The stresses due to dead load are negligible in all Systems.
DL+C	-0.289 0.256	-0.0162 -0.0162	-0.0162 -0.0162	-0.0167 -0.0084	-0.0139 -0.011	The effect of creep is significant in System A because of fixity. The final stresses (DL+C) are negligible in all other Systems.
LL	-0.067 0.0457	-0.0109 -0.0109	-0.0107 -0.0107	-0.0102 -0.0059	-0.0089 -0.0073	The stresses due to live load are negligible in all Systems.
TG	3.03 3.04	-0.0064 -0.0064	-0.0064 -0.0064	-0.0026 -0.000825	-0.00203 -0.0014	The stresses due to temperature gradient are significant in System A because of fixity. In all other Systems, the stresses are negligible.
SH	-0.787 0.787	0.0015 0.0015	0.0015 0.0015	0.00042 0.00267	0.0017 0.0019	The stresses due to shrinkage are significant in System A because of fixity. In all other Systems, the stresses are negligible.
SE	-0.0877 -0.0839	-0.0018 -0.0018	-0.0018 -0.0018	-0.00165 0.00049	-0.0017 0.00049	Settlement induce negligible stresses in all Systems.
EP	0.0063 -0.0063	-0.000009 -0.000009	-0.000024 -0.000024	-0.0627 0.0622	-0.0627 0.0622	Earth Pressure Induce negligible stresses in all Systems.
TOTAL	4.04 1.80	-0.092 -0.092	-0.034 -0.034	0.050 -0.093	0.045 -0.088	The total stresses are higher in System A because of fixity. Therefore, this System should be avoided for jointless bridges.

Note: Positive stresses indicate tensile stresses.
Total is the sum of DL+C, LL, TG, SH, SE and EP.

analysis was based on one-dimensional beam theory. More details on the methods of analysis can be found elsewhere (*4*).

DIFFERENT SYSTEMS FOR ANALYSIS

Lone Tree Road Bridge (Table 1) is analyzed as Systems A through E. The systems are schematically represented in Figure 2. Systems A through C idealize the bridge with spread footing type of foundation, whereas Systems D and E idealize the bridge with pile type of foundation. The maximum system stiffness is for System A, and the minimum system stiffness is for System E. In other words, System A has minimum flexibility or larger restraint to movement, and System E has maximum flexibility or least restraint to movement. For discussion purposes, jointless bridges on spread footing are regarded as stiffer systems, and jointless bridges on pile foundation are regarded as flexible systems.

RESULTS

The internal forces and moments were determined for various load cases and at various locations, such as superstructure and abutment joint, midspan, superstructure at pier, and foundation level. The top and bottom stresses computed at the above locations included the effect of bending moment and axial force. Because of the length limitation of this paper, tables showing stresses for only one bridge (Lone Tree Road Bridge, Iowa) are presented here. More details about the results of other bridges are available elsewhere (*4*). A qualitative summary is presented in the following sections, and it includes the effect of primary and secondary loads, the effect of secondary loads compared with primary loads, and the effect of various systems (boundary conditions) on stresses at these locations.

STRESSES AT SUPERSTRUCTURE AND ABUTMENT JOINT

Dead Load

Dead load produces considerable top tensile stresses in Systems A through C. These systems are founded on spread footings. The highest tensile stress (382 psi; Table 2) is for System A. With those bridges resting on piles, top tensile stresses caused by dead load are found to decrease drastically. The decrease in tensile stresses caused by dead load is about 300 times that of when the foundation type is changed from spread footing to piles (System A through System E). For the same bridge, weak axis bending of piles results in 3 times lower stresses than strong axis bending of piles. The bottom compressive stresses in steel stringer are higher in bridges without piles, and the maximum value is about 13 ksi. The bottom stresses are low in bridges resting on piles. Weak axis orientation of piles further reduces the bottom stresses. On the basis of the above discussion, it is preferable to have jointless bridges on piles that bend about their weak axis.

Creep

Change in the internal forces as a result of creep is advantageous with regard to the top tensile stresses at the superstructure and abutment joint. The advantage lies in the fact that the top tensile stresses caused by dead load at the superstructure and abutment joint are decreased. The advantage caused by creep is maximum in stiffer systems and minimum in flexible systems. The maximum decrease in top tensile stresses at the superstructure and abutment joint is about 40 percent (bridges on spread footing), and the minimum decrease is about 10 percent (bridges on pile foundation).

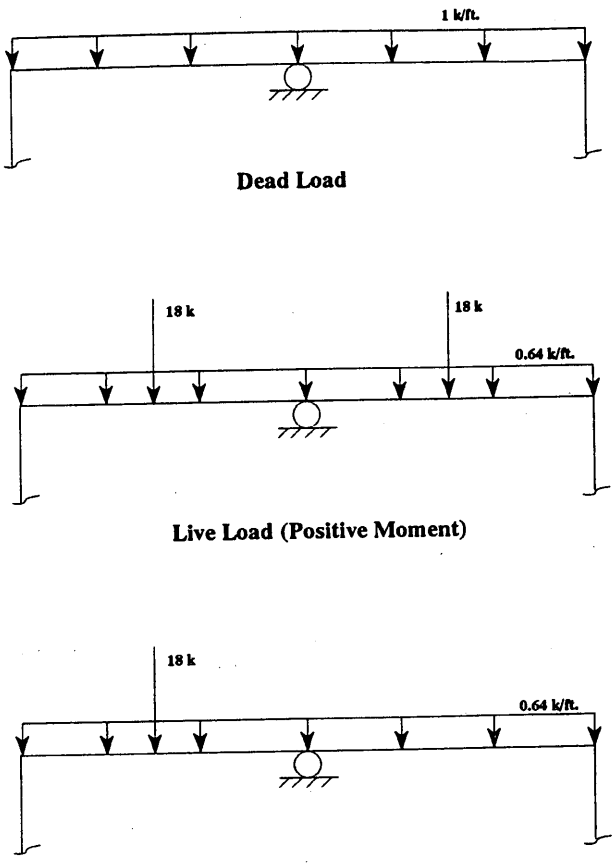

1 k/ft = 14.59 kN/m²
1 k = 4.448 kN

FIGURE 1. Loads considered for analysis (*continued on next page*).

Creep increases bottom compressive stresses in steel. However, the final stresses in bottom steel after an increase caused by creep are well within the allowable stresses for steel.

Live Load

Live load stresses at the superstructure and abutment joint are nearly 40 percent of dead stresses. The trend of live load stresses is the same as that of dead load. Therefore, the discussion presented above for dead load holds good for live load also. In conclusion, as far as dead and live loads are concerned, jointless bridges should be supported on piles that bend about their weak axes. This helps in reducing tensile stresses at the top of the superstructure and abutment joint.

Temperature Gradient

Stresses produced by temperature gradient at the superstructure and abutment joint are tensile in nature at top and tensile (flexible systems) or compressive (stiffer systems) in nature at the bottom. The maximum top tensile stress is found to be about 900 psi in the case of stiffer Systems B and C. These stresses are reduced to nearly half in the case of a jointless bridge with pile foundation. Furthermore, the maximum bottom tensile and compressive stresses are found to be, respectively, 7.5 ksi (Systems D and E) and 8.5 ksi (Systems A through C). The temperature gradient is detrimental to the bridge in terms of producing considerable top tensile stresses at the superstructure and abutment joint.

Shrinkage

In a superstructural system composed of concrete slab and steel girder, there is nonuniform shrinkage through the depth, in the sense that concrete shrinks and steel does not, and this effect complicates the analysis. Shrinkage produces top tensile stress in the superstructure and abutment joint of all systems. Shrinkage produces considerable top tensile stresses in stiffer System A and negligible stresses in flexible Systems D and E.

Settlement

Settlement stresses are considerable in bridges resting on spread footing. The stresses are negligibly small in bridges resting on piles (Systems D and E). The effect of settlement is the same as that of primary loads in all the systems. The stresses are nearly one-fourth of dead load stresses in stiffer systems (Systems A through C). Therefore, a pile foundation is preferable to avoid the development

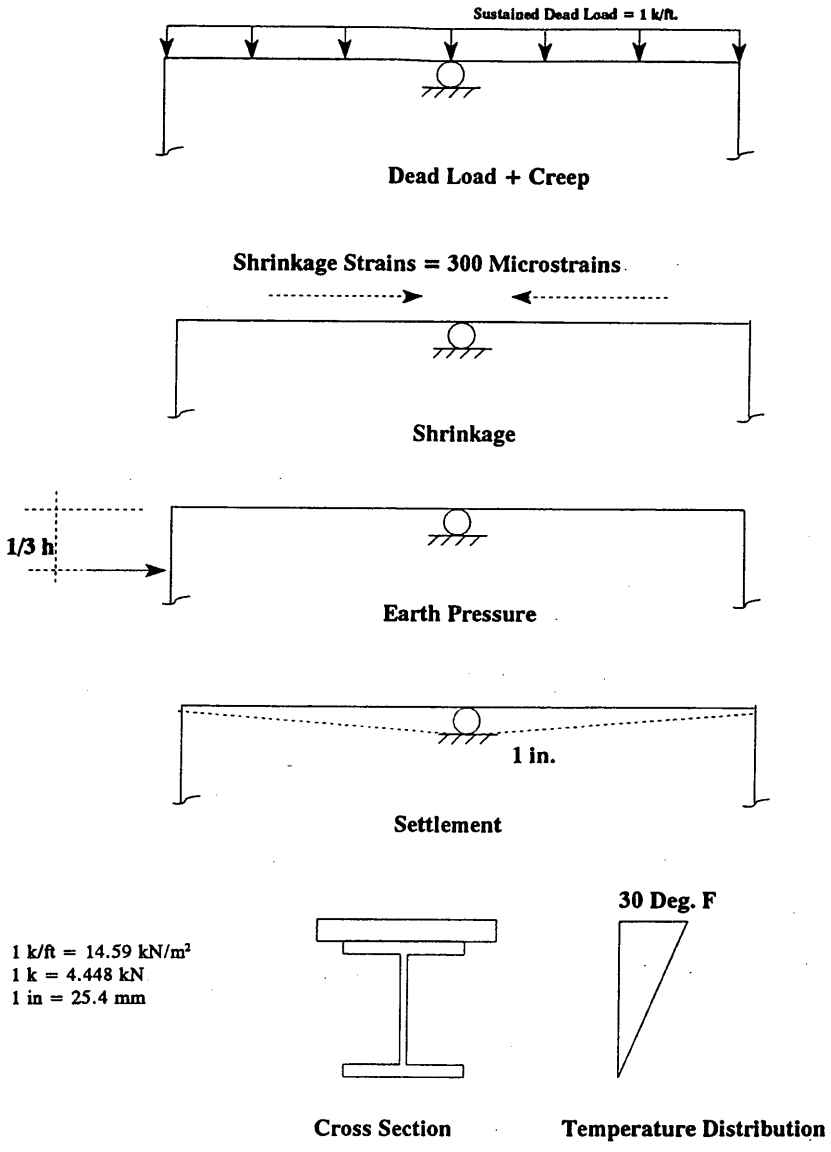

FIGURE 1 (*continued*).

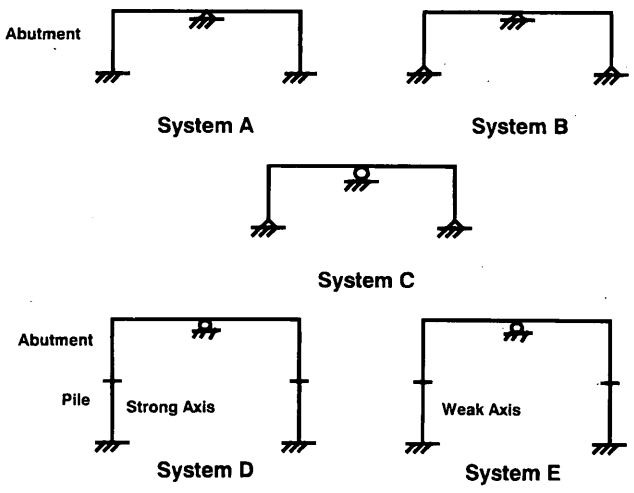

FIGURE 2. Analysis of Lone Tree Bridge (Iowa) Systems A through E.

of large stresses at the superstructure and abutment joint as a result of settlement.

Earth Pressure

Earth pressure (active case) acts on one leg in the form of a point load and produces negligible stresses at all locations in all systems. The stresses are not going to be significant even if the active case is converted (three to four times greater) to the passive case. Therefore, the effect of earth pressure is insignificant and is not presented in future sections. Also, while designing a jointless bridge the effect of earth pressure can be ignored.

Total Stresses

Top total stresses in bridges resting on pile foundation are 2.5 times lower than the same stress in bridges resting on spread footing. The maximum top and bottom stresses in bridges resting on pile foundations are found to be around 600 psi and 7.5 ksi, as against 1,600 psi and 36 ksi in stiffer systems, respectively. The major contributor to total stresses in flexible systems is the temperature gradient. A reverse temperature gradient in winter causes opposite stresses, which may be helpful in reducing the total stresses.

STRESSES AT MIDSPAN

Dead load

Dead load produces compressive stresses at top and tensile stresses at the bottom of the midspan section. The top compressive stresses at the midspan of the bridge with pile foundations are nearly the same as the stresses at the midspan of the bridge with spread footings. The bottom steel stresses are higher in flexible systems than in stiffer systems (Table 3). The maximum top compressive stress for concrete and bottom tensile stress for steel are found to be around 350 psi and 10 ksi in flexible systems and around 350 psi and 6 ksi in stiffer systems.

Creep

Top compressive stress caused by dead load at midspan section decreases as a result of creep. The maximum decrease in compressive stress is found to be nearly 40 percent. The dead load bottom tensile stresses increase because of creep. The maximum increase is less than 10 percent.

Live Load

Live load produces compressive stresses at top and tensile stresses at the bottom of the midspan section. The top and bottom live load stresses are nearly the same as those of the dead load stresses.

Temperature Gradient

Temperature gradient produces tensile stresses at the top and bottom of the midspan section for most of the systems. The tensile stresses produced by the temperature gradient are opposite those produced by gravity loads. Thus, temperature stresses nullify to some extent the compressive stresses produced by the gravity loads. The highest top tensile stress is found to be around 320 psi (Systems D and E), and the highest bottom tensile stress is found to be 12 ksi (Systems D and E).

Shrinkage

Shrinkage produces tension at the top and compression at the bottom of the midspan section in all the systems. The stresses caused by shrinkage are opposite those produced as a result of dead and live load. As a result, stresses caused by gravity loads are nullified to some extent. This is an added advantage in jointless bridges.

Settlement

The top and bottom stresses vary from 10 to 20 percent of the top and bottom dead load stresses in the midspan.

Combined stresses

The sum of stresses caused by all loads indicates that the midspan section of flexible systems is subjected to a smaller compressive stress at the top and larger tensile stress at the bottom when compared with stiffer systems. The bottom tensile stress in flexible systems is so high that it exceeds the allowable stress value in steel. A reverse gradient in winter would induce an opposite nature of stresses. This would decrease the bottom tensile stresses. The maximum compressive and tensile stresses developed at the top and bottom are nearly 200 psi and 30 ksi, respectively.

STRESSES IN SUPERSTRUCTURE AT PIER

Dead Load

The negative moment induced at the pier causes top tensile stresses and bottom compressive stresses. Most flexible systems have a disadvantage too: they produce larger top and bottom stresses at the pier than those produced in stiffer systems. The increase in tensile stresses in flexible systems can be nearly twice those found in stiffer systems (Table 4). To counteract the high tensile stresses the following may be necessary: additional reinforcement to confine concrete over the pier; an increase in the deck thickness by means of a haunch over the pier, or prestressing the slab over the pier.

Creep

The top tensile stresses caused by creep in all bridge systems decrease by about 50 percent. The bottom compressive stresses caused by creep increase by a maximum of 10 percent. As stated earlier, superstructure section over the pier of the most flexible systems is subjected to larger tensile stresses. These large tensile stresses are reduced to nearly half as a result of creep, thereby nullifying the tensile stresses to some extent.

Live Load

Live load stresses at the top of the deck over the pier are about 25 percent greater than the top dead load stresses. However, bottom stresses are nearly 40 percent lower than dead load bottom stresses.

Temperature Gradient

A temperature gradient produces tensile stresses at the top and bottom of all systems, which is somewhat detrimental to a jointless bridge system because it adds to the tensile stresses caused by other loads and increases the potential of cracking. The tensile stresses can be as high as 800 psi in concrete and 15 ksi in steel, as indicated in Table 4.

Shrinkage

Over a pier, shrinkage produces tensile stresses at the top and compressive stresses at the bottom in all the systems. This creates the worst scenario because the primary loads also produce tensile stresses at the top fiber and compressive stresses at the bottom. The top concrete may not be able to resist these tensile stresses and may crack. The crack thus formed may simulate over an artificial hinge at the pier. Because the abutment and superstructure joint acts like hinge because of large flexibility, the spans may behave as simply supported. The question then is whether jointless bridges should be designed as simply supported bridges. As discussed in earlier sections, there is a decrease in tensile stresses caused by creep, whereas an inducement of tensile stresses is noted because of shrinkage. Therefore, shrinkage stresses cancel out each other to some extent. In other words, "creep relieves shrinkage." Therefore, the common design assumption that creep and shrinkage have opposite effects is a reasonable one.

Settlement

The top and bottom stresses developed over a pier as a result of settlement is opposite in nature to those stresses developed under dead loads and live loads. This causes a relief in stress by reducing the large tensile stresses caused by other loads at the pier. Because of settlement, the maximum top and bottom stresses are found to be nearly 25 percent of dead load stresses. Therefore, stress reduction of a maximum of 25 percent in dead load stresses over a pier is reasonable.

Combined Stresses

The total stresses over a pier are higher in flexible systems than in stiffer systems. The maximum tensile stress at a top fiber is found to be 2,000 psi, and the maximum compressive stress at bottom fiber is found to be 20 ksi.

STRESSES AT FOUNDATION LEVEL

Dead Load and Live Load

With reference to stresses at the foundation level (footing level for bridges on spread footing-type foundations and abutment-pile junction level for bridges resting on pile-type foundations), System A necessitates the design of footing for large stresses induced because of fixity. The placement of a hinge at the footing level causes the stresses to decrease greatly. Therefore, it is better to have a hinge between the abutment and footing to reduce stresses if a jointless bridge is built with spread footings. In the case of jointless bridges that rest on piles, the stresses in concrete at the point where piles are fixed to the abutment are very small. Thus, there is no fear of concrete cracking or separation of abutment from piles.

Creep

The rigid spread footing (System A) is subjected to greater stresses compared with flexible spread footing (System B) because of the moment that develops as a result of support rigidity. A large increase in creep stresses is noted in the case of fixed footing, as all the internal forces are transferred to footing. An increase of nearly 125 to 150 percent is found at the footing level in the case of System A. Therefore, creep behavior is favorable for Systems B through E where hinged spread footings or piles are attached to an abutment.

Temperature Gradient

When compared with other bridge systems, the foundation stresses are the highest for System A. This is because of the fixity of the foundation, which develops large moment and axial force. All other systems are subjected to negligible stresses at the foundation level.

Shrinkage

Shrinkage stresses are negligible at the foundation level in all systems except in the case of a fixed foundation. The restraint produced by fixity induces large stresses caused by shrinkage. The stresses at the joint between the abutment and piles are negligible, and there is no danger of cracking or separation.

Settlement

Settlement stresses developed at the foundation level are very small in all systems except for System A. The fixity at the foundation level in System A is the reason for the inducement of high stresses. For sites where settlement of soil strata is anticipated, it is better to have jointless bridges on piles, and the piles should be driven to reach hard strata.

Combined Stresses

The stresses are higher in System A than in any other bridge system, which is attributed to fixed boundary conditions. In all other systems, the total stresses are negligible. Therefore, System A should be avoided in the design of jointless bridges. The lower stresses at the junction of the pile and the abutment indicate that the junction is safe against cracking or separation.

CONCLUSIONS

From the synthesized analytical data, the following conclusions can be drawn:

1. Combination of integral stub abutment and single row of piles to bend about their weak axis, makes the substructure flexible, and the jointless bridge behaves like a simply supported structure, with reduced stresses.

2. The major contributor to the total stresses is the temperature load.
3. Creep of concrete is helpful in reducing the bending-induced stresses.
4. Shrinkage relieves creep to some extent but not completely.
5. Earth pressure causes negligible stresses at all locations in the bridge.
6. Settlement stresses are considerable in multispan jointless bridges.
7. The total stresses at the superstructure and abutment (resting on pile foundations) joint are lower than the stresses in bridges resting on spread footings. The major contributor to total stresses is the temperature gradient. A reverse temperature gradient in winter causes opposite stresses, which may be helpful in reducing total stresses.
8. When the total stresses are taken into account, the midspan section is subjected to smaller compressive stresses at the top and larger tensile stress at the bottom. The total bottom tensile stress is so high that it exceeds the allowable stress value in steel. A reverse gradient in winter would induce an opposite nature of stresses, which would decrease the high bottom tensile stresses.
9. The top of the concrete deck over the pier is subjected to high tensile stresses. Additional reinforcement to confine concrete over the pier, increase the deck thickness by means of a haunch over the pier, or even prestress the slab over the pier may have to be adopted to counteract the high tensile stresses.
10. At the foundation level, total stresses are higher in System A than in any other bridge system, which is attributed to a fixed boundary condition. In all other systems, the total stresses are negligible. Therefore, System A should be avoided in the design of jointless bridges. The lower stresses at the pile and the abutment joint indicate that the joint is safe against cracking or separation.

ACKNOWLEDGMENTS

The research project was sponsored by the West Virginia Department of Highways and United States Department of Transportation, FHWA. Their financial support is gratefully acknowledged.

REFERENCES

1. *Design Calculations for Big Sandy Bridge and Bridge Over Little Kanawa River*. Project S-320-4-0.03. Haworth, Meyer & Boleyn, Inc., Frankfort, Ky., 1991.
2. *Design Calculations for Big Sandy Bridge and Bridge Over Little Kanawn River*. Project S-349-20-8.33. Haworth, Meyer & Boleyn, Inc., Frankfort, Ky., 1992.
3. Burke, M. P. Integral Bridges. In *Transportation Research Record 1275*, TRB, National Research Council, Washington, D. C., Jan. 1990.
4. GangaRao, H. V. S. and H. K. Thippeswamy. Study of Jointless Bridge Behavior and Development of Design Specifications. *WVDOH Research Project Report*. Constructed Facilities Center, West Virginia University, Morgantown, Oct. 1994.
5. Wolde-Tinsae, A. M., J. E. Klinger, M. Masi, P. Albrecht, J. White, and N. Buresli. *Performance and Design of Jointless Bridge*. FHWA Final Report. Department of Civil Engineering, University of Maryland, College Park, June 1987.
6. Griton, D. D. T. R. Hawkinson, and L. F. Greimann. Validation of Design Recommendations for Integral-Abutment Piles. In *Journal of Structural Engineering*, ASCE, Vol. 117. No. 7, July 1991.

Publication of this paper sponsored by Committee on General Structures.

Computationally Efficient Method for Inclusion of Nonprismatic Member Properties in a Practical Bridge Analysis Procedure

THOMAS E. FENSKE, MUZZ YENER, DONGFA LIU, AND SUE MOORE FENSKE

For purposes of bridge analysis, bridges typically are classified as either statically determinate or statically indeterminate. Continuous-span bridge structures, which generally are statically indeterminate, offer advantages over statically determinate, simply supported bridge systems, such as lighter weight, lower cost, greater stiffness, and smaller deflections. Therefore, most multispan bridge structures are designed to be continuous. In the past, one of the simplifying assumptions generally made during the bridge analysis process was that the bridge superstructure members could be analyzed as prismatic members. This was primarily because of the computationally intensive nature of the calculations necessary to include consideration of nonprismatic member properties. However, the widespread proliferation of the digital computer has eliminated the need for this particular analysis simplification. A comprehensive outline of a computer-based bridge analysis process that incorporates nonprismatic member behavior is prescribed. Application of this bridge analysis procedure is shown to be remarkably reliable and accurate compared with theoretically exact analysis results and is considerably more accurate than utilizing a simple prismatic analysis. The analysis procedure presented is economical in terms of computational time and computer memory requirements and is a practical alternative to currently used analysis methods that consider only prismatic member properties.

Bridges can be classified in many ways: for example, by type of girders or by type of material. With respect to analysis, bridges typically are classified as either statically determinate, for which all reactions and internal forces can be obtained directly from static equilibrium equations, or indeterminate, which requires a more sophisticated analysis. Continuous-span bridge structures, which are statically indeterminate (assuming the absence of interior moment releases), offer advantages over statically determinate, simply supported bridge systems. These advantages include lighter weight, lower cost, greater stiffness, and smaller deflections, as well as greater overload capability caused by stress redistribution.

In the past, analysis of indeterminate, continuous-span bridge structures has been performed by applying analysis methods that make use of several simplifications. These simplifications include the use of the AASHTO wheel load distribution factor, the AASHTO load impact factor, and the assumption of prismatic member section properties, among others. The use of any one of these analysis simplifications can cause an error in the analysis results, and using all of these can yield a significant discrepancy between the results of the simplified analysis and the theoretically exact values.

Steps recently have been taken to provide means by which to eliminate some of these simplifications from the analysis of indeterminate bridge structures. For example, NCHRP recently funded the development of a computer program to generate more accurate wheel load distribution factors. This program, LDFAC, calculates wheel load distribution factors using a finite element-based structural analysis, which extends the range of applicability of the wheel load distribution factors by a wide margin and allows more reliable and accurate analysis results to be obtained for cases such as bridges with skewed supports, continuous spans, and bridges for which geometric parameters such as span length or girder spacing fall outside the range of simplified formulas (*1*). Additionally, in a study sponsored by the National Science Foundation, the dynamic influence of moving vehicular traffic was investigated (*2*). In this study it was shown that the AASHTO load impact factor yields results that can be significantly in error and it presented an alternative method for including the effects of impact on bridge structures.

This paper focuses on the minimization of error introduced into girder bridge analysis results as a result of making the assumption that all of the structural members behave as prismatic members. The nonprismatic behavior of bridge structural members was ignored in the past primarily because of the computationally intensive nature of the mathematical calculations. However, the widespread proliferation of the digital computer makes unnecessary a continuation of this analysis simplification. This paper presents the development of an analysis methodology that incorporates rapid and accurate dead and live load internal force evaluation for nonprismatic girder bridges. This analysis procedure is remarkably successful in significantly reducing the error between the results of the bridge analysis procedure and the theoretically exact solution.

TYPICAL BRIDGE ANALYSIS METHODS

Classical methods, approximation methods, and numerical methods are the three types of analysis methods generally applied to civil engineering systems, including bridge structures. Classical analysis methods are based on the exact solution of the governing differential equations of the system. However, the limitations of these methods, which are applicable only to systems that possess relatively simple geometry, loading, and boundary conditions, restrict the usefulness to a narrow range of problems.

T. E. Fenske, D. Liu, S. M. Fenske, Department of Civil Engineering, University of Louisville, Louisville, Ky. 40292. M. Yener, Structural Engineering and Engineering Mechanics Division, Department of Civil and Environmental Engineering, Utah State University, Logan, Utah 84321.

More complex problems are typically solved using an approximation method or a numerical method. Approximation methods include energy methods, such as the principle of minimum potential energy; variational principles, such as the Galerkin method and the Ritz method; and perturbation methods. However, the application of approximate methods are limited to uncomplicated boundary conditions and simple variation of thickness. Also, it is important to remember that the use of an approximation method will yield just that—an approximate analysis solution.

The numerical methods of analysis are based on the principles of finite elements and finite differences. Numerical analysis allows for a more accurate analysis than can be achieved using the approximation methods and is applicable to a far wider range of problems than the other types of analysis methods. Numerical methods have been applied successfully to problems such as those that include tapered plates, circular plates, elements of varying thickness, and nonprismatic members.

All three analysis procedures are currently being used in bridge analysis. A classical approach based on the flexibility method is used in most older programs with a constant flexural stiffness *EI* to generate influence lines. A numeric successive approximation method known as Newmark's method is used in several computer programs because of the ease and simplicity of implementation. A number of direct stiffness matrix analysis programs are available that use a moving load to generate influence diagrams. Several of these programs use the "transfer matrix" approach to reduce the demands on computer memory and computation time. The analysis approach introduced in this paper has proven to be more accurate, based on a one-dimensional analysis, and is significantly more efficient in terms of computer storage requirements and execution time.

DEVELOPMENT OF GIRDER BRIDGE ANALYSIS METHODOLOGY

The bridge analysis approach developed in the computer program, termed GBRIDGE, consists of three segments: structural analysis based on the direct stiffness method, influence line generation, and determination of maximum moments and shears.

The direct stiffness method of structural analysis uses the principles of joint equilibrium and compatibility to solve for joint displacements. These actions and displacements are related through the matrix equilibrium equation

$$[A] = [S][D]$$

where

$[A]$ = action matrix of applied forces and moments,
$[S]$ = global stiffness matrix assembled from the member stiffness matrixes, and
$[D]$ = unknown displacement matrix.

In a physical sense, the global stiffness matrix contains coefficients that represent the actions taking place at a node caused by a unit displacement of a member end. This matrix, along with the appropriate boundary conditions, is then used to calculate the actual displacements caused by the actual dead load and live load forces and moments by the solution of simultaneous equations. After the joint displacements have been found, the forces, stresses, and displacements at the internal analysis points and at material breaks can be calculated through application of superposition for the dead load and superimposed dead load cases and through use of influence lines and superposition for the live load case.

A unique feature of the GBRIDGE analysis procedure is the inclusion of nonprismatic member behavior. Indeterminate bridge member section properties vary as a function of the construction process. In the dead load condition, prismatic bridge girders, such as AASHTO prestressed beams, can be analyzed on the basis of prismatic section properties before the hardening of the roadway deck. However, in the case of the composite bridge system, which has both positive and negative moment areas, the concrete roadway deck can contribute to composite action only in the positive moment area because concrete is effective only under compressive stress. In the negative moment area, the reinforcing steel can be considered in section property evaluation. Therefore, even in general continuous bridge systems with prismatic members, the bridge systems are composed of nonprismatic members if composite construction is used.

Incorporating nonprismatic member properties into the bridge analysis procedure presents particular problems when employing the direct stiffness analysis approach. The direct stiffness procedure assumes a continuous shape (displacement) function or interpolation polynomial in formulating the element stiffness matrix. Therefore, this method can lead to exact answers only when the displacement of the member's neutral axis is continuous. The difficulty associated with using the direct stiffness method becomes apparent when it is recognized that virtually all girder bridges are composed of segmental, nonprismatic supporting girders.

In the case of segmentally nonprismatic beams, any approximating shape function that represents the entire girder length must be discontinuous. This is explained through examination of the moment-curvature equation

$$\frac{d^2y}{dx^2} = \frac{M_x}{EI_x}$$

in which

y = displacement of the neutral axis,
x = location at any point on the member,
M_x = moment at location x,
I_x = moment of inertia at location x, and
E = modulus of elasticity at location x.

In this equation, y represents the displacements caused by bending of the beam member's neutral axis as a function of the member's length. However, on either side of a material change, the internal resisting moment M_x is the same but the member's neutral axis location and moment of inertia are different, as shown in Figure 1. Therefore, any analysis formulation must account for this discontinuity.

This discontinuity problem can be overcome provided that the girder is modeled by a series of prismatic beam elements. Each prismatic segment can utilize a continuous shape function because, for each segment, the neutral axis location remains constant. This type of formulation requires the use of a large number of prismatic beam elements to obtain accurate analysis results. This segmental formulation requires a large amount of the available computer random access memory and requires considerably longer execution time to solve the greater number of simultaneous equations that result. Even when using the "transfer matrix" approach, considerable central processing unit time is required. This difficulty is overcome in the GBRIDGE analysis procedure by integration of classical beam theory employing numeric integration and the traditional displacement-based direct stiffness analysis.

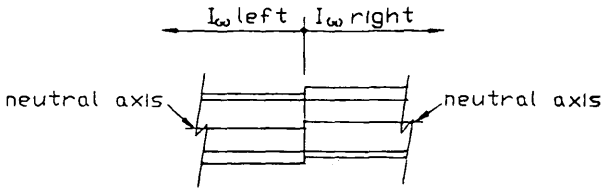

FIGURE 1 Nonprismatic girder material change.

Nonprismatic Stiffness Matrix

The development of the nonprismatic element stiffness matrix can be divided into two parts: the flexural contribution and the axial contribution. The flexural contributions to the girder stiffness matrix assume that the girder is bent in a principal plane and the effects of shear deformations can be neglected. In addition, it is assumed that the angle change between two adjacent cross sections is small after bending has occurred. The nonprismatic element formulation process employs the classical analysis approach of superposition in which the indeterminate structure is reduced to a statically stable and determinate structure by removing the redundant end moments M_L and M_R. These redundant end moments then are reapplied and the resulting member end rotations are related to the fact that the actual rotations at fixed ends are 0. Manipulating the solution of the resulting simultaneous equations will yield the nonprismatic element stiffness matrix and the equivalent nodal forces. The flexural stiffness components are

$$S_e = \frac{EI_L}{L^3(AC - B^2)} \begin{vmatrix} A & BL & -A & (A-B)L \\ BL & CL^2 & -BL & (B-C)L^2 \\ -A & -BL & A & -(A-B)L \\ (A-B)L & (B-C)L^2 & -(A-B)L & (A-2B+C)L^2 \end{vmatrix}$$

where

$$A = I_L \int_0^L \left(\frac{1}{LI_x}\right) dx$$

$$B = I_L \int_0^L \left(\frac{x}{L^2 I_x}\right) dx$$

$$C = I_L \int_0^L \left(\frac{x^2}{L^3 I_x}\right) dx$$

and I_L is the moment of inertia at the left end of the member, L is the length of the member, and x is a variable location along the member length.

The nonprismatic stiffness coefficients caused by flexure have been derived as closed-form integrals in terms of natural or global coordinates. The formal integration of these coefficients is tedious and susceptible to error and, because each new girder would require individual evaluation, formal integration is neither practical nor efficient for computer implementation. Instead, numerical integration is performed using Gaussian quadrature. The accuracy of this approach is shown via application to two illustrative problems shown in Figures 2 and 3; the results for each are given in Tables 1 and 2, respectively. In the segmental nonprismatic beam problem, all of the results obtained by the various methods are identical; however, the segmental beam approach (using three beam segments) required twice the amount of computer memory space and execution time compared with the single nonprismatic element method. In the tapered nonprismatic beam problem, not only did the segmental approach (15 segments) require eight times more memory and execution time, but it was also considerably less accurate.

The axial contribution to the element stiffness matrix is based on the standard displacement-based direct stiffness approach by employing the assumption of centroid segment alignment. The concrete roadway system is neglected in considering axial effect, that is, only the supporting girders are considered to carry axial loads. Therefore, the axial stiffness components are

$$S_e = \frac{A_R E}{L} \begin{vmatrix} 1 & -1 \\ -1 & 1 \end{vmatrix}$$

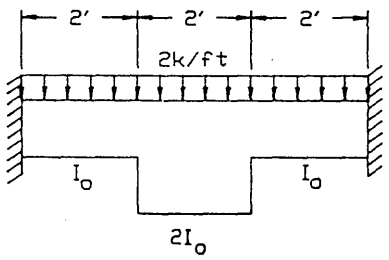

FIGURE 2 Segmental nonprismatic beam example.

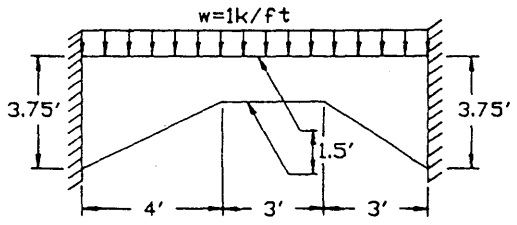

FIGURE 3 Tapered nonprismatic beam example.

TABLE 1 Solution Comparison for Segmental Beam

	Member End Moments (ft-k)		
Member End	Theoretically Exact	GBRIDGE Quadrature Solution	Traditional FEM
Left End	5.47	5.47	5.47
Right End	5.47	5.47	5.47

TABLE 2 Solution Comparison for Tapered Beam

Member End	Member End Moments (ft-k) Theoretically Exact	GBRIDGE Quadrature Solution	Traditional FEM
Left End	11.37	11.39	11.74
Right End	10.28	10.34	10.71

where A is the equivalent cross-sectional area, expressed as

$$A_x = A_L\,[1 + t_w(h_R - h_L)x]$$

The complete element stiffness matrix is formulated by adding the two matrixes together. If the local element axes are not parallel to the global structure axes, the stiffness matrix coefficients must be adjusted to correspond to the global axes through the use of direction cosines. Then, the global stiffness matrix for the bridge structure is formulated by summing the element stiffness matrixes for each structural member.

Structural Analysis

Once the global stiffness matrix has been obtained and appropriate boundary conditions applied, the analysis is performed for each loading condition. These loading conditions, per AASHTO specifications, are dead load, superimposed dead load, and live load plus impact. For the conditions of dead load and superimposed dead load, only the member end actions need to be computed. Once these member end actions are determined, the internal shears and moments at any point along the member can be evaluated directly from superposition, given the assumption of a uniformly distributed loading. The actual shears and moments for each analysis point for the dead load and superimposed dead load conditions can be calculated using the following:

$$M_{ap} = M_x = -M_n + (M_{n+1} + M_n)\frac{x}{L} + \frac{wx}{2}(L - x)$$

$$V_{ap} = V_x = \left(\frac{M_n + M_{n+1}}{L}\right) + w\left(\frac{L}{2} - x\right)$$

which are developed from the illustrations indicated in Figure 4. M_n is the member end moment at the left end of the member, M_{n+1} is the member end moment at the right end of the member, x is the location of the analysis point of interest, and L is the member length.

The analysis of the live load condition can be accomplished by using influence lines. An influence line shows the value of any action (shear, moment, deflection) as a result of a unit point load moving across the structure. (Note that the influence line unit load must represent the function sought at each analysis point, that is, a unit load for shear and a unit moment for moment.) In GBRIDGE, actual shear influence lines are used; however, the moment influence line used is actually an analogous end-moment distribution line generated for each girder analysis point. The use of this end-moment distribution line as the moment influence line is an important feature of GBRIDGE.

To develop the GBRIDGE live load influence lines, it is necessary only to obtain the end moments over the supports and apply distribution equations. The determination of member end moments can be accomplished by indirectly considering the effects of the fixed end moments for any specific unit loading. Final member end moment equations then can be developed for an arbitrary application of a 1,000 ft-k joint moment to each unrestrained rotational degree of freedom. The resulting end moments divided by 1,000 are the coefficients that, when multiplied by the fixed end moments, result in the true member end force. The fixed end moments are computed numerically for a unit load placed successively at each analysis point. Utilization of this analysis technique significantly reduces the computation time required in the evaluation of final member end moments for the multitudes of loads that must be considered since only a relatively few analyses are performed on the basis of applied joint moments. Also, the required amount of computer memory needed to accomplish the analysis is minimized

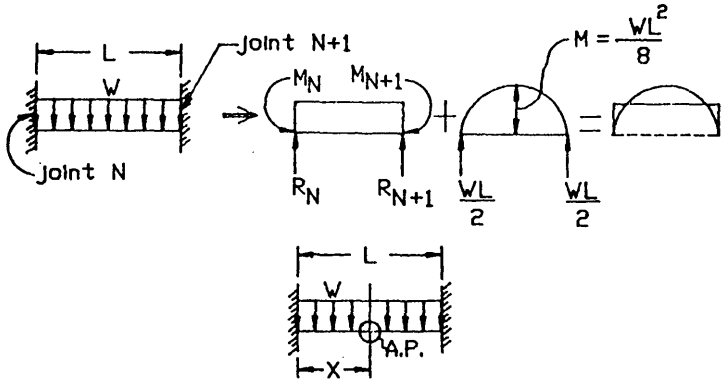

FIGURE 4 Analysis point forces for uniform loads.

because only the member end moments are stored, not the individually calculated ordinate values for each influence line. Rather, the influence lines for each analysis point can be rapidly computed as needed. This approach is much less expensive in terms of computation time and memory requirements.

On the basis of this approach, the true member end forces can be obtained for any loading condition without actually analyzing that loading condition. The ordinates for the moment and shear influence lines can be easily evaluated using the following equations:

$$x \le kL \quad M_x = -M_n + (M_{n+1} + M_n)\frac{x}{L} + (1 - k)x$$

$$x > kL \quad M_x = -M_n + (M_{n+1} + M_n)\frac{x}{L} + (L - x)k$$

$$x > L \quad V_{ap} = V_x = \frac{M_n + M_{n+1}}{L} - k$$

$$x \le kL \quad V_{ap} = V_x = \left(\frac{M_n + M_n + 1}{L}\right) + (1 - k)$$

where

M_{ap} and V_{ap} = moment and shear ordinates at the analysis point of interest,
x = location along the member length of the analysis point of interest, and
kL = location of the applied load.

Figure 5a and b shows examples of typical moment and shear influence lines for a three-span continuous bridge system that has been

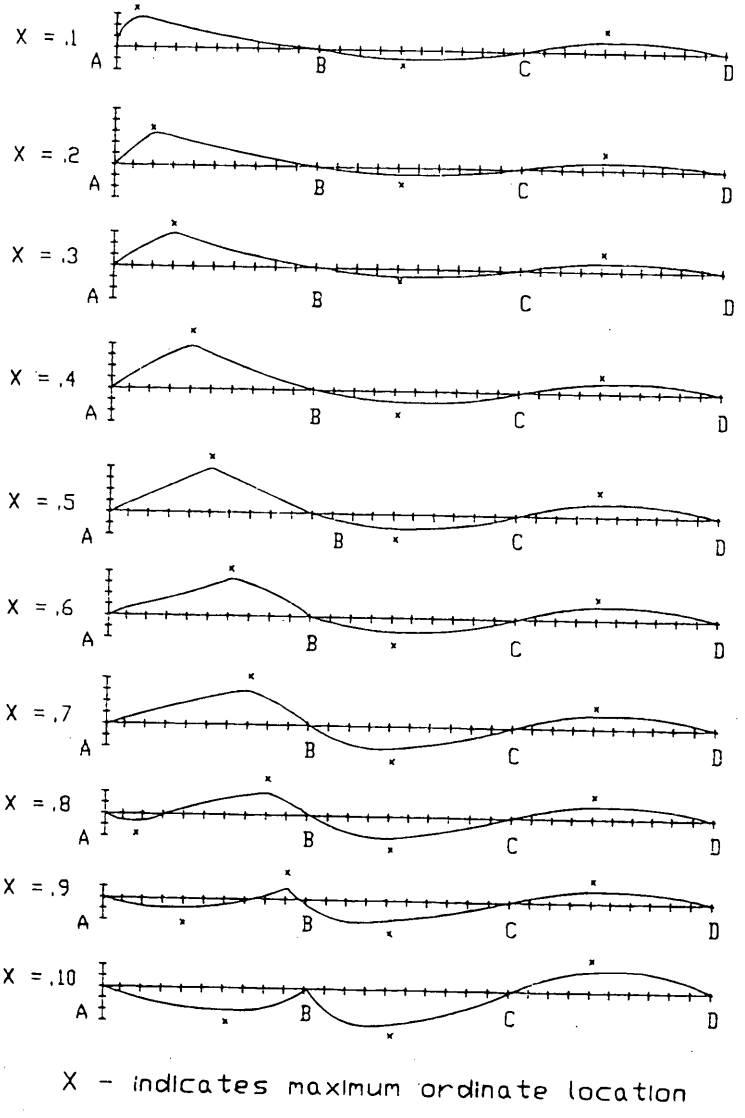

(a)

FIGURE 5 (*a*) Moment influence lines, (*b*) shear influence lines
(continued on next page).

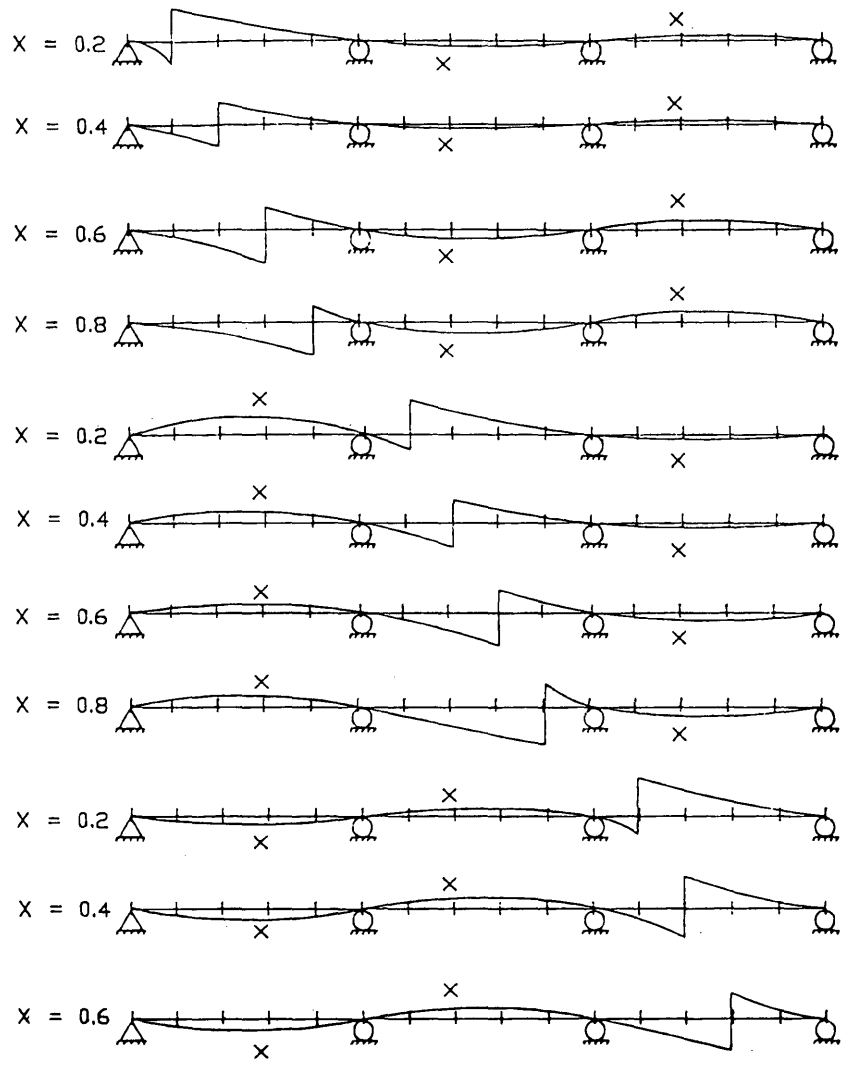

(b)

FIGURE 5 (*continued*).

developed using the approach outlined above. The nonprismatic fixed end moment equations used in the dead load, superimposed dead load, and live load cases are shown in Figure 6.

In addition to the efficient method developed for generating influence lines, GBRIDGE also incorporates a technique for rapid internal force evaluation. When the analysis point location and the position of the applied loading are in the same span, the internal force evaluation process is dependent on the analysis point position. If the analysis point is located farther than $0.2L$ away from the member ends, the maximum ordinate will be located at the location of the analysis point. However, if the analysis point is located within $0.2L$ of the member ends, then both positive and negative ordinate values will occur along the span and both the maximum positive and negative values must be determined.

A significant detail can be observed through study of Figure 5a and b. The location of the maximum ordinate for spans other than the loaded span will not vary, no matter where the load is applied on the loaded span. The magnitude of the ordinate value will vary,

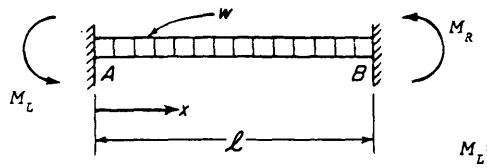

$$M_L = \left[\frac{-wl^2}{2(AC-B^2)}\right][BD-C^2]$$

$$M_R = \left[\frac{-wl^2}{2(AC-B^2)}\right][AC-B^2+BD-C^2-AD+BC]$$

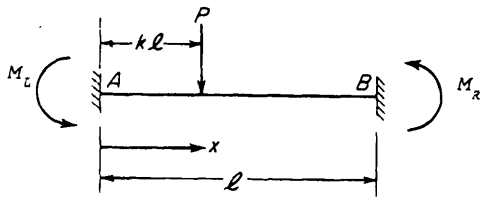

$$M_L = \left[-\frac{Pkl}{(AC-B^2)}\right]\left[AC-B^2+kC(F-E)-k^2B(G-F)\right]$$

$$M_R = \left[-\frac{Pkl}{(AC-B^2)}\right]\left[k(C-B)(F-E+k^2(A-B)(G-F)\right]$$

$$A = I_L\int_0^L \left(\frac{1}{LI_x}\right)dx \qquad D = I_L\int_1 \frac{x^3dx}{L^4I_x}$$

$$B = I_L\int_0^L \left(\frac{x}{L^2I_x}\right)dx \qquad E = I_L\int_1 \frac{dx}{(kl)I_x}$$

$$C = I_L\int_0^L \left(\frac{x^2}{L^3I_x}\right)dx \qquad F = I_L\int_1 \frac{x\,dx}{(kl)^2I_x}$$

$$G = I_L\int_1 \frac{x^2dx}{(kl)^3I_x}$$

FIGURE 6 Fixed end moment equations.

but not the location. This is because, in elastic analysis, the distribution of loading is dependent only on the member properties. GBRIDGE makes efficient use of this phenomenon by storing the location of the maximum ordinates in the unloaded spans after the initial internal force evaluation. As a result, the maximum shears and moments in the unloaded spans can be calculated directly for each successive evaluation of the loaded span.

The procedure for calculating maximum moments and maximum shears are identical to this point. In addition, both positive and negative shear effects must be examined for absolution maximum shear load. Also, fatigue and shear stud spacing both are dependent on shear range (i.e., the maximum difference between positive and negative shear forces), which varies only slightly throughout the bridge system, as indicated in Figure 7.

SUMMARY

This paper has presented a comprehensive outline of an analytical bridge evaluation process that incorporates nonprismatic member behavior. This behavior is considered in the analysis through the development of nonprismatic element stiffness matrixes. Applica-

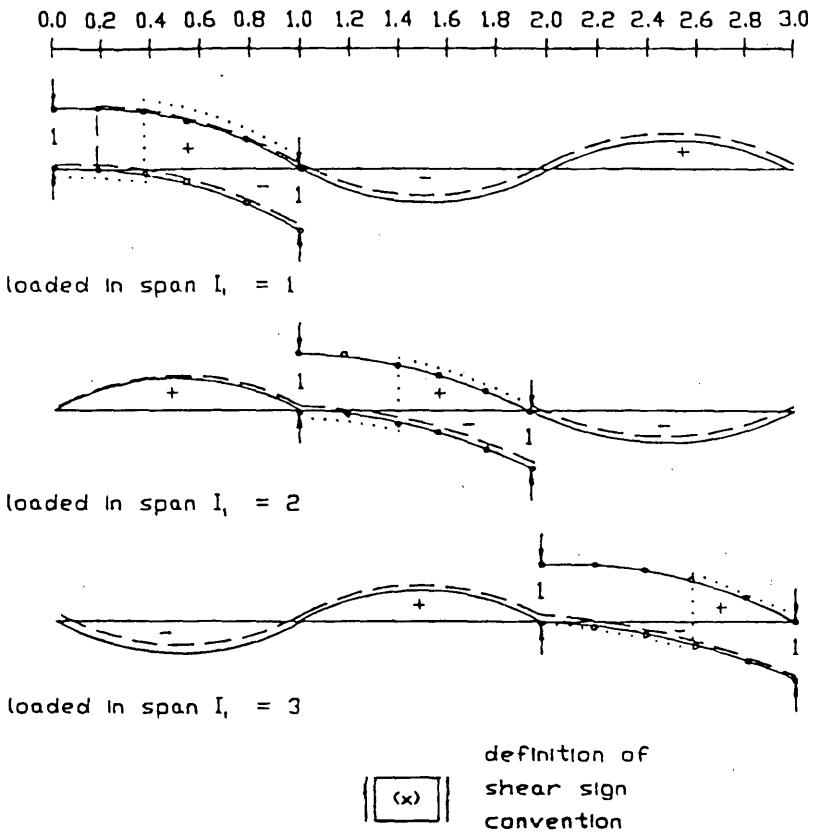

FIGURE 7 Shear range.

tion of this bridge analysis procedure is remarkably reliable and accurate, as shown in Figure 8, in which moment diagrams for a composite, two-span girder bridge are presented. These moment diagrams represent a comparison of the theoretically exact analysis results versus the results of the GBRIDGE analysis procedure plus a comparison of nonprismatic versus prismatic member analysis. The maximum percentage difference between the theoretically exact values and the GBRIDGE numeric solution is less than 1 percent. In addition, the maximum difference between the results obtained from a prismatic analysis and those obtained from a nonprismatic analysis is approximately 15 percent. This fact alone dramatically underscores the need to incorporate nonprismatic member properties into the general bridge analysis process.

CONCLUSIONS

The GBRIDGE analysis procedure is a practical alternative to currently used bridge analysis methods that consider only prismatic member properties. The GBRIDGE computer program is fully implemented and operational. The authors believe that the performance of the GBRIDGE program, in terms of accuracy of results and computation time, will impress the bridge designer when compared with other available software. To that end, the authors/developers of GBRIDGE will be pleased to share a scaled-down version of GBRIDGE with any not-for-profit organization, such as a state department of transportation, which may be interested in testing GBRIDGE in practice.

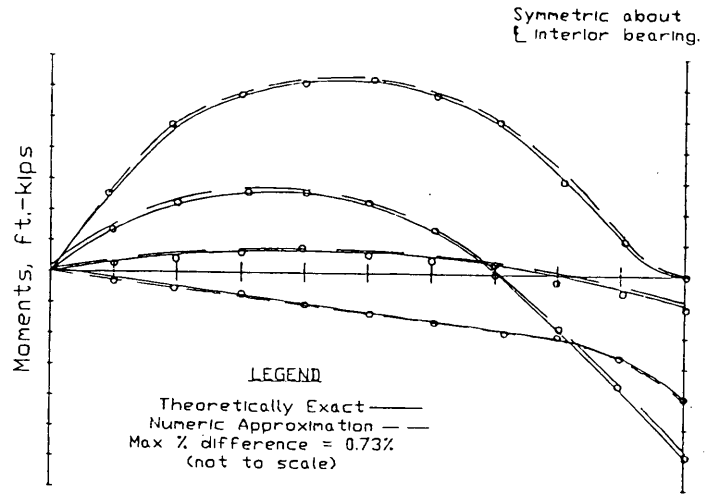

(a) Theoretically Exact vs. GBRIDGE Nonprismatic Members

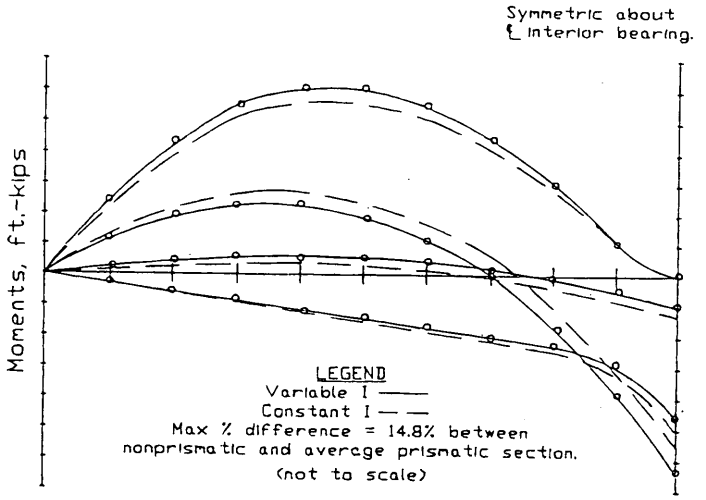

(b) Nonprismatic vs. Prismatic Member

FIGURE 8 Span moment variation.

REFERENCES

1. Zokaie, T. LDFAC: An Interactive Finite-Element Analysis Package for Generating Bridge Wheel Load Distribution Factors. Presented at the 1994 meeting of the AASHTO Subcommittee on Bridges and Structures, New Orleans, La. June 6, 1994.

2. Fenske, T. E., and S. M. Fenske. A Computer-Based Methodology for Investigation of Vehicle/Superstructure Interaction. In *Developments in Structural Engineering, Vol. I: Bridges and Space Structures*. E. & F.N. Spon/Chapman and Hall, London, England, 1990, pp. 191–199.

Publication of this paper sponsored by Committee on General Structures.

Twenty-Five-Year Performance History of Interlayer Membranes on Bridge Decks in Kansas

JOHN WOJAKOWSKI AND MUSTAQUE HOSSAIN

Interlayer membranes installed on six different bridge decks in Kansas were monitored for the last 20 to 25 years. Electrical resistivity measurements and visual distress surveys were made on these bridge decks in 1982 and 1991. The visual distress surveys were supplemented by the condition rating and maintenance history data from the Bridge Management System data base of the Kansas Department of Transportation. (KDOT). The membranes installed represented the preformed system, liquid/preformed systems, and liquid system. Electrical resistivity measurements taken in 1991 were compared with those obtained in 1982. The results show that the general performance of interlayer membranes installed between 1967 and 1971 has decreased since the last evaluation in 1982. However, the number of traffic carried by some of these decks has increased considerably. Two bridge deck membranes that have performed most effectively for the last 20 to 25 years were both liquid/preformed systems. These membranes were nonwoven polypropylene fabrics with an asphaltic overlay placed as a wearing surface. The lives of a coal tar-modified polyurethane elastomer interlayer membrane and a nonwoven polypropylene fabric system on a very old bridge have been exhausted. The poorest performance was obtained from a preformed polypropylene and coal tar sheet system and a liquid membrane system. In the recent past, KDOT used membranes as part of the maintenance overlays in which weight restrictions could not support concrete overlays. The agency now uses dense concrete/silica-fume concrete bridge decks during new construction.

Most bridge decks on the highways in Kansas are constructed of reinforcement portland cement concrete (RC) regardless of the type of bridge structure. The majority of these decks were designed to perform as both a structural unit and a wearing surface. Thus, deterioration of these decks usually result in poor riding quality and reduced structural strength, which eventually will make the bridges unsafe. The premature deterioration of RC bridge decks in Kansas was attributed to the spalling of concrete as a result of corrosion of reinforcing steel by chlorides from deicing salts (*1*). It was estimated that bridge decks in Kansas receive about 20 applications of salt per year at the rate of 369 kg/2-lane km (1,300 lb/2-lane mi) (*2*). Kansas experience also showed that corrosion of steel also resulted in horizontal cracks or delaminations as well as vertical cracks. According to Carl Crumpton of Kansas Department of Transportation (KDOT) (*3*, p. 165):

> The wedding of concrete and steel was an ideal union and we used lots of reinforced concrete for bridge decks. Unfortunately, we began tossing salt to melt snow and ice instead of rice for good fertility. That brought irritation, tensions, and erosion of previously good marital relations. No longer could the two exist in blissful union; the seeds of destruction had been planted and the stage had been set for today's bridge cracking and corrosion problems.

In the sixties, a study on bridge deck deterioration in Kansas considered treatment on bridge decks to prevent intrusion of salts (*1*). Hot-mix asphalt overlays were unsatisfactory and were not recommended unless they were placed over a membrane. A formal study of performance of interlayer membranes on bridge decks began in 1967 with an installation of polypropylene fabric on a 6-year-old, salted interchange bridge on rural I-70. A 3-mm (1/8-in.) overlay of cationic emulsion and crushed-chert-type chat aggregate was placed over this membrane. This installation marked the first time this proprietary membrane had been used on a bridge deck anywhere in the world. By 1970, the performance of this installation was satisfactory enough that from 1970 to 1974 four different types of membranes totaling nearly 10 000 m^2 (12,000 yd^2) were installed on seven salt-contaminated bridges by KDOT. The 12-year performance history of these membranes has been reported before (*4*). This paper describes the 25-year performance of six of the eight membranes installed between 1967 and 1974.

PROJECT DESCRIPTION

Installation and Location

Table 1 presents the types of interlayer membranes used on each bridge between 1967 and 1974. Data pertaining to each individual bridge is listed in Table 2. In 1983, a report was presented on the condition of these bridges (*1*). Each of the bridges had been exposed to varying degrees of traffic and weather before the placement of the membranes. At the time of membrane placement, these bridges were 16 to 35 years old. Some of the bridges had considerable seepage of water from the bottom of the deck during rainy or snowy seasons. However, this condition did not recur after the membranes were placed (*1*).

During the condition survey in 1983, the bridge decks showed some distresses, such as delamination, shallow spalling, and patched areas, but of very low severity. The appearance of the asphalt riding surface was generally satisfactory with the exception of some cracking. The shallow spalls were not patched before installing the membranes. This might have contributed to the cracking of the asphalt overlay. The membranes on Bridges B through G (Table 2) were 12 and 13 years old in 1983, whereas the membrane on Bridge H was 9 years old. During that time, they had been subjected to numerous salt applications for snow and ice control as well

J. Wojakowski, Materials and Research Center, Bureau of Materials and Research Center, Kansas Department of Transportation, 2300 Van Buren, Topeka, Kans. 66611-1195. M. Hossain, Department of Civil Engineering, Kansas State University, Manhattan, Kans. 66506.

TABLE 1 Interlayer Membrane Systems Used on Old Decks in Kansas

NCHRP 165 System No.[a]	System Type	Description
12	Preformed	A pliable sheeting construction from polypropylene and coal tar placed over a primer; a hot-mix overlay covers the membrane
52a	Liquid/ preformed	An applied in-place nonwoven polypropylene fabric with cationic emulsified asphalt; chat (chert) aggregate was rolled into CRS-2 emulsion for the wearing course
52b	Liquid/ preformed	Same as 52a, except that the fabric was placed over a thin coat of AC-5 and covered with a hot-mixed asphalt-concrete (AC) overlay
67	Liquid	A cold-applied, coal-tar modified, elastomeric polyurethane with a 55-lb grade asphalt-impregnated roofing sheet over it; all overlaid with 2.5 in. of hot-mix AC
80	Liquid	A coal-tar modified polyurethane elastomer cold-applied with catalyst (curing agent) added before application; the material was covered with No. 40 asphalt roofing sheet, which was topped with a hot-mix overlay

[a]See Table 9 of NCHRP Report 165 (2).

TABLE 2 Membrane Installation Data

1983 Bridge ID	NCHRP 165 System No.[a]	Date Membrane Installed	Date Bridge Constructed	Material Installed (yd^2)	Overlay Thickness (in.)	Bridge Type[b]
A	52a	1967	1961	112	0.125	RBGC
B	12	1970	1936	700	1.5	Cont. I-Beam
C	80	1971	1958	283	1.5	Cont. RC
D	80	1971	1959	404	1.5	Cont. RCDG
E	52b	1971	1953	254	2	Cont. RC
F	52b	1971	1936[c]	1,035	2	RCDG
G	80	1971	1936[c]	1,313	1.5	Steel I-Beam
H	67	1974	1924[d]	7,700	2.5	RC slab and Cont.

[a]as per Table 1 (Table 9 of NCHRP Report No. 165).
[b] bridge types are: RBGC = reinforced box-girder continuous; RCDG = reinforced-concrete deck girder; RC = reinforced concrete; Cont. = continuous.
[c] widened in 1971.
[d] widened in 1974.

as from 6.5 to 16 million vehicles. Trucks made up approximately 1.5 to 19 percent of that total traffic. It was concluded that the membranes had served quite well with little maintenance for 12 to 16 years (*4*). Since 1983, two of the decks with membranes (G & H) have been replaced. This paper discusses the current performance of the others (A through F). Table 3 lists the locational references of the bridges in this study.

Climate and Weather

The bridges in Kansas may be subjected to air temperatures as low as −40°C (−104°F) in the winter and as high as 49°C (120°F) in the summer. Winter windchill factors may reach −54°C (−129°F) in the winter, whereas the summer temperature of hot-mix asphalt overlays often reaches 71°C (160°F). Annual precipitation ranges from more

TABLE 3 Bridge Reference Data

Bridge ID	KDOT Bridge No.	County	Location
A	I70-21-272.62 (005)	Dickinson	Talmage Road IC over I-70
B	59-30-114.28 (050)	Franklin	US 59 over AT&SF RR and Local Rd. 0.02 mi. North of Anderson Co. Line.
C	39-103-44.48 (027)	Neosho	K-39 over Village Creek, west of Chanute, 5.74 mi. East of East Jct. US-75.
D	39-67-47.37 (021)	Neosho	K-39 over Cement Co. Road, west of Chanute, 1.66 mi. East of Wilson Co. Line.
E	54-104-317.27 (005)	Woodson	US-54 over MoPac RR, East of Yates Ctr. 2.49 mi. East of US-75
F	196-8-19.38 (061)	Butler	K-96 over Bakers Creek East of Potwin. 9.82 mi. S.E. of Harvey Co. Line

than 1,020 mm (40 in.) in the southeast part to about 410 mm (16 in.) in the southwest. The evaporation rate is higher than the precipitation rate all across the state. It is believed that if the bridge deck membranes can retard the downward movement of moisture and chlorides, evaporation will soon take over and keep them near the surface. Most Kansas bridges undergo an average of 60 or more freeze-thaw cycles each year (*4*). On the average, five to six winter snowstorms and one to three ice or sleet storm events are recorded. The snow and ice control are done by snowplows and deicing salts (mostly chloride salts).

Traffic History

The ridge decks with membranes have carried an increasing amount of traffic since 1982. Table 4 tabulates the 1982 and 1991 annual average daily traffic (AADT) as well as the percent trucks and cumulative traffic carried up to 1991. The bridges have carried from approximately 6.1 million vehicles to 22.5 million vehicles since the installation of the membranes. The percentage of trucks varied from 9.5 percent to approximately 20 percent.

TABLE 4 Traffic History of Bridge Decks with Membranes

Bridge ID	1982 ADT	1991 ADT	% Trucks (1991)	Cumulative Traffic (up to 1991)(millions)
A	890	977	-	> 6.1 (approx)
B	3,030	3,120	9.5	22.51
C	1,390	2,290	13.1	13.96
D	1,275	2,290	13.1	12.45
E	2,560	2,640	20.2	18.07
F	1,820	1,735	19.0	13.18

DATA COLLECTION

Resistivity Measurements

In July 1991, electrical resistivity of the water barrier membrane-pavement system was measured for each bridge listed in Table 2. The procedure outlined by ASTM D 3633-88 was followed to collect the data. Electrical resistivity measurements were recorded in ohms per square foot. Measurements were made on the centerline, both wheelpaths, and gutter on each deck. The total number of readings varied from 30 to 423 as shown in Table 5.

Visual Distress Survey

The visual distress survey during resistivity measurements consisted of surveying distresses, such as delamination, spalling, rust stains, and patched areas. However, the distressed areas were not quantified but rather observed qualitatively. The concrete bridge decks were not evaluated for chloride content because that would have involved breaching the interlayer membranes. Also, the original and 1982 conditions of the concretes were not available for comparison (with one exception).

Condition Survey and Maintenance History Data

The bridge condition and maintenance history data were also collected from the Bridge Management System (BMS) data base. In Kansas, bridges are inspected on a 2-year cycle, and a report is prepared with pertinent data on bridge inventory and geometry as well as condition of deck, superstructure, substructure, channel, approach roadway, and waterway adequacy (if applicable). The deck is rated on a scale of 1 (closed) to 9 (new, not open to traffic). In reality, the scale is 3 (unsafe, needs to be replaced) to 8 (good condition, no repairs needed). A rating of 7 indicates less than 5 percent deck area deterioration, whereas a rating of 6 shows 5 to 10 percent deterioration or spalls exposing rebars and delaminations. A rating of 5 indicates 10 to 20 percent deterioration and finally, a rating of 4 implies 20 to 40 percent deterioration. Any rating less than 4 will result in load-limit posting. A data base of bridge maintenance work and associated costs has been developed since 1978. Table 6 lists the biennial ratings of the bridge decks in this study from 1982 to 1991. The ratings are subjective.

DATA ANALYSIS

The 1991 resistivity readings were analyzed and the following guidelines were followed in this study to classify the condition of the interlayer membranes:

$>$ 1 076 300 ohms/m^2 (100,000 ohms/ft^2), good
107 630 to 1 076 300 ohms/m^2 (10,000 to 100,000 ohms/ft^2), questionable
21 500 to 107 630 ohms/m^2 (2,000 to 10,000 ohms/ft^2), poor
$<$ 21 500 ohms/m^2 (2,000 ohms/ft^2), very poor

TABLE 5 Electrical Resistivity Readings on the Bridge Deck in 1991

Bridge ID	Location	Total No. of Readings	Electrical Resistivity (ohm/m^2)					
			> 21500		> 107600		> 1,076,000	
			No.	%	No.	%	No	%
A	Wheel Path with Membrane	30	30	100	29	96.7	24	80
	Wheel Path without Membrane	28	17	60.7	10	35.7	2	7.1
B	Gutter	108	105	97.2	81	75.0	23	21.3
	Both Wheel Paths	108	108	100	100	92.6	76	70.4
	Centerline	54	54	100	44	81.5	11	20.4
C	Gutter	56	44	78.6	20	35.7	16	28.6
	Both Wheel Paths	112	110	98.2	71	63.4	28	25.0
	Centerline	28	16	57.1	5	17.9	2	7.1
D	Gutter	40	20	50.0	3	7.5	1	2.5
	Both Wheel Paths	80	80	100	76	95.0	68	85.0
	Centerline	40	25	62.5	22	88	1	2.5
E	Gutter	188	188	100	175	93.1	122	64.9
	Both Wheel Paths	188	188	100	187	99.5	178	94.7
	Centerline	47	47	100	47	100	47	100
F	Gutter	36	35	97.2	24	66.7	6	16.7
	Both Wheel Paths	72	72	100	67	93	41	56.9
	Centerline	18	18	100	18	100	12	66.7

TABLE 6 Condition Rating of Bridge Decks with Membranes

Bridge ID	NCHRP 165 System No.	Year									
		82	83	84	85	86	87	88	89	90	91
A	52a	4	4	-	5	-	4	-	4	-	4
B	12	7	-	6	-	6	6	5	5	5	5
C	80	-	8	-	8	-	8	-	8	-	8
D	80	-	7	-	7	-	7	-	7	-	7
E	52b	-	8	-	7	-	7	-	7	-	7
F	52b	7	-	7	-	8	-	7	-	7	-

Previous research has used a resistivity value of 5 382 000 ohms/m^2 (500,000 ohms/ft^2) as the standard of excellence for the interlayer membrane performance (*5*). However, analysis of data in this study showed little difference in the percent of the deck area greater than 1 076 300 ohms/m^2 (100,000 ohms/ft^2) and that percent greater than 5 382 000 ohms/m^2 (500,000 ohms/ft^2). Ideally, the membranes should be monitored so that they can be replaced when 50 percent of the bridge deck area with membrane no longer performs as designed. If a membrane is placed on an existing bridge deck, an effort should be made to determine the existing chloride content.

RESULTS AND DISCUSSION

Bridge A was constructed in 1961, and the interlayer membrane was placed on one half of the deck in 1967. The other half was kept bare for comparison as a control. This was the first time this polypropylene fabric membrane was installed anywhere in the world. Electrical resistivity measurement data taken in 1991, from the section covered with the interlayer membrane, showed that 80 percent of the readings were greater than 1 076 300 ohms/m^2 (100,000 ohms/ft^2). Only 7.1 percent of the readings exceeded 1 076 300 ohms/m^2 (100,000 ohms/ft^2) in the section without the interlayer membrane. A visual inspection of the bridge deck indicated that the section covered with the interlayer membrane had fewer asphalt wearing surface distresses. Fine cracks were observed on the underside of the deck near the abutments, and rust staining was evident.

During the 1991 evaluation by the BMS survey crew, the whole deck was rated as 4 on a scale of 3 (unsafe) to 8 (new, open to traffic) as shown in Table 6. The rating was also 4 in 1982 and the asphalt wearing surface condition was judged to be poor at that time. In the mean time, the traffic increased from 890 vehicles per day in 1982 to 977 vehicles per day in 1991. In 1991, exposed steel was observed in some areas and approximately 20 percent of the bridge deck area was badly spalled. Between 1983 and 1991, the deck spalls were repaired 17 times at a cost of $3,825.

The interlayer membrane was placed on the deck of Bridge B in 1970. The resistivity measurements showed that only 34.1 percent of the readings were greater than 1 076 300 ohms/m^2 (100,000 ohms/ft^2) or in other words, good. In 1982, 100 percent of the electrical resistivity measurements had been above 1 076 300 ohms/m^2 (100,000 ohms/ft^2) as shown in Table 7. Lower resistivity readings in 1991 were found near the gutter and centerline. In those areas, the asphalt overlay may not have been densified by the traffic as in the wheelpaths, or the coal tar used with the polypropylene membrane may not have been worked by tire pressure as expected. Visual inspection of the bridge showed large cracks in the asphalt overlay. The hubguard was badly spalled exposing the reinforcing steel. However, the hubguard deterioration was also reported by the BMS survey since 1982. The underside of the deck had a large longitudinal crack near the east edge of the deck. The steel girders had begun to rust at the contact point with the deck. In 1991, the wearing surface had map cracking and rutting and was rated to be poor in the BMS survey. However, no major maintenance has been performed on this bridge deck since 1978.

The interlayer membrane was installed on the deck of Bridge C in 1971. In 1991 resistivity measurements showed that 50 percent of the bridge deck membrane tested had resistivities higher than 1 076 300 ohms/m^2 (100,000 ohms/ft^2). The data collected in 1982 indicated that only 38.6 percent of the deck measured above 1 076 300 ohms/m^2 (100,000 ohms/ft^2). The asphalt overlay was noted to be in good condition in 1991. There was a full-length centerline crack with several shorter transverse cracks beginning at the centerline. The underside of the deck was in good condition, with dark staining only on the bottom side of the hubguards. In 1991, wearing surface condition was rated to be good by the BMS survey. Thus far, no major maintenance on this deck has been reported.

The membrane on Bridge D was placed in 1971 and the type is similar to that on Bridge C (NCHRP 165 System 80). Resistivity

TABLE 7 Comparison of 1982 and 1991 Electrical Resistivity Readings

Bridge ID	1982 Readings (ohm / m²)						1991 Readings (ohm / m²)					
	> 21,500		> 107,600		> 1,076,300		>21,500		>107,600		> 1,076,300	
	No.	%	No.	%	No.	%	No.	%	No.	%	No.	%
A					-	-	30	100	29	96.7	24	80.0
B	189	100	189	100	189	100	267	98.9	223	82.6	92	34.1
C	139	99.3	98	70.0	54	38.6	170	86.7	96	49.0	46	23.5
D	432	100	429	99.3	409	94.7	125	78	101	63.0	70	44.0
E	133	100	133	100	133	100	423	100	409	96.7	347	82.0
F					-	100	125	99.2	99	78.6	59	46.8

measurements taken in 1991 indicate that 23.5 percent of the deck was in good condition. Data from 1982 showed that the entire deck was in good condition, with each measurement above 1 076 300 ohms/m² (100,000 ohms/ft²). In 1991, the asphalt overlay appeared to be in very good condition. Several transverse cracks, which ranged from 1.8 m (6 ft) to 2.7 m (9 ft), were seen throughout the structure. The hubguard was spalling with reinforcing steel visible in several locations. The underside of the bridge deck had no visible damage. During 1991 survey, the wearing surface condition was rated to be good in the BMS survey, but the curb was found to be deteriorated with exposed rebars.

An interlayer membrane was placed on Bridge E in 1971. Resistivity measurements taken in 1991 indicate that 82 percent of the bridge deck tested above 1 076 300 ohms/m² (100,000 ohms/ft²) or, in other words, appeared to be good. The 1982 results showed that 94.7 percent of the area tested above 1 076 300 ohms/m² (100,000 ohms/ft²), as shown in Table 7. The mainline deck overlay was noted to be in excellent condition in 1991. Some cracks, both transverse and longitudinal, were observed in the shoulders of the deck overlay, which seemed older than the mainline deck overlay. The expansion joints on the underside of the bridge deck were in poor condition. The concrete was badly spalled, exposing reinforcing bars.

In 1971, the interlayer membrane was placed on Bridge F. The electrical resistivity data collected in 1991 indicated that 46.8 percent of the interlayer membrane was in good condition. In 1982, 100 percent of the membrane was deemed to be in good condition on the basis of the results from the resistivity testing. A visual inspection of the bridge in 1991 noted that the asphalt overlay was in poor condition. There were many large transverse and longitudinal cracks observed in the overlay. The concrete railing was in bad condition, "crumbling away." Stalactites, up to 102 mm (4 in.) long, were observed in a 3.1-m (10-ft) longitudinal crack on the underside of the deck. There were transverse cracks beginning at the longitudinal crack. The sides of the deck exhibited varying degrees of spalling from 0.3 m (1 ft) to 1.5 m (5 ft) from the edge of the bridge. Staining was evident in the areas in which spalling had occurred. This deck is programmed to be replaced in FY 1995.

Figure 1 shows the percentages of each deck area that had a resistivity measurement greater than 1 076 300 ohms/m² (100,000 ohms/ft²) in 1983 and 1991. The bare part of the deck on Bridge A is also shown as [ACON]. It is apparent that four of the six bridges

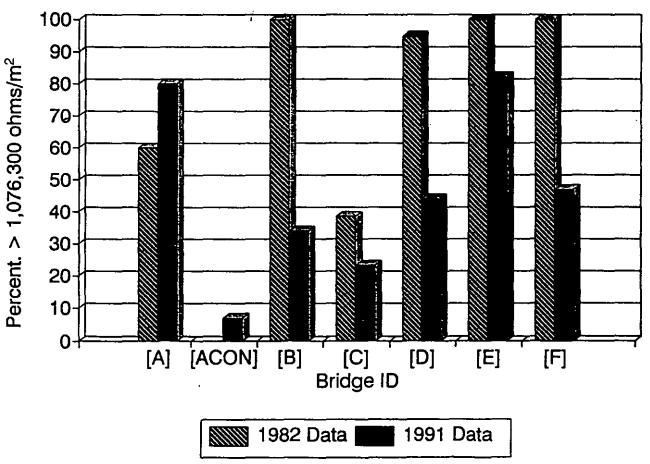

FIGURE 1 Comparison of 1982 and 1991 electrical resistivity readings (percentage of deck > 1 076 300 ohms/m²).

showed a decrease in the performance of the membranes from 1983 to 1991. However, there is some variability in the data presented, and that may be a result of the condition of the asphalt overlay at the time the electrical resistivity measurements were taken, the way a specific mastic responds to the traffic or other factors.

Electrical resistivity data obtained on Bridges B through F, which received interlayer membranes during 1970 and 1971 changed markedly from 1982 to 1991. In 1982 86.7 percent of the total bridge deck area tested had resistivity higher than 1 076 300 ohms/m^2 (100,000 ohms/ft^2), whereas in 1991 only 47.3 percent of the area showed resistivity higher than 1 076 300 ohms/m^2 (100,000 ohms/ft^2). The bridges were showing signs of deterioration that were most likely related to salt contamination. However, traffic on some of these bridges also has increased considerably. When the electrical resistivity values measure below 1 076 300 ohms/m^2 (100,000 ohms/ft^2) for 50 percent of a bridge deck area, the useful life of the interlayer membrane should be considered complete. The state of Oregon uses the same guidelines for determining the useful life of an interlayer membrane (*6*). Using the data from the bridge decks in this study, the useful life of an interlayer membrane in Kansas would range from 15 to 20 years. The membrane should be replaced before deterioration of the concrete structure begins.

The two bridge deck membranes that have performed most effectively were both liquid/preformed systems on Bridges A and E. The nonwoven polypropylene fabric was installed on both of these with an asphaltic overlay placed as a wearing surface.

The coal-tar-modified polyurethane elastomer interlayer membrane on Bridge C, and another liquid/preformed membrane on Bridge F, have reached the end of their useful lives. Over 50 percent of the bridge deck area measured below 1 076 300 ohms/m^2 (100,000 ohms/ft^2) for these two bridges. These interlayer membranes should be replaced before deterioration intensifies on the structures. Bridge F is old compared with Bridges A and E and carries a higher percentage of truck traffic.

The poorest performance was obtained from a preformed polypropylene and coal tar sheet on Bridge B, and a liquid membrane system on Bridges C and D. These decks were most likely already salt contaminated when the membranes were installed. The bridges may need major structural repair before the placement of another protective system.

CURRENT KDOT PRACTICE WITH RESPECT TO MEMBRANES

KDOT installed membranes on 14 bridges in Wichita, Kansas, area in 1980s. In addition to these, one membrane was installed on a deck on route K-77 near Manhattan, Kansas, in 1986 and another one on a viaduct on I-70 in Topeka, Kansas, in 1990. All these membranes were part of maintenance overlays used where weight restrictions could not support concrete overlays. Currently, KDOT uses dense concrete/silica-fume concrete bridge decks during new construction.

Two bridge deck overlays in Wichita on I-235 with Petromat over AC-5 and surfaced by a 51-mm (2-in.) wearing course of bituminous mixes were constructed in 1985 and have been monitored since then. In 1993, surveys were made on both bridge decks to assess the performance of the membranes. The surveys consisted of visual observations on the structures, chaining to check for delamination, resistivity readings, and crack measurements. Over 70 percent of the readings were above 1 076 300 ohms/m^2 (100,000 ohms/ft^2) after 8 years. Other results of these surveys are shown Table 8. Very little cracking was observed on either overlay. The resistivity readings were somewhat lower than those of the previous year. Overall, performance of these decks with membranes was satisfactory.

CONCLUSIONS

The general performance of interlayer membranes installed on six existing bridge decks between 1967 and 1971 in Kansas has decreased since 1982 as judged in terms of electrical resistivity measurements and visual distress survey results. The visual distress surveys were supplemented by the condition rating and maintenance history data from the Kansas BMS data base. The membranes used represented the preformed system (NCHRP 165 System 12), liquid/preformed systems (52a and 52b), and liquid system (System 80). Electrical resistivity measurements taken in 1991 on all six bridge decks were compared with those obtained in 1982. The results showed that the two bridge deck membranes that have performed most effectively for the last 20 to 25 years were both liquid/preformed systems (Systems 52a and 52b). These were nonwoven polypropylene fabrics with an asphaltic overlay placed as a wearing surface. The lives of a coal-tar modified polyurethane elastomer interlayer membrane (System 80) and a nonwoven polypropylene fabric system (System 52b) on a very old bridge have been exhausted. The poorest performance was obtained from a preformed polypropylene and coal tar sheet system (System 12) and a liquid membrane system (System 80). In the recent past, KDOT used membranes as part of the maintenance overlays where weight restrictions could not support concrete overlays. Currently, KDOT uses dense concrete/silica-fume concrete bridge decks during new construction.

TABLE 8 Results of Bridge Deck Surreys, 1993

Bridge No.	Percent Delamination	Electrical Resistivity (ohms/m^2) (% greater than)		
		21,500	107,630	1,076,300
235-87-10.07	1.40	100.0	84.8	54.5
235-87-12.39	1.49	100.0	99.2	84.8

ACKNOWLEDGMENTS

The authors acknowledge the financial support provided by KDOT for this study. Thanks are due to Richard McReynolds of KDOT for his support of this study. Contributions made by Karthik Vaidyanathan of Kansas State University and David Heston of KDOT to this study are gratefully acknowledged.

REFERENCES

1. Bukovatz, J. E., C. F. Crumpton, and H. E. Worley. *Bridge Deck Deterioration Study*. Final Report. State Highway Commission and FHWA, 1973.
2. McCollom, B. F. Design and Construction of Conventional Bridge Decks That Are Resistant to Spalling. In *Transportation Research Record 604*, TRB, National Research Council, Washington, D.C., 1976, pp. 1–5.
3. Mehta, P. K., and P. J. M. Monteiro. *Concrete-Structure, Properties and Materials*, 2nd ed. Prentice Hall, N.J., 1986.
4. Bukovatz, J. E., and C. F. Crumpton. Kansas' Experience with Interlayer Membranes on Salt-Contaminated Bridge Decks. In *Transportation Research Record 962*, TRB, National Research Council, Washington, D.C., 1983, pp. 66–68.
5. Van Til, C. J., B. J. Carr, and B. A. Vallegra. *NCHRP Report 165: Waterproof Membranes for Protection of Concrete Bridge Decks: Laboratory Phase*. TRB, National Research Council, Washington, D.C., 1976.
6. Heston, D., and J. Wojakowski. *Interlayer Membranes on Salt Contaminated Bridge Decks*. Internal Report. Kansas Department of Transportation, Topeka, Kan Aug. 1992.

Publication of this paper sponsored by Committee on General Structures.

Behavior of a Red Oak Stress-Laminated Bridge in Rhode Island

EILEEN DOBER-YOUNG AND GEORGE TSIATAS

The results of a 15-month monitoring program of a red oak stress-laminated timber bridge are evaluated. The bridge is the first of its kind in the state of Rhode Island and one of the earliest of its type constructed of red oak in the United States. The monitoring program included inspecting the bridge periodically, reading the load cell, measuring the wood moisture content, and recording the ambient temperature and relative humidity at the bridge site. The evaluation demonstrates that additional design factors may need to be considered before red oak is completely accepted as a construction material for stress-laminated bridges. Specifically, the monitoring program revealed fluctuations in the wood moisture content, and ambient temperature affected the stress levels in the steel rods to an extent that these factors may need to be considered in the design of this type of bridge. The loss of the initial rod stresses in the bridge were investigated; these losses correlated very well with exponential functions. The exponential functions are used to predict when and if the bridge will have to be restressed to maintain the design minimum stress levels.

Stress-laminated timber deck bridges were initially conceived in Ontario, Canada, in the mid-1970s as a method of rehabilitating structurally deficient nail-laminated timber bridges. The process involves threading steel rods transversely through the wide face of the timber deck and tensioning the rods so the individual laminae are compressed together. Loads are distributed through the structure via friction developed between the laminae as opposed to nail-laminated deck bridges in which the loads are transferred through the nails. Today, stress laminating is used not only as a method of strengthening existing bridges but also as a method of designing new bridges. In Europe, the rods are sometimes outside the laminations to avoid reducing the wood section.

A number of stress-laminated timber bridges have been constructed in the United States under the Timber Bridge Initiative, which was sponsored by Congress in 1989 and has been administered by the USDA Forest Service (*1*). Traditionally, short-span bridges have been replaced with concrete and steel; however, many design engineers favor timber as a viable alternative, mainly because timber is not subject to the detrimental effects of salt and corrosion. Also the initiative promotes the use of locally grown timber; therefore, many municipalities are replacing the structurally deficient or functionally obsolete bridges within their jurisdictions with new stress-laminated timber bridges constructed of local materials and by local labor.

E. Dober-Young, Bridge Engineering Section, Rhode Island Department of Transportation, 2 Capitol Hill, Providence R.I. 02903. G. Tsiatas, Department of Civil Engineering, University of Rhode Island, Kingston, R.I. 02881.

NORTH ROAD BRIDGE

The North Road Bridge over Hemlock Brook in the town of Foster is the first stress-laminated timber deck bridge in Rhode Island. Funding for the construction of the bridge was partially provided by the USDA Forest Service through the Timber Bridge Initiative. The bridge is a single-span structure on a 6-degree skew. An elevation and cross section are shown in Figures 1 and 2, respectively. The bridge replaces an older steel beam bridge that had severely deteriorated. The new superstructure rests on the original concrete abutments that were modified slightly to accommodate the new superstructure width.

The superstructure consists of red oak laminations 50.8 × 64.5 mm that are not continuous over the bridge span. Instead, staggered butt joints are provided (Figure 3). The bridge span is 6.405 m measured parallel to the road centerline. The out-to-out bridge width measures 7.32 m perpendicular to the road centerline. The bridge is covered with a bituminous wearing surface that measures approximately 76.2 mm at the crown and 50.8 mm at the curbs. The wearing surface is composed of 38.1 mm of binder and a varying amount of surface course.

The stressing system consists of 13 ASTM A722 steel rods 15.875 mm in diameter. The spacing of the rods is shown in Figure 4. This figure also shows the location of the load cells that were placed on four of the rods to monitor rod stress levels. The rods have an ultimate strength of 1033.5 MPa, and the plans called for the rods to be galvanized or epoxy coated. The bulkhead system consists of ASTM A36 bearing plates 203.2 × 203.2 × 19.05 mm and ASTM A36 anchorage plates 76.2 × 76.2 × 19.05 mm. The red oak was green when ordered and was dried to a 17 percent moisture content just before treatment with creosote. Figures 5 and 6 show the elevation of the bridge and a detail of the bulkhead system, respectively.

The deck was originally assembled on the bridge approach roadway. The rods were initially stressed to 124.6 kN, and the deck was lifted and positioned on the abutments. One week later, the rods were stressed again to the same level. Final stressing (to 124.6 kN again) was completed 5 weeks after the second stressing. A single hydraulic jack was used for all stressings, and multiple passes were completed each time that the bridge was stressed to ensure a uniform stress.

MONITORING PROGRAM

When construction of the bridge was completed in the fall of 1992, a monitoring program was started to evaluate the performance of the actual structure. Although it is in general expensive and not usually used for bridge construction, red oak is in abundance in the area and

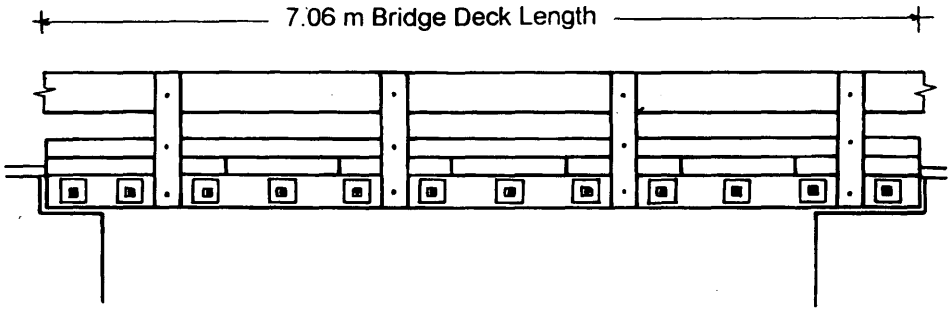

FIGURE 1 Elevation of the North Road Bridge.

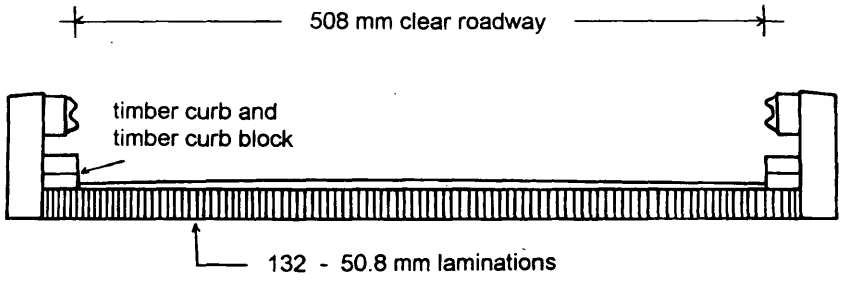

FIGURE 2 Cross section of the North Road Bridge.

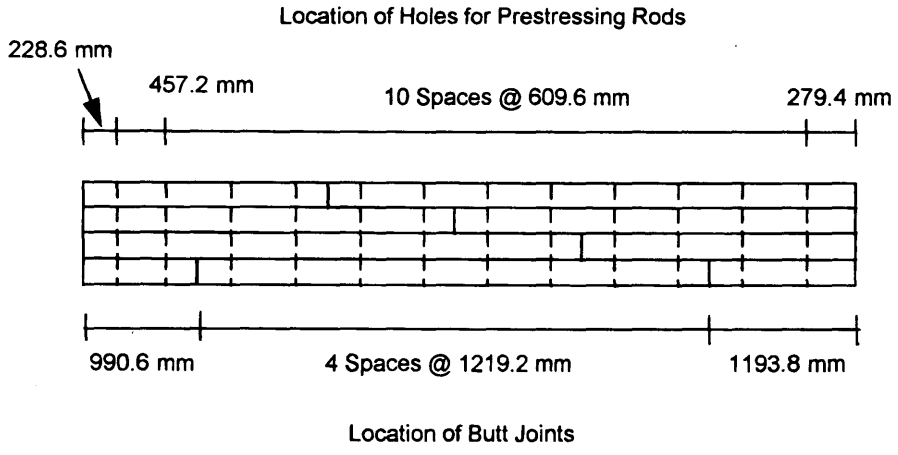

FIGURE 3 Butt joint pattern of the North Road Bridge.

was selected as the natural choice. The monitoring program included the following procedure.

General Condition of the Bridge

The bridge was visually inspected several times during a 15-month period. The performance of the wearing surface was monitored; specifically, it was inspected for cracks and for signs of how well it was binding to the timber deck. The timber deck was visually inspected at the abutments for signs of crushing and also for signs of crushing near the anchor plates at each rod. In the areas exposed to drainage, the deck was also inspected for signs of decay. The deck underside was investigated for splitting, sagging, checking, cracks, and water penetration. Overall, the deck was inspected for signs of distress and delamination.

Stress Levels

Four load cells were installed to monitor the force in the corresponding rods. These were numbered 1458, 1459, 1460 and 1461 by the manufacturer and are referred to by these numbers in this paper. Figure 4 shows the exact positioning of the load cells. The

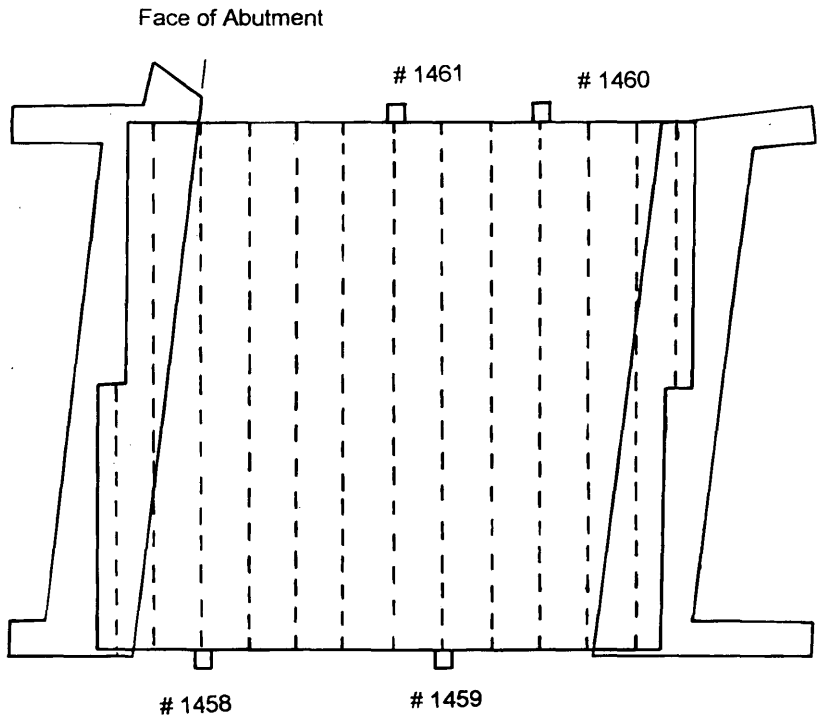

FIGURE 4 Plan view of bridge showing spacing of prestressing rods and location of load cells.

FIGURE 5 Side view of bridge.

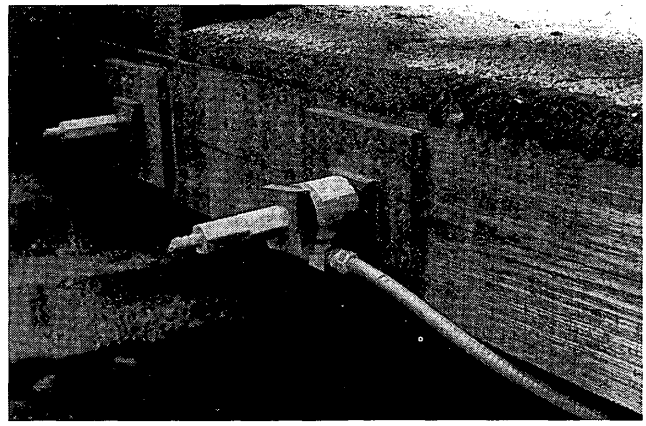

FIGURE 6 Detail of load cell attachment.

force in each rod was measured beginning on the day the superstructure was lifted into place, which coincided with the second stressing of the bridge. Daily readings were taken beginning on that day for 10 consecutive days; thereafter, weekly readings were taken for 11 consecutive weeks. The weekly readings were followed by 11 monthly readings.

MOISTURE CONTENT

Two moisture meters were used to monitor the moisture of the red oak laminae. The first meter was a "protimeter mini" and measured moisture at a depth of 12.7 mm. The second, known as a "hammer electrode," measured moisture at a depth of 44.45 mm. The moisture content of the bridge timber was measured beginning with the first weekly stress reading. Therefore, 11 moisture content measurements were taken weekly, and 11 moisture content measurements were taken monthly. The moisture content was measured on the underside of the deck at ten random locations each time. The average of the ten measurements was calculated and recorded. Because 2 different probes were used, a total of 20 measurements were made each time.

Ambient Temperature and Relative Humidity

A pocket psychrometer was used to obtain the ambient temperature and relative humidity at the bridge site. The ambient temperature

was recorded weekly for 11 weeks and monthly for 11 months on the same days as those for which the wood moisture content was measured. In addition, the ambient temperature was recorded 15 times during one 24-hr period. The relative humidity at the bridge site was measured each time the ambient temperature was recorded.

EVALUATION OF RESULTS

General Condition

In general, the pavement on the North Road Bridge was found to be performing very well after more than 1 year in service. There were fine transverse cracks in the pavement along the bridge end joints, running across the full width of the bridge, but these appeared because the pavement inadvertently was not sawn and sealed at these joints. The steel rods exhibited light rusting at their ends where they were field cut but not treated with a protective coating. The rods were field cut so they would not extend more than 152.4 mm beyond the nuts. There was a split (a longitudinal crack parallel to the wood grain) extending the full length of the bridge in the fascia laminae on both sides of the bridge. The split occurred sometime after the bridge was assembled. There was also some light crushing of the fascia laminae near the bearing plates at most of the rods. (Crushing of the fascia laminae has occurred in many other stress-laminated bridges.) The underside of the deck revealed that two inside laminae were split. This splitting probably occurred during the first stressing, which was used primarily to eliminate the warps in the wood.

Loss of Rod Stresses

Adequate stress levels in the steel rods are essential for this type of timber bridge construction. Many factors affect the prestressing force, including creep in the wood, moisture content, temperature, and humidity (*2,3*). It is difficult to separate the effects of each individual factor in the total loss of prestressing force. Loss of prestress caused by creep is predominant in the early stages of the bridge life. However, contrary to laboratory tests, it is difficult in the field to capture the initial effect. In this particular bridge, stressing was done during assembly as a means of flattening warped planks. The load cells were placed on the rods during the second stressing (Day 7); therefore, the loss of prestress in the interim between Days 0 and 7 was not recorded. Between the second stressing (Day 7) and the final stressing (Day 43), the rod equipped with Load Cell 1461 exhibited the sharpest decline in prestress, losing 39 percent of its initial value. The rods equipped with Load Cells 1458, 1459, and 1461 lost 13, 22, and 30 percent, respectively, during this period. It can be assumed that most of this loss was attributable to creep in the wood.

The rod instrumented with Load Cell 1461 showed the greatest loss of prestress over the monitoring period of 415 days; however, it maintained 47 percent of its initial prestress, which was considered acceptable in other stress-laminated bridges constructed of other wood species. The rods instrumented with Load Cells 1458, 1459, and 1460 have maintained 76, 86, and 58 percent of their initial prestress levels, respectively. These have been considered high retention levels in other stress-laminated bridges constructed of other wood species.

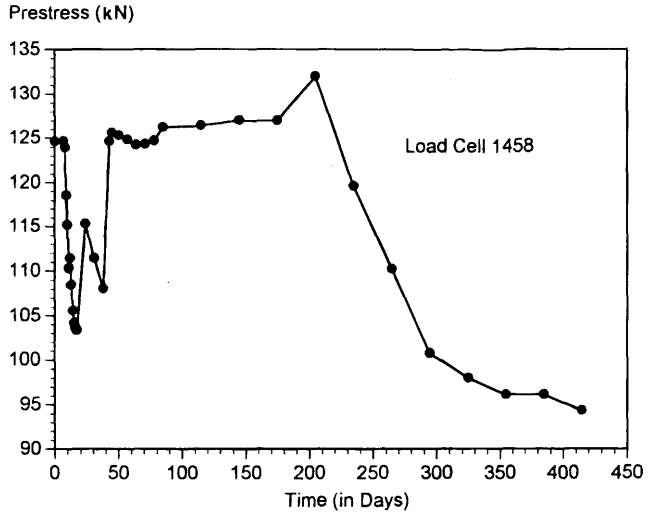

FIGURE 7 Variation of stressing force in Cell 1458.

Figures 7 through 10 show the loss of prestress over time for the instrumented rods. The graphs show that the prestress levels did not constantly decline between readings. After an initial decrease that was attributable again to creep, increases as well as decreases in prestress levels were evident. The variation in prestress levels can be attributed to fluctuations in the wood moisture content, relative humidity, and ambient temperature as discussed in the following paragraphs.

Of further interest, the force in the rod instrumented with Load Cell 1458 remained at or above 124.6 kN for 3 weekly readings from the third stressing (Day 43) up to and including Day 57. It is suspected that this rod actually was stressed to a value greater than 124.6 kN on the third stressing.

A power regression analysis and an exponential regression analysis were performed on the data from each of the rods. The results for Load Cells 1458 and 1461 are shown graphically in Figures 11 and 12. The analyses incorporated only the load cell readings after

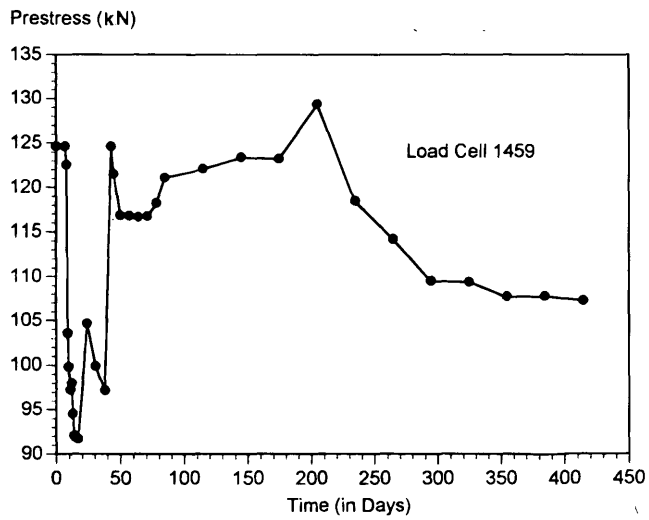

FIGURE 8 Variation of stressing force in Cell 1459.

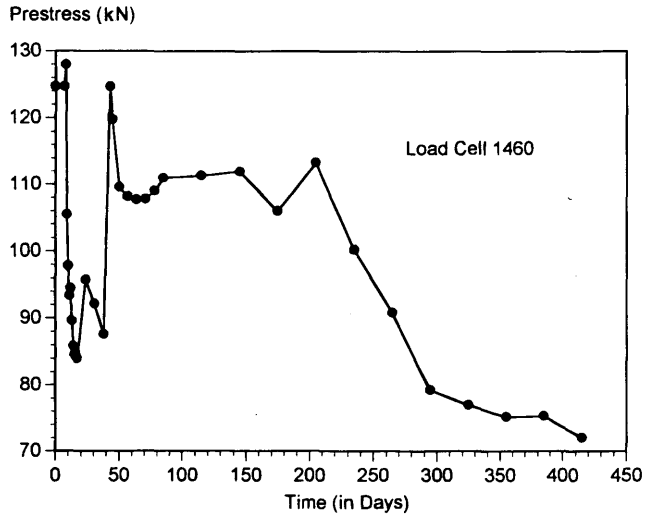

FIGURE 9 Variation of stressing force in Cell 1460.

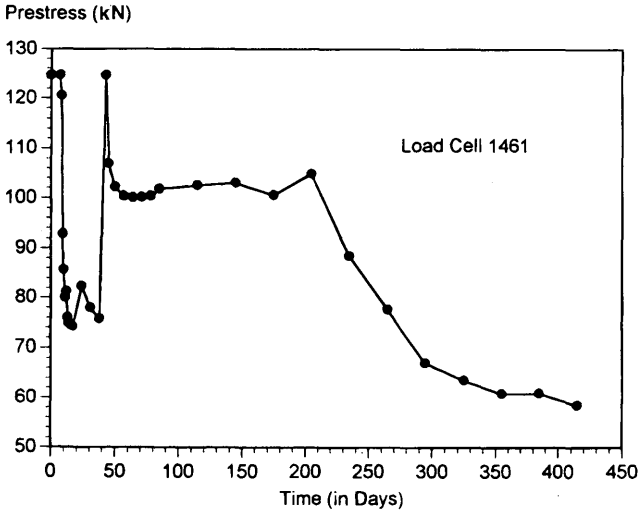

FIGURE 10 Variation of stressing force in Cell 1461.

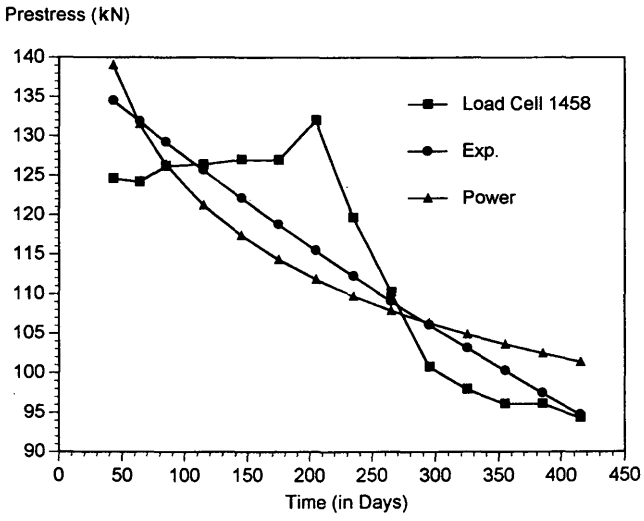

FIGURE 11 Regression curves for Cell 1458.

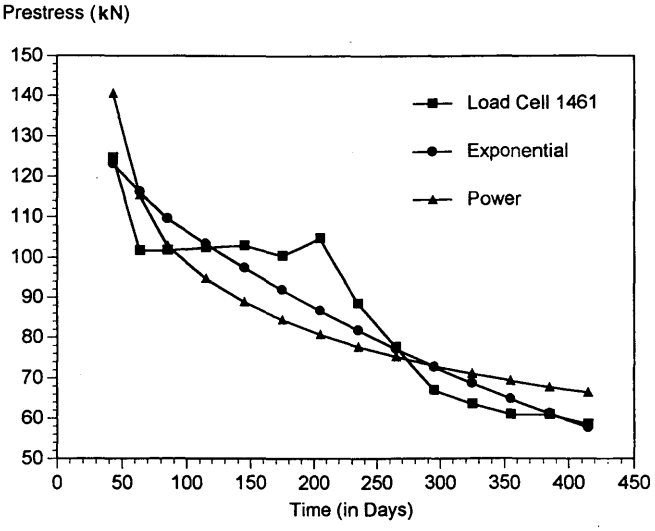

FIGURE 12 Regression curves for Cell 1461.

the third stressing. Most of the readings after the third stressing were taken monthly; however, the first few were taken weekly. The weekly readings were averaged to represent monthly readings before the regression analyses were attempted. The figures and the associated equations can be used to predict the stressing forces at various times. For instance, for the rod instrumented with Load Cell 1458, the exponential regression curve gives $P = 99.235$ kN and the power regression curve gives $P = 102.35$ kN after 385 days of the stressing.

According to AASHTO, the loss of prestress in a stress-laminated bridge caused by wood creep varies in an exponential way. AASHTO further gives the minimum level of prestress in service as 40 percent of the initial prestress (*4*). Therefore, for the North Road Bridge, the minimum level of prestress allowed by AASHTO is 49.84 kN. Using this minimum, the regression functions can be used to predict whether the bridge will have to be restressed and when this restressing would have to occur. The exponential regression curve predicts that the North Road Bridge will have to be restressed on the 484th day from the initial stressing on the basis of Load Cell 1461, which gave the most critical results. Similarly, the power regression curve predicts that the bridge will have to be restressed in 939 days from the initial stressing. Study of the individual correlation coefficients of the regression analyses indicates that the exponential fit represents the data slightly better than the power one. In the exponential case, the coefficients varied from 0.87 to 0.93, but under the power law assumption they varied from 0.73 to 0.85.

A better estimate can be obtained by performing regression analyses on the average forces from all load cells. The equation for the case of the exponential regression is found to be

$$P = 129.05\ (0.999)^T \tag{1}$$

and the equation for the power regression is given by

$$P = 259.435\ T^{-0.178} \tag{2}$$

where P is the prestress force in kilonewtons and T is the number of days from the initial stressing. The results are shown graphically in Figure 13. The exponential regression function for the average of

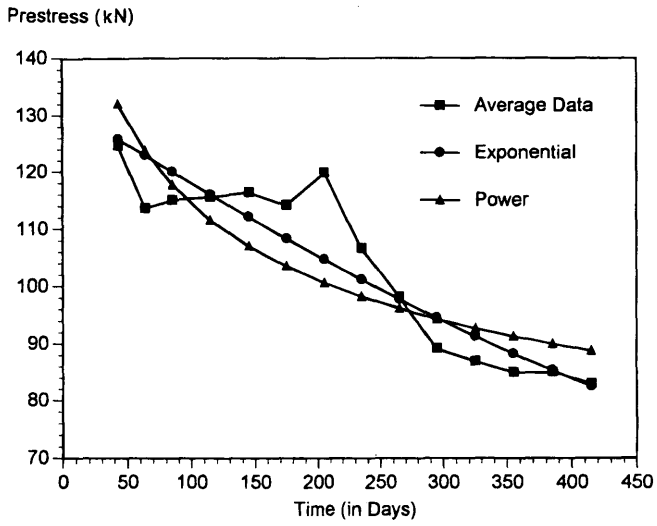

FIGURE 13 Regression curves for average of all cells.

the forces in all four instrumented rods predicts that the bridge will have to be restressed in 3 years from the initial stressing, whereas the power regression predicts that it will have to be restressed in 29 years from the initial stressing. The correlation coefficients reveal that the data correlated better with the exponential regression curve; however, the difference between the correlation coefficients is not as great as the difference between those of the individual load cells.

The regression analyses mentioned earlier for the loss of prestress over time represent the loss of prestress not only caused by wood creep but also by changes in the wood moisture content, ambient temperature, and relative humidity.

The variation of the wood moisture content with time is shown in Figure 14. When moisture is gained in the wood, the wood expands. This causes the prestress forces to increase. Similarly, as the wood dries, it shrinks, which can contribute to a decrease in the prestress levels. This in general held true for the North Road Bridge. By comparing Figures 14 and 8 it is evident that the moisture versus time curve follows a similar pattern as the force versus time curves. Generally, as the percent change in moisture content increased, the percent change in prestress force also increased. However, the data show some exceptions, which are probably caused by other factors, such as temperature variations.

The variation of temperature with time is shown in Figure 15. It has been reported that stressing forces decline with lower temperatures because of the different coefficients of thermal expansion for timber and steel. However, a temporary gain in the prestress forces was recorded during the winter months, which is attributable to the high moisture content in the bridge during this time. The high levels of precipitation during the winter months in Rhode Island caused the moisture content in the wood to increase, thereby causing a swelling of the wood and an increase in the prestress forces. The drop in temperature during the winter months may have caused the wood to shrink; however, the shrinkage was counteracted by the tendency of the wood to swell because of increases in moisture content.

Daily fluctuations in the prestress forces in the North Road Bridge did occur. The prestress levels and the temperature at the bridge site were monitored during a 24-hr period. The data reveals that the prestress levels in a stress-laminated bridge will fluctuate proportionately to fluctuations in temperature. However, the fluctuation appeared to be of the order of 4.45 kN for an 11C° temperature variation.

Relative humidity at the bridge site was recorded first weekly and then monthly. Results indicate that the ambient humidity level does not have a very pronounced effect on the prestressing force other than it can affect the wood moisture. The high levels of relative humidity at the bridge site during the summer had little effect on the prestress levels. The low levels of precipitation during that summer in Rhode Island must have caused the wood to shrink, thereby counteracting any tendency of the wood to swell because of high humidity.

CONCLUSIONS

The North Road Bridge, the first stress-laminated timber deck bridge in Rhode Island and one of the earliest of its type constructed of red oak in the United States, has been in service for almost 2 years, and its behavior has been monitored. This paper presents

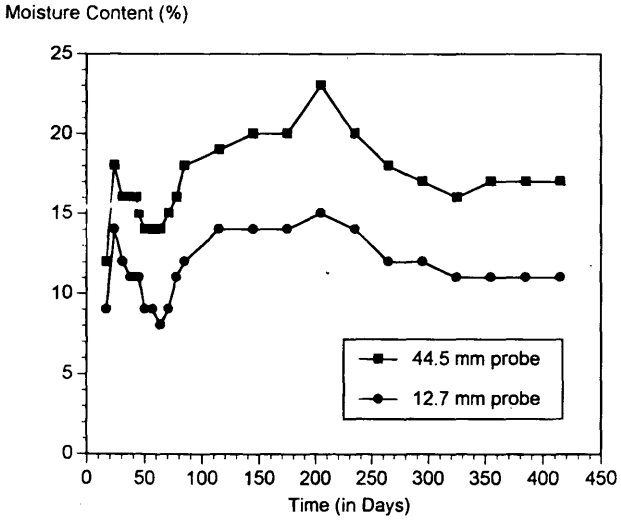

FIGURE 14 Variation of moisture content.

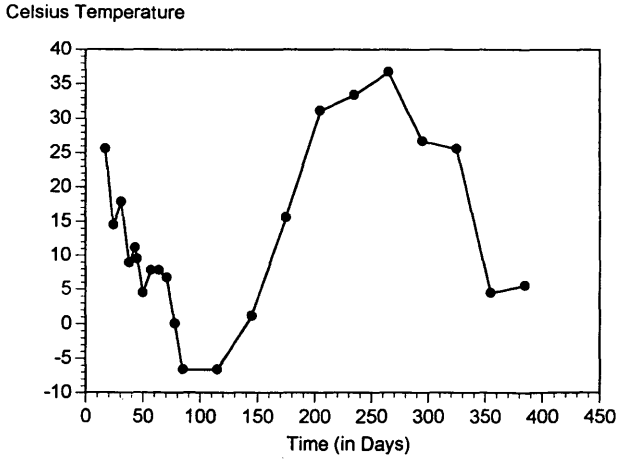

FIGURE 15 Variation of ambient temperature.

and evaluates the results of the first 415 days of the monitoring program, which included monitoring the loss of prestress over time, the variation of wood moisture content, the fluctuation in ambient temperature and relative humidity at the bridge site.

The study found that the four instrumented steel rods have maintained 47 percent or more of their initial prestress values. The residual stress levels are acceptable according to the AASHTO Guide, which requires the prestress levels to be 40 percent or more of the initial values. The loss of prestress over time was found to be more of an exponential nature than of a power nature. The data for each instrumented rod correlated well with exponential curves as did the data for the average of the forces in each instrumented rod. Exponential functions were empirically derived and were used to predict when and if the bridge would have to be restressed on the basis of the 40 percent minimum level of prestress allowed by AASHTO. On an individual rod basis, the functions predict that the rods will have to be restressed very soon. However, on an average basis, the functions predict that more time is allowed before restressing is necessary. The prestress levels in other stress-laminated bridges constructed of other wood species have leveled off much sooner than the levels in the North Road Bridge.

The study has found that besides wood creep, the wood moisture content plays an important role in the fluctuations of the stressing forces. On the other hand, fluctuations in ambient temperature at the bridge site had a minor influence on the prestress levels. During one 24-hr period, the forces in the rods were seen to fluctuate proportionately with ambient temperature; that is, a rise in temperature was accompanied by an increase in rod forces and vice versa. However, the effect of seasonal temperature changes on the prestress levels was opposite. A seasonal decrease in temperature at the North Road Bridge site was accompanied by an increase in rod forces. This was attributed to the increase in precipitation during the winter months of this monitoring program.

The general condition of the bridge was monitored, and it was found that the outside laminae were crushing in the vicinity of the bearing plates, which is typical of many stress-laminated timber deck bridges, and the fascia laminae exhibited full-length splits. Besides these and minor problems with the pavement at the joints, the general condition of the bridge is satisfactory. One of the steel rods exhibited much higher stress loss than the remaining three. This rod is located at the midspan point of the bridge. It is possible for higher stress levels in that location to have caused higher creep levels as well as increased crushing around the bearing plates. Also, higher warping levels may have existed in the planks in that location.

The conclusions reported herein correspond to this particular bridge and may not be applicable to all stressed timber bridges. However, the results of this monitoring program have contributed to the pool of data needed to develop a reliance on red oak as a viable material to be used for stress-laminated timber bridge construction. The monitoring program will be continued for some time to assess the long-term effects of moisture cycles. Specifically, it has been suggested that during high moisture periods when the wood expands and the force increases, higher creep losses occur, and the losses do not reverse when the moisture levels reduce. These additional periodic creep losses can contribute to increased loss of prestress over time.

ACKNOWLEDGMENTS

Partial support for this study was provided by the USDA Forest Service. The plans for the North Road Bridge were provided by Commonwealth Engineers and Consultants, Providence, R.I.

REFERENCES

1. Sarisley, E. F. Jr., and M. L. Accorsi. Prestress Level in Stress Laminated Timber Bridges. *Journal of Structural Engineering*, Vol. 116, No. 11, No. 1990, pp. 3003–3019.
2. Ritter, M. A. Timber Bridges Design, Construction, Inspection and Maintenance. USDA Forest Service, Washington, D.C., June 1990.
3. Oliva, M. G., and A. Dimakis. Behavior of Stress-Laminated Timber Highway Bridge. *Journal of Structural Engineering*, Vol. 114, No. 8, Aug. 1988.
4. *Guide Specifications for the Design of Stress-Laminated Wood Decks*. AASHTO, April 1991.

Publication of this paper sponsored by Committee on General Structures.